LA-5250-PR

PROGRESS REPORT

C.3

Progress Report

LASL Controlled Thermonuclear Research Program

for a 12-Month Period Ending December 1972

los alamos
scientific laboratory
of the University of California
LOS ALAMOS, NEW MEXICO 87544

UNITED STATES
ATOMIC ENERGY COMMISSION
CONTRACT W-7405-ENG. 36

This report presents the status of the LASL Controlled Thermonuclear Research program. Previous annual status reports in this series, all unclassified, are:

LA-4351-MS
LA-4585-MS
LA-4888-PR

Printed in the United States of America. Available from
National Technical Information Service
U. S. Department of Commerce
5285 Port Royal Road
Springfield, Virginia 22151
Price: Printed Copy $5.45; Microfiche $0.95

LA-5250-PR
PROGRESS REPORT
UC-20
ISSUED: June 1973

los alamos
scientific laboratory
of the University of California
LOS ALAMOS, NEW MEXICO 87544

Progress Report

LASL Controlled Thermonuclear Research Program

for a 12-Month Period Ending December 1972

Compiled by

F. L. Ribe

CONTENTS

I. INTRODUCTION

(F. L. Ribe)

This year has seen the completion of experiments on both the 5-m toroidal Scyllac sector and the 5-m linear Scyllac experiment. The Scyllac system is now being converted to its final toroidal configuration. Results on the sector and on the Scylla-IV-3 feedback experiment indicated the necessity of increasing the Scyllac major radius from 5 to 8 m to decrease the growth rate of the $m = 1$, $k = 0$ instability and to accommodate the technical characteristics of the feedback apparatus.

The theoretical MHD equilibrium of the toroidal Scyllac sector has been verified in detail. Plasma confinement is terminated in 6 to 12 μsec by $m = 1$, $k = 0$ transverse motion, whose character has not yet been differentiated between instability and loss of equilibrium. Confinement times are approximately equal to the transit time of rotational effects from the ends, which are observed to have an appreciable effect on the loss of confinement.

The linear Scyllac has provided scaling data on end loss and electron temperature with plasma length which confirm the simple theories. However, the large effects of end stoppering predicted by theory for high-β mirrors are not realized.

The ZT-1 toroidal high-β Z pinch has provided extensive data on field profiles and has been brought into full operation with crowbarring and reversed toroidal field. There are indications that as the stable reversed-field distribution with positive pressure gradient on axis is approached, the stability of the discharge is increased. In one particular case, good stability for 7 μsec, terminated by a (possibly diffusive) change to unstable field profiles, is seen. A laser-scattering apparatus is being applied to the device.

The experimental work on anomalous absorption of electromagnetic waves near the electron-plasma frequency has produced extensive results on anomalous resistivity and the coupling of electric fields to collective plasma modes. The resistivity agrees with theory at low electric fields for underdense plasmas. However, for ω_p near to ω (the microwave frequency), and for higher electric fields, strong anomalous or enhanced resistivity due to the parametric excitation of plasma waves is observed. This is correlated with quantitative measurements of the energy spectrum of the anomalously heated electrons. These results may have far-reaching connotations in the anomalous resistance of Tokamaks, laser plasma heating, and heating of plasmas in various confinement experiments.

Work has begun on implosion heating of θ pinches in higher-voltage regimes. This work is of primary importance to the staged θ-pinch concept to be incorporated into the θ-pinch scientific feasibility experiment.

High-β plasma theory has had an exceptionally fruitful year, both in respect to Scyllac and high-toroidal Z pinches. In the Scyllac context, the plausibility of wall stabilization of the $m = 1$, $k = 0$ mode has been strengthened by investigation of MHD mode structures in $\ell = 0$ and $\ell = 1$ systems with diffuse plasma profiles. This provides theoretical justification for far-reaching plans to eliminate feedback stabilization in staged θ pinches. Work is beginning on

equilibria and stability of toroidal Z pinches with noncircular cross sections (belt pinches) and continues to demonstrate stable high-β programmed diffuse pinch distributions appropriate to ZT-1.

In the area of reactor technology we now have a program approaching maturity, with interrelated systems design and reactor core design, and related neutronics programs and materials research. A conceptual design in collaboration with the Argonne National Laboratory will be completed in the next half year.

In the superconducting magnetic energy storage research, the 20-kJ experiment has served to show solutions for switch material choice and construction. It also demonstrates the systematics of "current" switching by exceeding the critical current density and "latching" by heating to above the critical temperature. A 300-kJ apparatus is under construction.

II. THETA-PINCH PROGRAM

A. Summary of θ-Pinch Activities (G. A. Sawyer)

During the past year an extensive series of experiments on the Scyllac toroidal sector was completed (Sec. II.B), and conversion of the apparatus to the full Scyllac torus has been started. The toroidal sector was operated with nine variations of $\ell = 0$ and $\ell = 1$ magnetic fields to furnish equilibrium against the toroidal drift force F_R. The $\ell = 0$ bumpy field was always furnished by grooving the main compression coil. In the early experiments, the grooves had 2 rectangular steps (land and groove) per wavelength, later coils had 8 steps per wavelength, and finally 260 steps per wavelength were used to improve the accuracy of the fields. In the early experiments the $\ell = 1$ field was provided either by capacitor-driven helical windings or by grooving the main compression coil. Figure II-1 shows the final coil grooved for both $\ell = 0$ and $\ell = 1$ fields in 260 steps. Some of the experiments either included stuffers to delay penetration of the field into groove regions or provided for the addition of small vertical fields. In all cases there was a persistent sideways motion of the plasma (probably the m = 1, k = 0 instability), which carried it to the wall in 6 to 12 μsec. When the length of the toroidal sector was decreased from 5 to 3 m, the onset of the plasma motion moved earlier; also, the plasma behavior became more reproducible. This result leads us to believe that end effects have influenced plasma behavior in the toroidal sector.

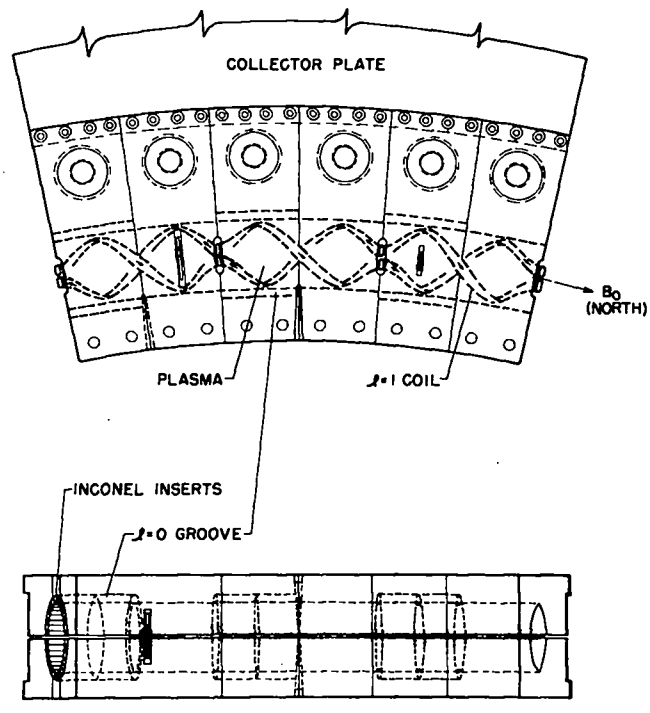

Fig. II-1.
Arrangement of $\ell = 1$ coils and $\ell = 0$ grooves (with time-delay inserts) to give a toroidal equilibrium in the Scyllac 5-m toroidal sector.

Experiments on the 5-m linear Scyllac began in March 1972 and ended in March 1973 (Sec. II.C). A prominent feature in the results is a wobble of the plasma column that begins a few microseconds after the start of the discharge. In operation without magnetic mirrors, the wobble has limited amplitude of about 1.5 cm. We believe the wobble to be induced by an end effect. When strong magnetic mirrors are applied (mirror ratio about 3.0), there is evidence of instability and the plasma column often hits the wall. Plasma end-loss rates were measured by holographic interferometry. The end-loss time (1/e) is 18.9 μsec with magnetic mirrors and 11.5 μsec without mirrors. The end loss with mirrors occurs at a somewhat faster rate than predicted by high-β mirror theory.

In view of the pronounced end effects observed in both toroidal sector and linear Scyllac experiments, we expect plasma behavior to be quite different in the full Scyllac torus where there will be no end effects.

Development of the feedback equipment to handle residual plasma unbalance in Scyllac is being carried out on the Scylla-IV experiment (Sec. II.D). Ten feedback modules were used in a successful test of their ability to handle an instability that is deliberately induced with $\ell = 1$ fields. The feedback system involves difficult technology. On Scyllac we will be able to generate only about 200 G of $\ell = 0$ field from the feedback modules with a risetime of 1.6 μsec. We expect the resulting feedback to provide the necessary force balance in Scyllac. However, a decision to build the full Scyllac torus at 8-m-major diam instead of 4.8 m as originally planned was made partly to provide a more favorable force balance for the feedback system (Sec. II.E).

Development of new plasma diagnostics, refinement of old methods, and development of the Scyllac computer system are continuing as important activities of the θ-pinch group (Secs. II.F-J).

B. Scyllac 5-Meter Toroidal Sector Experiment (W. R. Ellis, C. F. Hammer, F. C. Jahoda, W. E. Quinn, G. A. Sawyer, R. E. Siemon, and E. L. Zimmermann)

1. Introduction. When a straight θ pinch is bent into a torus the combination of plasma pressure and the gradient of the toroidal longitudinal compression field B_o forces the plasma toward the outside of the torus. For a plasma of major radius R and minor radius a the force per unit length is $F_R = \beta B_o^2 a^2/4R$, where β is the ratio of plasma pressure to the external magnetic pressure $B_o^2/8\pi$. In the Scyllac experiment[1-3] the force F_R is opposed by a combination of $\ell = 1$ helical transverse fields and $\ell = 0$ bumpy fields. The toroidal equilibrium[4,5] of this system and the stability[6-9] of a straight $\ell = 1$ or $\ell = 0$ plasma column have been treated in the MHD approximation. In the experiments on the Scyllac toroidal sector, the $\ell = 1$ helical field is chosen because theory[6-9] predicts a growth rate for the dominant $k \approx 0$, $m = 1$ mode that vanishes in leading order. The $\ell = 0$ fields produce asymmetry in the overall plasma excursions $\delta_1 + \delta_o$, which is necessary to produce the equilibrating force,

$$F_{1,0} = [\beta(3-2\beta)/8] \quad B_o^2 h^2 a^3 \delta_1 \delta_o \quad (ha \ll 1), \qquad (1)$$

where $2\pi/h$ is the wavelength of the $\ell = 1,0$ fields.

A description of the toroidal-sector device and the initial plasma experiments have been given.[2] These initial experiments included (1) control experiments to measure the plasma heating and toroidal drift in the presence of a pure toroidal field with no helical or bumpy fields, (2) initial measurements with $\ell = 1,0$ toroidal equilibrium field configuration with $\ell = 0$ groove depths of 1.8 cm, and (3) initial plasma measurements with reduced $\ell = 0$ groove depths of 0.9 cm. During the past year, plasma experiments were continued on the $\ell = 1,0$ helical equilibria and stability of the high-β, θ-pinch plasma in toroidal geometry. In the first set of experiments the $\ell = 1,0$ equilibrium configuration was varied by changing the conditions of the $\ell = 0$ grooves in the main coil, which generate the bumpy field. For each of these $\ell = 0$ geometries, the $\ell = 1$ fields, which were generated by driven windings inside the main toroidal coil, were used to optimize the plasma containment. This set of experiments included (1) additional plasma measurements with $\ell = 0$ groove depths of 0.9 cm, both unstuffed and stuffed with time-delay Inconel inserts, (2) experiments with conducting shells and $\ell = 0$ groove depths of 0.75 cm, and (3) measurements with conducting shells and 0.6-cm $\ell = 0$ groove depths. A second set of experiments was performed in two different compression coils, whose inner surfaces were shaped to provide both $\ell = 1$ helical and $\ell = 0$ bumpy field components superimposed on the main toroidal field.

2. Experimental Arrangement. The Scyllac toroidal sector[1-3] has a major radius of 237.5 cm, extends through an angle of 120°, and has a coil arc length of 5 m. Each meter section of the compression coil is driven by a 700-kJ capacitor bank of 210 1.85-μF, 60-kV capacitors. The experiments reported here were performed with one-half the bank charged to 45 and 50 kV to produce peak magnetic compression fields of 33 to 50 kG with risetimes of ~4 μsec, followed by crowbarred waveforms with L/R times of 250 μsec.

Figure II-1 shows the initial arrangement for applying $\ell = 1$ and $\ell = 0$ fields to the Scyllac plasma. The $\ell = 1$ fields were applied by means of bifilar helical windings, divided into one-period ($\lambda = 33.2$ cm) lengths with 5.75-cm radius. The $\ell = 1$ coils' current, driven by a capacitor bank, rose to its maximum value in ~3 μsec, followed by a crowbarred L/R decay of 95 μsec. The $\ell = 0$ fields were generated by annular grooves in the inner surface of the compression coil (Fig. II-1). In some experiments the onset of the $\ell = 0$ fields was delayed a few tenths of microseconds by annular sets of stainless steel trapezoidal sections (stuffers). In other experiments split copper cylinders (shells) were installed over the $\ell = 0$ grooves, with appropriate flux gaps at the edges, to provide an effectively uniform wall for the $\ell = 1$ image currents. These shells were also used to reduce the effective depth of the $\ell = 0$ grooves.

A second set of experiments was performed in shaped compression coils in which the flux surfaces of the $\ell = 1$ and $\ell = 0$ fields were machined into the inner surface of the main coils. The advantages of this $\ell = 1,0$ configuration are: (1) a constant ratio of both the $\ell = 1$ and $\ell = 0$ fields to the main field in time, (2) an improvement in the uniformity of the $\ell = 1$ and $\ell = 0$ fields, and (3) a technical simplification of the generation of the $\ell = 1$ and $\ell = 0$ fields. A disadvantage of this geometry is the fixed ratios of the $\ell = 1$ and $\ell = 0$ fields to the main toroidal field B_o.

The following measurements were made of the plasma properties: (1) three high-speed streak cameras that viewed the plasma column side-on were used to record the transverse motions of the plasma column, (2) a coupled-cavity helium-neon laser interferometer was used to measure the time history of plasma electron density integrated along a chord of the plasma cross section, (3) a magnetic loop and probe arrangement was used to measure the magnetic flux excluded by the plasma. Combined with density profiles from the luminosity, the excluded flux can be expressed in terms of the plasma β, (4) a ten-channel, side-on luminosity experiment was used to obtain the intensity profiles of the plasma column. These luminosity profiles, in conjunction with the coupled cavity interferometer data, gave absolute density profiles,

and (5) scintillation and silver-foil activation counters were used to measure the neutron emission.

3. Summary of Initial Results (Experiments A and B). Table II-I lists the $\ell = 1,0$ geometries and experiments performed in the various equilibrium configurations where B_o is the average toroidal field, $\bar{b}$ is the average radius of the coil bore, δ_o is determined from luminosity profiles and calculated from Eq. (6), and δ_1 is derived from magnetic fields and β through Eq. (7).

a. Measurements with a Compression Coil of Constant Minor Diameter and No $\ell = 1$ or $\ell = 0$ Fields. Control experiments[1,2] in a smooth-bore coil (14.4-cm diam) with a pure toroidal field (no helical or bumpy fields) showed that (1) the plasma-heating processes are unaffected by the toroidal curvature and (2) the plasma column drifts to the discharge tube wall (inside radius = 4.3 cm) in 2.2 (P_{D_2} = 10 mTorr) to 2.7 μsec (20-mTorr filling) because of the toroidal force. The peak plasma β was ~0.8, the ion temperature ~1 keV, and the density on axis 2 to 3 x 10^{16} cm^{-3} with a 10-mTorr deuterium filling pressure. Similar plasma parameters are measured in the experiments described below.

b. Initial Measurements with $\ell = 1$ and $\ell = 0$ Fields ($\ell = 0$ Groove Depth = 1.8 cm). With the 1.8-cm $\ell = 0$ grooves (Exp. B, Table II-1), the $\ell = 1,0$ fields balanced the toroidal force.[1,2] However, the plasma lifetime was limited to 4 to 6 μsec by a "ballooning" effect [or z dependence of the plasma sideward (m = 1) motion], which carried the plasma column to the wall periodically in each $\ell = 0$ groove region. Probing of the $\ell = 1$ fields showed them to be 35% stronger in the region of the 1.8-cm-deep grooves due to differences in $\ell = 1$ image current effects in groove and land regions. This electrical effect was anticipated in the original design; its considerable consequences for plasma behavior were not.

4. Plasma Measurements with 0.9-Centimeter, $\ell = 0$ Groove Depths.

a. Plasma Equilibrium and Stability. Reduction of the $\ell = 0$ groove depths to 9 mm (Exp. C, Table II-1) and the associated reduction of the z dependence of the $\ell = 1$ fields to 14% had a marked effect in largely eliminating the ballooning. The m = 1 (sideward) motion was nearly the same in the land and groove regions, with improved plasma containment times of 6 to 9 μsec. The streak photographs of Fig. II-2A show the horizontal plasma motions without the $\ell = 1$ coils excited. The motion is a simple toroidal "drift" to the walls with no observable effect induced by the bumpy $\ell = 0$ fields. In Fig. II-2B the $\ell = 1$ coils were excited to 56 kA. Following the initial implosion the plasma column takes up an equilibrium position, which is shifted slightly inward in the groove regions, outward in the land regions, and vertically in the planes between the groove and land regions as expected from the helical equilibrium shift of the plasma column. After remaining in equilibrium for 6 μsec, the plasma begins to drift outward in both the land and groove regions and strikes the wall in the land region.

In Experiments C through F of Table II-1, with $\ell = 0$ groove depths in the range of 6 to 9 mm, the transverse motions of the plasma column were similar. A few percent increase in the $\ell = 1$ current changes the plasma motion from being radially outward to inward in both land and groove regions. The observed transverse motions of the plasma at various positions around the torus show that (1) the plasma column takes up an initial helical shift and comes into an equilibrium position that lasts 4 to 11 μsec in contrast to a complete absence of equilibrium without the $\ell = 1,0$ fields, (2) as the plasma moves away from the equilibrium position, the motion in the land and groove regions is usually similar, i.e., the column either moves radially outward or inward, and (3) the motion of the plasma column develops largely in the horizontal plane of the torus rather than in random directions. The values of the quantity $hRB_{\ell=0}\ B_{\ell=1}/B_o^2$ required experimentally to achieve toroidal equilibrium are in the 0.36 to 0.41 range (Exps. C-F, Table II-1) compared with 0.62 to 0.33 for sharp boundary theory for respective β values of 0.6 to 0.8.

The similar plasma motions observed in the land and groove regions, which occur predominantly in the horizontal plane of the torus, suggest that either the expected long wavelength m = 1 plasma instability is developing or an imbalance in the applied equilibrium force and the toroidal force is occurring. The development of a force imbalance could result from (1) failure of the $\ell = 1$ fields to track the toroidal B_o field in time (there is field tracking to within ± 15%), (2) change of plasma β in time, and (3) the relaxation of an enhanced δ_o (the distortion of the plasma column produced by the $\ell = 0$ grooves), which likely occurs in the implosion phase of the discharge due to the absence of "stuffers" in the $\ell = 0$ groove regions. If the m = 1 instability is developing, the growth rates are in the range of 0.8 to 1.0 MHz.

b. Neutron Emission. The neutron emission decreases rapidly at about 3.5 μsec, which is at a time near the maximum of the magnetic field, while the streak photographs show the plasma to be confined. In the present mode of operation with the neutron emission (~2 x 10^6 m^{-1}) near its threshold, the majority of neutrons may result from an initial hotter plasma in the land regions followed by a decrease in the average temperature as plasma equilibrium is achieved between the land and groove regions, thereby resulting in decreased neutron emission. The

TABLE II-1

SUMMARY OF SCYLLAC SECTOR EXPERIMENTS

Experiment	R (M)	$\ell = 0$ Groove Depth (cm)	Groove Condition	$\ell = 1$ Windings	$\ell = 1$ Grooves	$\bar{b}$ (cm)	B_0 (kG)	$B_{\ell=0}/B_0$	$B_{\ell=1}/B_0$	β	a (cm)	h (cm^{-1})	ha	δ_0	δ_1
A	2.375	0	—	No	No	7.21	50	0	0	—	—	—	—	0	0
B	2.375	1.8	Stuffed	Yes	No	8.11	42.6	0.220	0.06	0.8	1.0	0.19	0.19	0.3[a] 0.49	0.54
C	2.375	0.9	Unstuffed	Yes	No	8.57	40.0	0.105	0.08	0.75	1.0	0.19	0.19	0.2[a] 0.19	0.68
D	2.375	0.9	Stuffed	Yes	No	8.57	40.0	0.105	0.086	0.65	1.0	0.19	0.19	0.2[a] 0.14	0.68
E	237.5	0.75	Unstuffed 1.5-mm shells	Yes	No	8.50	40.2	0.089	0.090	0.8	0.7	0.19	0.133	0.27	1.19
F	237.5	0.6	Unstuffed 3.0-mm shells	Yes	No	8.42	40.9	0.071	0.096	—	—	0.19	—	—	—
G	237.5	Sinusoidal	(8 step)	Yes	Yes	8.02	41.0	0.09	0.07	0.95	0.88	0.19	0.167	0.60	0.82
H	237.5	Sinusoidal	(8 step)	No	Yes	8.02	41.0	0.09	0.07	—	—	0.19	—	—	—
J	237.5	Sinusoidal	(260 step)	No	Yes	10.25	36.3	0.08	0.08	0.85	0.7	0.19	0.15	0.24	1.06

[a]Measured.

plasma is heated more in the land regions because of (1) the enhanced δ_o, which decreases the plasma loading in the land sections and increases it in the groove regions, (2) the 23% larger magnetic compression field in the land regions, and (3) the 11% larger initial azimuthal electric field ($E_\theta \propto dB/dt$) in the land regions. The luminosity profile data show that an axial redistribution of the plasma line density occurs after the implosion on a time scale of microseconds. The line density decreases in the groove regions and increases in the land regions. A similar variaton is observed in the local plasma β as measured in land and groove regions. The luminosity data provide the variation of the plasma radius a, in time, which indicates that $\delta_o \equiv (a_{land} - a_{groove})/(a_{land} + a_{groove})$ is decreasing in time as expected with unstuffed grooves.

c. Excluded Flux and Luminosity Measurements. Figure II-3 shows the time variation for typical discharges of the excluded flux, plasma radius a, and computed β on axis. These data are derived from the side-on luminosity and balanced probe measurements by curve fitting, under the simplifying assumptions that the plasma has a Gaussian density profile and a uniform temperature. The Gaussian profile provides a good fit to the luminosity data, and the plasma radius a is taken as the e-folding width of the density profile.

These data have been used to study the approach to axial pressure equilibrium as shown in Figs. II-4 and II-5 for the unstuffed case. Figure II-4 shows the plotted ratio β_L/β_G, which should equal $(B_G/B_L)^2$ and $(b_G/b_L)^4$ if plasma pressure is independent of length along the column as it should be. (Here L and G refer to the center

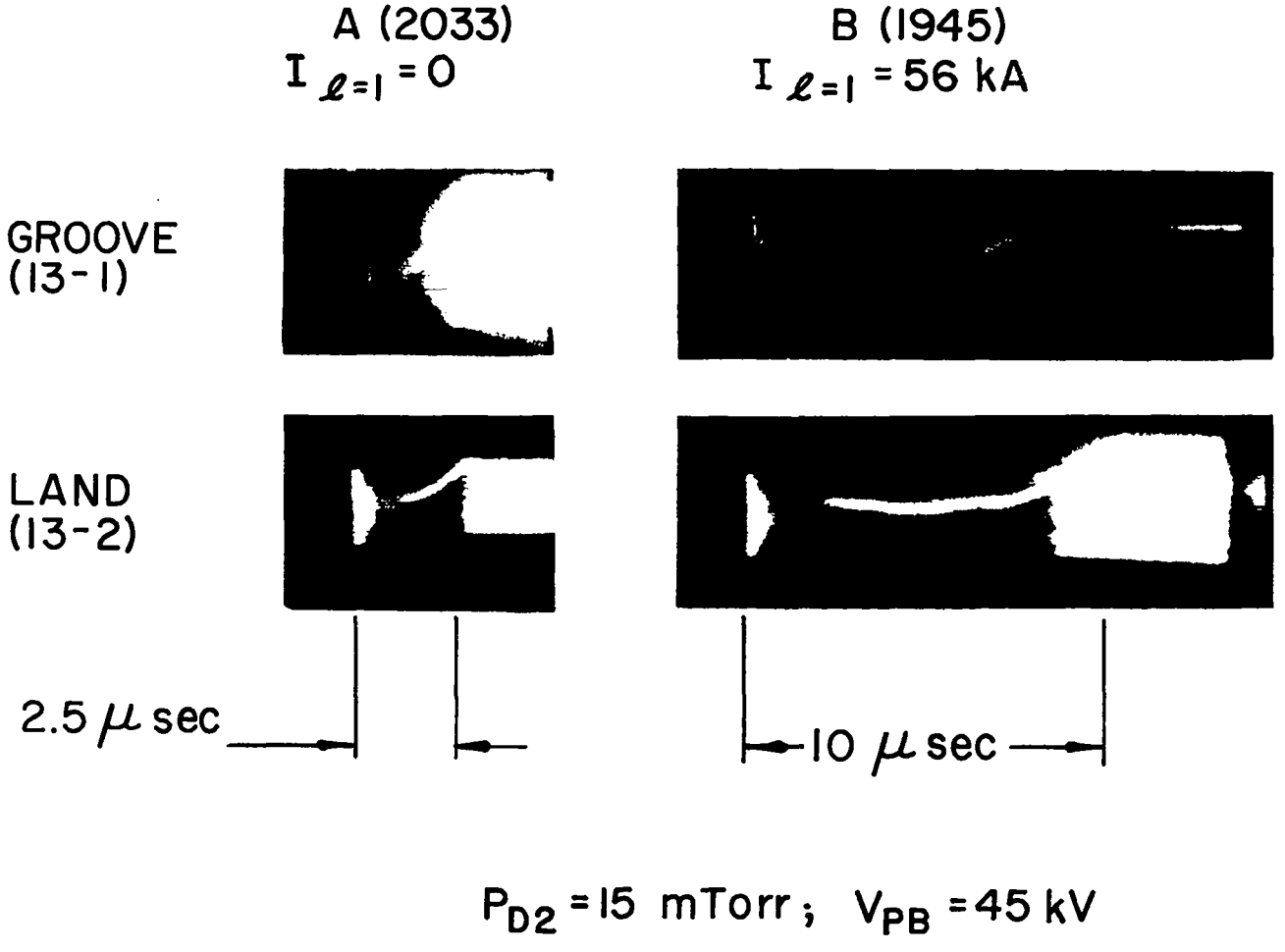

Fig. II-2.
Streak photographs near the center of the toroidal sector plasma showing horizontal motions (Exp. C, Table II-1).

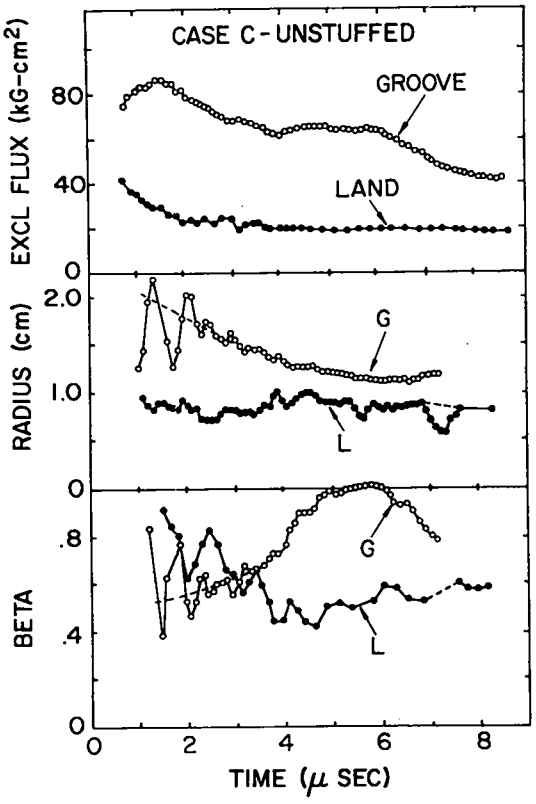

Fig. II-3.
Observed time variatons of excluded flux, plasma radius from luminosity profiles, and computed β on axis (Exp. C, 50 kV).

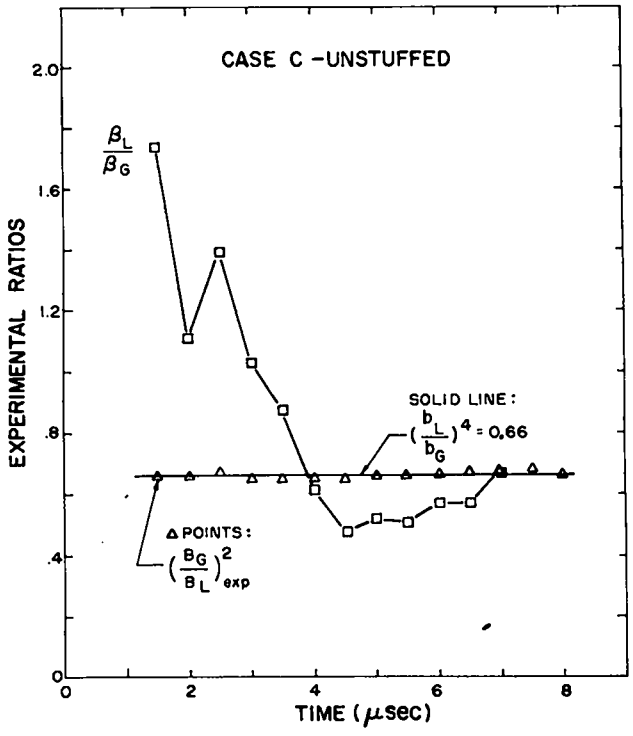

Fig. II-4.
Comparison of measured ratio of βs in the land and groove regions with the values (horizontal line) corresponding to axial pressure equilibrium.

of the land and groove regions, respectively, B is the measured compression field, and b is the local compression-coil radius.) At early times the ratio β_L/β_G is larger than the equilibrium value to which it relaxes in about 4 μsec. This corresponds to a transfer of energy density from the land to the groove regions.

The same phenomenon is apparent in the plasma column bumpiness δ_o, as shown in Fig. II-5. The values $(\delta_o)_{lum}$, directly measured as $(a_G - a_L)/(a_G + a_L)$, are initially greater than the values $(\delta_o)_{th}$ that should be the response to the fields B_L and B_G at axial pressure equilibrium. This indicates that the grooves are "overloaded" with plasma initially, corresponding to an "enhanced" δ_o.

d. Slow Plasma Rotation. In some series-C shots, a plasma rotation about its local axis, or m = 2 motion, has been identified. The plasma takes on an elliptical cross section and has a rotation period of ~8 μsec. The sense of the rotation is counterclockwise when viewed parallel to $\overline{B}$ (the same direction in which a single positive ion

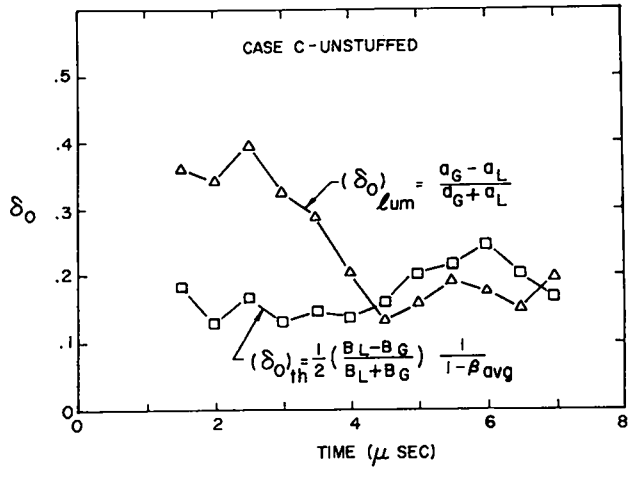

Fig. II-5.
Comparison of plasma column bumpiness $(\delta_o)_{lum}$ derived from luminosity profiles with the theoretical value $(\delta_o)_{th}$ corresponding to the axial field variations in the land and groove regions.

gyrates in $\overline{B}$). This motion appears infrequently and at random, and seems to be stable or at worst slowly growing. The degree of ellipticity, defined as b/a, is about two. No effect on confinement (m = 1 motion) has been noted.

5. Plasma Experiments with "Stuffed" $\ell = 0$ Groove Regions with 0.9-cm Depths (Experiment D). Plasma experiments with unstuffed $\ell = 0$ groove regions (Exp. C) suggested that an enhanced bumpiness, δ_o, of the plasma column was produced by the unstuffed grooves. In the initial implosion phase of the discharge, the effect of the unstuffed grooves is likely to increase the plasma density in the groove regions and decrease it in the land regions. In addition, with unstuffed grooves, magnetic field lines intersect the discharge tube wall during the initial sheath formation at the wall. In the stuffed case, the onset of the $\ell = 0$ fields is delayed by means of annular sets of stainless steel trapezoidal sections to maintain a homogeneous field during the time of the initial plasma implosion. The observed L/R penetration time of the magnetic fields into the stainless steel stuffers is ~0.2 μsec.

a. Transverse Motions of the Plasma Column. With initial deuterium filling pressures in the 10- to 20-mTorr range, the general plasma characteristics are similar to those obtained with the unstuffed $\ell = 0$ groove regions with the same 0.9-cm depths. However, the observed confinement times of the plasma are less with the stuffed grooves, being in the 5- to 7-μsec range. The similar plasma motions observed in the land and groove regions, which occur predominantly in the horizontal plane of the torus, again suggest that either the m = 1, k $\approx$ 0 plasma instability is developing or that a loss of equilibrium is occurring.

The magnitude of the current required in the helical $\ell = 1$ windings to achieve the toroidal plasma equilibrium with the stuffed $\ell = 0$ grooves is ~35% larger than with the unstuffed grooves. The plasma equilibrium is also more critically dependent on the $\ell = 1$ current than in the unstuffed case as evidenced by the tendency for the plasma column initially to drift outward more rapidly with the stuffed grooves. The increased $\ell = 1$ current and the initially more rapid outward drift of the plasma column with the stuffed $\ell = 0$ grooves can be understood in terms of an enhanced bumpiness, δ_o, of the plasma column in the unstuffed case. The enhanced bumpiness results from the unstuffed grooves in the initial implosion phase of the discharge and is initially frozen into the column to increase the $\ell = 1,0$ force as the helical $\ell = 1$ field is applied. Note that an enhanced δ_o, resulting from unstuffed grooves, can account for the unexpected small increase of $\ell = 1$ current required to achieve plasma equilibrium when the stuffed 1.8-cm $\ell = 0$ grooves were reduced to the 0.9-cm unstuffed groove depths.

b. Neutron Emission. The neutron emission with the stuffed grooves (oscillogram, Fig. II-6B) peaks near the maximum of the magnetic field and decreases at a slower rate than in the unstuffed groove case (oscillogram, Fig. II-6A). In this mode of operation with a relatively large bore coil (mean diameter = 17.1 cm) and one-half bank capacity, the neutron emission rate is near threshold with yields of 1 to 5 x 10^6 per meter. The decrease in the neutron emission following the compression field maximum probably results from the decrease in the magnetic field due to the imperfect crowbar and from the energy equilibration between the perpendicular and the axial degrees of freedom.

6. Experiments with "Shells" and $\ell = 0$ Groove Depths of 0.75-cm Unstuffed (Experiment E).

a. Experimental Arrangement. Measurements of the vertical $B_{r\text{-}V}$ field generated on the minor axis of the Scyllac torus by the bifilar $\ell = 1$ coils show an expected asymmetry of 14% due to an axial variation in the $\ell = 1$ image currents caused by the presence of the $\ell = 0$ grooves in the compression coil wall. Magnetic probe measurements, Fig. II-7, show this undesirable z dependence in the $\ell = 1$ field can be reduced or eliminated by the use of specially designed inserts, which provide an effectively uniform wall for the image currents. The semicylindrical shells, which were fabricated from 1.5-mm-thick copper, were shaped to the toroidal curvature and installed on the $\ell = 0$ groove regions with their inner surface flush with the coil bore of the land regions. The top and bottom "clam" shells were spaced 5-mm apart in the horizontal plane as required by the main coil insulation. A 3.7-mm gap was provided between each shell edge and the adjacent land region to allow the B_o flux to fill the $\ell = 0$ groove region behind the $\ell = 1$ shell.

Figure II-7 shows the field plots of the absolute magnitudes of the $\ell = 1$ field and B_z as a function of z with the $\ell = 1$ shells. The addition of the shells reduced the 14% difference in $B_{r\text{-}V}$ between the land and groove regions to essentially zero. The amplitude of $B_{r\text{-}H}$ is 6% larger than that of $B_{r\text{-}V}$. This results from image current effects due to the semicylindrical split in the shells, which is required for the main coil insulation. The $\ell = 1$ shells eliminate the z dependence of $B_{r\text{-}V}$ and leave a projected elliptical polarization in the radial plane, which is symmetrical about the minor axis of the torus. This is in contrast to the asymmetrical z-dependent polarization that existed without the shells.

In addition to providing an effectively uniform wall for the $\ell = 1$ image currents, the shells also reduce the depth

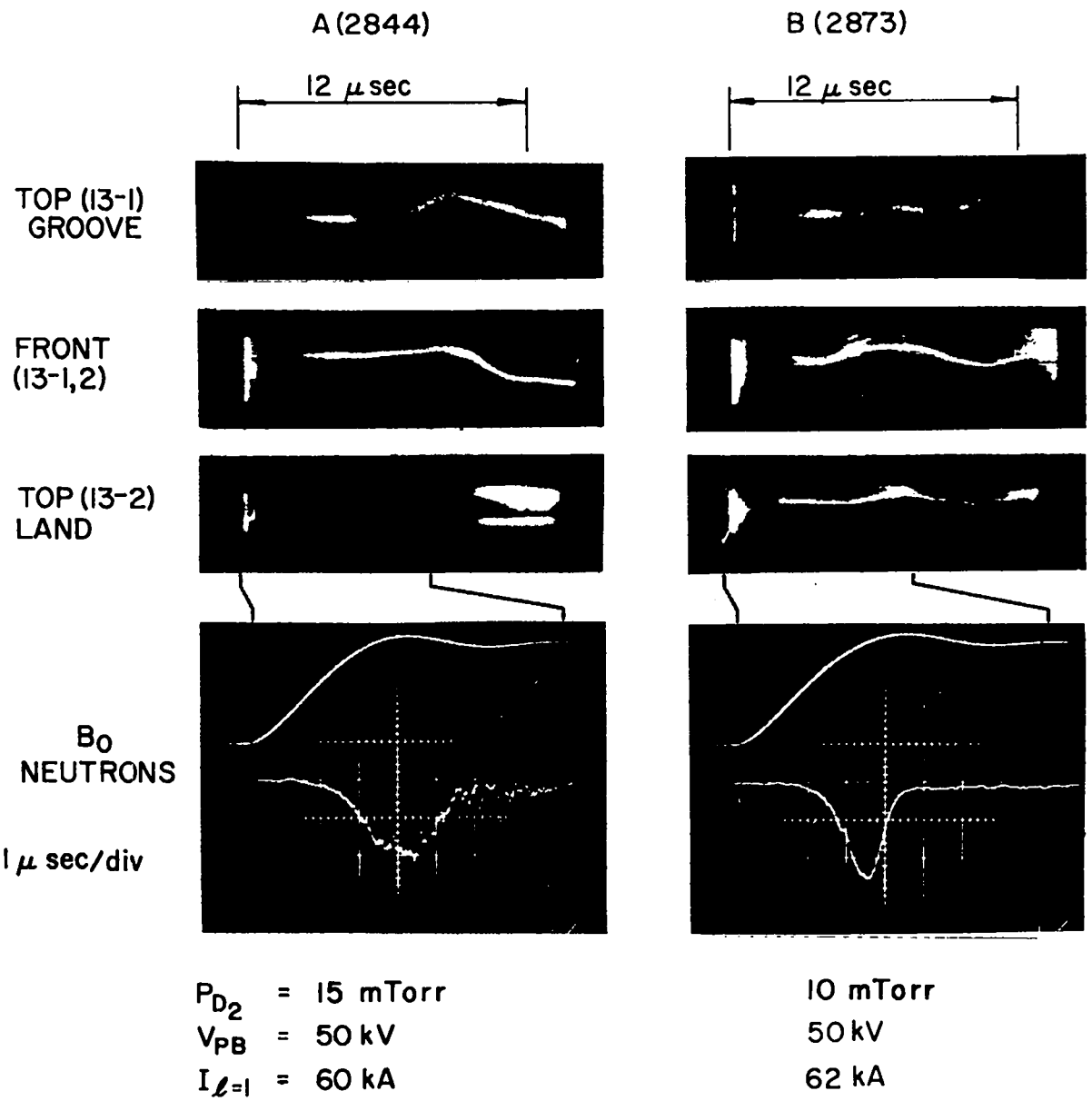

Fig. II-6.

Streak photographs of the toroidal sector plasma showing the horizontal (upper and lower photographs) and vertical (center photographs) motions (Exp. E, Table II-1). Oscillograms of main compression field and neutron-scintillator signal from Exp. E, Table II-1 (lower left) and Exp. D (lower right).

of the 9-mm $\ell = 0$ groove regions by 16.7% to an effective depth of 7.5 mm.

Plasma experiments with initial deuterium filling pressure of 10 and 15 mTorr and main bank voltages of 45 and 50 kV were performed with the $\ell = 1$ shells.

b. Transverse Motions of the Plasma. Streak photographs taken near the center of the sector and neutron emissions from two of the better discharges are shown in Fig. II-6. The streak photographs with a 15-mTorr filling pressure (Fig. II-6A) show the plasma column in a well-confined equilibrium position for the first 6 μsec of the discharge. An outward plasma motion develops in both the groove and land regions with the plasma striking the outer wall in the land region at 10 μsec. In the groove region at 9.6 μsec the plasma column appears to deflect

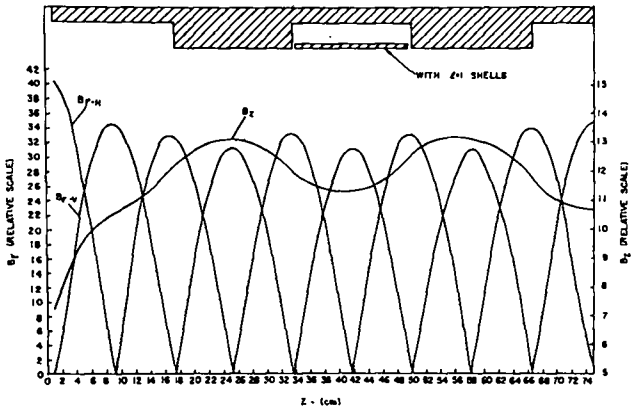

Fig. II-7.
Magnetic field plots of the absolute magnitudes of the vertical B_{r-V} and horizontal B_{r-H} components of the $\ell = 1$ field, and B_z field as a function of z with the $\ell = 1$ shells.

inward from the wall without coming into contact with the wall. Simultaneously, a similar change in the vertical motion occurs (front view between land and groove regions). The neutron emission rate (Fig. II-6A) attains a maximum at peak magnetic field (4 μsec) and subsequently decreases as the plasma column remains confined. Figure II-6B presents streak photographs with a 10-mTorr filling pressure. The plasma column remains confined to ~12 μsec at which time the streaks indicate a decrease in the column diameter characteristic of plasma end loss. An oscillatory but confined motion of the plasma column occurs in the vertical plane of the torus (front view) between the land and groove regions.

7. Plasma Experiments with "Shells" and 0.6-cm $\ell = 0$ Grooves, Unstuffed (Experiment F). The 0.9-cm $\ell = 0$ groove depths of the toroidal coil were partially filled with 3-mm-thick copper shells, which except for the additional thickness were of the same configuration as those described in the above section, to exclude the magnetic field. Plasma discharges were taken with a main bank voltage of 50 kV and initial deuterium filling pressures of 10, 14, and 18 mTorr. The maximum of the average toroidal compression field, B_o, was 40.9 kG, and the average ratios of the $\ell = 0$ and $\ell = 1$ fields to B_o were $B_{\ell=0}/B_o = 0.071$ and $B_{\ell=1}/B_o = 0.096$.

The gross behavior of the plasma was similar to the previous experiments with larger $\ell = 0$ groove depths. The observed transverse motions of the plasma at various positions around the torus show that the motion in the land and groove regions are similar, the column moving either radially outward or inward predominantly in the horizontal plane of the torus. The plasma confinement times were in the 4- to 7-μsec range, which are less than those with the 0.75- and 0.9-cm $\ell = 0$ groove depths (as in Table II-1).

8. Plasma Experiments with a Combination $\ell = 1$, $\ell = 0$ Grooved Compression Coil (Experiment G).

a. Experimental Arrangement. The main objectives in going to a compression coil with $\ell = 1$ as well as $\ell = 0$ grooves are (1) to achieve a constant ratio of the $\ell = 1$ field to the main field in time, (2) to improve the uniformity of the $\ell = 1$ field, and (3) to verify experimentally the double groove design that simplifies the production of the $\ell = 1$, $\ell = 0$ field configuration. To achieve these objectives and retain the capability of variable $\ell = 1$ fields, the $\ell = 1$ groove depths were underdesigned by 25% from the equilibrium values predicted from previous experiments, and the $\ell = 1$ driven windings were retained to provide the additional $\ell = 1$ field and the variable feature.

The desired sinusoidal variations of the $\ell = 1$ and $\ell = 0$ fields in z are approximated by eight discrete sections in a given wavelength of 33.15 cm. The $\ell = 1$ helical fields are generated by circular cross sections whose axes are displaced on a stepped helix from the minor toroidal axis and with the axis of each successive section rotated 45° about the minor axis relative to its neighbor. The central tangent circle has a 13.6-cm diam, whereas the $\ell = 1$ circular cross sections have diameters of 15.13 cm with their centers displaced 0.76 cm off the minor axis. The $\ell = 0$ grooves are superimposed on the $\ell = 1$ groove with a considerably better approximation to a toroidal sinusoidal dependence than was used in the previous experiments. Figure II-8 shows the combined $\ell = 0$ and $\ell = 1$ grooved coil in cross section. The cross-sectional view in the horizontal plane of the torus shows a main feature of the $\ell = 1,0$ equilibrium field configuration, which is to equalize the lengths of the magnetic field lines around the torus ($\int B.dl$ = constant).

Figure II-9 shows magnetic probe results obtained on the axis (r = 0) in a straight, full-scale model of the double-grooved compression coil in the absence of $\ell = 1$ windings. These results give $B_{\ell=0}/B_o = 0.09$ and $B_{\ell=1}/B_o = 0.07$. The main magnetic field, B_o, is 40 kG in the present experiments with one-half the capacity of the bank operating at 50 kV. The probe results (Fig. II-9) show an asymmetry in the vertical component of the $\ell = 1$ helical field of approximately ± 7%. This asymmetry results from the superposition of the $\ell = 0$ bumpy field grooves on the $\ell = 1$ helical field grooves. It can be eliminated by a second iteration of the $\ell = 1$ design.

b. Results with Auxiliary $\ell = 1$ Windings. In the composite coil configuration, the reproducibility of the

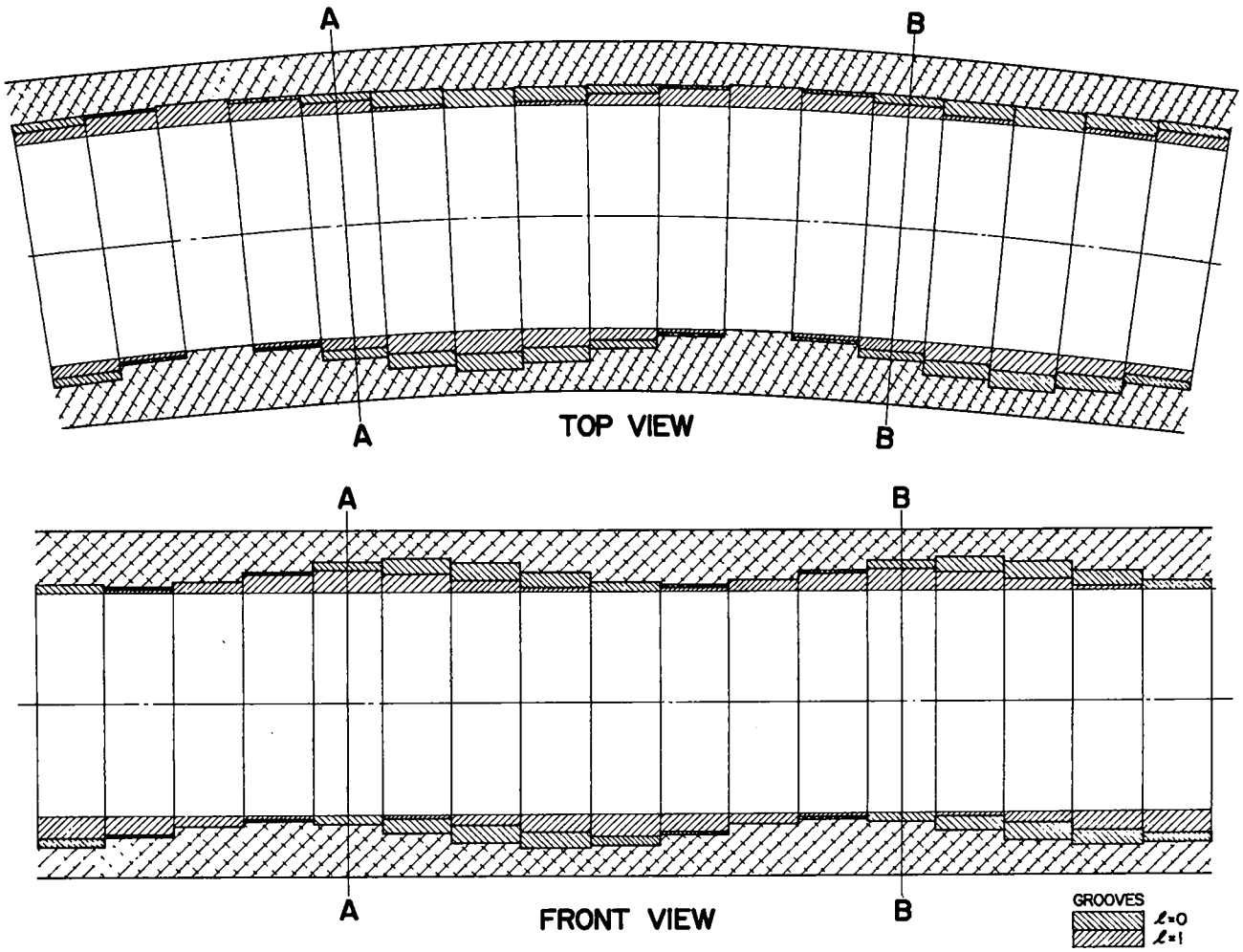

Fig. II-8.
Cross-sectional views of the combined ℓ = 1 and ℓ = 0 grooved compression coil. coil.

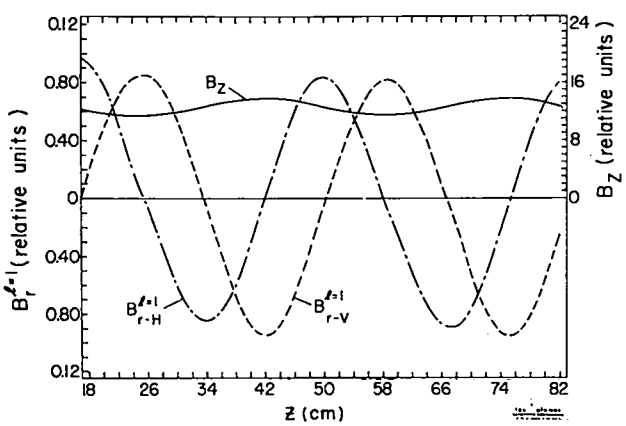

Fig. II-9.
Magnetic field plots of the ℓ = 1 and B_z fields on axis (r = 0) of the double-grooved compression coil.

plasma phenomena from discharge to discharge is considerably improved. In the initial experiments, the current required in the auxiliary ℓ = 1 windings to achieve plasma equilibrium with P_{D_2} = 14 mTorr was approximately the predicted 25% of that required previously. However, as the discharge tube cleaned up, we found that the auxiliary windings were not required to balance the outward toroidal force for deuterium filling pressures in the 12- to 14-mTorr range. Figure II-10 shows the transverse motions of the plasma column near the center of the 5-m sector. Similar observations of the transverse motions of the plasma at various positions around the torus show that (1) the plasma column takes up the usual helical shift and comes into an equilibrium position that lasts 4 to 7 μsec, (2) the plasma moves away from the equilibrium position in a long wavelength m = 1 sideward motion and strikes the wall at about 8 μsec, and (3) the motion of the

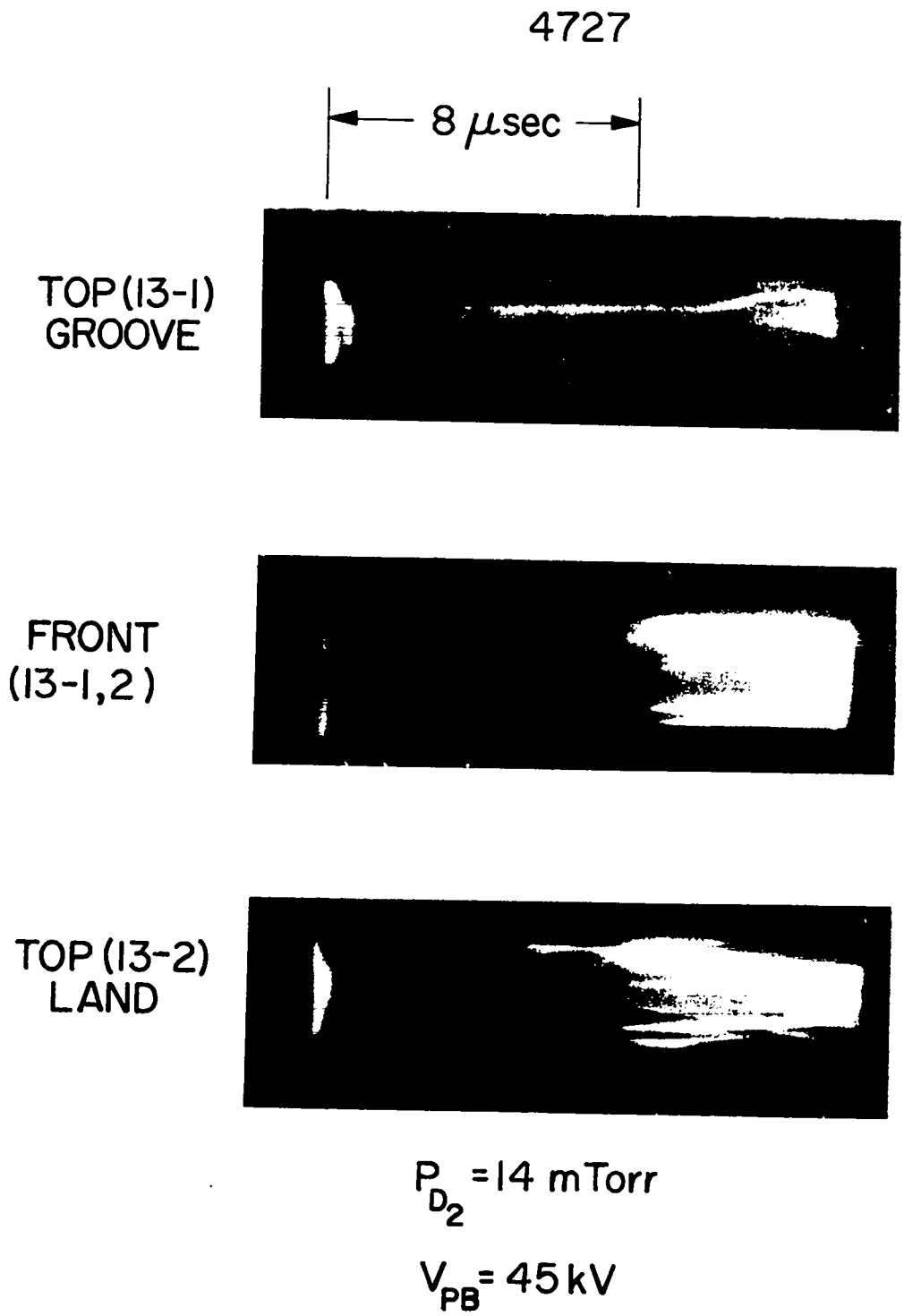

Fig. II-10.

Streak photographs showing the transverse motions of the plasma in the horizontal (groove and land regions) and vertical (front) planes of the torus near the center of the sector in the double-grooved compression coil.

plasma column develops more nearly in the vertical plane of the torus in contrast to the previous horizontal motions, which resulted with the $\ell = 1$ fields produced entirely by driven windings. The vertical downward motion (the front view of the streak photographs is inverted) of the plasma column is reproducible and develops independently of a force balance in the horizontal plane and of the excitation of the $\ell = 1$ windings. Computer fits of the observed transverse plasma motions show that the motions are fitted by parabolas rather than exponentials, although an exponential can be fitted to the initial plasma motion.

In comparing the present results with the previous ones with driven $\ell = 1$ windings, a variation in the asymmetry or z dependence of the vertical components of the $\ell = 1$ fields became evident as follows: (1) with the previous 9-mm $\ell = 0$ grooves the $\ell = 1$ image current effects reduced the vertical component of the $\ell = 1$ fields in the land regions by 14% relative to the groove regions. The $m = 1$ sideward motion of the plasma was almost completely in the horizontal plane of the torus with little or no vertical motion, (2) in the previous experiments with the 1.5-mm-thick shells installed over the $\ell = 0$ groove regions to provide a uniform wall for the $\ell = 1$ image currents, the z dependence of the $\ell = 1$ field was nearly eliminated. The plasma motion was predominantly in the horizontal plane of the torus, but there was some plasma motion in the vertical plane, and (3) in the present experiments with the double-grooved coil, the vertical components of the $\ell = 1$ fields in the $\ell = 0$ groove regions were reduced by ~14% relative to the land regions owing to the superposition of the $\ell = 0$ grooves on those of the $\ell = 1$ field. The plasma motion is predominately in the vertical plane of the torus.

c. Temperature Measurements. The plasma temperature can be calculated from the pressure balance condition,

$$k(T_e + T_i) = 2.48 \times 10^{13} \frac{\beta B^2}{n}, \qquad (2)$$

where $k(T_e + T_i)$ is in keV for B in kG and n in cm^{-3}. On an analyzed discharge β,B, and n are all known functions of time, where B refers to the magnetic field outside the plasma column and β and n refer to β and density on axis. On a typical discharge (in a land region at 4 μsec) we find that $a = 0.53$ cm, $n = 3.7 \times 10^{16}$ cm^{-3}, $\beta = 0.85$, and $B = 47$ kG, giving

$$k(T_e + T_i) = 1.26 \text{ keV}. \qquad (3)$$

Subtracting an assumed electron temperature, $kT_e = 400 \pm 100$ eV, yields $kT_i = 860 \pm 100$ eV, which is consistent with the observed neutron production. The line density in the plasma column is given by

$$\pi a^2 n = 3.3 \times 10^{16} \text{ ions/cm}, \qquad (4)$$

which is roughly 60% of the indicated filling density at 14 mTorr.

9. Experiments in the $\ell = 1$, $\ell = 0$ Grooved Compression Coil with Added Vertical and Horizontal Magnetic Fields (Experiment H).

a. Experimental Arrangement. The auxiliary $\ell = 1$ windings were removed from the double-grooved coil and pairs of toroidal windings installed on the discharge tube in the horizontal and vertical planes of the torus at radii of 5.3 cm. With these windings, vertical and horizontal magnetic fields of 200 to 600 G can be superimposed on the toroidal $\ell = 1,0$ field configuration with risetimes of 3 to 5.5 μsec.

With fixed ratios of $B_{\ell=0}/B_o$ and $B_{\ell=1}/B_o$ from the grooved coil, the initial plasma equilibrium is achieved by adjusting the initial deuterium filling pressure to give a balance between the $F_{1,0}$ and toroidal F_R forces through their β dependence. On the basis of sharp boundary theory, the ratio of the two forces is given by

$$\frac{F_{1,0}}{F_R} = h^2 aR \delta_1 \delta_o \left[1 + (1-\beta) I_o(\epsilon)/I_1'(\epsilon)\right] /2 , \qquad (5)$$

where

$$\delta_o = \frac{I_o(\epsilon)K_o'(\epsilon)\left[1 - I_o'(\epsilon)K_o(\epsilon)/I_o(\epsilon)K_o'(\epsilon)\right]}{\epsilon K_o(\epsilon)\left[1-(1-\beta) I_o(\epsilon)K_o'(\epsilon)/I_o'(\epsilon)K_o(\epsilon)\right]} \frac{B_{\ell=0}}{B_o} \qquad (6)$$

and

$$\delta_1 = \frac{B_{\ell=1}/B_o}{\epsilon^2 I_1'(\epsilon)K_1(\epsilon)\left[1 - (1-\beta) I_1(\epsilon)K_1'(\epsilon)/I_1'(\epsilon)K_1(\epsilon)\right]} \qquad (7)$$

The I_ℓ and K_ℓ are the modified Bessel functions and $\epsilon = ha$ is the product of the $\ell = 1,0$ wavenumber h and the plasma radius a. Figure II-11 shows a plot of $F_{1,0}/F_R$ as a function of β for the grooved-coil field ratio product of $(B_{\ell=0}/B_o)(B_{\ell=1}/B_o) = 0.0064$.

b. Transverse Motions of the Plasma. With the $\ell = 1$ coils removed and the discharge tube repositioned in the compression coil, the vertical $m = 1$ motion of the plasma column usually occurs only when there is a good balance of the $F_{1,0}$ and toroidal forces in the horizontal plane, i.e., with very little horizontal motion. When the toroidal

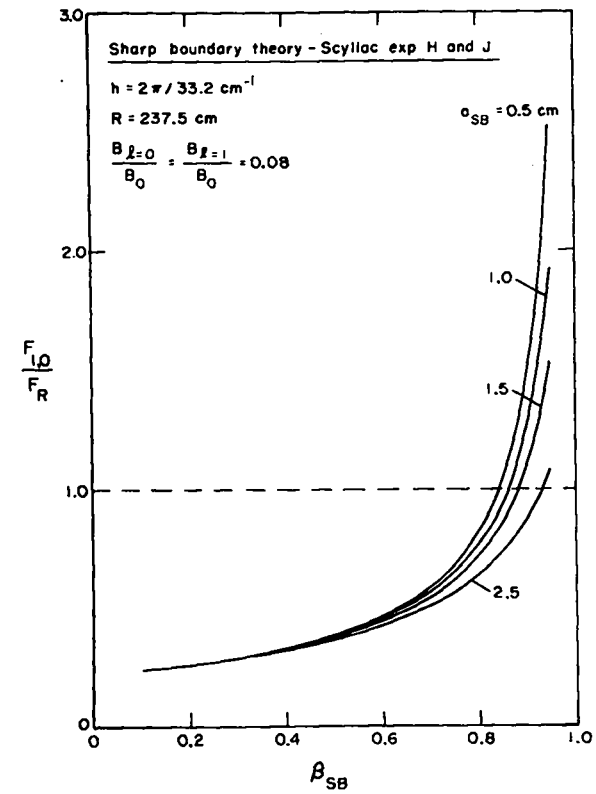

Fig. II-11.
Ratio of the $F_{1,0}$ force to the toroidal force as a function of β for the indicated plasma radii a.

force is not balanced by the $F_{1,0}$ force, the plasma column generally moves only in the horizontal plane without vertical motion. This result is to be contrasted with above results in Exp. G where the vertical motion occurred independently of the horizontal plasma motion. This difference may result from perturbations in the field configurations produced by the presence of the $\ell = 1$ windings or by a slightly different position of the discharge tube in the compression coil.

The superposition of a vertical field, B_v, of either polarity with a magnitude of ~600 G improves the plasma confinement. With the initial deuterium filling pressure and the resulting plasma β adjusted such that the inward $F_{1,0}$ force is slightly greater than the outward toroidal force, the superposition of an upward vertical field results in local plasma containment of up to 12 μsec. A similar good containment mode is achieved with a downward vertical field when the outward toroidal force becomes slightly larger than the inward $F_{1,0}$ force. The transverse plasma motions for this case are shown in Fig. II-12. These streaks however show a nonuniformity of the plasma containment around the toroidal sector. In discharge 6143 (Fig. II-12) the plasma is confined in the central meter 13, as shown by the upper two streaks on the left (13-1 and 13-1,2), whereas it strikes the discharge tube wall in coil meter 12 at 6.3 μsec after the initiation of the discharge as shown by the lower streak (12-3). In discharge 6101 (Fig. II-12) there is good containment in coil meter 12 (streak 12-3) although vertical motion carries the column to the wall in meter 13 (streaks 13-1,2 and 13-1). The transverse excursions of the plasma column are less in this mode than in the case of the upward vertical field. This good localized containment case is also critically dependent on the initial filling pressure, which with fixed ratios of $B_{\ell=1}/B_o$ and $B_{\ell=0}/B_o$ implies that it is critically dependent on the $F_{1,0}$ and toroidal forces through the plasma β (cf., Fig. II-11).

The superposition of a horizontal field of either sense with magnitudes up to 600 G does not appear to affect the plasma motion significantly, although less data have been obtained for this case.

10. Plasma Experiments in an Improved Shaped Compression Coil with "Pure" $\ell = 1$ and $\ell = 0$ Fields (Experiment J).

a. Experimental Arrangement. A new compression coil was designed and fabricated for the previously planned feedback stabilization experiments on the toroidal sector. This coil was designed to accommodate both $\ell = 1$ field coils and $\ell = 0$ feedback coils inside its "tangent" bore. The inner surface of the coil was grooved to generate "pure" $\ell = 1$ helical fields, "pure" $\ell = 0$ bumpy fields, and a small vertical field in addition to the main toroidal field. Freidberg developed a procedure to determine numerically the inner coil surface by calculating the shape of the magnetic flux surfaces for the required vacuum fields from

$$B = \hat{e}_z B_o \left(1 - \frac{r}{R}\cos\theta\right) + \nabla\phi \quad , \tag{8}$$

where

$$\phi = B1\left[2I_1(hr)/h\right]\sin(\theta - hz) + BO\left[I_o(hr)/h\right]\sin hz + BV\, r\sin\theta. \tag{9}$$

Here B_o, B1, BO, and BV are the amplitudes of the main toroidal field $\ell = 1$, $\ell = 0$ and vertical fields, respectively; $h = 2\pi/\lambda$ ($\lambda = 33.15$ cm); I's are the modified bessel functions; and R is the major radius of curvature. Each wavelength of the $\ell = 1,0$ fields was divided into 260 steps (1.25 mm/step), and flux surfaces were calculated for each step. This design provides an improvement over the double-grooved coil used in Exps. G and H above, which

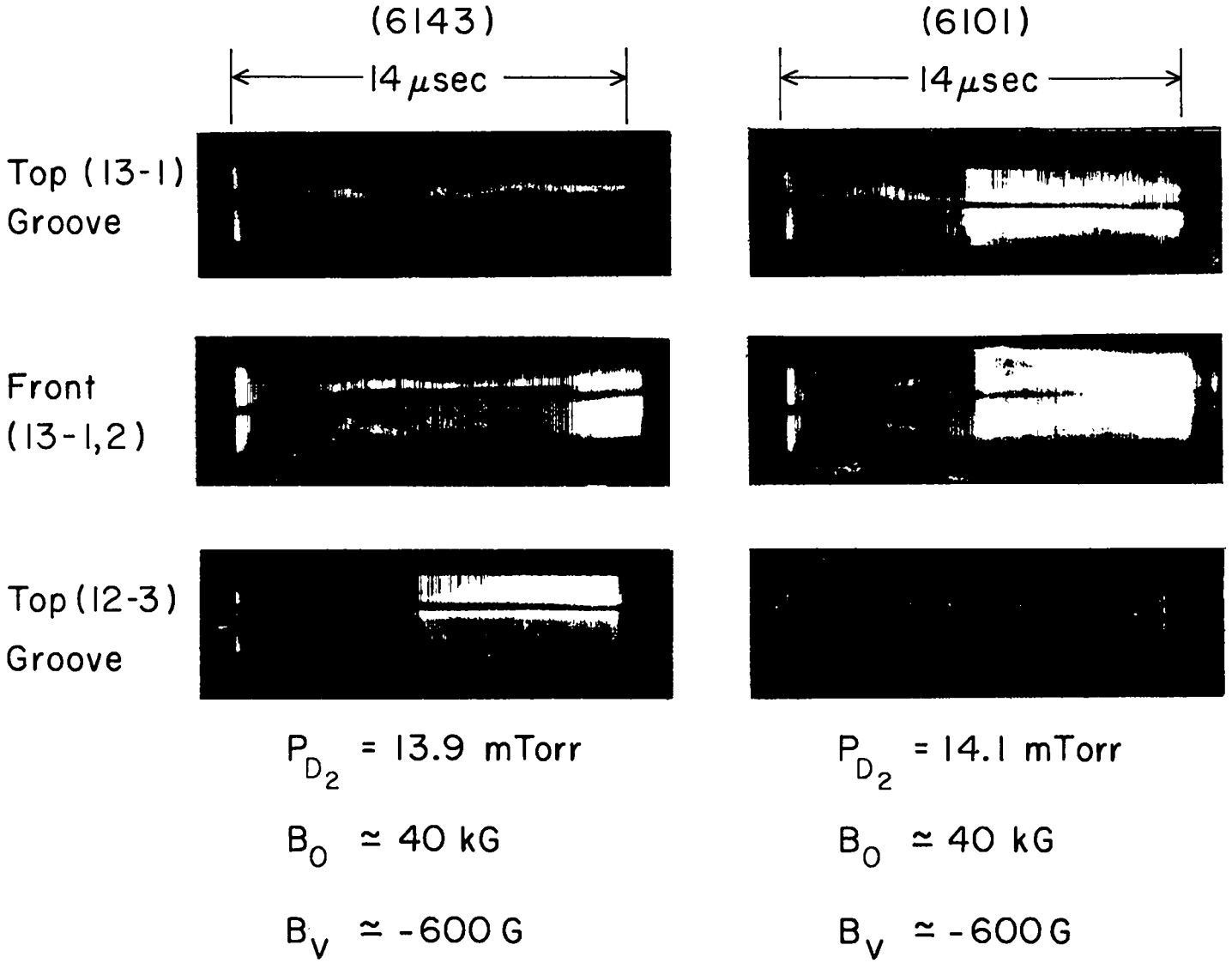

Fig. II-12.

Streak photographs in coil meters 12 and 13 (sector center meter) with a downward vertical field of ~600 G. The dark central band on the photographs results from the auxiliary toroidal windings, which block off approximately one centimeter of the center region in both the horizontal and vertical planes.

approximated the toroidal sinusoidal variations of the $\ell = 1$ and $\ell = 0$ fields with eight groove steps per $\ell = 1,0$ wavelength. This previous coil had $B1 = B_{\ell=1}/B_o = 0.07$ and $BO = B_{\ell=0}/B_o = 0.09$. Because of earlier experiments and the increase of the feedback force with the $\ell = 1$ field, the latter was increased to $B_{\ell=1}/B_o = 0.08$, and the $\ell = 0$ field reduced to $B_{\ell=0}/B_o = 0.08$, which keeps the $F_{1,0}$ equilibrium force constant.

In the sharp boundary theory of the high-β toroidal plasma equiilibrium, Ribe[10] and Weitzner have shown that a small vertical field, B_v, given by

$$\frac{B_v}{B_o} = \frac{1}{4}\,\frac{B_{\ell=1}}{B_o}\,\frac{B_{\ell=0}}{B_o} \qquad (10)$$

is required to give centered flux surfaces for equilibrium. We found that in the computer design of the coil surfaces the vertical field shifted the flux surfaces in the horizontal plane and changed the ellipticity of the flux-surface cross sections. The graphs in Fig. II-13 show two flux surfaces obtained for each of three values of vertical field. For the case $BV = B_v/B_o = 0.0016$ the nature of the calculation is indicated by the plot of the position of the magnetic field line as it traverses each period (hz is a multiple of 2π). After 57 periods the line proceeds on a curve indistinguishable by computer accuracy from the curve shown, which is taken to be the flux surface. The strongest vertical field shown in Fig. II-13 is the field necessary to make the coil cross section round. The criterion isn't exact, but the departure from a circle in the view shown is less than one-half percent and at other z locations no more than a few percent.

Examples of the flux surface for four values of hz are shown in Fig. II-14 for BV = 0.0016 and in Fig. II-15 for BV = 0.004779. Figure II-14 shows that an unshifted flux surface near the axis means one that makes equal excursions up-down and right-left. Although not plotted for other values of BV (Figs. II-15), the small flux surfaces shift about their initial position in about the same way as shown in Fig. II-14 for BV = 0.0016.

The effects of a high-β plasma on the flux surfaces were estimated by putting a 1-cm radius conductor, uniform in z, on the axis. The results show that near the rod the flux surfaces surround it, but a few centimeters away the flux surfaces resemble the vacuum surfaces. At the metal wall there is a shift in the flux surfaces of less than 0.01 cm.

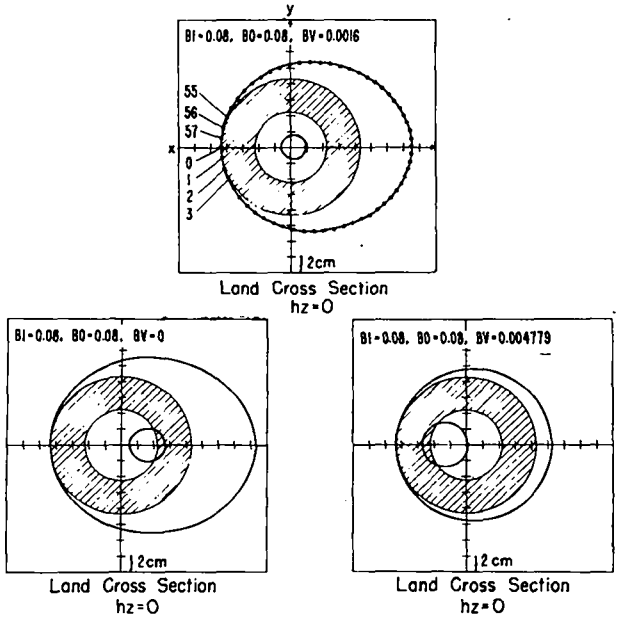

Fig. II-13.

Two flux surfaces for three values of vertical field. The outer surface encloses the shaded area representing discharge tube, $\ell = 1$ coils, and $\ell = 0$ feedback coils. The x-coordinate points outward along the major radius of curvature and y is directed upward from the plane of the torus.

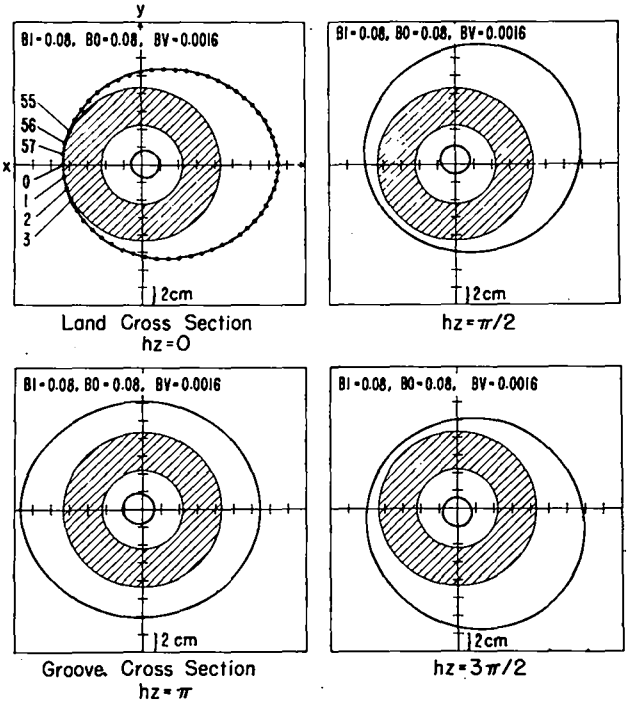

Fig. II-14.

Flux surfaces at four z locations with BV = 0.0016. The radial plane where B_z is maximum on axis due to the $\ell = 0$ field is referred to as the land ($h = 0$), and where B_z is minimum on axis is referred to as a groove ($hz = \pi$).

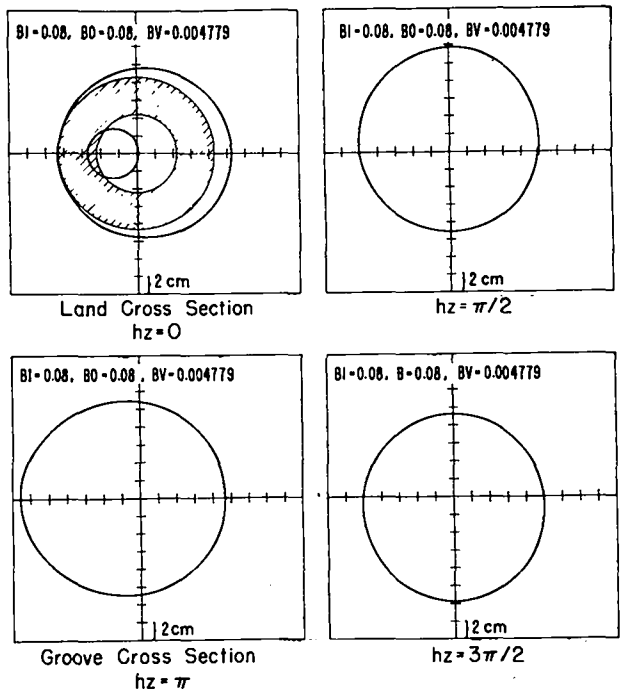

Fig. II-15.
Flux surfaces at four z locations with BV = 0.004779.

The final choice of coil design (BV = 0.004779) was influenced by practical considerations. Machining an elliptical cross section is expensive and time consuming. The obvious choice of BV = 0.0016 also has a larger area than the coil under construction that would lower B_o in the experiment by ~15%. Also, the possibility of centering the vacuum flux surfaces is available by adding vertical field windings.

A section of the shaped compression coil is shown in Fig. II-16. The coil surfaces near the horizontal plane of the torus show an important feature of the $\ell = 1,0$ equilibrium field configuration, which is to equalize the lengths of the magnetic field lines around the torus. This weakens the magnetic field on the inner side of the coil bore relative to the outside and thereby reduces the magnetic field gradient across the bore. This coil, which was designed to accommodate both $\ell = 1$ windings and $\ell = 0$ feedback coils, has a "tangent" bore of 17.36 cm, a maximum diameter in the groove region of 22.12 cm, a minimum diameter in the land region of 19.17 cm, and an average diameter of 20.50 cm.

Figure II-17 shows magnetic probe results obtained on the axis (r = 0) of the shaped compression coil that was driven by a 40-kHz oscillator and amplifier. The bumpiness produced by the $\ell = 0$ field is evident in the graph of the toroidal B_z field. These results give $B_{\ell=0}/B_o = 0.082$ and $B_{\ell=1}/B_o = 0.075$. The main toroidal field, B_o, is 36.3 kG with a risetime of 4.75 μsec in the present experiments with one-half the capacitance of the bank operating at 50 kV. The probe results indicate an asymmetry in the vertical components of the $\ell = 1$ field of ~6% and a difference between the vertical and horizontal components of ~8%. However, these differences are approaching the accuracy of the probing.

Two pairs of toroidal vertical field windings were installed on the discharge tube at radii of 5.6 cm. Each pair of windings was positioned at 30° from the horizontal plane of the torus. These windings were driven in parallel from a capacitor bank to produce vertical fields of 30 to 600 G with risetimes that approximately matched that of the main field. With the main bank operating at 50 kV, the main toroidal coil generates an upward vertical field of $\simeq$ 174 G.

b. Plasma Equilibrium and Stability in the $\ell = 1,0$ Shaped Coil. The equilibrium and stability of the high-β plasma produced in the shaped $\ell = 1,0$ coil were studied in the toroidal sector under the following conditions: (1) main bank operating at 45 kV both without and with an applied vertical field B_v ~100 G applied downward in opposition to the vertical field generated by the main coil, (2) main bank operating at 50 kV without and with B_v ~100 G applied both in oppostion and in aiding the vertical field of the main coil, and (3) with higher applied vertical fields, B_v ~600 G, in both polarities.

In these experiments, the $\ell = 1$ and $\ell = 0$ fields were generated only by the $\ell = 1,0$ shaped surface of the main toroidal coil. With fixed ratios of of $B_{\ell=1}/B_o$ and $B_{\ell=0}/B_o$ from the shaped coil, the plasma equilibrium is achieved by adjusting the initial deuterium filling pressure to give a balance between the $F_{1,0}$ and toroidal F_R forces through their β dependence. Graphs of the ratio of these forces, $F_{1,0}/F_R$, as a function of the plasma β are shown in Fig. II-11.

The streak photographs of Fig. II-18, taken near the center of the sector, show typical radial motions of the plasma column with the indicated vertical fields and the main bank operating at 50 kV. These photographs compare the radial motions of the plasma column without (Fig. II-18A) and with (Fig. II-18B) a vertical field applied in opposition to that of the main coil. Figure II-18A shows the plasma in equilibrium to 6.6 μsec at which time the column moves outward in the horizontal plane to strike the wall at 8.5 μsec. The plasma confinement is slightly improved in Fig. II-18B with the vertical field windings excited to produce the prescribed vertical field amplitude of Eq. (10). Although some "motion" of the plasma occurs in the horizontal plane, it appears to remain generally in equilibrium to ~9 μsec. The development of an outward motion in the horizontal plane results in the plasma approaching the wall at ~10 μsec.

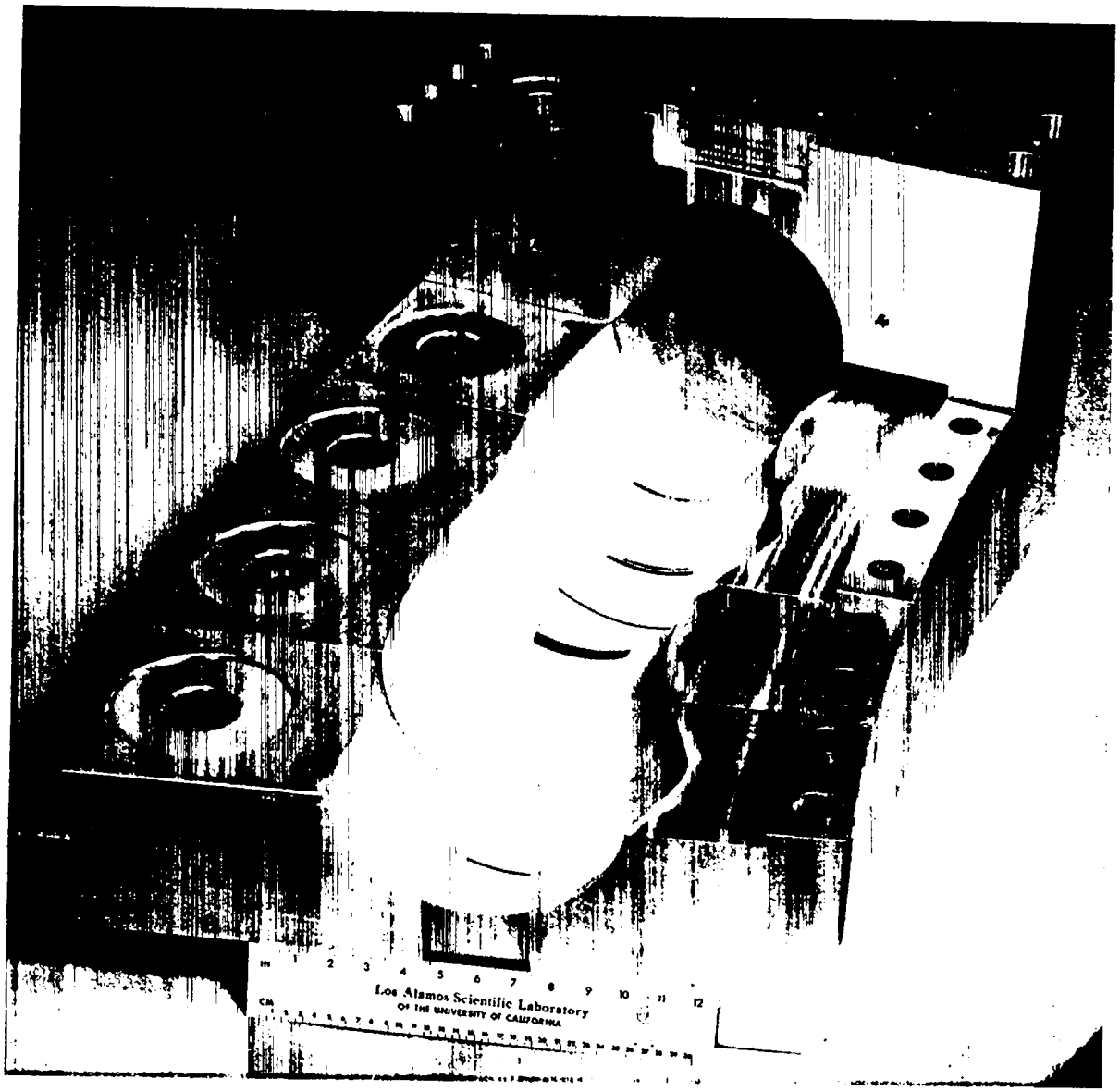

Fig. II-16.

Photograph of a section of the shaped compression coil with 260 steps per period having $B_{\ell=0}/B_o = 0.08$, $B_{\ell=1}/B_o = 0.08$, *and* $B_v/B_o = 0.004779$.

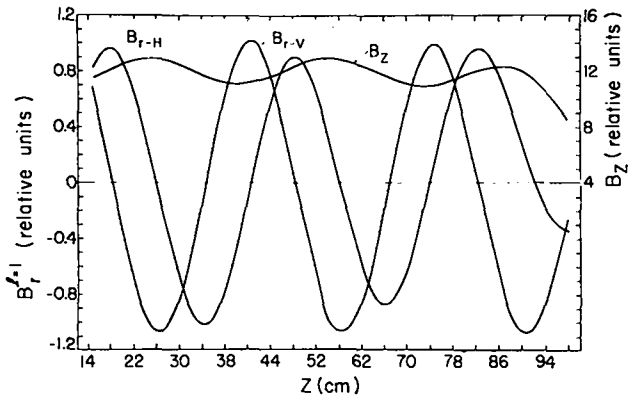

Fig. II-17.
Magnetic field plots of the $\ell = 1$ and B_z fields taken on axis of the shaped compression coil. The radial components of the $\ell = 1$ field are $B_{r\text{-}H}$ in the horizontal plane and $B_{r\text{-}V}$ in the vertical plane.

In this mode of operation the plasma exhibited similar transverse motions around the 5-m sector coil, i.e., $k \simeq 0$, $m = 1$ sideward motions of the column. The equilibrium dependence on the initial filling pressure, which is related to the plasma β, was observed to be reversed from that found previously in the "eight-step" grooved coil (Exps. G and H). It was necessary to increase the filling pressure to reduce the $F_{1,0}$ force, which implies that β decreases with increasing filling pressure. This reversed pressure dependence for $F_{1,0}$ may result from the lower fields in the present large-bore coil.

With the main bank operating at 45 kV ($B_o \simeq 32.7$ kG) and similar vertical magnetic fields the plasma characteristics were the same except the reproducibility from discharge to discharge was considerably better than at 50 kV, particularly the dependence of the equilibrium on the initial deuterium filling pressure.

The streak photographs of Fig. II-19 show the transverse plasma motions with larger vertical field amplitudes of −430, 290, and 770 G. In each case the plasma motions are similar to each other and also to those of Fig. II-18 with smaller vertical fields of 58 and 174 G. These results show that the plasma confinement is not critically dependent on the magnitude of the vertical field. This result indicates that flux surfaces are not too important in the 5-m toroidal sector because the large vertical fields of −430 and 770 G shift the flux surfaces at least partially out of the discharge tube cross sections. This is not too surprising because the flux surfaces are formed by lines that typically travel $50\,\ell = 1{,}0$ wavelengths (Fig. II-13), whereas the 5-m sector experiment has a finite length of 15 wavelengths. Thus, flux surfaces are probably not a dominant consideration in the present experiments, but are likely to be important on the longer time scale of a full torus.

c. Measurements of Plasma Parameters. Measurements were made of the plasma radius as a function of time, determined by luminosity profiles, and plasma excluded flux as a function of time, determined by the balanced probe method. These measurements were made in positions of minimum and maximum plasma radius (land and groove, respectively) to study the approach of the plasma column to theoretically predicted axial and radial force equilibrium.

Figures II-20 and II-21 show representative data taken at 45 kV. The data are seen to be generally reproducible from shot to shot. The oscillations observed in the plasma radius, which tend to damp out in 3 to 4 μsec, cause similar oscillations in the derived plasma β. These oscillations may be due to $m = 2$ rotations of an elliptical plasma column, to particle "sloshing" along the axis as $\ell = 0$ bumps are formed, or to as yet unidentified causes. The oscillations in land and groove are not in phase, the effects occurring earlier in a groove by about 0.25 μsec, or 90° ($\tau \sim 1$ μsec). The plasma β is computed assuming a rigid rotor density profile as described in Sec. II.F.

1. Toroidal Equilibrium. According to sharp boundary (SB) theory, Eqs. (5-7), the plasma βs for which toroidal equilibrium is possible are restricted to a relatively narrow range for plasma radii of interest, as shown in Fig. II-11. At equilibrium ($F_{1,0} = F_R$) there is a unique relationship between the plasma radius and β as shown in Fig. II-22. For typical plasma radii of ~0.7 cm, we see $\beta_{SB} \approx 0.85$.

To relate theoretical sharp boundary quantities to the experimental data, we may use the following relationships,

$$\frac{\beta_L + \beta_G}{2} = \beta_{SB} \quad \text{and} \quad \frac{a_L + a_G}{2} = a_{SB} \,, \tag{11}$$

where L refers to the center of a "land" or "neck" region of the bumpy plasma column and G refers to the center of a "groove" or "bulge" region.

Experiment. Figure II-23 shows the experimental curves for β_L and β_G as a funtion of time, obtained by averaging the data of Figs. II-20 and II-21. The smooth dashed lines drawn through the data are used in the calculations that follow. Likewise, average curves of a_L and a_G vs time are derived for use in the calculations.

Theory. A basic assumption in the sharp boundary theory, Eqs. (5-7), is that of axial pressure equilibrium, i.e., nkT independent of length. From the definition of β,

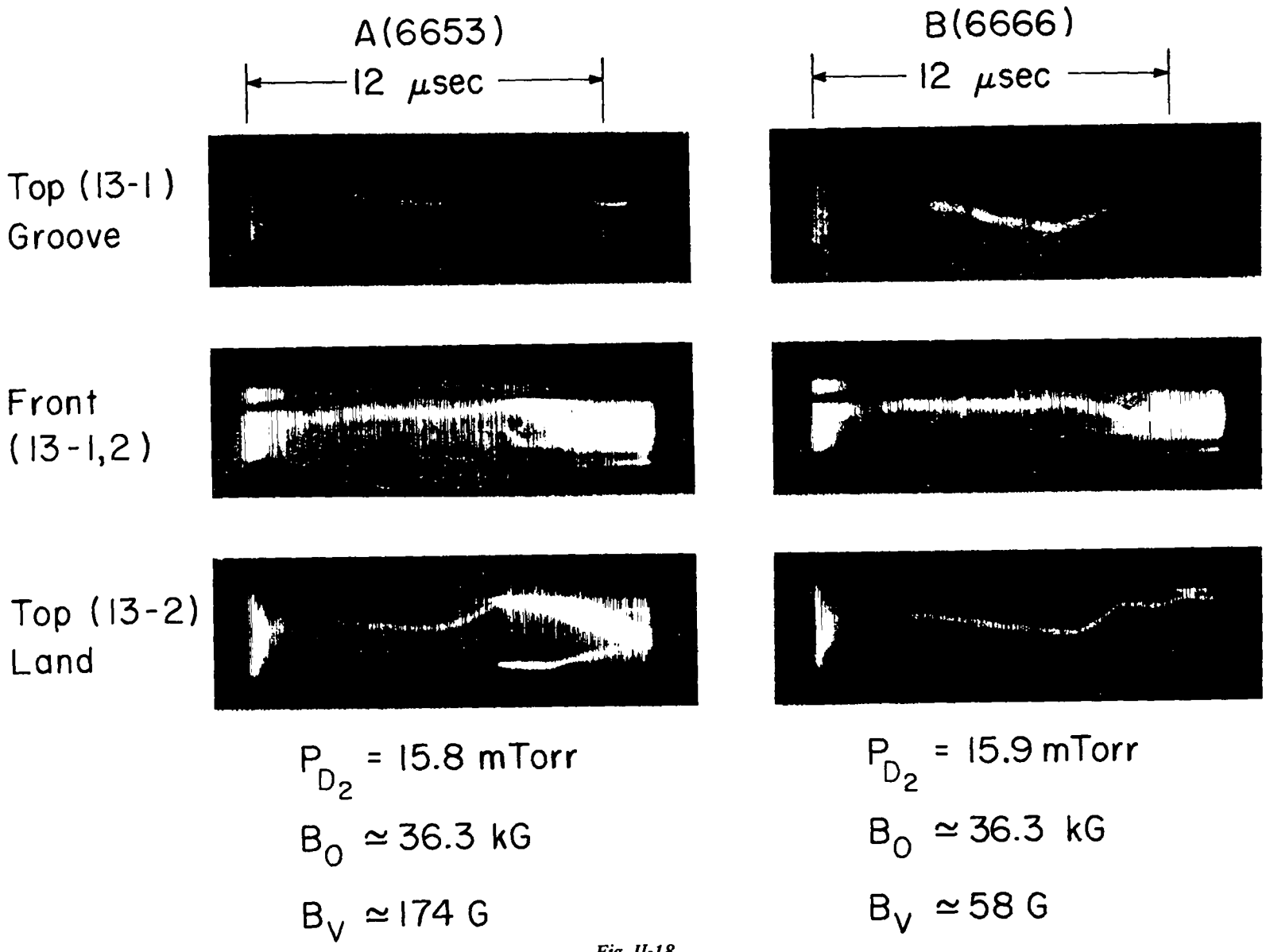

Fig. II-18.

Streak photographs showing the transverse plasma motions in the horizontal plane (top) of adjacent land and groove regions and in the vertical plane (front) midway between these regions.

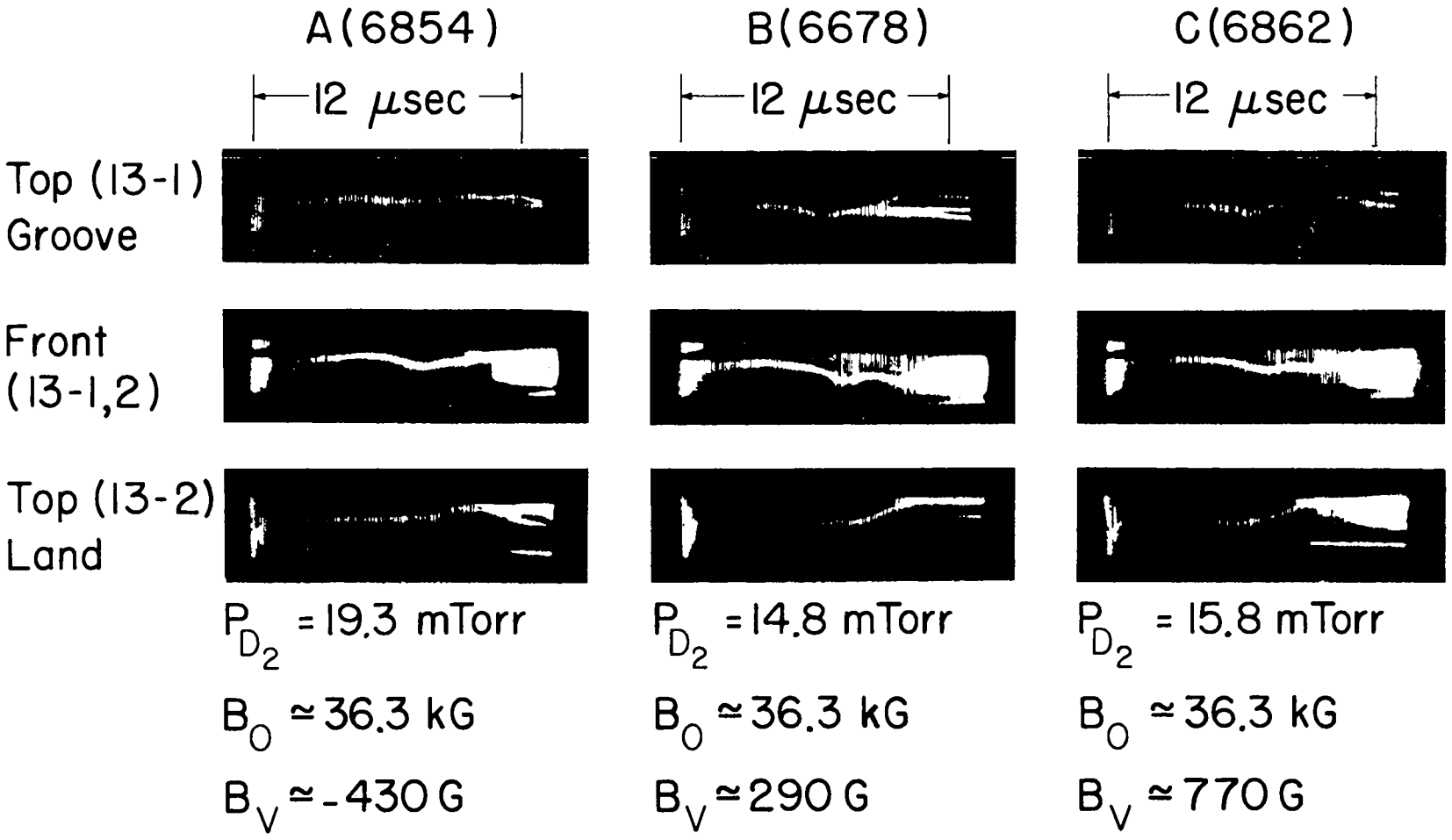

Fig. II-19.
Streak photographs taken near the center of the sector with larger vertical fields.

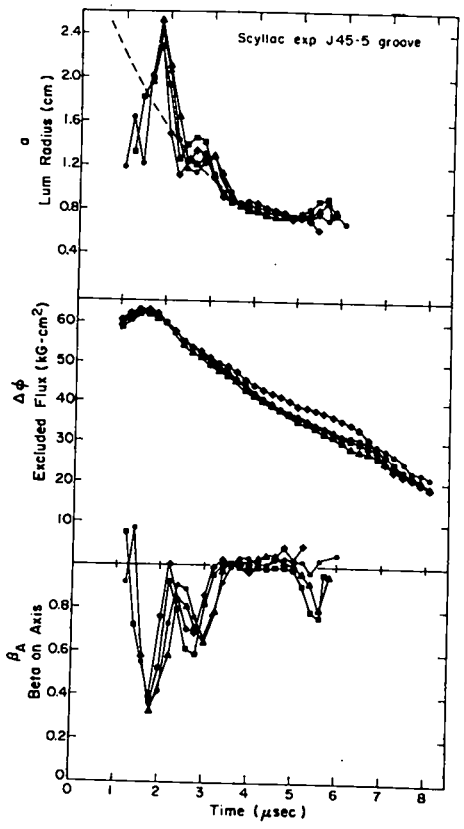

Fig. II-20.
Observed time variations of plasma radius, excluded flux, and computed β on axis in a land region (Exp. J, 45 kV).

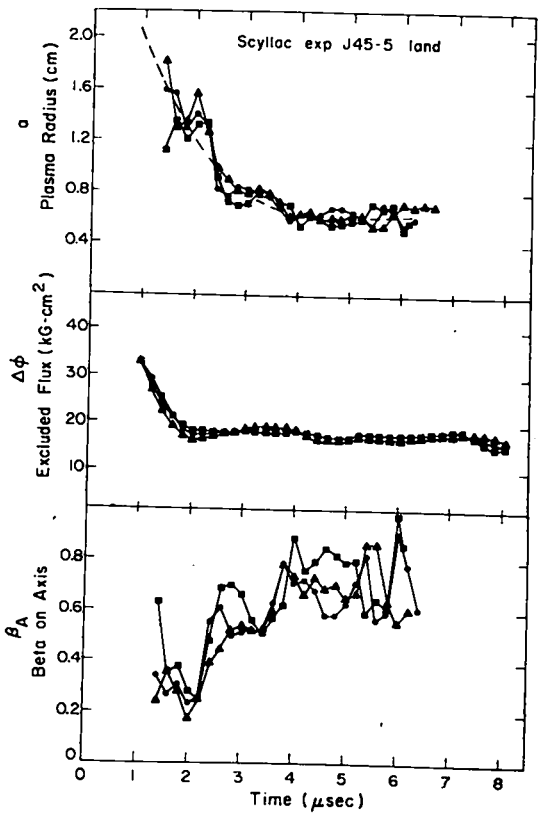

Fig. II-21.
Observed time variations of plasma radius, excluded flux, and computed β on axis in a groove region (Exp. J, 45 kV).

$$\beta = \frac{nkT}{B^2/8\pi} \quad , \tag{12}$$

this condition requires that β in a land and a groove region be related by the square of the magnetic fields, i.e.,

$$\frac{\beta_L}{\beta_G} = \left(\frac{B_G}{B_L}\right)^2 \quad . \tag{13}$$

In the series J experiments we are considering here,

$$\frac{B_G}{B_L} = \frac{1-0.08}{1+0.08} = 0.852 \tag{14}$$

by design. Combining Eqs. (11), (13), and (14) yields

$$\beta_L = 0.84\,\beta_{SB} \quad \text{and} \quad \beta_G = 1.16\,\beta_{SB} \quad . \tag{15}$$

The quantity β_{SB} is found from Fig. II-22 as a function of time using measured values of a_{SB}. The value of β_{SB} is not very dependent on a_{SB}. Theoretical curves calculated from Eq. (15) are shown in Fig. II-23. The agreement between theory and experiment is very good for times greater than 4 μsec.

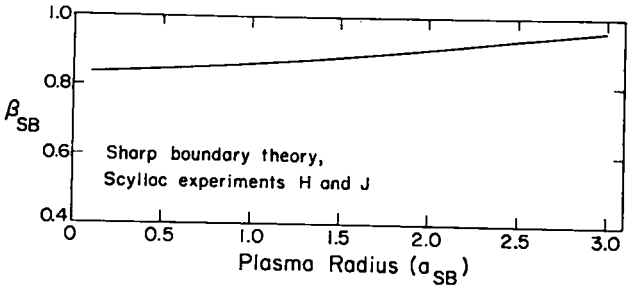

Fig. II-22.
Theoretical variation of β vs radius for toroidal equilibrium using sharp boundary theory (Exps. H and J) from Fig. II-11.

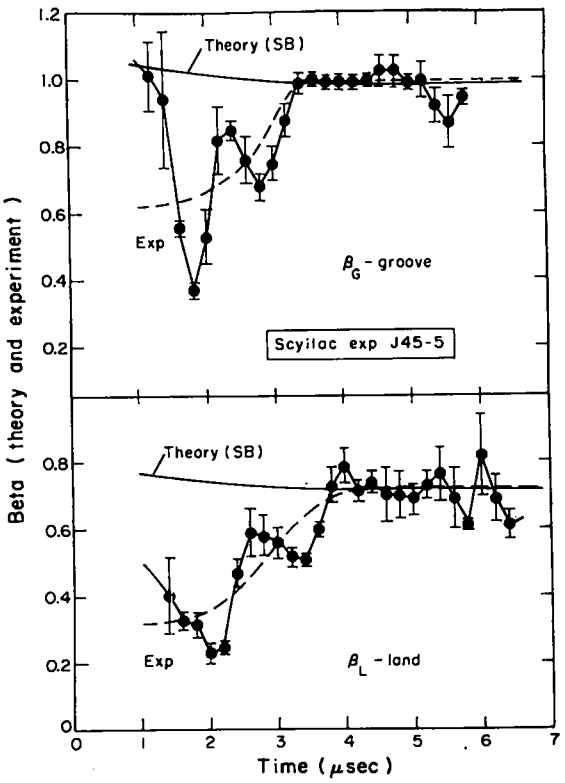

Fig. II-23.
Comparison of experimental values of β in land and groove regions with theoretical values corresponding to toroidal equilibrium.

Streak photographs of the plasma (for example Fig. II-18) show apparent toroidal equilibrium for times greater than 4 μsec, in agreement with the above calculations, but also for earlier times. The resolution of this seeming paradox appears to lie in the absence of axial pressure equilibrium during the first 4 μsec of the discharge, a question that is examined below.

2. Axial Pressure Equilibrium. There are two simple tests that can be applied to the data to check on axial pressure equilibrium. The first involves the use of Eq. (13), which relates the equilibrium ratios of β and magnetic field in a land and a groove. Figure II-24 shows these experimental ratios and the theoretical curve corresponding to the design value $(B_G/B_L)^2 = 0.726$. The magnetic field ratios are measured at a probe location of $r \simeq 5.3$ cm (just outside the quartz discharge tube). A correction factor of ~4% is applied to the data to allow for the Bessel function dependence on radius (see Sec. II.F). The plasma reaches axial equilibrium in about 4 μsec, and the indicated β variation with time is consistent

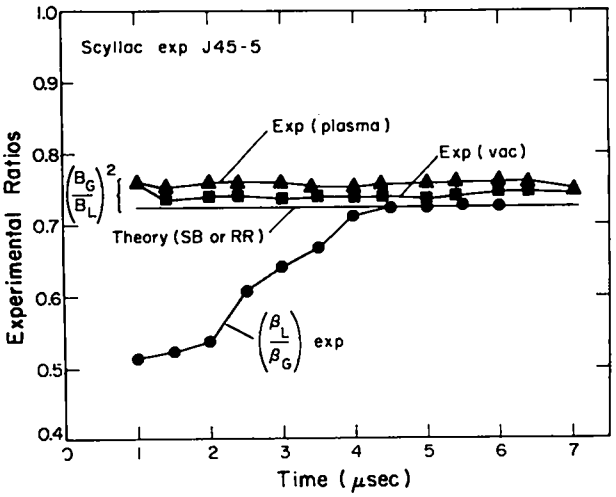

Fig. II-24.
Comparison of measured ratio of βs in land and groove regions with magnetic field ratios [see Eqs. (13) and (14)] corresponding to axial pressure equilibrium.

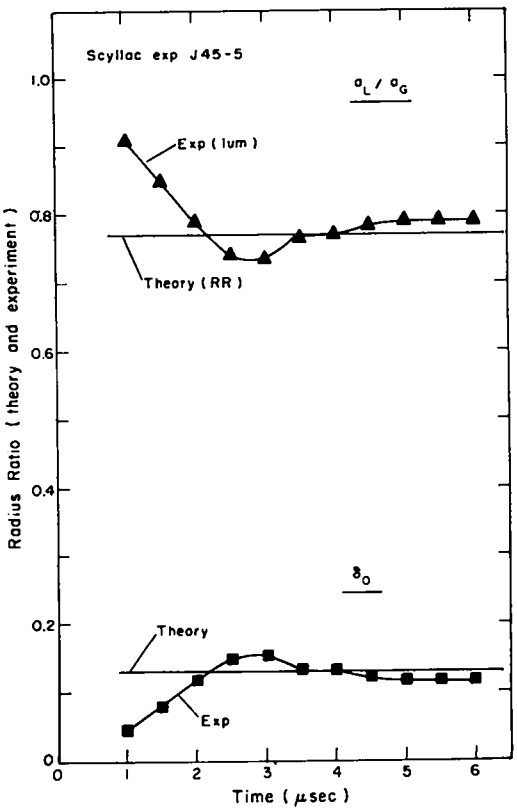

Fig. II-25
Comparison of measured plasma column bumpiness (a_L/a_G or δ_o) derived from experimental luminosity profiles, with the theoretical values derived from rigid rotor theory.

with a transfer of energy density from grooves to lands during this period.

A second test of axial equilibrium can be based on the plasma radius ratio for which we need a specific model of the radial pressure profile. Here we assume $k(T_e + T_i)$ = constant, and n(r) is given by the rigid rotor (RR) profile (see Sec. II.F).

With these assumptions it can be shown that, in axial pressure equilibrium, the plasma radius and β are related by

$$\frac{a_L}{a_G} = \left(\frac{\beta_L}{\beta_G}\right)^{1/4} \left(\frac{1+\sqrt{1-\beta_G}}{1+\sqrt{1-\beta_L}}\right)^{1/2} . \qquad (16)$$

We now evaluate Eq. (16) according to theory. The ratio $(\beta_L/\beta_G)^{1/4}$ is replaced by Eqs. (13) and (14). Theory and experiment both predict $\beta_G = 0.99$ and $\beta_L = 0.71$ for equilibrium, as shown in Fig. II-23. Substituting into Eq. (16) yields the theoretical radius ratio as $a_L/a_G = 0.77$.

Figure II-25 compares this theoretical prediction to the experimentally measured a_L/a_G and δ_o, where

$$\delta_o = \frac{1 - a_L/a_G}{1 + a_L/a_G} . \qquad (17)$$

As noted, the plasma appears to approach axial equilibrium, not monotonically here, in about 4 μsec.

3. Discussion. These studies show that axial equilibrium is reached during approximately the first 4 μsec of the discharge, the adjustment in nkT being such as to increase in a land and decrease in a groove during this time. This behavior is opposite to that noted in Exp. C (Figs. II-3 through II-5) for rectangular grooves. The sharp boundary theory for toroidal equilibrium, which assumes axial equilibrium as a starting point, is probably not valid for calculations during this period. However, after 4 μsec, the theory should apply within the sharp boundary approximations, and theory and experiment then agree (within 3% in Fig. II-23). Such close agreement must be regarded as somewhat fortuitous because it exceeds the accuracy of the measurements and probably the applicability of the theory.

11. Plasma Experiments With a 3-Meter Toroidal Sector in the $\ell = 1,0$ Shaped Coil. Before the shutdown of the toroidal sector to allow conversion to the full Scyllac torus to begin, the arc length of the sector was reduced from 5 (120°) to 3 m (72°). The objective was to attempt to determine the role of end effects in the sector experiments. Figure II-26 shows the transverse plasma motions near the center of the sector with vertical fields of 58 and 174 G. The plasma motion is similar all around the sector. The plasma confinement time is comparable to that observed in the 5-m sector. The plasma column tends to begin a contained wobble earlier than in the 5-m sector, and the shrinking of the column diameter shows that end loss is occurring sooner than in the 5-m case. The plasma is more reproducible from discharge to discharge than in the 5-m sector.

A comparison of the results in the 3- and 5-m sector suggests that line tying at the ends of the sector is influencing the plasma behavior in the sector and could be a more dominant effect in the sector than that of a change in plasma parameters, such as β, due to plasma end loss.

12. Discussion. In the toroidal sector experiments the plasma is observed to take up a helical toroidal equilibrium for 5 to 8 μsec when the $\ell = 1$ fields are applied, in contrast to the case with no $\ell = 1$ field where the plasma accelerates immediately to the outer wall of the torus. Following the equilibrium period, when the plasma stays on axis, an m = 1 plasma motion usually takes place. With $\ell = 1$ driven windings this motion is predominantly in the horizontal plane of the torus. With the $\ell = 1,0$ grooved or shaped coils the m = 1 motion is more random in direction. No higher-m unstable modes are observed. The m = 1 motion is the same in land and groove regions. Thus the "ballooning" observed earlier with large δ_o and square grooves has been eliminated. We conjecture that the m = 1 motion may have either of the following causes: (1) The $k \approx 0$, m = 1 instability, observed when $\ell = 1$ fields are applied to a linear plasma column,[9] may be occurring. However, in this toroidal case, the plasma remains stable for 5 to 8 μsec, whereas in the linear case the instability sets in immediately, (2) A loss of equilibrium due to an imbalance in the applied $\ell = 1,0$ and toroidal forces may be developing because of a change of plasma β, radius, or δ_o with time (e.g., Figs. II-3 and II-5). The plasma motion to the wall may occur because the loss of equilibrium excites the m = 1 instability. The observed containment times are sufficient for the end effects (particularly the wobble) observed in the linear case[11] to set in, initiating such a loss of equilibrium. We note that the m = 1 plasma trajectory is best fit by a parabola rather than an exponential, although an exponential fits the initial m = 1 plasma motion.

The replacement of the $\ell = 1$ driven windings by the $\ell = 1,0$ double-grooved or shaped compression coil eliminated the failure of the $\ell = 1$ fields to "track" the toroidal B_o field in time and improved the spacial uniformity of the $\ell = 1,0$ fields. However, the plasma behavior is similar to that observed with the driven windings. The results in the $\ell = 1,0$ grooved coil show a predominant vertical motion of the plasma column in the case of a force balance in the horizontal plane. This motion could possibly be resulting from the m = 1

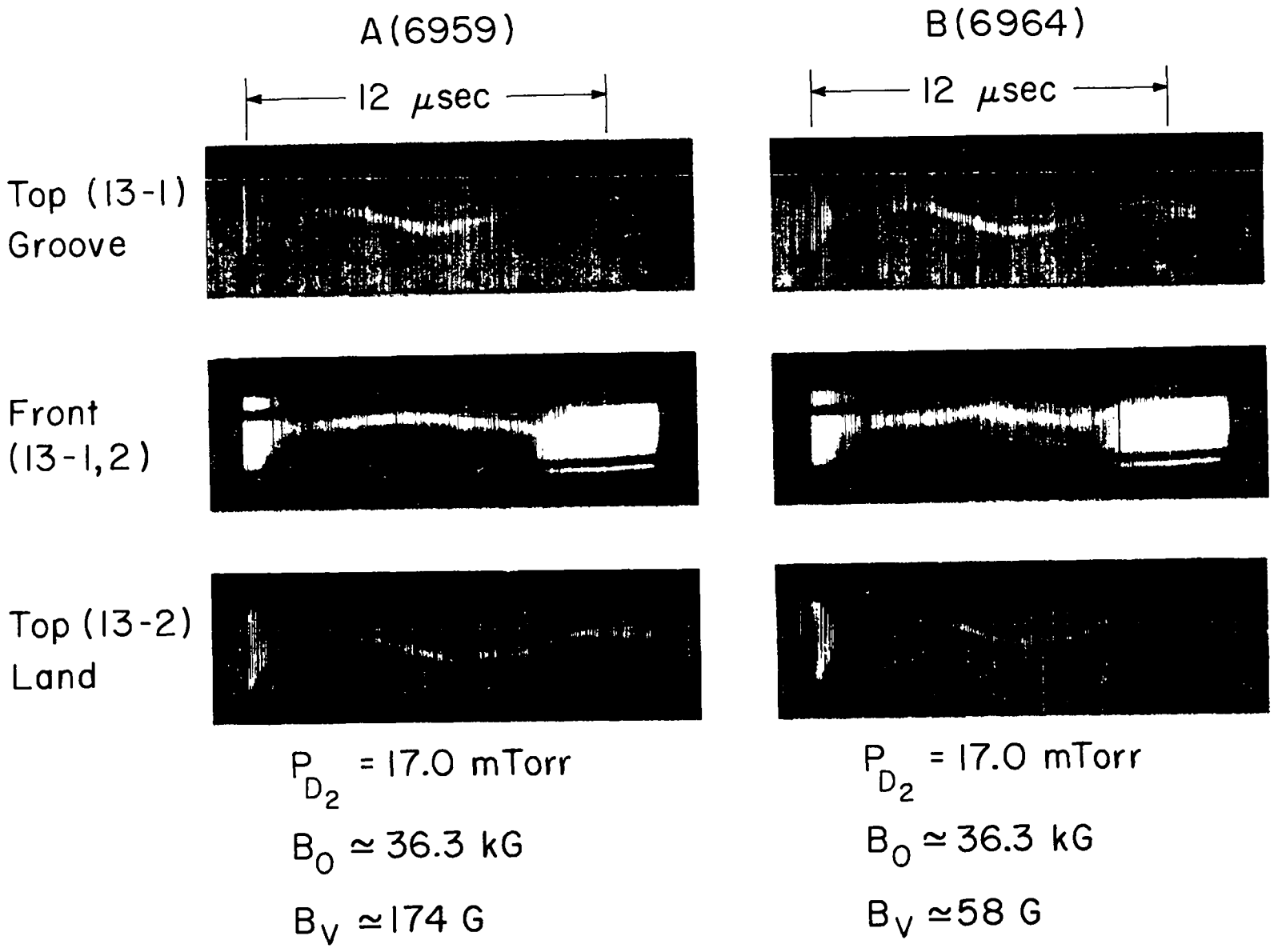

Fig. II-26.
Streak photographs showing the transverse plasma motions near the center of the 3-m sector.

instability with some field inhomogeneity giving it a preferred direction or from an interference force that arises from higher field harmonics, such as $\sin(\theta - 2hz)$, beating with the fundamental $\sin(\theta - hz)$. The double-grooved coil design is only an approximation to pure $\ell = 0$ and $\ell = 1$ fields. It is likely that it also generates other harmonic field components.

The superposition of a vertical field, with a magnitude of ~600 G on the $\ell = 1,0$ toroidal field configuration of the double-grooved coil results in plasma containment times of 10 to 14 μsec in localized meter sections of the sector. The addition of this vertical field, by a pair of toroidal windings in the horizontal plane, restores the plasma column as it attempts to move off its equilibrium position in the horizontal plane. The fact that a restoring effect is not observed in the case of a horizontal field suggests that the phenomena responsible for the better containment cases involve more than just a restoring force from a transverse field.

The experiments in the shaped coil with vertical fields in the −430 to 770 G range show that plasma confinement is not critically dependent on magnetic flux surfaces, which are approximately centered on the toroidal axis. A comparison of the results in the 3- and 5-m sectors suggests that magnetic line tying at the ends is influencing the plasma behavior. These results also indicate that the plasma "wobble," which is observed in linear θ pinches, may possibly initiate or cause the $m = 1$ motion by which the plasma equilibrium is lost in the toroidal configuration. The wobble of the compressed plasma column is interpreted as an $m = 1$ instability induced by a plasma rotation, which is associated with end effects.[11]

These experiments in the toroidal sector have demonstrated the existence of the $\ell = 1,0$ toroidal equilibrium. The plasma remains in equilibrium for times as large as 10 μsec, followed by an $m = 1$ (sideward) motion of the plasma column, which is nearly the same all around the sector. The $m = 1$ motions suggest either an imbalance between the $F_{1,0}$ and toroidal forces at later times or a long wavelength $m = 1$ instability. It has not been possible to discriminate between these effects. Measurements of the plasma parameters and the applied magnetic fields show that the product of $\ell = 1$ and $\ell = 0$ fields for plasma equilibrium agree with sharp-boundary MHD theory. End effects, which include plasma end loss, magnetic line tying, and plasma wobble, suggest that further experimentation on the high-β equilibrium and stability in toroidal geometry would best be performed in a full torus in the absence of end effects. A feedback stabilization system (cf. Sec. II.D) is being prepared for the Scyllac torus to compensate the $k \approx 0$, $m = 1$ instability and to correct the toroidal equilibrium.

REFERENCES

1. S. C. Burnett et al., Plasma Phys. Contr. Nucl. Fusion Res. 3, 201 (1971).
2. Los Alamos Scientific Laboratory report LA-4888-PR, p. 4 (1971).
3. W. R. Ellis, C. F. Hammer, F. C. Jahoda, W. E. Quinn, F. L. Ribe, and R. E. Siemon, "Plasma Experiments on $\ell = 1,0$ Helical Equilibria in the Scyllac 5-Meter, θ-Pinch Toroidal Sector," Proc. 2nd Topical Conf. Pulsed High-Beta Plasmas, Max-Planck-Institut für Plasmaphysik report IPP 1/127, July 1972.
4. F. L. Ribe and M. N. Rosenbluth, Phys. Fluids 13, 2572 (1970).
5. H. Weitzner, Phys. Fluids 14, 658 (1971).
6. H. Grad and H. Weitzner, Phys. Fluids 12, 1725 (1969).
7. J. P. Freidberg and B. M. Marder, Phys. Fluids 14, 174 (1971).
8. J. P. Freidberg, Plasma Phys. Contr. Nucl. Fusion Res. 3, 215 (1971).
9. K. S. Thomas, C. R. Harder, W. E. Quinn, and R. E. Siemon, Phys. Fluids 15, 1658 (1972).
10. F. L. Ribe, Los Alamos Scientific Laboratory report LA-4098, March 1969.
11. R. F. Gribble, W. E. Quinn, and R. E. Siemon, Phys. Fluids 14, 2042 (1971).

C. Linear Scyllac (K. S. Thomas, H. W. Harris, F. C. Jahoda, R. Kristal, G. A. Sawyer, and R. E. Siemon)

1. Apparatus. The Scyllac linear experiment was a 5-m-long θ pinch built of components that are now being used in the full Scyllac torus. The arrangement of this device as well as the Scyllac toroidal sector[1] in the experimental area is shown in Fig. II-27. The Scyllac torus will consist of 15 capacitor racks with associated collector plates. Seven of these racks were used in the Scyllac linear θ pinch. Each rack has a total main-bank capacitance of 390 μF. As shown in Fig. II-27, the 5-m-long, 11-cm-i.d. main compression coil was fed from alternate sides in 1-m sections. A main-bank voltage of 45 kV produced a main compression field that rose to 60 kG in 4.3 μsec. The two end racks each supplied current for the magnetic mirror coils. The main coil and the mirror coils had different trigger systems so that they could be fired independently. Because adjacent coils were fed from different sides, they were electrically insulated from each other, which required a 1-cm gap between the main compression coils. This decoupled the coils sufficiently so that to obtain a

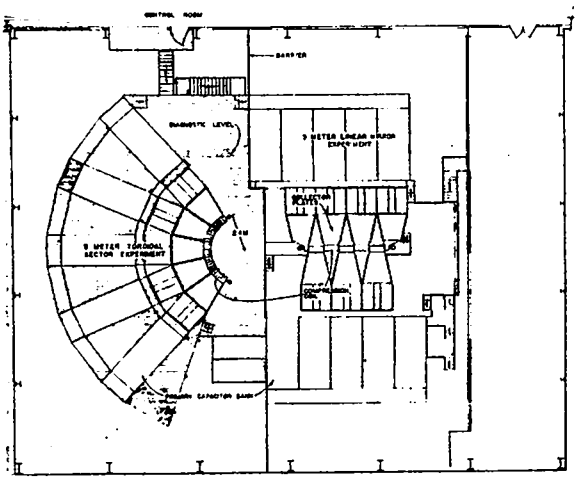

Fig. II-27
Diagram of linear Scyllac experiment.

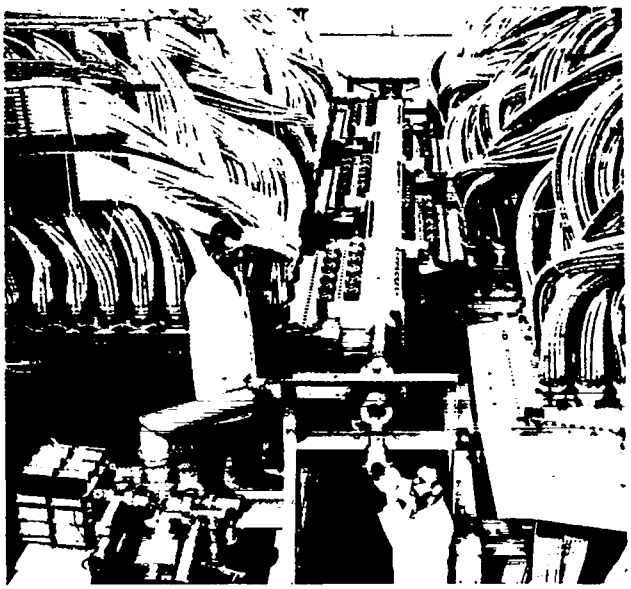

Fig. II-28.
Linear Scyllac experiment.

homogeneous compression field and good plasma production in the machine, all racks must operate with proper simultaneity and equal current. Operation was highly reliable, and good results were obtained on more than 90% of the machine discharges. To date, all operation with plasma has been at 45 kV on the main bank. The banks are designed for operation at as high as 60 kV and have been electrically tested to 55 kV.

Operation with plasma began on March 13, 1972. The experiment was terminated on March 1, 1973, because the components and experimental area were needed for the full Scyllac torus.

2. Results Without Mirrors. Early operation of the machine was without magnetic mirrors (Fig. II-28). Operation was mostly at 10-mTorr D_2 filling pressure without applied bias field. The plasma produced inside the 88-mm-i.d. discharge tube had a density profile that was approximately Gaussian with an inflection-point radius of 0.8 to 1.0 cm, a peak density of 1.5 to $2.0 \times 10^{16}/cm^3$, and an ion temperature (as indicated by neutron yield) of 2 to 3 keV. Total neutron yields were about 5×10^6/cm of tube length. The plasma column exhibited the previously observed[2,3] "wobble," which usually begins 4 to 5 μsec after the initiation of the main discharge. The time for propagation of an Alfvén wave from the ends of the coil using the peak field and the denisty on axis was about 4 μsec, and the "wobble" was probably related to the shorting out of the electric fields in the plasma and the transfer of the diamagnetic current from the electrons to the ions.[4,5] The maximum amplitude of the wobble was about 1.5 cm off the discharge tube axis and averaged 0.5 to 1.0 cm. Stereoscopic views of the plasma column show that the "wobble" was an m = 1 rotation with a frequency of about 300 kHz, and it had an amplitude and phase that often varied along the coil axis.

End-on holographic interferograms of the plasma column showed a rapid buildup of fringes near the discharge tube walls, which was sufficient to start obscuring the central plasma column in 6 to 8 μsec. Side-on gas-laser interferometer and multichannel plasma luminosity profile data at the center of the 5-m coil showed that the plasma causing these fringes was not inside the main coil. Also, after a few plasma discharges, it was observed that on random discharges (but never on consecutive discharges) there were decreases of about an order of magnitude in the neutron yields in the two end meters of the coil, although the neutron yields in the center of the coil remained normal. At the same time the diagnostics viewing the end coil sections recorded a large increase of plasma illumination and an increase of plasma density. An excluded flux measurement on one of the end coil sections showed a slower implosion of the plasma column and an increased mass as indicated by the bounce frequency[6] of the plasma column. Also, end-on interferograms taken at 1 μsec after discharge initiation showed a large amount of plasma well separated from the discharge tube wall but at a radius (2 to 3 cm) larger than that observed on discharges where neutron production was almost constant along the entire coil. Examination of the quartz discharge tube outside the ends of the coil indicated intense bombardment of the tube about 30 cm

outside the ends of the coil. Owing to the good crowbar system, the magnetic field produced by the compression coil was constant to within 20% during the time of plasma loss; therefore, the bombardment of the discharge tube by plasma streaming out the ends of the coil was localized to a small region. The phenomenon is interpreted to be due to contamination of the discharge tube inside the main coil near the ends of the coil by material "boiled" off the discharge tube by the previous plasma discharge.

To lessen the effects of plasma bombardment of the discharge tube, enlarged quartz sections, 20 cm in diameter and 45 cm long, were added to a shortened quartz discharge tube just outside the mirror coils. Figure II-29 shows the configuration before and after the addition of the enlarged sections. Operation of the 5-m coil without the mirror coils was considerably improved with this configuration. Figure II-30 shows end-on interferograms (λ = 6943 Å) taken at peak field before and after the addition of the enlarged sections. A buildup of fringes near the wall was still noted, but at a greatly reduced rate, indicating that some of the plasma streaming out the ends was probably still hitting the main discharge tube. Some shot-to-shot variation in plasma properties was still observed, but was greatly reduced from the case without the enlarged sections.

During one period of operation the mirror coils were removed and the enlarged section lengthened so that the small discharge tube extended only 7 cm out the ends of

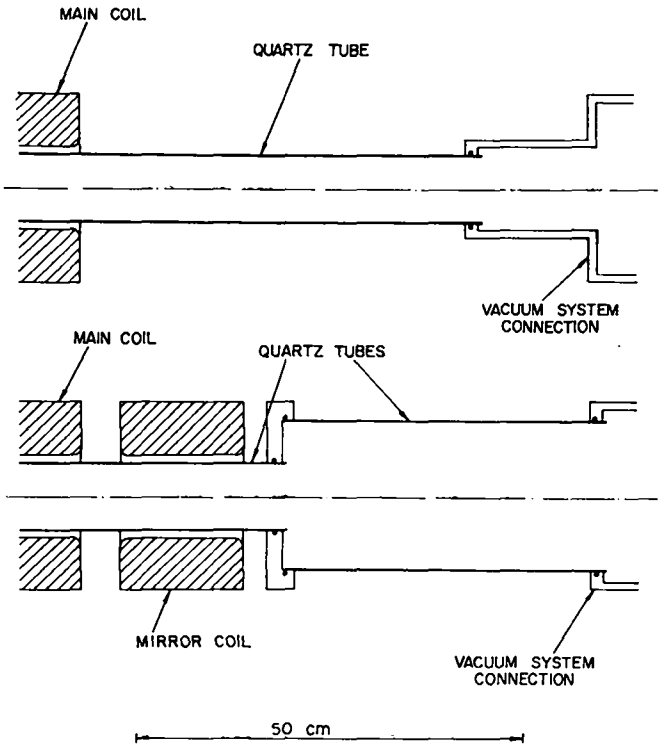

Fig. II-29.
Diagram of enlarged quartz sections at the ends of the coil. Top--original arrangement. Bottom--enlarged sections.

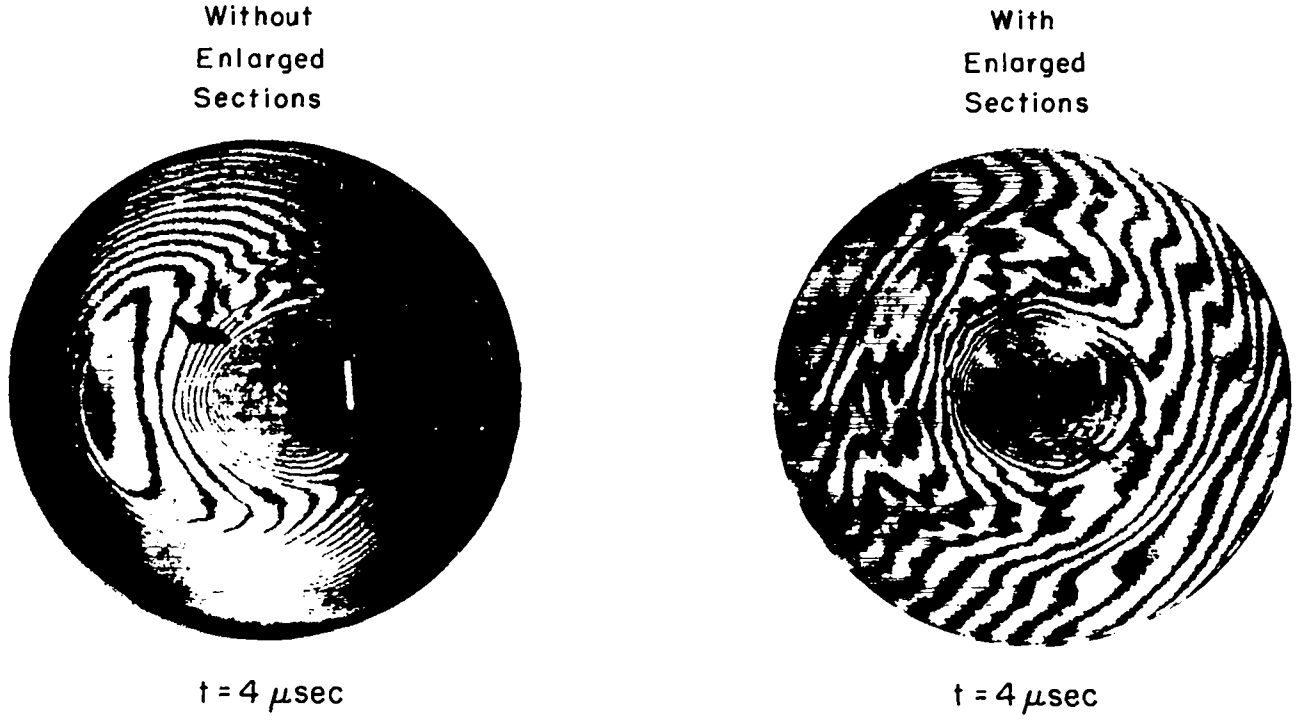

Fig. II-30.
End-on interferograms taken at 4 μsec before and after the installation of the enlarged sections.

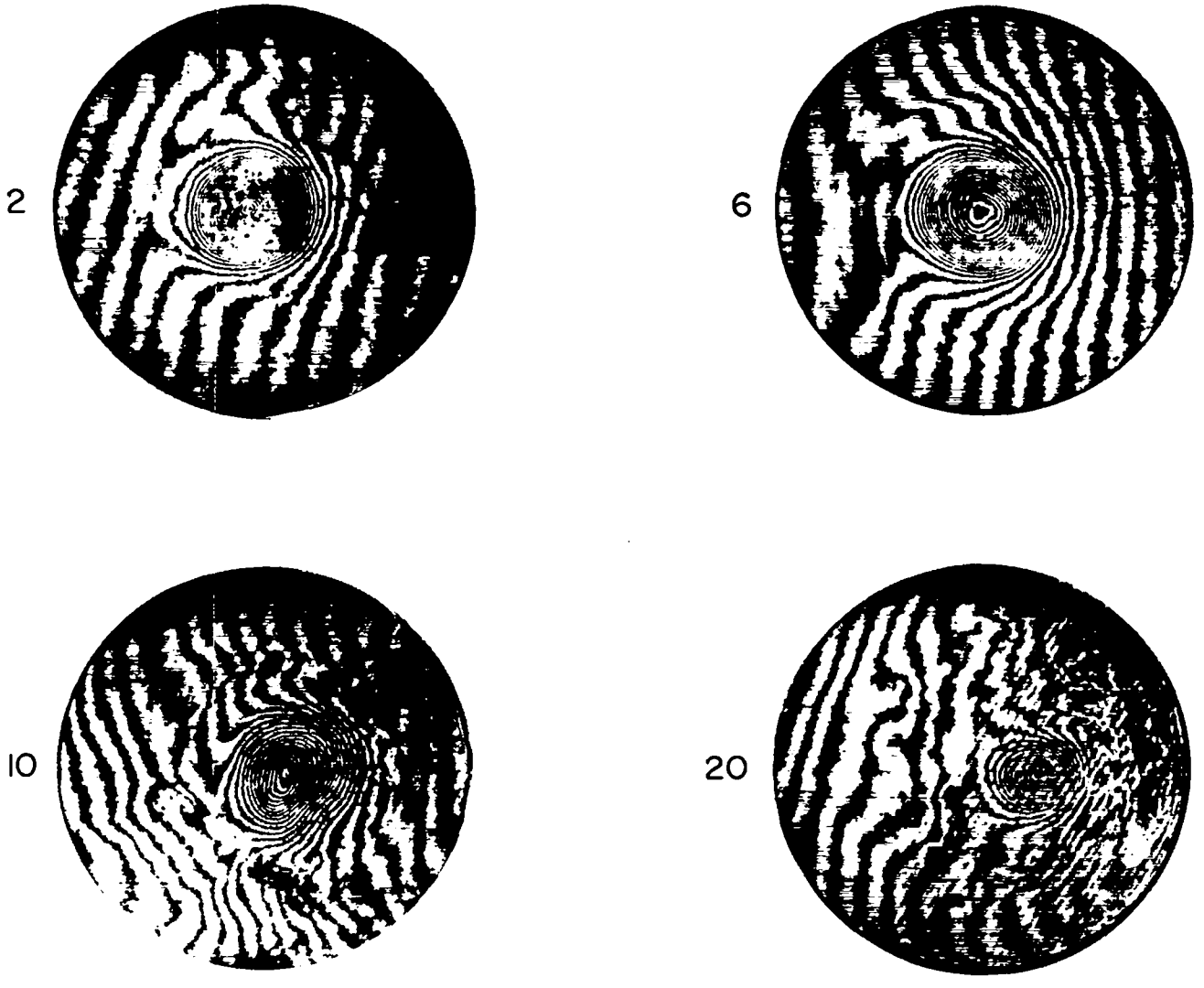

Fig. II-31.
End-on interferograms taken at four times during plasma discharges.

the main 5-m-long compression coil. With this arrangement the contamination problems were reduced even further. While operating in this configuration, the plasma loss rates out the ends of the machine were measured using holographic interferograms taken at two times during each plasma discharge. Figure II-31 shows interferograms taken at four times during plasma discharges, and Fig. II-32 shows the results of the measurements. The line drawn through the experimental points corresponds to a plasma loss rate with an e-folding time of 11.5 μsec.

Also during this time, the plasma electron temperature was measured using a double-foil soft x-ray detector. A new detector system was constructed for the experiment. Calibration of the relative gain of the two channels in previous x-ray detectors was difficult because the phosphors used to detect the x rays are very thin (0.010 in.) to eliminate signals due to fast neutrons. To obtain a system that could be more easily calibrated, the device was constructed so that foils could be added in front of the detector in one channel by turning a lever. Thus the

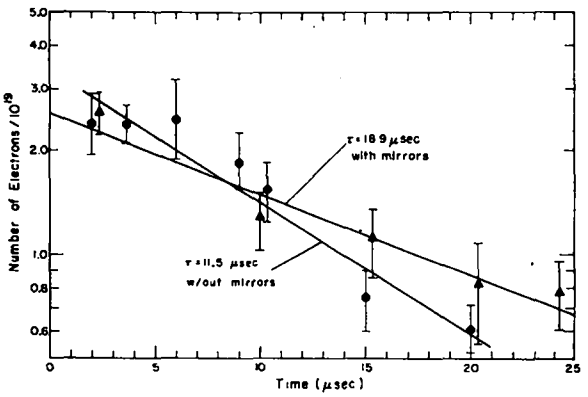

Fig. II-32.
End-loss results. Triangular points are for operation with magnetic mirrors. Other points are for operation without magnetic mirrors.

system could be calibrated by putting equal foil thicknesses in both channels and using the soft x rays from the plasma as a source. This method had the additional advantage of taking into account any geometric differences in the two channels. The foil thicknesses used were 8 mg/cm^2 of beryllium in each channel for calibration. The thickness in one channel was increased to 16 mg/cm^2 for the temperature measurement. The result of the measurement was an electron temperature of 600 ± 100 eV. This was constant within experimental error during the time (3 to 9 μsec after discharge initiation) that the measurements were made.

After the mirror coils had been reinstalled and the configuration returned to that shown in the lower part of Fig. II-29, the electron temperature was measured using Thompson scattering. First the temperature was measured as a function of time in the center of the 5-m compression coil on the discharge tube axis. The electron temperature at peak field (660 ± 90 eV) agreed with the soft x-ray measurement. However, at later times the electron temperature showed a drop not seen with the x-ray measurement. This drop was about a factor of 2 by 10 μsec after discharge initiation. Even though scattered signal levels indicated that the laser beam was still hitting the dense part of the plasma column, it was considered possible that the plasma "wobble" that moves the plasma column off the discharge tube axis was resulting in a measurement of electron temperature off the axis of the plasma column. A strong radial dependence of electron temperature could then be responsible for the lower temperature measured at late times. To test this possibility the Thompson scattering apparatus was moved to examine a plasma volume 1 cm off the discharge tube axis. A consideration of the rates at which energy is supplied to the electrons from the ions and the loss through thermal conduction out the ends of the machine predicts a temperature dependence proportional to $n^{2/5}$ where n is the electron density. Preliminary analysis of the data indicates that the results are consistent with this relation. The off-axis signals were considerably smaller than those obtained with the late-time data; thus the drop in electron temperature at later times is real.

Because the decrease in electron temperature was inconsistent with that from the soft x-ray apparatus, the x-ray measurement was repeated. The results from this measurement showed large shot-to-shot variations sufficient to prevent a good quantitative measurement. The qualitative results agreed with those from the Thompson scattering experiment, that is, a drop in electron temperature at later times was observed. In fact, there was a shot-to-shot variation in behavior at later times, the drop in temperature being greater on shots where the other diagnostics indicated an increased contamination level. Because the radiation detected by the two channels does not come from exactly the same plasma volume and it is known that the contamination level varies along the discharge tube axis, the shot-to-shot variation in calibration shots as well as data shots was probably due to variations in the amount of line radiation from high-z impurity ions. The presence of these high-z impurities was also probably the cause of the drop in electron temperature. This drop was faster than would be predicted from thermal conduction losses and indicates that the electrons are giving up energy to ionize the impurity atoms.

3. Results with Mirrors. The mirror coils were 16-cm long, 11-cm i.d., and had corners radiused to 1 cm. The gap between main and mirror coils was 5 cm. The mirror coils were constructed of high-strength steel. Figure II-33 shows a mirror coil viewed from above. At 45-kV bank voltage, the field in the mirror coil rises to 150 kG in 7.5 μsec. Figure II-34 shows the B_z field in the main coil for a bank voltage of 45 kV and in the mirror coils for bank voltages of 40 and 45 kV. The quantity t is the time from initiation of the magnetic fields. The number of mirror shots was limited by electrical breakdowns through the insulation in the transition region between the collector plates and the coil. This was finally traced to mechanical cutting of the Mylar and polyethylene insulation by motion of the mirror coils. For later operation, the mirror insulation was replaced every ten mirror shots. This was a tedious process but prevented additional electrical failures.

The experiment was operated with the magnetic mirror fields applied both simultaneously with the main compression field and delayed 0.5 to 1 μsec with respect to the main field. Figure II-35 shows the mirror ratios as a function of time for (a) mirror bank 45 kV, $\Delta t_o = 0$, (b) mirror bank 45 kV, $\Delta t_o = 1$ μsec, and (c) mirror bank

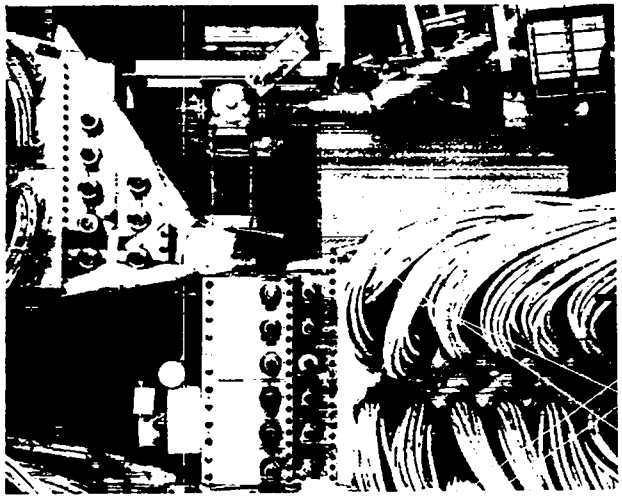

Fig. II-33.
Photograph viewed from above one end of the linear Scyllac experiment showing magnetic mirror coils.

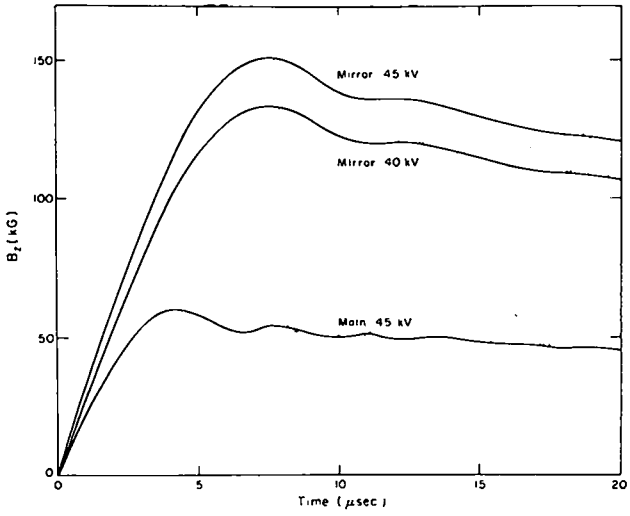

Fig. II-34.
B_z vs time for main 5-m coil and two operating voltages for mirror coils.

40 kV, Δt_o = 1 μsec. Main bank voltage was 45 kV in all cases.

When the main and mirror fields were applied simultaneously, the plasma column, as indicated by streak pictures at two locations, side-on luminosity at another location, and end-on interferograms, always showed some motion off the discharge tube axis. At early times (5 to 8 μsec) this often had the form of an m = 1 long wavelength instability. (The e-folding time was ~3.0 μsec.) Usually the plasma column seemed to touch the discharge

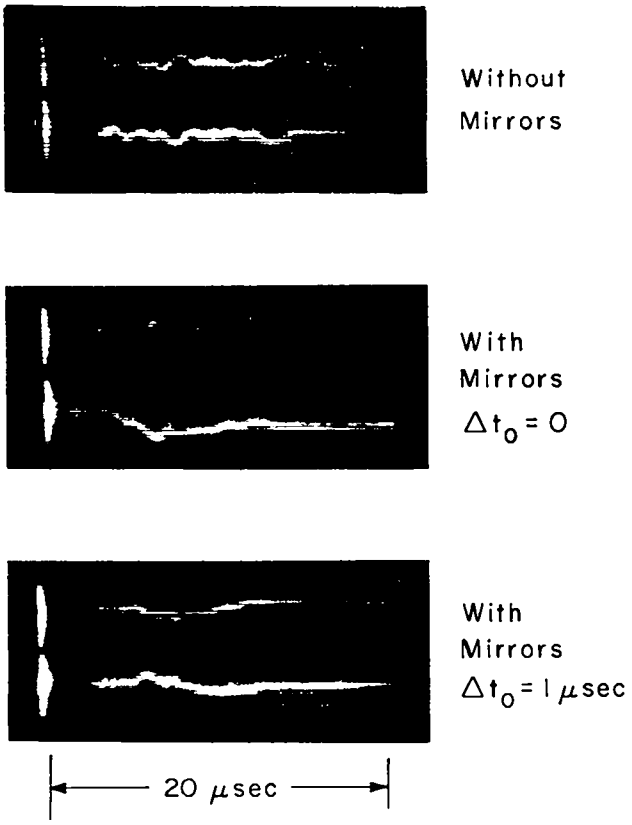

Fig. II-35.
Mirror ratios as a function of time for (a) mirror bank 45 kV, $\Delta t_o = 0$, (b) mirror bank 45 kV, Δt_o = 1 μsec, and (c) mirror bank 40 kV, Δt_o = 1 μsec. Main bank voltage was 45 kV in all cases.

tube wall at some point, but not at every axial position. The plasma column, as indicated by neutron yields, did not, however, cool rapidly. When the application of the mirror fields was delayed (Δt_o = 0.5 and 1 μsec) it was observed that the motion of the plasma column off axis was slower, the column usually striking the discharge tube wall 15 to 20 μsec after discharge initiation. Also, unlike the Δt_o = 0 case, the direction of motion of the plasma column was always toward the mirror coil feed slot. Figure II-36 shows stereoscopic streak pictures taken 1 m from the center of the main coil for the three cases of no-mirror fields and mirror fields with Δt_o = 0 and 1 μsec. End-on holographic interferograms indicate that the motion of the plasma column off the discharge tube axis was the same everywhere (k≈0), thus the streak view at the one location was indicative of the plasma motion everywhere along the discharge tube.

When the magnetic field was reduced 10 to 20% in the mirror coils, the plasma column often did not strike the

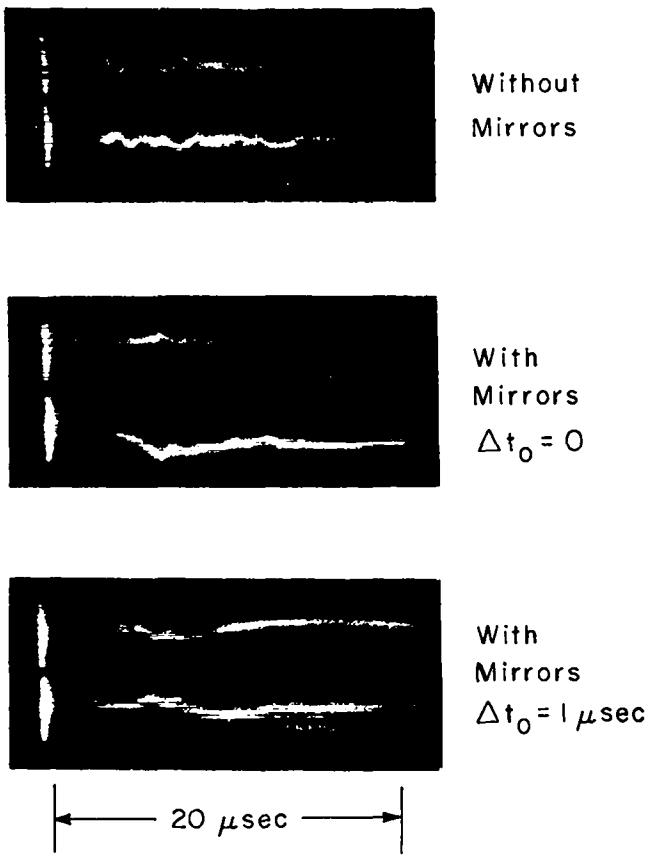

Fig. II-36.
Stereoscopic streak pictures for three different machine shots, one without magnetic mirrors and two with. Streak duration is 20 μsec.

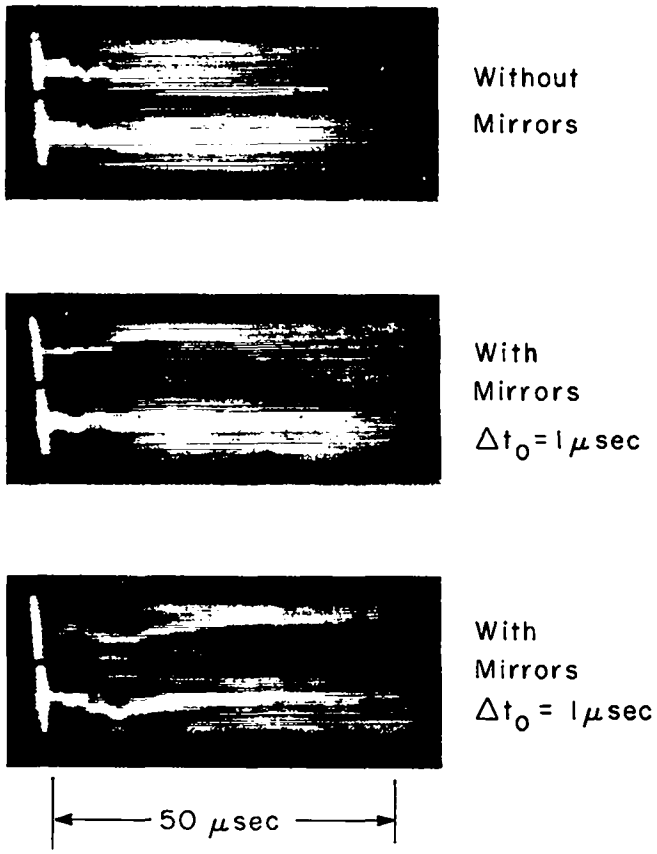

Fig. II-37.
Stereoscopic streak pictures for three different machine shots, one without magnetic mirrors and two with. Streak duration is 50 μsec.

discharge tube wall. This resulted in a situation where, on about one-half of the plasma discharges with mirror fields ($\Delta t_0 = 1\ \mu sec$), the plasma column stayed off the discharge tube wall. Figure II-37 shows streak pictures of a no-mirror case and two cases with mirrors applied: one where the plasma hit the wall at about $t = 20\ \mu sec$ and the other where it never hit. Because the late time motion of the plasma column was always in the same direction, it seemed possible that the motion was caused by a field asymmetry in the magnetic field of the mirror coil. To test this possibility, metal plates were attached to the mirror coil opposite the feed slot. Modeling tests indicated that these plates should have been large enough to reverse the asymmetry in the mirror coils. The motion of the plasma was not effected when the mirror fields were applied, although a slight motion of the plasma column in the expected direction was observed when the mirror fields were not activated.

The existence of plasma discharges, with magnetic mirror applied, that did not strike the discharge tube wall allowed the making of end-on interferograms as late as $t = 40\ \mu sec$. The 20 interferograms clear enough for quantitative analysis have been analyzed and are plotted as triangles in Fig. II-32. Each point represents the average for a number of shots and the standard deviation due to shot-to-shot variation. The end-loss time of 18.9 μsec represents an improvement by a factor of 1.6 over the data without mirrors. This does not agree with theoretical calculations, which would predict that the confinement should increase about as much as the mirror ratio of 2.5.

In summary, the addition of magnetic mirrors to the linear Scyllac θ pinch, although increasing plasma confinement, causes an instability in the plasma column. With delayed application of mirror fields this instability was very weak, and late time behavior of the plasma column ($t > 10\ \mu sec$) might have been due to magnetic field asymmetries, although attempts to modify plasma behavior by changing field asymmetries were unsuccessful.

The difference in plasma behavior for $\Delta t_o = 0$ and $\Delta t_o = 0.5$ to 1 μsec was probably due to either or both of the following. (1) When the mirror fields are delayed, the mirror ratio is much smaller until about peak field of the main compression field. Thus, line tying, which is a stabilizing effect, has a chance to become more effective before the bad magnetic field line curvature that would drive an MHD instability becomes severe. (2) The initial conditions are different in the two cases. When the fields are applied simultaneously, a high-β (ratio of plasma pressure to external magnetic field pressure) plasma is formed in the mirror region. If the equilibrium condition of constant pressure along a magnetic field line is considered, it is seen that if the plasma β in the main coil is 0.8 then that in the mirror region should be less than 0.2. Thus the plasma in the mirror region has too high a β for equilibrium. Also, results from the Scyllac toroidal sctor show that the bumpiness of a plasma column is enhanced over its equilibrium configuration when the bumpiness of the magnetic field is applied during the implosion phase of the θ pinch. This could increase the effects of adverse field curvature in the mirror region.

The only stability theory available for comparison with experiment is one formulated by J. P. Freidberg and B. M. Marder of LASL and H. Weitzner of New York University. This theory was developed to consider the stability of the $\ell = 0$ system used on the Scyllac torus. It incorporates a diffuse plasma profile but does not take into account the streaming of plasma in the mirror regions. Freidberg and Marder's theory[7] is numerical and could model an infinite system with 2.5 mirrors every 5 m. It predicts that the dominant $m = 1$ instability would have $k \approx 0$ in agreement with experimental observations. It also predicts, however, an instability growth rate 3 to 4 times larger than that observed experimentally with simultaneous timing of the main and mirror magnetic fields. In the theory, when the field lines are tied at the throat of the mirrors (much stronger line tying than is present experimentally), the plasma column is stable. If the streaming of the plasma through the mirror region and the effect on the equilibrium configuration of plasma loss does not greatly affect the stability calculation, it indicates that line tying is an important effect in the experiment, and could explain the observed experimental results.

The only other experiments with magnetic mirrors on θ pinches are experiments with a 30-cm-long θ pinch with mirror formed by shaped coils and mirror ratios of 1.1 to 3.0 (Ref. 8) and with a shaped coil (mirror ratio 1.4) on the 1-m Scylla-IV device.[9] In both of these cases no gross instabilities were observed.

REFERENCES

1. S. C. Burnett et al., *Plasma Physics and Controlled Nuclear Fusion Research* (International Atomic Energy Agency, Vienna, 1971), Vol. III, p. 201.
2. H. A. B. Bodin, T. S. Green, A. A. Newton, G. B. F. Niblett, and J. A. Reynolds, *Plasma Physics and Controlled Nuclear Fusion Research* (International Atomic Energy Agency, Vienna, 1966), Vol. I, p. 193.
3. R. F. Gribble, W. E. Quinn, and R. E. Siemon, Phys. Fluids 14, 2042 (1971).
4. K. S. Thomas, Phys. Rev. Lett. 23, 746 (1969).
5. M. Kaufmann, E. Fünfer, J. Junker, J. Neuhausen, and U. Seidel, Max-Planck-Institut für Plasmaphysik report IPP 1/123, Garching bei Munchen, Germany.
6. T. S. Green, Phys. Fluids 6, 864 (1963).
7. J. P. Freidberg and B. M. Marder, Los Alamos Scientific Laboratory, private communication.
8. A. Heiss, H. Herold, and E. Unsöld, *Proceedings of APS Topical Conference on Pulsed High-Density Plasmas*, Los Alamos, New Mexico, 1967. Paper D-7.
9. R. F. Gribble and W. E. Quinn, Los Alamos Scientific Laboratory, unpublished data.

D. Feedback Experiments on Scylla IV (S. C. Burnett, R. F. Gribble, C. R. Harder, K. J. Kutac, and A. S. Rawcliffe)

1. Introduction. The feedback stabilization system to control $k \sim 0$, $m = 1$ plasma motion in Scyllac was described in the last annual report (LA-4888-PR). The systems four basic components are: a position detector, a signal processor, a power amplifier, and $\ell = 1,0$ field coils. The basic system was installed on Scylla IV-3 for initial testing and preliminary evaluation of the feedback capability. Ten power amplifier modules are being used to drive 20 $\ell = 0$ coils. Phasing of these coils relative to the $\ell = 1$ fields provides for control of the plasma column motion in the plane of the observed $\ell = 1$ field-induced instability.

Component failures, particularly in the $\ell = 1$ coils, have caused many problems. A new coil insulation wrapping technique has produced improved $\ell = 1$ coils. Only two failures of the new coils occurred in 66 main bank discharges, but the $\ell = 1$ coil failures are still sufficiently troublesome that a new $\ell = 1$ grooved compression coil is being made to provide the $\ell = 1$ fields for further studies.

A series of definitive discharges with the new $\ell = 1$ coils showed that the present feedback system can balance an instability growth rate of 0.7×10^6 sec^{-1}.

2. **Experimental Results.** Since installing the new set of $\ell = 1,0$ windings, there have been 66 main bank discharges on Scylla IV-3. The first series of discharges with $\ell = 1$ fields, where $B_r/B_z = 0.09$, demonstrated an $m = 1$, $k \sim 0$ instability with a growth rate (γ) of ~0.9 to 1.0×10^6 sec^{-1}. The feedback modules were unable to control the instability at this growth rate. Modification of the $\ell = 1$ capacitor bank to reduce it from 18 to 14 capacitors resulted in $B_r/B_z = 0.068$ and an average instability growth rate of about 0.7×10^6 sec^{-1}. On some discharges the growth rate was as high as 0.9 MHz, depending on primary bank performance and axial position observed. In this instability regime, nine feedback discharges, along with $\ell = 1$-only control discharges, were fired using the turn-on time of the modules as the only variable manipulated. The feedback loop was not closed on these discharges. Instead, the modules were pulsed on from an external generator, and the pulse was sustained for a full 10 μsec without tube arcing at a current level of ~5.5 kA. A set of streak photographs from an $\ell = 1$-only control discharge and a feedback discharge is shown in Fig. II-38. Cameras 1, 2, and 3 are viewing the plasma column 75, 125, and 225 cm, respectively, from the east end of the coil. Note that the image in Camera 1 is inverted relative to that in Cameras 2 and 3, and that the top streak of Camera 3 views the same plane as do the other two cameras. Control discharge (Shot 806) exhibits a nearly $k = 0$ behavior with growth rates of 0.7 MHz in Camera 1 and 0.9 MHz in Cameras 2 and 3. The preceding feedback discharge (Shot 805) shows the plasma column definitely held off the wall in Cameras 1 and 3 and possibly hitting the wall in Camera 2, although apparently not in the plane or axial position viewed. In both of the above discharges the $\ell = 1$ fields were turned on 1.2 μsec after the main bank so that they peaked with the main compression field. In the feedback discharge the modules were turned on 1.0 μsec after the main bank. Plasma and field parameters relating to this series of discharges since installation of the new coils are:

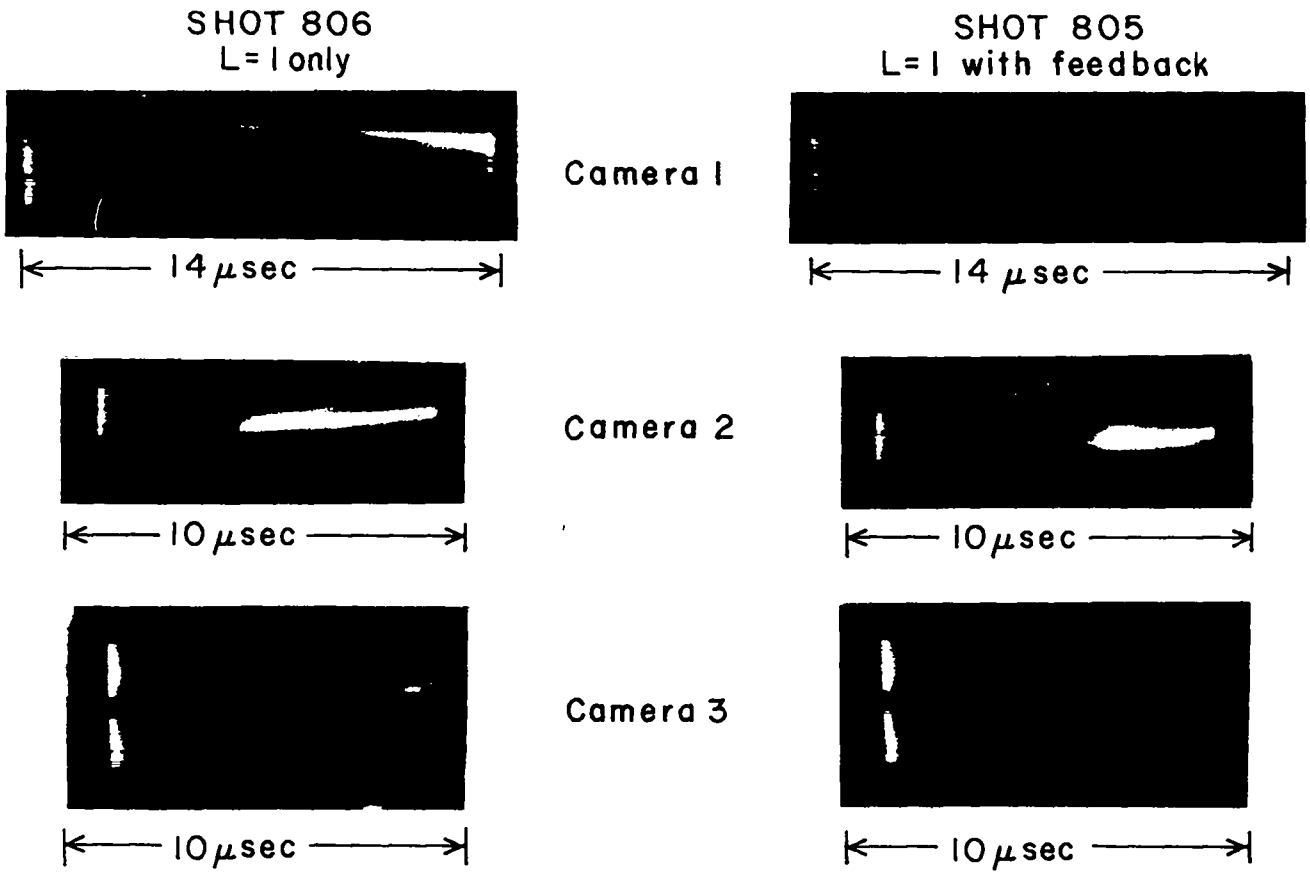

Fig. II-38.

Streak photographs of the Scylla-IV plasma with and without feedback applied. The view in Camera 1 is inverted from that in Cameras 2 and 3. Shot 806 on the left is without feedback force, and Shot 805 on the right is with feedback force.

$n_e \sim 2.4 \times 10^{16}/cm^3$ From holographic analysis shot No. 724 D_2 at 20 μ

a	~	0.67 cm	
δ_1	~	0.6	
B_r	=	2.6 kG	Field mapping
ΔB_z	=	180 G	
B_z	=	42.4 kG (vacuum shot)	
Module current	=	5.5 kA (differing somewhat from module to module).	

The results shown in Fig. II-38, which show an $F_{1,0}$ force that is just able to balance the instability growth, are typical of the entire series. The present $\ell = 0$ coils are placed only 7 mm from the wall of the main compression coil. The image currents induced in the compression coil by the $\ell = 0$ coils act to reduce the $\ell = 0$ fields. A new set of coils, with a 10.5-cm diam that will approximately double the ΔB_z modulation and hence the $F_{1,0}$ force, is currently being fabricated and will be used with the new $\ell = 1$ grooved compression coil.

The position detector signal was monitored and compared to a streak photograph viewing the plasma column at the same position (Camera 2). Figure II-39 shows a plot of plasma column position read from the streak photograph along with the position detector difference signal that is directly proportional to the distance off axis the plasma has moved (as well as proportional to light amplitude). The ability of the position detector to follow the plasma excursions in time is satisfactory. The signal magnitudes indicate that the detector was positioned too low to view the plasma because the signal is shifted toward positive values of displacement.

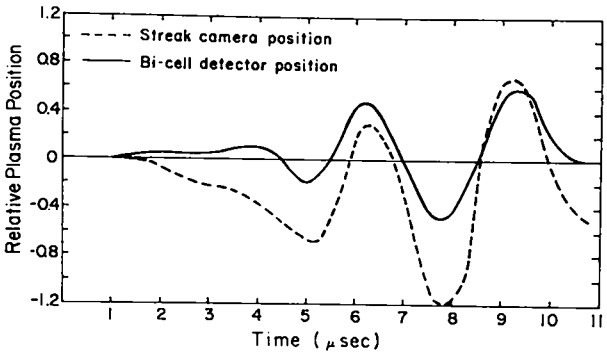

Fig. II-39.
Comparison of plasma position determined by the feedback position detector and a streak camera.

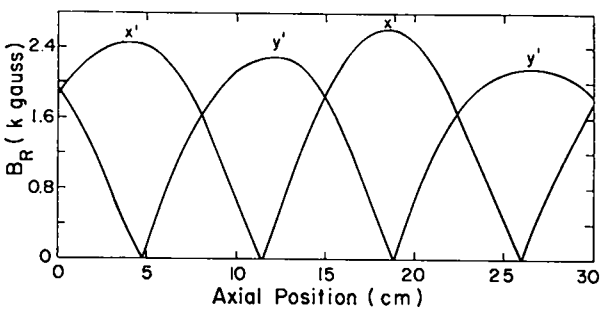

Fig. II-40.
Plot of the $\ell = 1$ field generated by windings in the Scylla-IV experiment.

3. **Field Mapping.** Because of our decision to groove the main compression coil for $\ell = 1$ fields and our observation of a very weak or marginal $F_{1,0}$ force, the $\ell = 1$ and $\ell = 0$ fields within the compression coil were mapped. The $\ell = 1$ field waveform mapped in the fourth wavelength from the east end of the machine is shown in Fig. II-40. The waveform itself was mapped while driving the $\ell = 1$ header with a 100-kc oscillator delivering 40 A. The absolute value of the field was determined by pulsing the $\ell = 1$ bank into the coils with a calibrated probe positioned to measure the peak B_r field in the x'-direction. Position coordinates are aligned parallel to the primary feedback force vectors, which, with the current phasing of $\ell = 1$ and $\ell = 0$ circuits is a 45° clockwise rotation of the normal Cartesian coordinates. The discrepancy in amplitude between the central peaks in both the x'- and y'-coordinates has been shown to be due to the absence of $\ell = 0$ coils 1 and 3, which were removed to facilitate rapid fabrication of the new set of $\ell = 1$ coils. Inserting copper shells with nearly the same dimensions as the $\ell = 0$ windings corrected this amplitude variation. The smaller field depression at the end peaks (both x' and y') is probably due to the feed tabs of the $\ell = 1$ coils themselves. The relative peak amplitudes from wavelength to wavelength were found to vary only a small amount.

The $\ell = 0$ field waveform, also mapped in the fourth wavelength from the east end of the machine, is shown in Fig. II-41. The $\ell = 0$ coils were driven by the feedback modules operating at 30-kV plate voltage and 7.5 V on the filaments. The fields produced by each of the 20 $\ell = 0$ coils within the machine were scanned for absolute magnitude and are plotted in Fig. II-42. Also plotted is the current by each module into its respective coils and the resulting field per unit current produced. The observed variation in gauss per kiloampere from coil to coil is probably due to nonuniformities in coil fabrication and subsequent variation in the wall factors influencing the magnitudes of the image currents. However, the degree of variation is not serious.

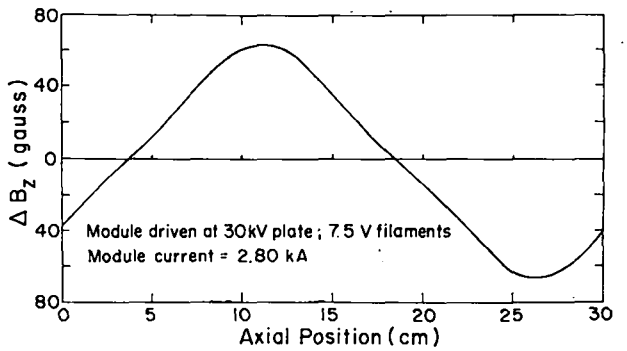

Fig. II-41.
Plot of the ℓ = 0 field in the Scylla-IV experiment.

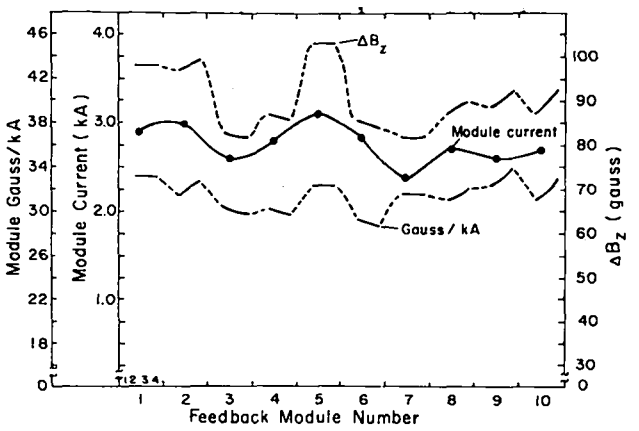

Fig. II-42.
Plot of feedback module output current, the ℓ = 0 magnetic field produced by feedback, and the G/kA produced in the Scylla-IV geometry.

E. Scyllac Torus (W. E. Quinn and G. A. Sawyer)

Conversion to the full Scyllac torus began on January 2, 1973. The toroidal sector was closed down on December 29, 1972, to allow the conversion to begin. The 5-m-linear device with strong magnetic mirrors continued to operate until March 1, 1973. The initial conversion work on the sector involves the increase of the major radius of curvature from 2.4 to 4.0 m. We plan to complete the conversion of the 120° toroidal sector to the larger radius by April 10, 1973. Experiments will resume on the sector with an 8-m coil in April while conversion continues on the remainder of the torus. The objective is to study the plasma equilibrium and stability in the larger radius of curvature. We plan to begin experiments with the complete 8-m-diam torus in January 1974.

F. Plasma Diagnostic Measurements (W. R. Ellis, J. P. Freidberg, R. E. Siemon, and E. L. Zimmerman)

1. Luminosity Measurements. Luminosity measurements have become a standard diagnostic for θ-pinch plasmas. Typically, the light from 10 chords through the plasma is imaged by an optical system onto an array of 10 photomultipliers. In principle, the luminosity profiles so obtained must be Abel inverted to yield light emission (hence relative plasma density) as a function of plasma radius. Abel inversion is sensitive to the detailed shape of the wings of the luminosity profile, where the signal-to-noise ratio is always poor. Our approach to this problem has been to best-fit a calculated intensity profile based on an analytic expression for the density distribution. The simplest density profile is a Gaussian because the calculated intensity distribution is also a Gaussian.

The arrangement shown in Fig. II-43 is accurate and reliable. A variable aperture stop one focal length behind the objective lens serves the dual function of collimating the viewing direction and providing adjustment for plasma light intensity. By using such an aperture, the light for each channel is collected along nearly parallel chords through the discharge tube. A strobe light, diffuser, lens, aperture, and beam splitter provide a uniform pulse of light for calibration purposes. The light pipe array, consisting of 22 adjacent channels with independent output bundles, can be connected in various ways to the 10 1P-21 photomultipliers normally used. Alignment is facilitated by illuminating the first and last optical bundles and viewing the projected image at the coil.

It has been found that, within shot-to-shot variations, the profiles obtained are independent of whether one uses a narrow band-pass filter (known to view only continuum) or the entire S-4 spectral response of the 1P-21. The latter was chosen for recent Scyllac experiments because the greater intensity permits highly collimated viewing and thus better spatial resolution.

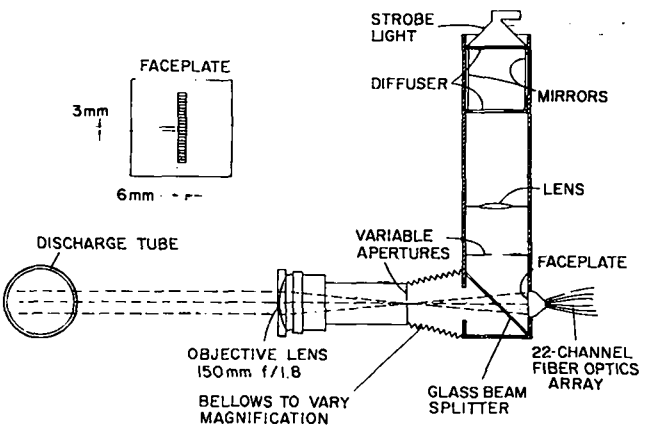

Fig. II-43.
Luminosity apparatus.

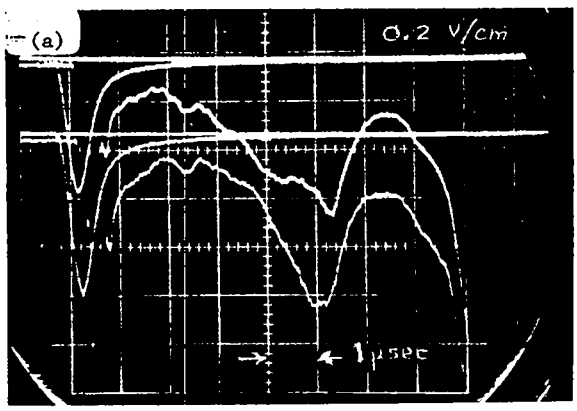

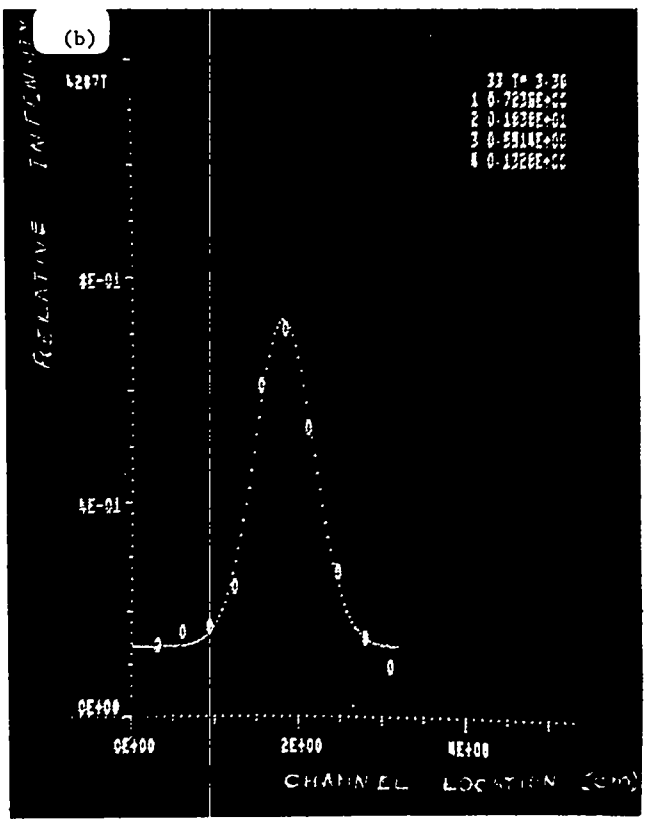

Fig. II-44.
Sample luminosity data. a. Two photomultiplier signals. b. Least-squares best fit of a Gaussian profile at one instant of time.

Typical luminosity data are shown in Fig. II-44. Channels of phototube output consisting of a baseline, a calibration pulse taken about 100 μsec before the machine fires, and the actual discharge are shown at the top of the figure. Computer analysis consists of digitizing the plasma trace, forming the ratio with the calibration

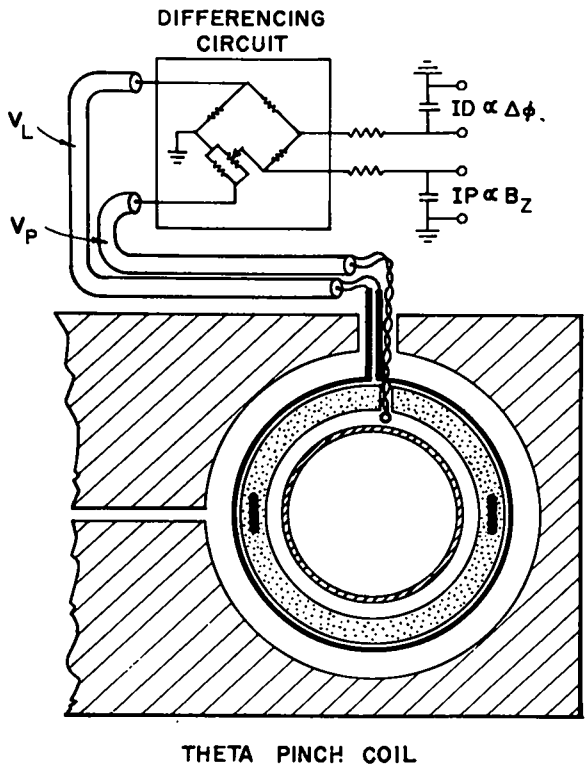

Fig. II-45.
Balanced loop-probe arrangement.

pulse, and displaying the 10 channels at a single instant of time on the computer CRT unit. The bottom of Fig. II-44 shows such a display and also shows a computer-generated, least-squares fit of a Gaussian profile with four free parameters (Gaussian width, Gaussian amplitude, centerline, and baseline). Generally, such a fit agrees well with the data, and the plasma is therefore usually taken to have a Gaussian density profile. The time history of the plasma radius, defined as a in the distribution $n_e(r) = n_A \exp(-r^2/a^2)$, is combined with excluded flux to determine plasma β.

2. Excluded-Flux Measurements. The excluded flux is defined as

$$\Delta\phi = \int_0^\infty \left[B_z(\infty) - B_z(r)\right] 2\pi \, r\,dr \quad , \qquad (1)$$

where $B_z(\infty)$ is the magnetic field far from the plasma. The balanced loop-probe arrangement for measuring the excluded flux is shown in Fig. II-45. The small probe is positioned outside the discharge tube and produces a voltage

$$V_p = k_1 \; NA_p \; \dot{B}_z(\infty) \; , \tag{2}$$

where k_1 is a constant adjusted by a potentiometer in the differencing circuit and NA_p is the probe area. The larger single-turn loop of area A_L encircles the discharge tube (and $\ell = 1$ coil if present), and generates a voltage

$$V_L = \frac{k_2}{C_1} \int_{A_L} \dot{B}_z(r) \, 2\pi r \, dr \; , \tag{3}$$

where C_1 is the step-down ratio of the voltage divider in series with the loop, typically ~100.

In vacuum one adjusts k_1 to obtain $V_p = V_L$ (the balance condition) so that when plasma is present the difference signal, after integration, is given by

$$ID = \int (V_p - V_L) \, dt$$

$$= \frac{k_2}{C_1 \; RC(ID)} \int_{A_L} \left[B_z(\infty) - B_z(r) \right] 2\pi \, r dr \; , \tag{4}$$

RC(ID) being the integration time constant. Because $B_z(\infty) \equiv B_z(r)$ for all points external to the plasma, the integral in Eq. (4) is equal to the integral in Eq. (1). Therefore,

$$\Delta\phi = \left(\frac{RC(ID) C_1}{k_2} \right) ID \; . \tag{5}$$

We determine k_2 by a choice of units; thus, for $\Delta\phi$ in kG-cm^2, RC(ID) in microseconds, and ID in volts, $k_2 = 10$.

The magnetic field is obtained by separately integrating the probe signal

$$IP = \int V_p \, dt = \frac{k_2 A_L}{C_1 \; RC(IP)} \; B_z(\infty) \; . \tag{6}$$

Hence,

$$B_z(\infty) = \left(\frac{RC(IP) \; C_1}{k_2 A_L} \right) IP \; . \tag{7}$$

For $k_2 = 10$, IP is in volts, RC(IP) is in microseconds, A_L is in square centimeters, and $B_z(\infty)$ is in kilogauss. The two quantities ID and IP are usually displayed as shown in Fig. II-46. These data are typical of the groove and land positions. The upper trace is the magnetic field (IP) and the lower trace the excluded flux (ID). The ID is notably larger in a groove than in a land position. Any departures from a true balance in vacuum, as shown in the bottom trace of Fig. II-46, must be subtracted from the ID signal before calculating $\Delta\phi$. Losses in the differencing circuit (Fig. II-45) must also be counted.

3. Determination of β. From Eq. (1), together with the pressure balance relation

$$B_z(r) = \sqrt{1 - \beta(r)} \; B_z(\infty) \; , \tag{8}$$

we obtain

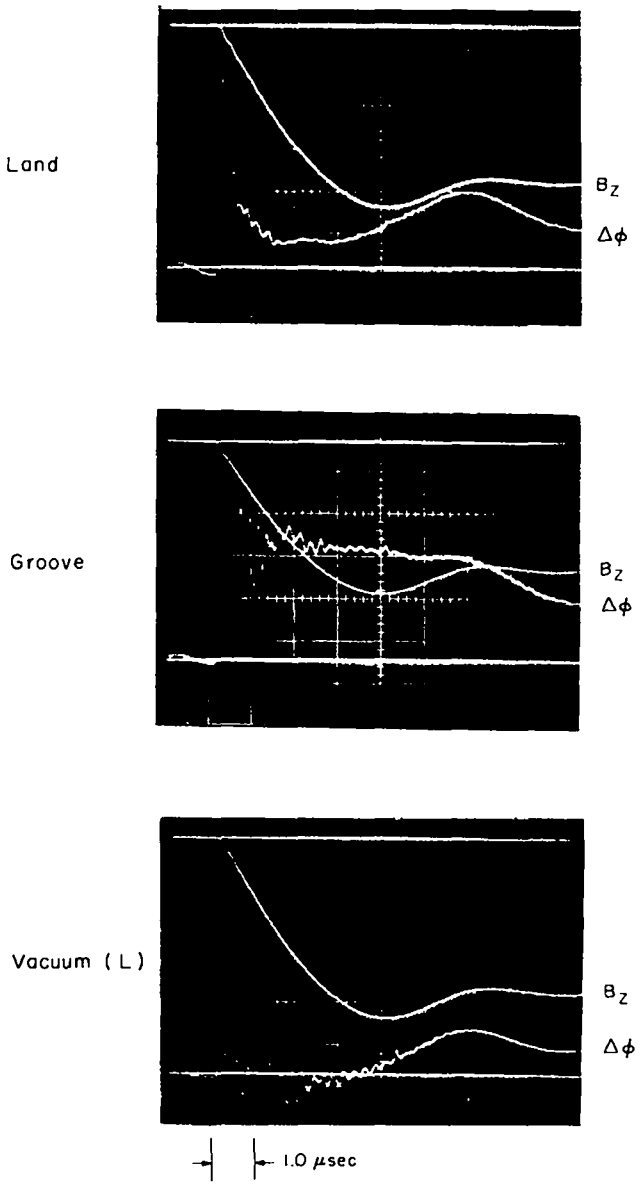

Fig. II-46.
Sample excluded-flux data.

$$\Delta\phi = 2\pi B_z(\infty) \int_0^\infty [1 - \sqrt{1-\beta(r)}]\, r\,dr \quad . \tag{9}$$

Assuming that temperature is independent of radius and $n_e(r) = n_A f(r)$ (n_A is the density on axis), we have

$$\beta(r) = \beta_A f(r) \tag{10}$$

and

$$\beta_A = \frac{8\pi n_A k(T_e + T_i)}{B_z^2(\infty)} \quad , \tag{11}$$

where β_A is the value of β on axis. We will consider three profiles on common interest.

$$\text{(a) Sharp boundary} \quad \begin{cases} f(r) = 1 & r \leqslant a \\ f(r) = 0 & r > a \end{cases} \tag{12}$$

$$\text{(b) Gaussian} \qquad f(r) = e^{-(r/a)^2} \tag{13}$$

$$\text{(c) Rigid rotor (RR)} \begin{cases} f(r) = \dfrac{\operatorname{sech}^2[(r/r_o)^2 + \alpha]}{\operatorname{sech}^2 \alpha} \\ \alpha = \tanh^{-1}\sqrt{1-\beta_A} \\ r_o^2 = a^2\,(1 + \sqrt{1-\beta_A}) \end{cases} \tag{14}$$

The plasma radius a is defined so as to preserve line density

$$\pi a^2 n_A = \int_0^\infty n_e(r)\, 2\pi\, r\,dr \quad . \tag{15}$$

Substituting Eqs. (12) through (14) into Eq. (9), we find the excluded flux by direct integration

$$\frac{\Delta\phi}{B_z(\infty)}(\text{cm})^2 = \begin{cases} \pi a^2\,(1 - \sqrt{1-\beta_A} & \text{(a) Sharp boundary} \\ 2\pi a^2 \left\{\left(1 - \sqrt{1-\beta_A}\right) + \ell n \left(\dfrac{1+\sqrt{1-\beta_A}}{2}\right)\right\} & \text{(b) Gaussian} \\ \pi a^2 \left\{\left(1 + \sqrt{1-\beta_A}\right) \ell n \left(\dfrac{2}{1+\sqrt{1-\beta_A}}\right)\right\} & \text{(c) RR} \quad . \end{cases} \tag{16}$$

The quantity $\Delta\phi/B_z(\infty)$ has the units of area. Thus we are led to define

$$\frac{\Delta\phi}{B_z} = A_{eff} = \pi\, r_{eff}^2 \quad . \tag{17}$$

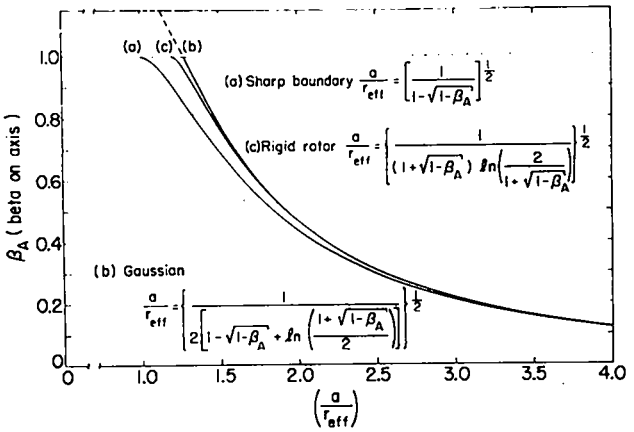

Fig. II-47.
Theoretical curves of β on axis vs a/r_{eff} for three assumed density distributions.

The names "effective area" and "effective radius" are suggested by the fact that, for a sharp boundary profile, $A_{eff} = \pi a^2$ when $\beta_A = 1$.

Figure II-47 compares curves of β_A vs a/r_{eff} for the three profiles discussed above. Experimentally, a is determined by curve-fitting the luminosity data, and r_{eff} is found from the excluded-flux quantities ID and IP as follows:

$$r_{eff}(\text{cm}) = \sqrt{\frac{A_L(\text{cm}^2)}{\pi} \times \frac{RC\ (ID)}{RC\ (IP)} \times \frac{ID\ (\text{volts})}{IP(\text{volts})}} \quad . \tag{18}$$

The choice of which profile to fit with the data is made empirically. Usually a Gaussian profile is adequate. In the data presented in Sec. II.B.10.c the rigid rotor, curve (c), was used. The maximum difference in B_A between (b) and (c) is only a few percent, occurring near $\beta_A = 1$.

4. Effect of Nonuniform Magnetic Fields. The measurement of β in the presence of $\ell = 0$ fields is straightforward only if the magnetic field outside the plasma is unaffected by induced $\ell = 0$ plasma current, and the

vacuum field is radially uniform from the axis to the loop-probe position.

The magnetic field induced by $\ell = 0$ plasma currents, B_K, has a $K_o(hr)$ radial dependence, and just outside the plasma boundary (using a sharp boundary model) it can be shown to equal

$$B_K = \tfrac{1}{2}(\delta_o/\delta_{wall})\,\beta(ha)^2\,\ell n(ha)\,B_{\ell=0}\ ,$$

where δ_o and δ_{wall} are the normalized flux surface excursions at the plasma and wall, respectively, and $B_{\ell=0}$ is the applied $\ell = 0$ field.

For quantities typical of our experiment

$$B_K/B_o \leqslant 0.009\ ,$$

where B_o is the average applied B_z field.

The radial dependence of the magnetic field outside the plasma is therefore nearly independent of the presence of plasma. It is given by

$$B_z(r) = B_o + B_{\ell=0}\,I_o(hr)\sin hz.$$

For $B_{\ell=0}/B_o = 0.08$ and a loop-probe location at $hr \approx 1.0$, departure from uniformity is about 2%. This small systematic error is easily taken into account when computing β.

5. Electron-Density Measurements. Absolute electron-density measurements are obtained by using the coupled cavity laser interferometer measurement of integrated electron density in conjunction with the plasma density profile obtained from luminosity measurements. The operation of the coupled cavity interferometer is described in LA-4888-PR.

G. Diagnostic Development (P. R. Forman, R. Kristal, and R. E. Siemon)

1. Coupled-Cavity Interferometer. We are implementing the Pockels effect for phase modulation in the coupled-cavity interferometer. In replacing the rotating wheel by a set of electro-optical crystals, one gains the ability of external triggering, as well as a much simpler and quicker machine setup. Further, this new technique can be used with multiple beam probing, for which the rotating wheel is impractical. The multiple beams can be used for profile and peak density determination without recourse to other diagnostic data.

Previous calculations indicated that with lithium niobate crystals totaling 16 cm in length, and with a 10 kV/cm peak transverse modulating field oriented along the c-axis (as is the beam polarization), a total of about 12 fringes could be obtained in one sweep. Also this should entail only ~6% optical loss per transit. The crystals would be driven by a ramp waveform with about a 3-μsec period.

A preliminary experiment was performed to check the fringe count with a small sample and at a low voltage. The experimental arrangement is shown in Fig. II-48. The results are given in Fig. II-49. The lithium niobate crystal is 0.5 by 0.5 by 4.0 cm, giving an electric field swing of 4 kV/cm. The data show one fringe in about 1.6 kV. Extrapolating to an applied voltage swing of 5 kV and a total length of 16 cm gives the predicted 12 fringes. A 5-kV ramp generator with fast retrace for use on a full-scale modulator is presently under construction.

2. HF Laser. To obtain space-resolved electron density on the Scyllac torus, side-on holographic interferometry is being used. The short path length across the plasma column favors the longest possible wavelength within the passband limit of the quartz discharge tube of ~3.5 μ.

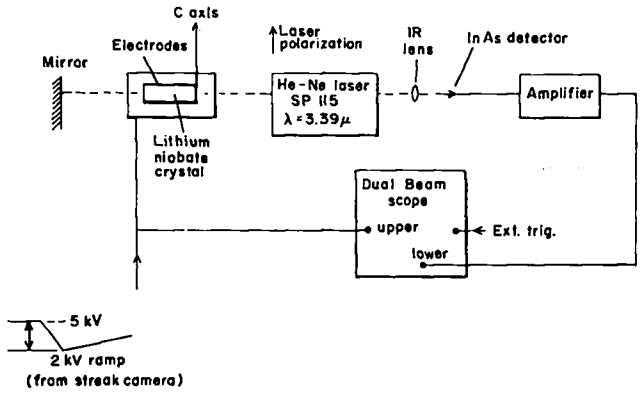

Fig. II-48.
Electro-optical phase modulator experiment.

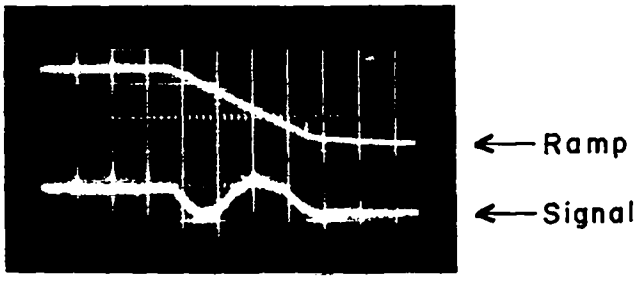

Fig. II-49.
Driver and output signal traces from electro-optical modulator. Ramp scale: 1 kV/cm, signal scale: 0.2 V/cm, time base: 10 μsec/cm.

Only recently has a laser suitable for this type of work been developed. This is the transversely pulsed hydrogen-flouride (HF) chemical laser reported by Wentzel and Arnold.[1] Using mixtures of SF_6 and C_2H_6, pulse energies of ~1 to 10 J in times of $\lesssim$ 100 nsec have been obtained with efficiencies in the 1 to 5% range. Prominent wavelengths are in the 2.5- to 3-μ region.

These features are attractive for side-on holographic interferometry. Construction has begun of a prototype system for development as a diagnostic tool on Scyllac. Initial energy storage will be about 300 J at 50 kV in a simple bank with triggered sparkgap. The gas-handling system, laser housing, and bank and power supply are nearly complete. The active volume is about 0.3 ℓ with 1-m length.

The detection medium at this wavelength will be a thin bismuth film, the fringe pattern being produced by local evaporation. Energy density requirements are in the 0.3 J/cm^2 range, which is compatible with expected output energies of ~1 J from the HF laser.[2]

3. Thomson Scattering on Scyllac. A Thomson scattering experiment for measuring plasma electron temperature and relative density is being developed for Scyllac. The incident laser beam, the light-beam dump, and the scattered light collection must all be side on because there are no end windows in Scyllac. We hope that measurements will be made possible by completely rejecting stray light from the incident beam, although that implies that calibration by Rayleigh scattering to determine absolute density will not be possible.

In general, we would like to do Thomson scattering measurements without the usual cumbersome incident beam collimation and dumping. On Scyllac an arrangement like that in Fig. II-50 is convenient but has the awkward feature that a significant fraction of the incident beam (10^{-3} to 10^{-6}) is directed toward the detector. Normally such a high level of equipment scattering precludes observation of the Thomson scattered light (about 10^{-12} times the incident intensity) although the latter has shifted in frequency hundreds of angstroms. The essential difficulty is that typical resolving apparatus (filters or gratings) reject only about 10^{-4} to 10^{-5} of unwanted wavelengths. Double monochromators can obtain 10^{-10} rejection for the transmission of a narrow band of wavelength but nothing available commercially can reject a single wavelength while transmitting a wide range of adjacent wavelengths. The Thomson scattered Gaussian spectrum for 1-keV electrons has a 500-Å half-width.

These considerations led to the design of a three-grating polychromator shown schematically in Fig. II-51. With this device it should be possible to obtain 10^{-10} to 10^{-12} rejection of 6943-Å light (wavelength of incident ruby laser beam). It is possible to transmit a broad

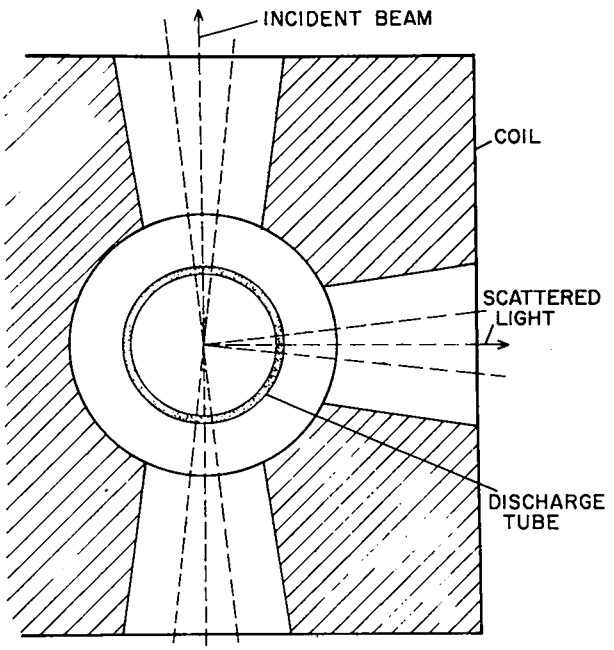

Fig. II-50.
Incident- and scattered-beam configuration for the Scyllac Thomson scattering experiment.

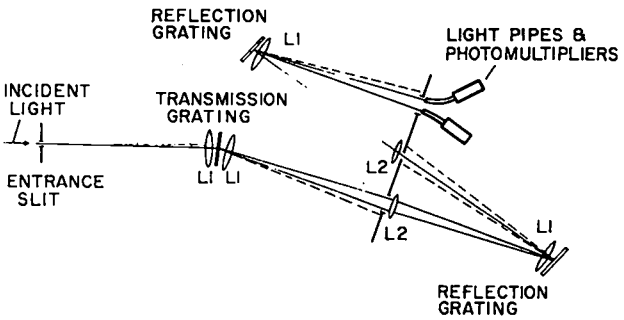

Fig. II-51.
Three grating polychromator with high laser-light rejection for use with the Thomson scattering experiment.

spectrum because of the arrangement of the second grating. It reverses the dispersion of the first grating and thereby recombines the light to pass through a narrow slit. The 6943-Å light, shown with dashed lines, is therefore rejected at each grating slit combination permitting a rejection of 10^{-3} to 10^{-4} at each stage. Lenses (L1) form parallel light for the gratings, as in a Littrow mount, and field lenses (L2) image one grating to the next. The final dispersed spectrum is relayed by eight plastic light pipes to photomultipliers.

The polychromator is being fabricated and will be tried with the new toroidal sector during this coming year.

REFERENCES

1. R. G. Wentzel and G. P. Arnold, IEEE J. Quant. Elec. QE-8, 26 (1972).

2. G. Decker et al., Appl. Phys. Lett. 20, 490 (1972).

H. Scyllac Computer and Data Acquisition (J. W. Lillberg, E. T. Nelson, G. A. Sawyer, and D. M. Weldon)

1. Second Computer. A second Sigma-2 computer has been acquired for use on non-Scyllac applications within the CTR program. We have been able to use our existing programs and software systems because the new computer has a configuration almost identical to the Scyllac computer. The new computer was installed in the existing shield room in the Scylla-IV area, near the experiments it serves. The direct data links from the Scyllac computer to Scylla IV and to Group P-13 experiments were transferred to the new computer. The second computer is now used for direct data acquisition from Scylla IV and the alkali plasma experiments in the experimental plasma physics group, and for off-line reduction of data obtained by other means. Both computers are in nearly constant use.

2. Digitizer. Curve digitizers were added to both Sigma-2 computers and are used primarily for digitizing oscilloscope traces for computer data reduction. The digitizers are interfaced to the computer so that data are transferred directly into computer core for analysis. These devices operate on a sonic ranging principle and measure time of flight of sound from a tiny spark source in a pen as it is drawn along the curve to be digitized. We have found curve digitization to be convenient and accurate with the new digitizers. Also, data handling has been greatly facilitated.

3. Data-Acquisition Devices. Our development of fast data-acquisition devices is continuing. Ten of the sixteen scan converter units are now in use on the Scyllac data-acquisition system but some problems in scan converter reliability still persist. Considerable maintenance has been needed on the high-voltage circuits, but the principal problems have been in the R-6294C scan-converter tube. The original tube manufacturer (Rauland Corporation) discontinued the tube, and we were forced to find another vendor (Warnecke Corporation). Warnecke had some production startup problems that delayed delivery of enough tubes to complete the scan-converter system. Also, we have had to return several defective tubes to Warnecke. The targets in both Rauland and Warnecke tubes have had surprisingly short lives, and we have had to modify the system to put the tubes on a standby status between Scyllac shots. Because of the somewhat disappointing results with scan converters, other fast data-acquisition devices are being evaluated. Figures II-52 and II-53 show computer displays of scan-converter data. Figure II-52 shows a luminosity diagnostic calibration pulse with a risetime of 100 nsec on the pulse and a total sweep duration of 10 μsec for the entire trace. Figure II-53 shows a display of Scyllac crowbar trigger voltage.

A Biomation 8100 transient analyzer was tested on line with the computer, utilizing both signals from test instruments and from the Scyllac diagnostics. The device contains a 100-MHz analog-to-digital converter with a 2048-word 8-bit-wide memory and is computer controllable. This analyzer can digitize one point every 10 nsec to 8-bit accuracy and has an input bandwidth of dc to 25 MHz for dc coupling on all ranges. It has an input voltage range of from ± 50 mV to ± 5 V full scale. The sample interval is variable from 10 nsec to 10 sec between

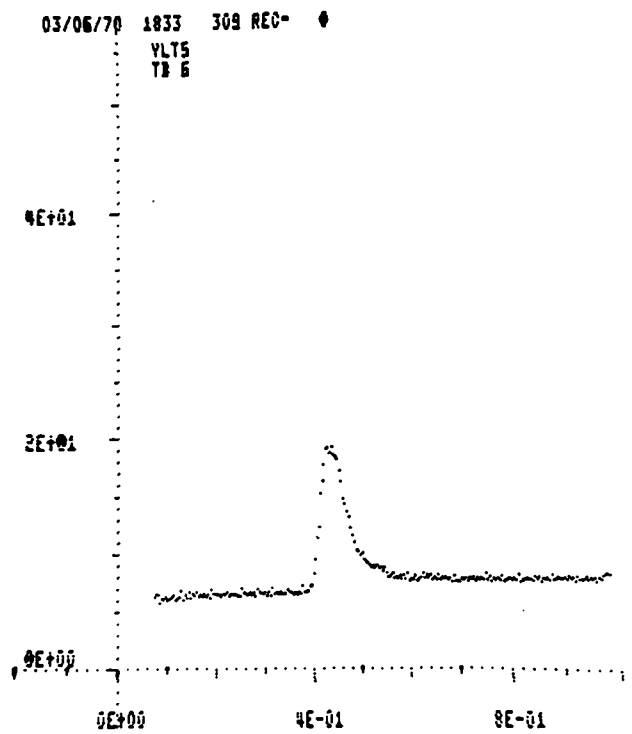

Fig. II-52.
Scan converter trace of a diagnostic calibration pulse with 100-nsec risetime. The full sweep time is 10 μsec.

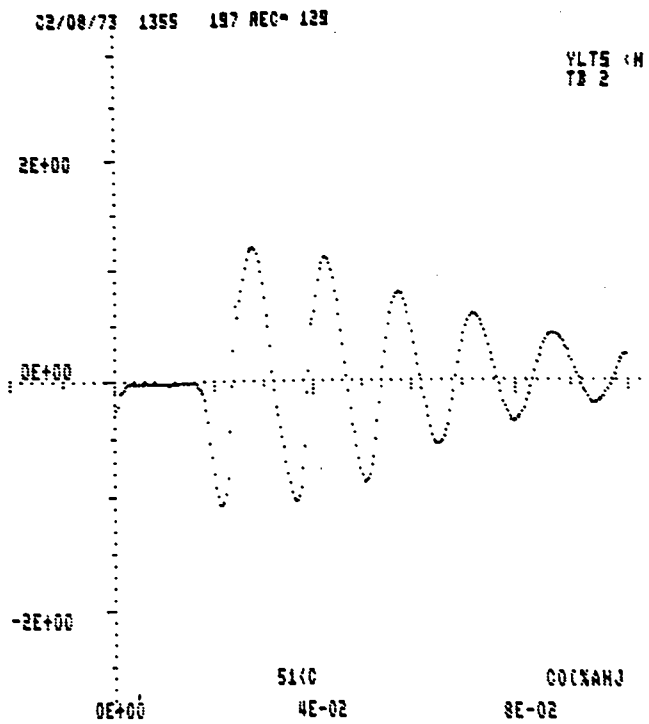

Fig. II-53.
Scan converter trace of the Scyllac crowbar trigger at 10 μsec full-scale sweep.

samples. Figure II-54 is a primary trigger trace from the linear machine. The single trace is broken into four parts because the device has a 2048 word memory, and it was convenient to plot only 512 points per line. The bottom trace contains points 1-512, and the top trace contains points 1537-2048. This signal was digitized at a rate of one point every 100 nsec and covers a total time of 20.48 μsec.

A prototype for a TV camera vidicon system to digitize from existing oscilloscopes is also being tested. Sandia Laboratories has reported good results with a similar system.

Installation of 28 Biomation 610 transient recorders on the Scyllac computer has been completed. These units are slated to be the primary monitors for the radio-frequency module during the Scyllac feedback experiment. Because they are to be used on the feedback experiment, a patch panel was cabled and installed to make the feedback signals readily available to the units when the experiments begin.

The Biomation 610 is a relatively economical device and has considerably reduced performance compared to scan converter or Biomation 8100. It has a 6-bit-wide

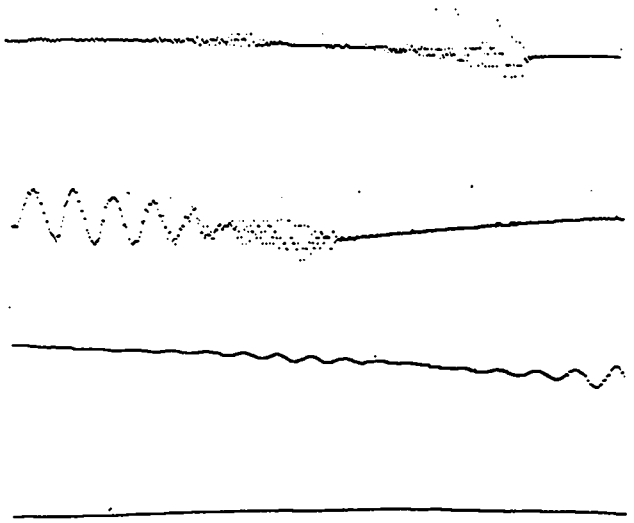

Fig. II-54.
Test signal displayed on the Biomation 8100 transient recorder.

256-word-long memory coupled to a 10 MHz analog-to-digital converter. The signal bandpass is 2.5 MHz for the 5 V and above scales. The Biomation 610 is quite useful for signals that are in the range, such as the crowbar triggers and neutron trace.

The Scyllac operating program was extensively modified to allow the inclusion of the Biomation data in the display programs. Figure II-55 shows the CTR display of the data from five of these units. Figure II-56 is a single display of a crowbar trigger taken on shot No. 7139 on the linear Scyllac (the same type of trace as displayed on a scan converter in Fig. II-53). It shows that these units are very useable for some of the machine diagnostic signals.

4. Gap Monitor. The spark-gap monitor has proved to be very valuable in finding malfunctioning capacitors and spark gaps in the Scyllac bank. Because the spark-gap monitor has proved to be so valuable, extra effort was made to keep it operational for the linear machine during the early stages of Scyllac conversion.

The Scylla-IV gap monitor was also repaired and made operational. A foreground program was written for the Scylla-IV computer to enable the automatic use of the gap monitor on Scylla IV. This has proved very useful to the operation of the feedback development on Scylla IV.

We expect to expand the gap-monitor system to include monitoring of the crowbar trigger system by the time the full Scyllac torus comes into operation.

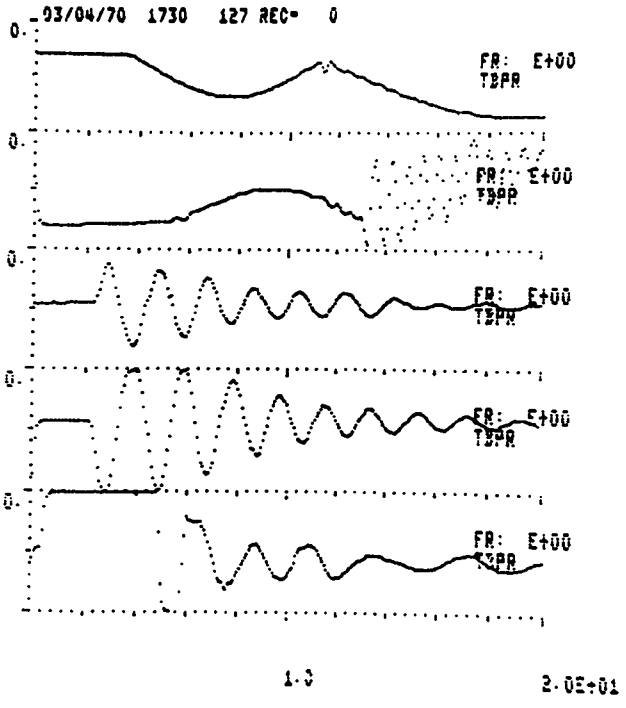

Fig. II-55.
Five traces of Scyllac data recorded on Biomation 610 transient recorder. The full scale time is 20 μsec.

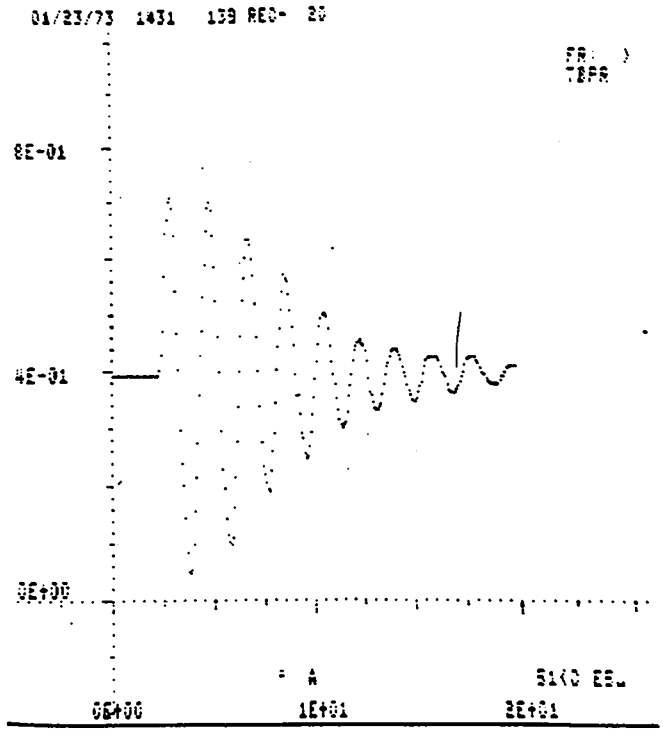

Fig. II-56.
Crowbar trigger trace recorded on the Biomation 610 recorder.

5. Other Activities. A super-sense switch device that utilizes four channels of the analog-to-digital convertor was designed and installed on the Scyllac computer. This device is operational and will enable programming options in the Scyllac program to be selected remotely at the Scyllac control desk. Appropriate modifications were made in the Scyllac program. Operation from the Scyllac console has proved to be a great convenience for the Scyllac operators. Also, a considerable effort was made to update and refine the Scyllac program and to write handling programs for the new peripheral hardware devices.

Construction has begun on a design unit that will mechanize the measurement of fringes for the coupled-cavity diagnostic unit. This device will consist of two fast 150 to 300 MHz counters, two registers, and two 8-bit-wide 256-bit-long shift register memories and a control unit, and will count the time between pulses in a string of pulses from the coupled-cavity unit.

I. Scyllac Feedback System (R. F. Gribble, G. A. Barnes, D. D. Carney, L. D. Caudill, J. R. Chavez, C. F. Hammer, K. J. Kutac, R. D. Hicks, M. R. McClannahan, L. H. McDowell, J. A. Meyer, D. Ortega, L. S. Schrank, E. G. Sherwood, J. F. Trujillo, J. O. Velasquez, and T. J. Zaugg)

Thirty-two power modules for the Scyllac 8-m-sector experiment were assembled and tested. Twenty-nine new ML-8618 power tubes for stage II of the feedback system construction have been received. The feedback control system for the 5-m-sector device has been installed and checkout is proceeding.

The major concern in the feedback system reliability is the tendency of the ML-8618 power tube to arc under the severe operating conditions required of the tube in this application. With a purely resistive load the tube is quite reasonably reliable. However, because of the almost purely inductive load in the experimental arrangement, the large L di/dt voltage impressed on the plate when the

tube is turned off or when the adjacent connected tube is turned on greatly increases the probability of arcing. This tube instability problem was further compounded when we increased the number of turns on the driver transformer (to obtain larger transformer core saturating times) due to the resulting increase in driver or grid circuit impedance.

To reduce the magnitude of the L di/dt pulse an RC network was connected between grid and plate of the 8618 so that the current fall time was reduced to about that of the risetime. This circuit worked well with a 26-μH load, the value anticipated for the experiments. However, the load on Scylla IV-3 is 32 μH and that for the module checkout bay (simulated Scyllac conditions) was 36 μH. This larger load inductance required an additional RC network from the 8618 tube grid to cathode to achieve improved stability. Because in the 8-m-sector experiment a module will drive four $\ell = 0$ coils rather than two as originally planned, the increased inductance will require another RC network design. A new module output transformer to connect to four series $\ell = 0$ coils has been fabricated to use in the test bay. Final selection of the RC compensation networks awaits the complete construction of a realistic load.

Owing to the difficulty in handling modules where the module output transformer was mounted in the module with 32 14-59 cables connected from the transformer to the $\ell = 0$ coils, we tried to mount the transformer as close as possible to the $\ell = 0$ junction headers with two RG-14 or 14-59 cables connecting the transformer primary to the modules. As anticipated, this connection resulted in reduced 8618 tube stability due to coupling of high-frequency cable ringing, although the net load inductance was reduced. Again, the tube instability problem was improved by changing the 8618 grid RC networks, however, at the expense of about 10% increase in current rise and fall times. Because of the increased load inductance of the new sector experiment connection, the net effect of placing the transformer at the load will probably be much less than for the original arrangement. We then tried 15- and 35-ft cables. The modules will work with 35-ft cables at the expense of a further 10 to 20% increase in rise and fall times over that for 15-ft cables.

A further investigation involved the increase of the effective operating time of the module from about 30 to 100 μsec. This included adding a tertiary winding to the driver interstage transformers and cross connecting them so that the driver side that was on supplied a reset voltage to the transformers of the nonconducting side. In this "quasi" push-pull arrangement, the module will operate until its "average" output reaches 20 μsec times full output. The main problem here is the load put on the driven side when a core on the opposite side saturates and reduces the tertiary winding inductance.

J. Electronics Development (A. T. Brousseau)

Several new devices have been designed and constructed for specialized electronics applications in CTR research. Detailed descriptions and drawings of these devices are available.

(1) Preamplifier/Line Driver for Infrared Detectors. A battery-powered wide-band preamplifier for use with infrared detector systems is used in connection with coupled-cavity interferometry on Scyllac. It was designed for high noise immunity and for driving long lines.

(2) Neutron-Counter System. A new neutron-counting system was built for Scyllac silver counters. Improved design using integrated circuitry has resulted in a cheaper, more compact unit.

(3) High-Voltage Trigger Generator. A variable 0 to 10 kV, 6.25 J trigger unit was designed for use in METS experiments.

(4) CTR Blanking Generator. A blanking generator was designed to provide variable time markers on Scyllac oscilloscopes.

(5) Pulse Generator. A multiple waveform pulse generator was built for testing feedback stabilization equipment.

(6) Seven-Channel Delay Trigger Generator. The LASL designed delay timing and pulse generator system has been used extensively for firing capacitor bank systems. It has now been completely redesigned and updated.

(7) Oscilloscope Calibrator. An oscilloscope calibrator has been designed for convenient calibration of the Scyllac oscilloscope system.

(8) Instrument Maintenance. Considerable effort has been expended on maintenance and improvements for the Imacon streak cameras and the Tektronix 556 oscilloscopes that have been subject to frequent failures.

III. Z-PINCH PROGRAM

A. Summary (J. A. Phillips)

In the Z-pinch program at LASL, we are investigating the diffuse Z pinch in toroidal geometry. Our approach is unique in that plasma heating is by the very fast-rising magnetic field (~60 kG/μsec) of the increasing Z current. Stability is achieved by (1) a close conducting wall, (2) an internal toroidal B_z magnetic field, and (3) reversal of this field outside the plasma column. The design of our toroidal experiment, ZT-1, has been described.[1]

MHD stability theory for the diffuse Z pinch imposes relatively stringent conditions on the magnetic-field and plasma-pressure profiles. To establish stable profiles, we have examined the various stages in the formation of the Z pinch, which are (1) the preionization of the initial gas filling before the initiation of the main Z-pinch discharge, (2) plasma compression and heating by the fast Z-pinch discharge, (3) reversal of B_z outside the pinch column, and (4) crowbarring the Z and θ currents to extend pinch lifetimes. The main conclusions at present are

(1) Close to 100% preionization of the initial gas filling minimizes the amount of plasma outside the main pinch column (Sec. III.B.1),

(2) When the pinch is driven by a fast-rising Z current, a positive gradient in plasma pressure is produced near the axis as required for stability (Sec. III.B.2),

(3) B_z reversal outside the pinch column reduces the number of unstable wavelengths (Sec. III.B.3),

(4) Crowbarring the Z and θ currents extends the Z current zero to ~55 μsec (Sec. III.B.4), and

(5) Plasma-pressure profiles deduced from measured magnetic-field profiles suggest plasma temperatures ($T_i + T_e$) of ~2 keV and β_θ values of ~0.4 (Sec. III.B.2).

We have found that during B_z reversal the plasma conductivity is apparently so high that the reversed B_z field compresses the plasma rather than diffuses into the pinch column. The result is that field reversal extends inward only a few millimeters from the wall.

A stability analysis of the measured magnetic fields on a crowbarred discharge shows only slowly growing, $\gtrsim$ 30 μsec, m = 1 modes. However, at ~6 μsec the discharge goes unstable possibly due to a gradual change in the magnetic-field profiles (Sec. III.C.1). The effect of diffusion on an m = 1 theoretically stable profile has been examined for the ZT-1 experiment. Classical diffusion alone does not prevent the Lawson criterion from being satisfied (Sec. III.C.2).

These results are encouraging in that a stable, hot Z pinch may be within our grasp. Further measurements should explain the present loss of stability and make possible a considerable improvement in confinement time.

The existence of diffuse Z-pinch equilibria in toroidal geometry, which are MHD stable, has now been demonstrated theoretically. Previous analyses have applied to cylindrical straight systems only.

We have also been investigating other geometries, in particular, the toroidal belt pinch in cooperation with the Garching group. Diffuse belt-pinch equilibria have been found that have $9 > 1$ for all flux surfaces and have $\beta_{total} \sim 1$.

Two-dimensional double-exposure holographic interferograms have been obtained using a pulsed 10.6-μm CO_2 laser. Interferometry transverse to the discharge tube in Z and θ pinches is now feasible (Sec. III.D).

Engineering support for the ZT-1 experiment includes the following:

(1) Studies have continued on the transfer capacitor circuit[2] that may replace the fuses on the experiment. The circuit described earlier was modified to reduce circuit oscillations and ease requirements on circuit components (Sec. III.E).

(2) The detonator crowbar switch[3] has been modified and installed on the experiment (Sec. III.F).

(3) An all-metal toroidal discharge tube for the ZT-1 experiment is being fabricated. This tube is designed[4] to support Z electric fields of ~1 kV/cm and an asimuthal voltage of ~1 kV/turn (Sec. III.G).

REFERENCES

1. Status Report of the LASL Controlled Thermonuclear Research Program for 12-Month Period Ending October 1971, LA-4888-PR, p.56.

2. LA-4888-PR, p. 64.

3. LA-4888-PR, p. 63.

4. Status Report of the LASL Controlled Thermonuclear Research Program for 12-Month Period Ending October 1970, LA-4585-MS, p. 39.

B. The Shock-Heated Toroidal Z-Pinch Experiment (L. Burkhardt, J. DiMarco, P. Forman, H. Karr, J. Phillips, and A. Schofield)

1. Preionization Studies on ZT-1. The energy source for the preionization is four 15-μF capacitors that can be charged to a maximum of 10 kV. Each capacitor drives one quadrant of the torus, giving a maximum of 40 kV around the torus.

Measurements have been made of the electron density and magnetic-field distributions in the preionized plasma. The electron density as a function of time is obtained with an Ashby-Jephcott laser interferometer. This helium-neon infrared laser beam traverses the torus across a minor diameter through the vacuum pumping ports. Fringe shifts result from the line integral of the plasma density along the path of the laser beam; the error resulting from the unconfined plasma that enters the pumping ports is assumed negligible.

The electron density as a function of time is shown in Fig. III-1 for a B_z bias field of 2.5 kG and filling deuterium pressure of 30 mTorr. To facilitate time comparisons, the preionization current at 6 kV is also displayed. The dashed line on the graph indicates 100% ionization assuming a uniform density distribution across the torus. As the bank voltage is increased, the percent ionization increases; the percent ionization at a fixed filling pressure follows a V^2 dependence (Fig. III-2).

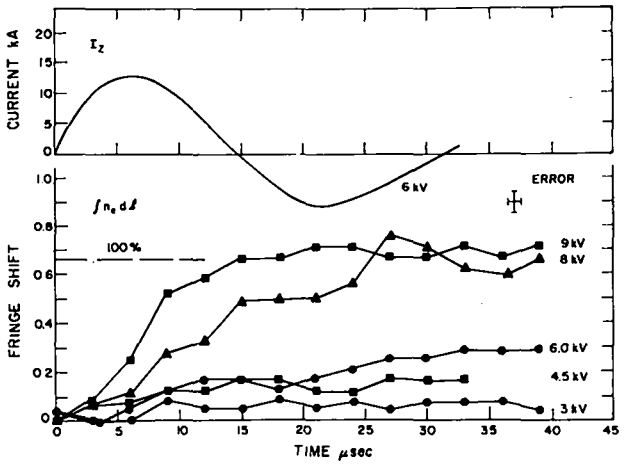

Fig. III-1.
Preionization current (upper trace) and laser interferometer fringe shift produced by the preionization electron density. The Ashby-Jephcott interferometer method was used with the 3.39-μ infrared helium-neon laser line.

Magnetic coupling loops are used to determine the $B_\theta(r)$ profile. The ten loops are mounted in a 6-mm-diam ceramic tube, which is then inserted into the torus through a pumping port 90° from the one used for the density measurement.

When the 6-mm-diam ceramic tube, which shields the magnetic probes, is initially inserted 5 cm into the discharge, the electron density is increased by about 25%. After 10 cleanup discharges, however, the presence of the probe cannot be detected within the experimental error.

Radial distributions of the B_θ magnetic field due to the preionization current are shown in Fig. III-3. At 30 mTorr, the z-current density distributions are uniform, while at 5 mTorr a peaking of the current density on axis with an approximate r^{-1} falloff is apparent. The cause for the peaking is not clear, but it may be due to the higher electron drift velocity at the lower pressure.

During the preionization current cycle, hard x rays are detected. In Fig. III-4 the signal from a fast scintillator x-ray detector is superimposed on the plasma current for two different preionization currents. The longer period (z) current shown in the bottom pair of traces is achieved by doubling the series inductance in the preionization circuit. The same peak current is maintained for the two cases. The gas is deuterium at 30 mTorr and the B_z bias field is 2.5 kG. In both cases, the x-ray emission starts at peak current ($\tau/4$) with the maximum occurring at about $(3/8)\tau$. The time shift in the x-ray signals in the two

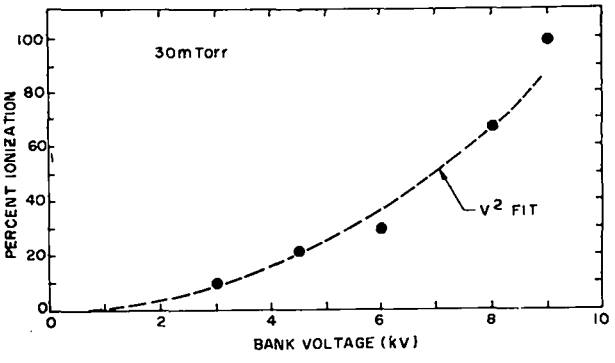

Fig. III-2.
Percent preionization vs preionization bank voltage for 30-mTorr deuterium gas filling pressure. The experimental points follow closely the V^2 dependence indicated by the line drawn in the figure.

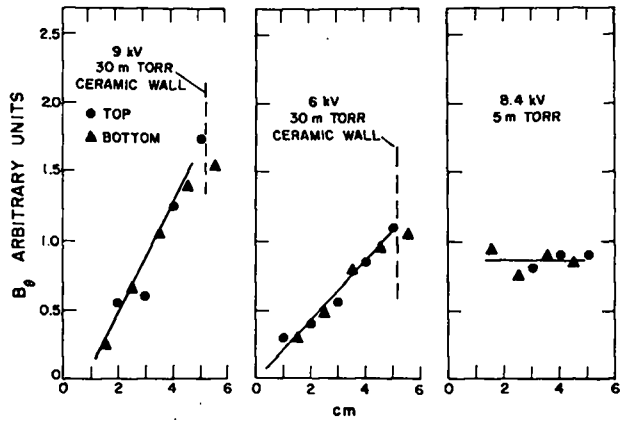

Fig. III-3.
Radial dependence of B_θ magnetic field produced by the preionization currents at 30- and 5-mTorr initial deuterium gas pressures. Nearly uniform current densities occur for the 30-mTorr pressure, but a 1/r current density distribution is observed for the 5-mTorr case.

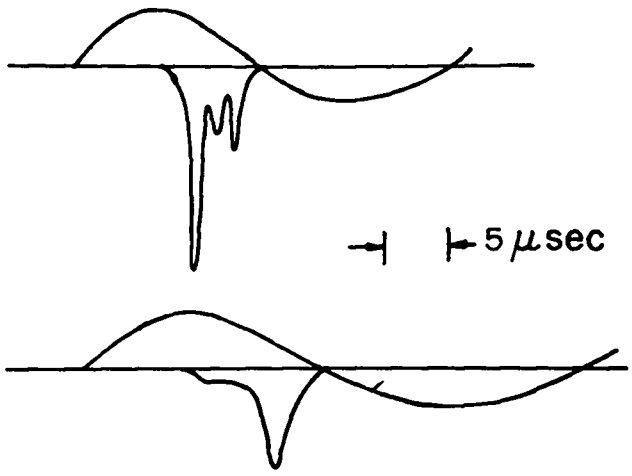

Fig. III-4.
X rays generated during the preionization current cycle. The x-ray bursts occur after preionization peak current and have photon energies in the range of several hundred keV. These x rays are usually not observed during the main current pulse.

examples indicates that the x-ray emission may be associated with the reversal of voltage on the Z pinch rather than a specific time required for acceleration of the electrons. X-ray films show a rather uniform background of radiation around the outer major circumference of the torus with more intense sources located near the four feedplates. From lead-absorption measurements, the x-ray energy is ~400 keV. The total peak voltage around the torus is 30 kV before gas breakdown; once the preionization current starts to flow, the voltage around the torus is $\lesssim$2 kV. Insertion of a 6-mm-diam ceramic probe 6 cm into the discharge eliminates the x rays. The general behavior of the x rays is to increase in amplitude with increasing B_z field, filling density, and voltage; the signal is detectable at 5 mTorr filling pressure.

To determine the effect of the degree of preionization on the formation of the pinch, the experiment is run in the slow mode by coupling the main Z-capacitor bank directly to the pinch. Peak pinch currents of 120 kA having a risetime to peak of 10 μsec are obtained. The plasma-pressure profile is then determined from the measured magnetic-field distribution. Figure III-5 shows the pressure profiles for four different discharges. The time of the start of the 120-kA main current for each successive discharge is delayed with respect to the firing of the preionization as indicated by the arrows on the graph. To reduce confusion, the pressure profiles are plotted for only two times, 6 and 7 μsec after the start of the main pinch current. The last three pressure profiles indicating a pinched plasma column about the discharge tube axis are obtained for those times in the preionization cycle corresponding to an initial ionization of ~100%. There is no obvious change in the profile after the main discharge is started when the preionization current passes through zero, is reversed, or is adding to the main discharge. The first pressure profile corresponds to the main discharge starting ~10 μsec after the start of the preionization current at which time the ionization is ~30%. The pressure profile shows the formation of two peaks, the second centering around a radius of ~2.5 cm. From an analysis of the plasma-pressure and magnetic-field profiles, this latter behavior is thought to arise from a pinching of the initial ionized gas that forms the pressure peak on axis. The plasma pressure is balanced by the magnetic field outside the central column. As the discharge current continues to rise, more of the neutral background gas outside the pinch becomes ionized, which also tends to pinch. However, the magnetic field in the discharge holds this second pinch away from the axis, resulting in a separation of plasma, magnetic field and plasma with a large fraction of the plasma pressure close to the wall.

2. Fast Mode of Operation. The above data with the slow mode of operation show that a high degree of ionization is required if a large percentage of the gas is to be brought into the central pinch, and plasma close to the wall is to be minimized. The main discharge is then initiated when the preionization is ~100%.

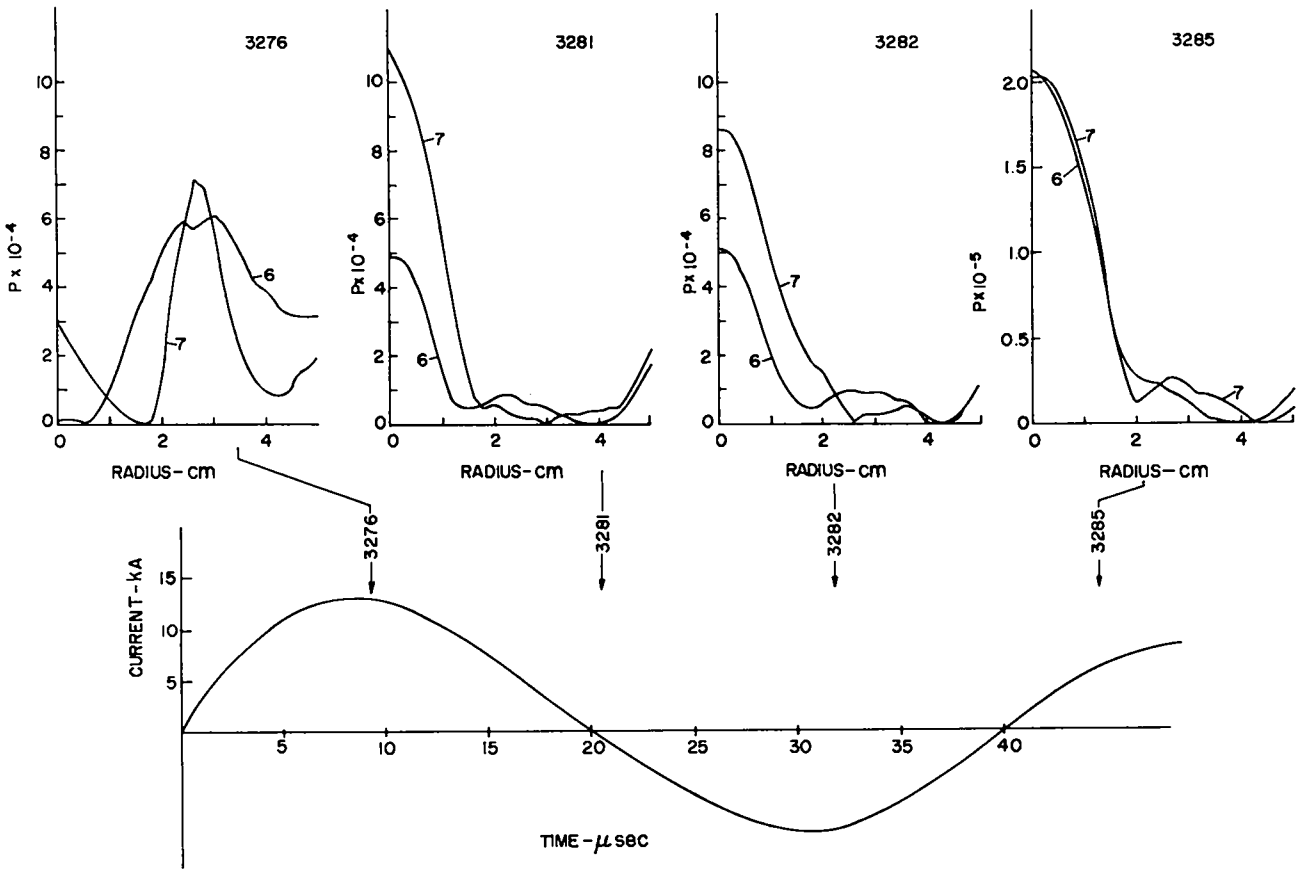

Fig. III-5.
Dependence of plasma-pressure profiles on preionization. With low preionization, the pressure profile (top left) indicates the formation of a second pinch from gas ionized during the main discharge superimposed on the pinch formed from the preionized gas.

In the fast mode of operation, the main Z bank discharging through the fuses transfers its energy to the coaxial magnetic energy storage volume at the base of the system. When the fuses vaporize, the combined inductive voltage multiplication and the 4:1 primary-to-discharge transformer ratio develops a fast-rising voltage of ~250 kV around the torus of ~0.1-μsec risetime and short duration. Electric fields of ~1 kV/cm are applied in the Z direction, and peak currents of ~200 kA with fast initial rise are developed.

The reproducibility of magnetic-field data was determined in a series of fast discharges at 5-mTorr pressure and 4-kG B_z bias field. The 10 magnetic probes were positioned to measure B_z across the diameter of the discharge on 2 successive discharges. They are presented in Fig. III-6 and within the experimental error show that the magnetic-field profiles are reproducible and well defined at 6 μsec. Analysis was not carried further in time because of the diminishing plasma current. From these data and those taken at earlier times, it is inferred that the pinch is grossly stable in that a large-scale kink is not destroying the integrity of the pinch. However, because the magnetic field is not reversed on the outside of the pinch, this configuration is predicted by MHD theory to be unstable to radial modes localized around the pitch minimum at ~3.8 cm.

It should be remembered that to be stable against pressure-driven modes the pressure gradient near the axis should be greater than or equal to zero. Figure III-7 shows that this can be achieved when ZT-1 is operated in the fast mode. With 4-kG B_z bias field and filling pressures of 2 or 5 mTorr, the pressure profiles have the necessary gradient near the axis and the general shape is maintained for the measurable duration of the current pulse, which passes through zero at 11.5 μsec.

The plasma temperature ($T_i + T_e$) is calculated from the pressure profiles by means of the equation

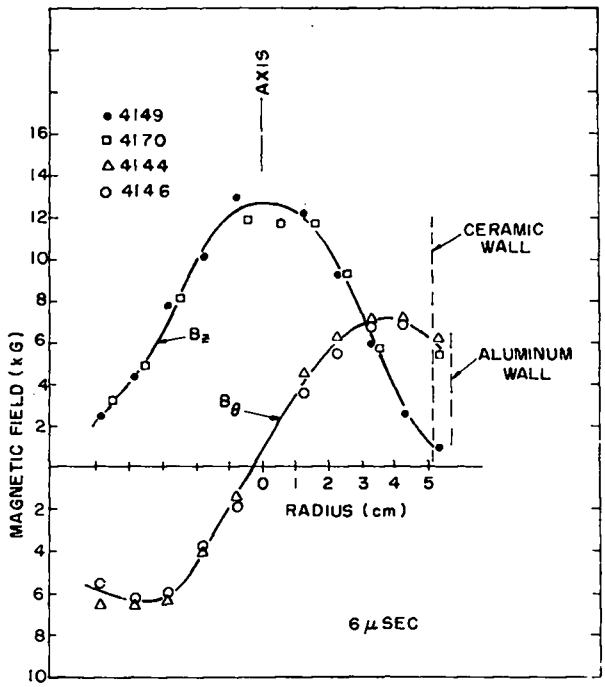

Fig. III-6.
Reproducibility and symmetry of probe measurements in the fast mode discharge.

$$T_e + T_i = \frac{1}{Nk} \int_0^r 2\pi \, rpdr \quad ,$$

where N is the total line density, which is assumed to be constant and equal to the initial line density. In addition, the temperature is assumed independent of radius. β_θ as defined by the Bennett relation is

$$\beta_\theta = \frac{200 \int_0^{r_\omega} 2\pi \, rpdr}{I^2} \quad .$$

Numerical integration of the plasma-pressure profiles leads to the data shown in Figs. III-8 and III-9. The temperature shows an inverse dependence on filling pressure. However, no clear dependence of the temperature on the initial bias magnetic field is evident over the range from ~2500 to ~3300 G.

MHD theory predicts that β_θ must be less than one-half for stability, and the highest stable profile obtained numerically by Robinson[1] has a central β of about 0.31. We calculate from his figure a β_θ of about 0.5. From our data, the field configurations having the lowest β_θ, ~0.4, and most constant value of β_θ as a function of time, while also having a positive pressure gradient at the axis, are obtained with B_{Z_0} = 4000 G and either 2- or 5-mTorr filling pressure. The variation of β_θ for some of the other cases indicates a large exchange of magnetic energy and plasma energy must be taking place.

REFERENCE

1. D. C. Robinson, Plasma Phys. 13, 439 (1971).

3. B_z Reversal Outside the Pinch. The circuit that drives the B_z winding is shown in Fig. III-10. The capacitor-switch combinations on the left, $C_{1,2,3}$ and $SW_{1,2,3}$, provide the slow forward B_z bias current. The four B_z windings on the torus, one on each quadrant, are connected in parallel. The crowbar switch SW_4 is closed immediately ahead of the main Z pinch and prevents further energy transfer from the slow bank to the fast circuit on the right. Closure of switches $SW_{5,6,7}$ connects the reverse bank $C_{4,5}$ across the load. The 1-Ω resistor has a low inductance and to some extent isolates the reverse bank from the crowbar SW_4. Either the field distortion gap SW_9 or the metal-to-metal explosive switch SW_8 can be used to crowbar the B_z field. At a charge voltage of 12 kV on C_4 and C_5, a 200-G/μsec rate of change of magnetic field in the vacuum field volume can be applied.

Figure III-11 shows a comparison of radial distributions for B_z, B_θ, and pitch ($p = r\,B_z/B_\theta$) with and without the externally applied reverse B_z field with the experiment run in the fast mode. Apparently, the plasma conductivity is high near the wall because the B_z reversal compresses the plasma thereby increasing the B_z on axis and moving the B_θ flux lines inward. The resulting equilibrium prevents the zero in B_z from moving away from the wall more than a few millimeters. The Z and θ currents are also shown in Fig. III-12.

Typical streak photographs taken across a minor diameter with and without B_z reversal are shown in Fig. III-12. With field reversal, the streaks are significantly decreased in luminosity with a marked decrease in the bright filamentary structure seen without reversal; rather, there are bands of light separated by dark spaces spread across the discharge tube.

The MHD stability analysis of measured magnetic-field distribution for cases with and without B_z field reversal is described in Sec. III.C below.

The streak photographs (Fig. III-12) show a rather filamentary uncorrelated plasma structure that may be caused by localized modes. These localized modes

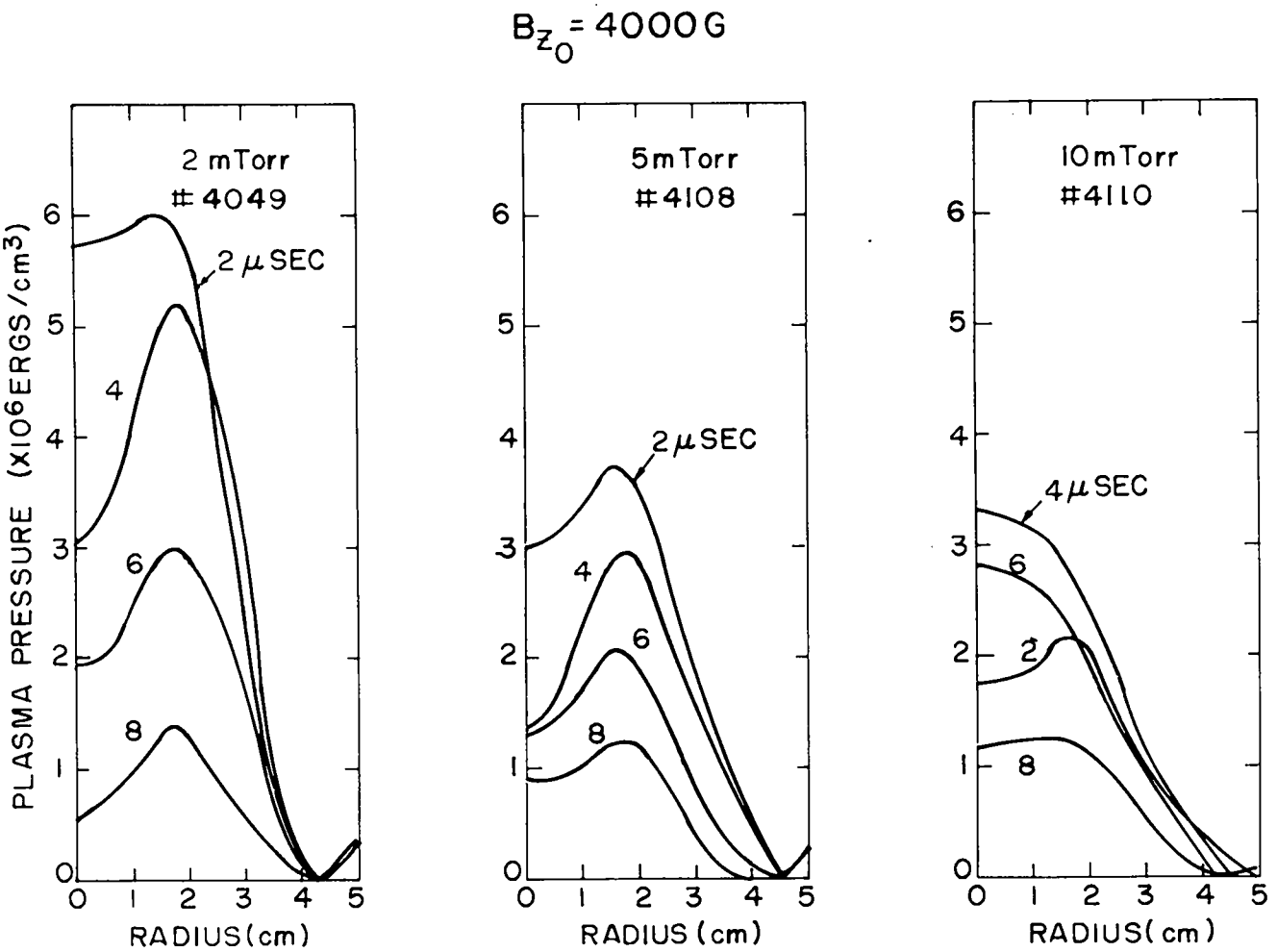

Fig. III-7.

Smoothed plasma-pressure profiles calculated from measured magnetic-field distributions for the fast mode of operation at 2-, 5-, and 10-mTorr deuterium gas pressures. Positive pressure gradients near the axis, as required for stability, are observed for 2 and 5 mTorr and the general shape is maintained for the duration of the current pulse.

presumably lead to large plasma loss, but do not destroy the gross behavior of the pinch. Attempts to analyze the mode structure by measuring the ($\Delta B/B$) fluctuations seen with the magnetic probes produce a spatial correlation with the gradient in the magnetic-field profiles. They are then assumed to be caused by a small scale motion of the plasma column. No direct spatial correlation, however, is determined between the B_Z and B_θ fluctuations.

4. Crowbar of Z and B_z Currents. Explosive metal-to-metal crowbar switches, described in Sec. III.F, have been installed in ZT-1. One switch, which is located between the torus and the fuse transfer switch, crowbars the primary currents at the feedplate of each quadrant.

The results from the ZT-1 experiment run in the fast mode with the z and θ currents crowbarred are still preliminary. The crowbarring of I_z causes a substantial lengthening of the current pulse. Without crowbarring, the current falls to zero in 11 to 13 μsec. This pulse width is increased from 50 to 55 μsec with crowbarring. This extended current pulse width under crowbarred conditions permits plasma measurements beyond the time interval limited by the rapid current falloff without crowbarring. Figures III-13 through III-16 show results for a

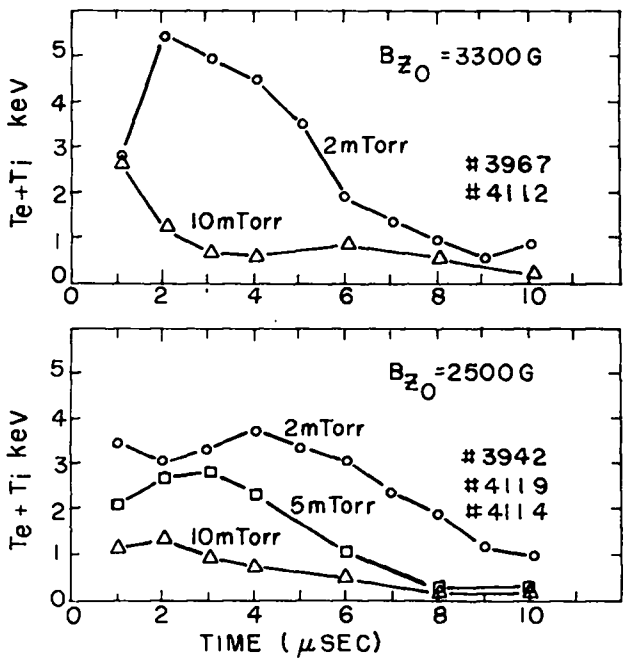

Fig. III-8.
Plasma temperature, $T_e + T_i$, vs time determined from probe measurements of the magnetic-field distributions.

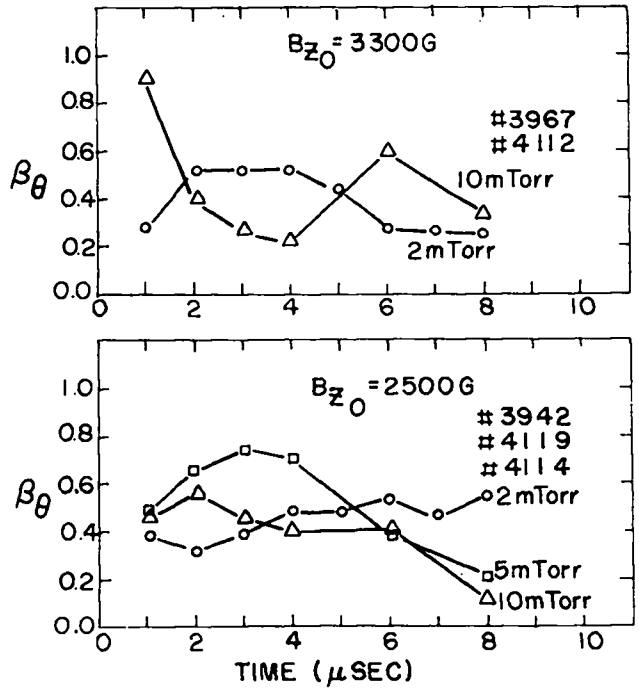

Fig. III-9.
β_θ vs time as determined from probe measurements of the magnetic-field distributions.

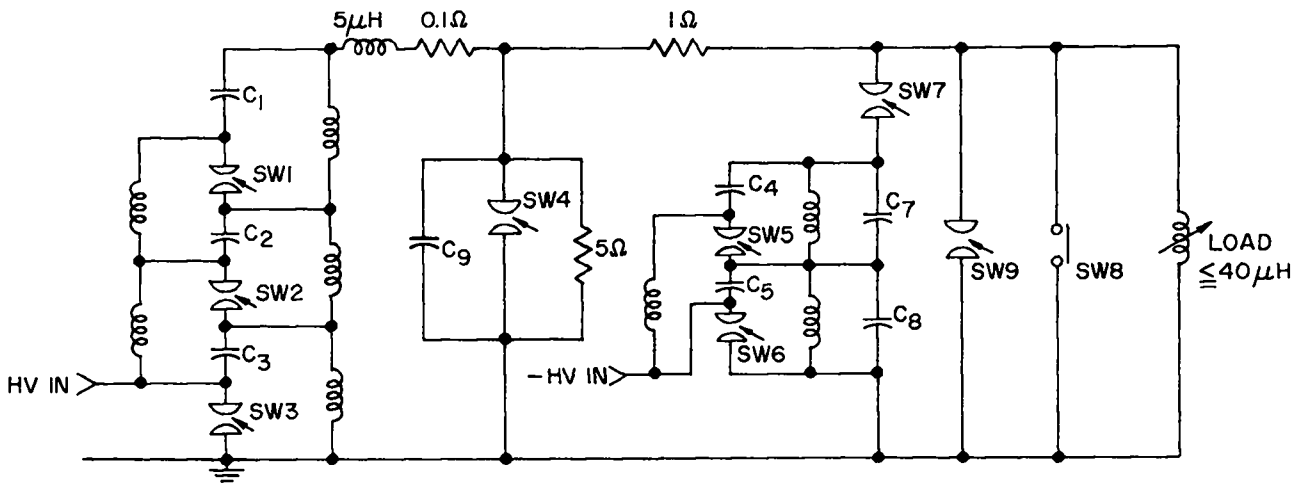

$C_{1,2,3}$ 480μf 10kV	SW 1,2,3, SIZE "A" IGNITRONS
$C_{4,5}$ 90μf 20kV	SW4 SPECIAL TRIGATRON
$C_{7,8}$ 0.004μf 20kV	SW 5,6,7,9 FIELD DISTORTION GAPS
C_9 1.1μf 50kV	SW8 EXPLOSIVE SWITCH

Fig. III-10.
Circuit for the B_z toroidal magnetic field for the sequence B_{z0}, crowbarring, reverse B_z, and final crowbarring.

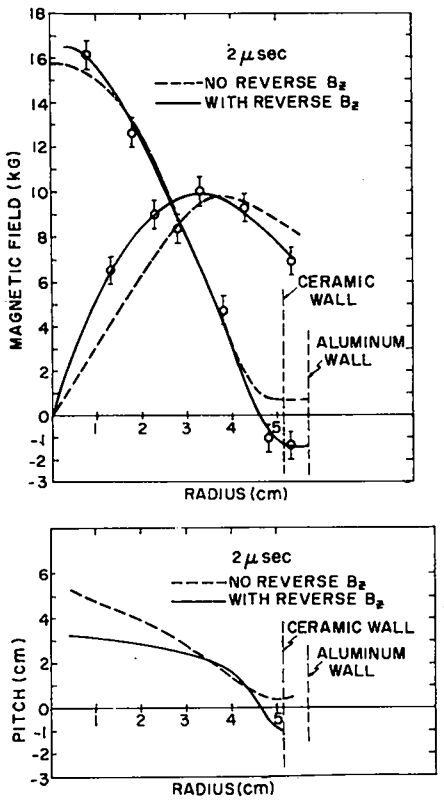

Fig. III-11.
Comparison of B_z, B_θ, and the magnetic-field line pitch ($p = rB_z/B_\theta$) with and without an externally applied reverse B_z magnetic field with operation in the fast mode.

fuse shot (No. 4974) with both reverse B_z and crowbarred I_z. The plasma current, B_z winding current, and the toroidal flux are shown in Fig. III-13. This discharge is triggered at t = 0, and the pinch current I_z rises ripidly to ~200 kA in $< 1\ \mu$sec. The I_z crowbar is applied at ~3 μsec and the current then falls off exponentially with a decay period of 37 μsec. The current, I_{BZ}, in the toroidal field windings drops rapidly toward zero as the pinch traps and compresses the B_z field. There is a small reversal of I_{BZ} due either to a dynamic paramagnetic effect or residual instability. At ~3 μsec, the reverse B_z is applied further reversing the I_{BZ} current and causing a drop in φ_z. At ~8 μsec, the reverse B_z is crowbarred causing an exponential decay of I_{BZ} and stopping the reduction in φ_z.

The plasma-pressure profiles determined from probe data for this shot are shown in Fig. III-14. The plasma-pressure profiles reach peak amplitude in $\lesssim 2\ \mu$sec and maintain this amplitude for 8 μsec. Hollow-pressure profiles, as required by MHD theory, are obtained from the probe data out to ~20 μsec. Without the I_z crowbar the peak pressure falls off rapidly in time, due to I_z falloff, with the amplitude at 8 μsec typically approximately one-fifth of that obtained at 2 μsec (see Fig. III-7).

The plasma temperature, $T_i + T_e$, is plotted in Fig. III-15, and β_θ is plotted in Fig. III-16. The temperature is nearly constant at 1 keV to 8 μsec and then falls to ~700 eV at 10 μsec. The β_θ is maintained in the 0.3 to 0.4 range over this time interval. The theoretical analysis of the stability of this discharge is discussed in Sec. III.C.1.

C. MHD Stability Analysis (Albert Haberstich)

Theory predicts the existence of completely MHD stable reversed B_z pinch configurations. A large part of the experimental effort is directed at achieving such magnetic-field distributions. Our task has been to find (1) how closely such configurations are approximated and (2) to what extent the theory agrees with the experiment.

To answer item (1) above, magnetic-field profiles measured by multiple magnetic probes have been analyzed using the various methods described below. Except for some localized modes, it appears that stable reversed B_z profiles have been obtained for times of the order of 6 μsec (see Fig. III-17). Instability then sets in, apparently as a result of diffusion.

Item (2) above could best be answered by measurements of the position, size, and growth rate of unstable modes. Due to the low firing rate of the experiment and insufficient access to the discharge, it has not yet been possible to perform such measurements. Direct observations of the instabilities have essentially been limited to streak photography, measurements of the centroid of the z-current distribution, and measurements of the B_z field in the space between the discharge tube and the interior of the primary conductor. These measurements agree with the stability analysis of measured profiles in that they show an instability when a gross instability is predicted by the theory.

1. Analysis of Measured Profiles. The B_θ and B_z magnetic fields are measured at five minor radial positions of the experiment and smoothed by a least-square spline fit. The smoothed profiles are then analyzed for stability assuming a cylindrical geometry and ideal MHD. The calculation is limited to m = 1 modes because they are the more dangerous ones experimentally. In principle, every discrete axial wavelength $2\pi/k_z$ allowed by the toroidicity of the experiment must be investigated.

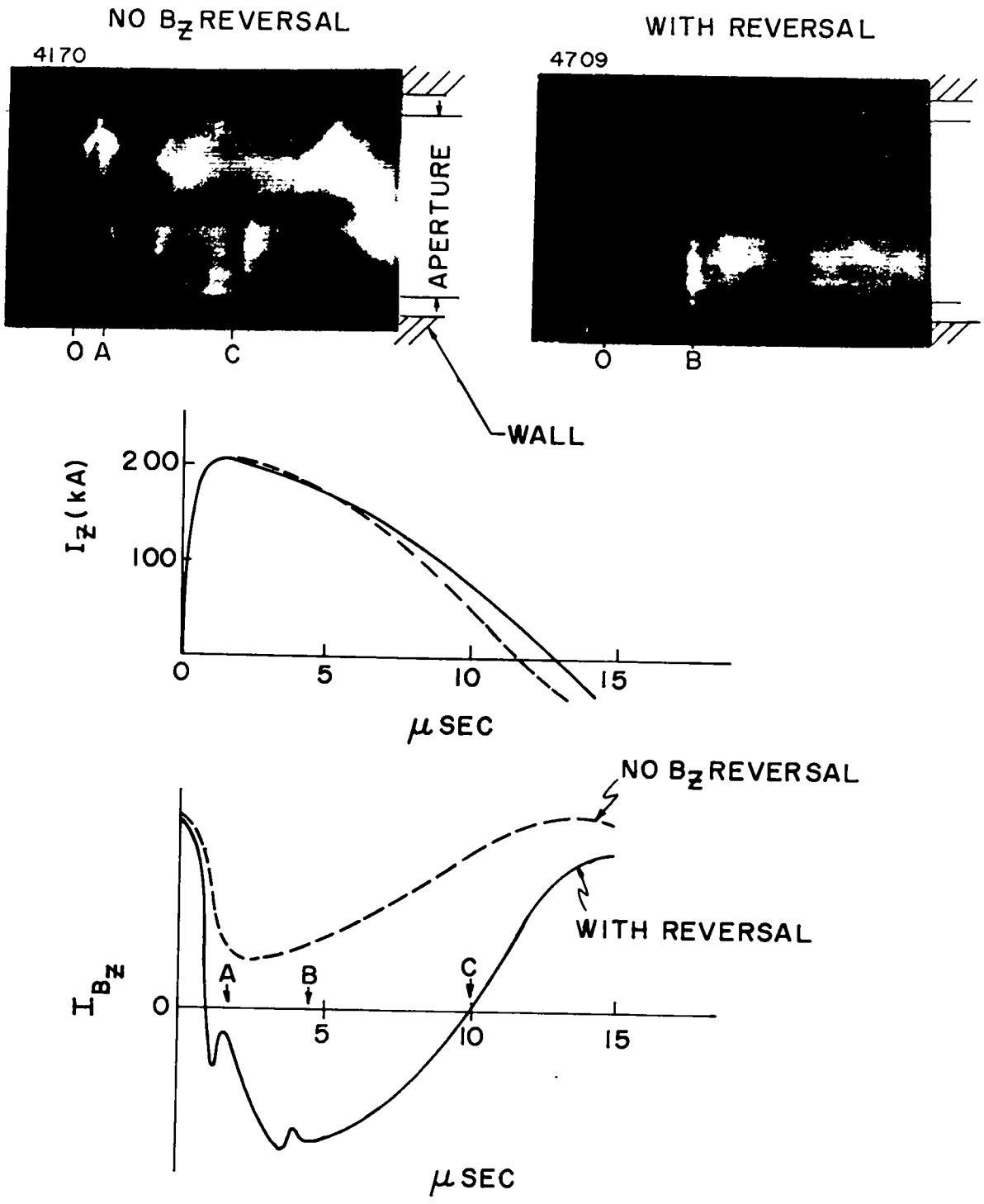

Fig. III-12.

Comparison of streak photographs taken with and without reverse B_z. Reverse B_z applied ~1 μsec after initiation of the discharge. The effect on the I_z and I_θ current waveforms is shown at the bottom of the figure.

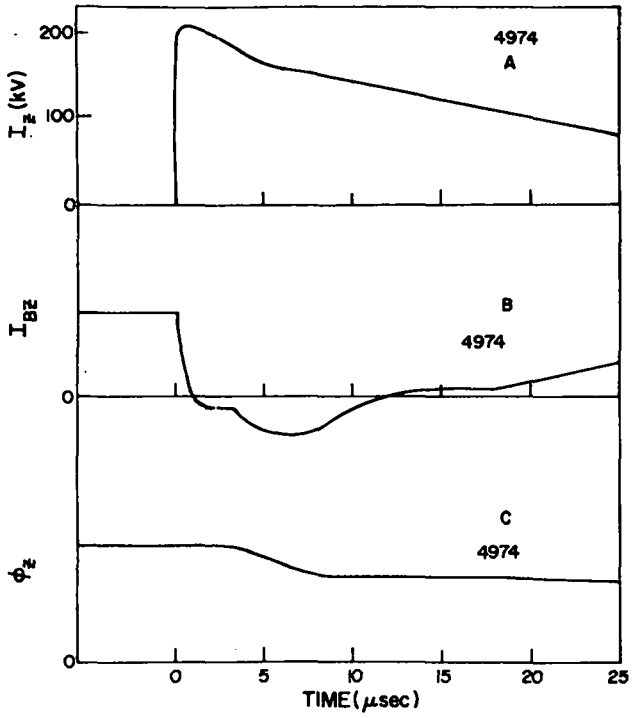

Fig. III-13.

(A) I_z current waveform with crowbar applied at ~3 μsec;

(B) I_{Bz} current waveform with B_z crowbar at t ~ 0, reverse B_z applied at ~3 μsec, and reverse B_z crowbar at ~8 μsec; and

(C) The toroidal magnetic flux φ_z. The decrease in φ_z due to reverse B_z is apparent from 3 to 8 μsec, but φ_z remains of the same sign as required for MHD stability.

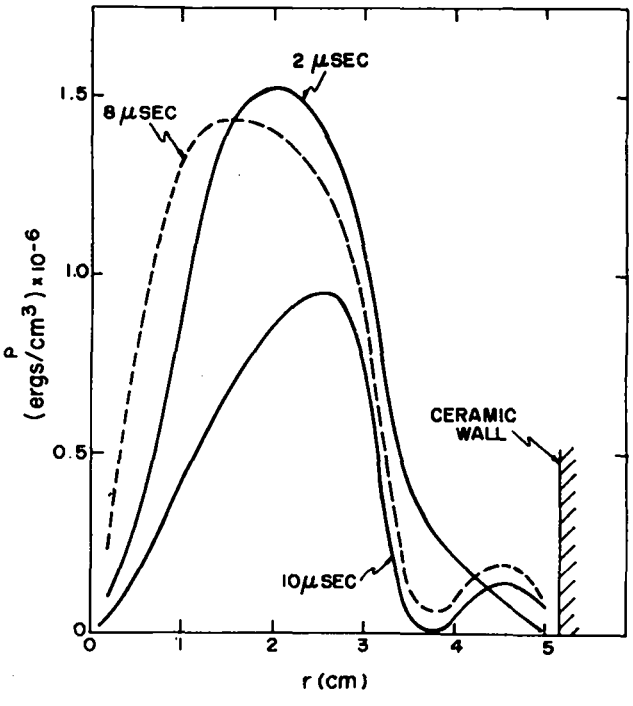

Fig. III-14.

Plasma-pressure profiles calculated from magnetic probe measurements for the fast mode conditions shown in Fig. III-13. With the I_z current crowbarred, the peak plasma pressure remains nearly constant for 8 μsec. Without the crowbarring of I_z, the pressure falls off rapidly with time as shown in Fig. III-7.

We use Suydam's method of completing squares[1] to determine the sign of the potential energy integral

$$W = \frac{\pi}{2}\int_0^{r_w}\left[f\left(\frac{d\xi}{dr}\right)^2 + g\,\xi^2\right]dr \quad ,$$

where ξ is the radial displacement from equilibrium and f and g are functions of B_θ, B_z, k_z, and m. The method is extremely fast but is somewhat insensitive to localized modes when the ratio

$$2\frac{dp}{dr}\Big/ rB_z^2\left(\frac{d\ln P}{dr}\right)^2$$

is only slightly smaller than the limit -0.25 set by the Suydam stability condition.[2] Here p is the magnetic pressure and $P = rB_z/B_\theta$ is the pitch length of the magnetic lines. Incompressible normal modes are obtained by integration of Freidberg's differential equation,[3] whereas the earlier result of Hain and Luest[4] is used to calculate compressible modes.

The reason for operating the diffuse pinch with a reversed B_z field at the wall is to avoid a minimum in the pitch while maintaining a low-current density near the wall.[2,5] A discharge containing a pitch minimum is almost invariably unstable, unless rescued by periodic boundary conditions (q value). Figure III-18 shows the stability diagram of such an unstable configuration at time t = 4 μsec. In Fig. III-18, r is the minor radial position and k_z is the axial wave number. The short horizontal lines are stable wave numbers according to the normal mode solutions, whereas the lines crossing the diagram horizontally indicate unstable modes. The triangles and circles represent roots of the functions f and g, respectively, appearing in the energy integral. Only g can become negative in this representation. Unstable modes, therefore, tend to be

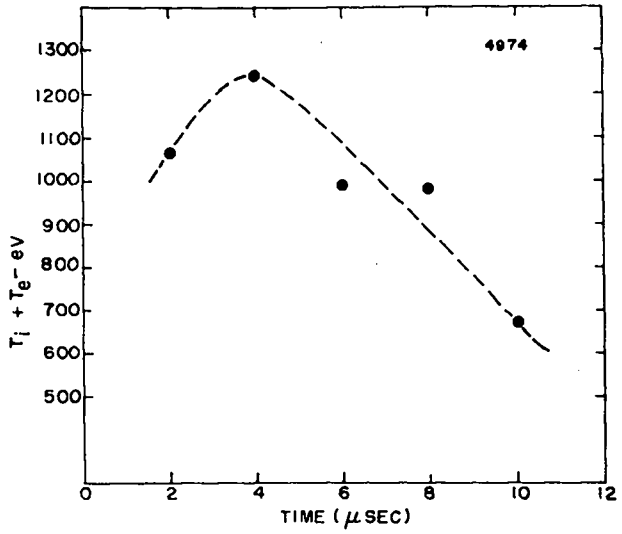

Fig. III-15.
Plasma temperature, $T_e + T_i$, calculated from probe measurements for the crowbarred conditions shown in Fig. III-13. $T_e + T_i$ remain nearly constant at ~1 keV for ~8 μsec with I_z crowbarred and reverse B_z.

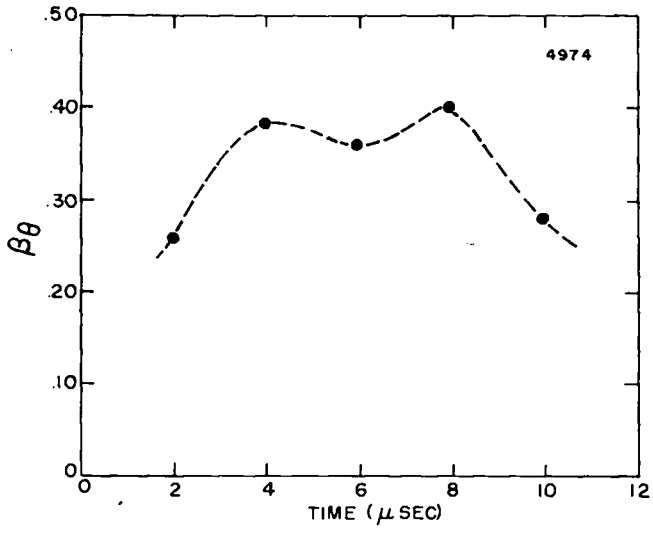

Fig. III-16.
β_θ vs time with crowbarred I_z and reverse B_z with conditions as shown in Fig. III-13.

confined to the negative g region situated between the two g = 0 lines in the diagram. The location and width of the fastest compressible m = 1 modes are indicated by heavy horizontal bars at their respective values of k_z. The fastest growth time with this geometry is of the order of 0.5 μsec. Compressible modes occupy the same regions of the diagram and their growth times are ~30% shorter.

Figure III-17 shows the streak photograph and stability diagrams at times t = 4, 6, and 8 μsec of a reversed B_z pinch. The hatched portion of the abscissa represents Suydam unstable radii. Note that there is no longer a minimum in the pitch. The fastest growth times are 40, 60, and 0.7 μsec, respectively. The profiles indicate that the discharge goes unstable at time $t \approx 6$ μsec, in coincidence with the onset of luminosity in the streak photograph. The growth rates are much slower and the unstable wave numbers much fewer before 6 μsec than for the nonreversed B_z pinch. In fact, during the first 6 μsec, the stability of the pinch is improving in time. The sudden disruption, therefore, seems to be due to a change of the magnetic-field profiles, perhaps due to diffusion, leading to an unstable configuration rather than the slow growth of an early instability.

2. Analysis of Diffusing Profiles. We have studied the effect of diffusion on the m = 1 stable theoretical profile shown in Fig. III-19. The temperature is assumed uniform and constant in time at 100 eV and the diffusion coefficient is derived from classical electrical resistivity. Figure III-20 shows various stable times as functions of programmed rates of decay of the total z-current I_z and B_z winding current I_{Bz}.

The lower curve shows the time at which the discharge becomes Suydam unstable. This particular stable time can be lengthened by as much as a factor of 3 by allowing I_z and I_{Bz} to decay exponentially in time at the rates shown in the abscissa. The middle curve shows the time at which the method of completing squares detects an instability. The upper curve, finally, indicates the time at which the pressure profile becomes flat on axis, thus giving rise to gross modes of instability.

Suydam modes are localized, as one would expect, and are very slow growing. At time t = 60 μsec, for example, the fastest-growing Suydam mode occurs at the radius where the Suydam ratio goes through a minimum and has a growth time of 500 μsec. There is, in fact, the possibility that Suydam modes might be ion Larmor radius stabilized.[6] Therefore, a practical stable time for this geometry appears to be of the order of 60 μsec. If the diffusion time scales as $T_e^{3/2}$ and as r_w^2, and if one excludes trapped particle effects, then classical diffusion is not an obstacle to satisfying Lawson's criterion $nt_{stab} \geq 10^{14}$.

Some of the diffusion calculations have been repeated using the full one-dimensional MHD code with classical transport coefficients.[7] The Suydam stable time becomes 11 μsec for τ = 1000 μsec. Allowing I_z and I_{Bz} to vary in time as before does not improve the Suydam stable time

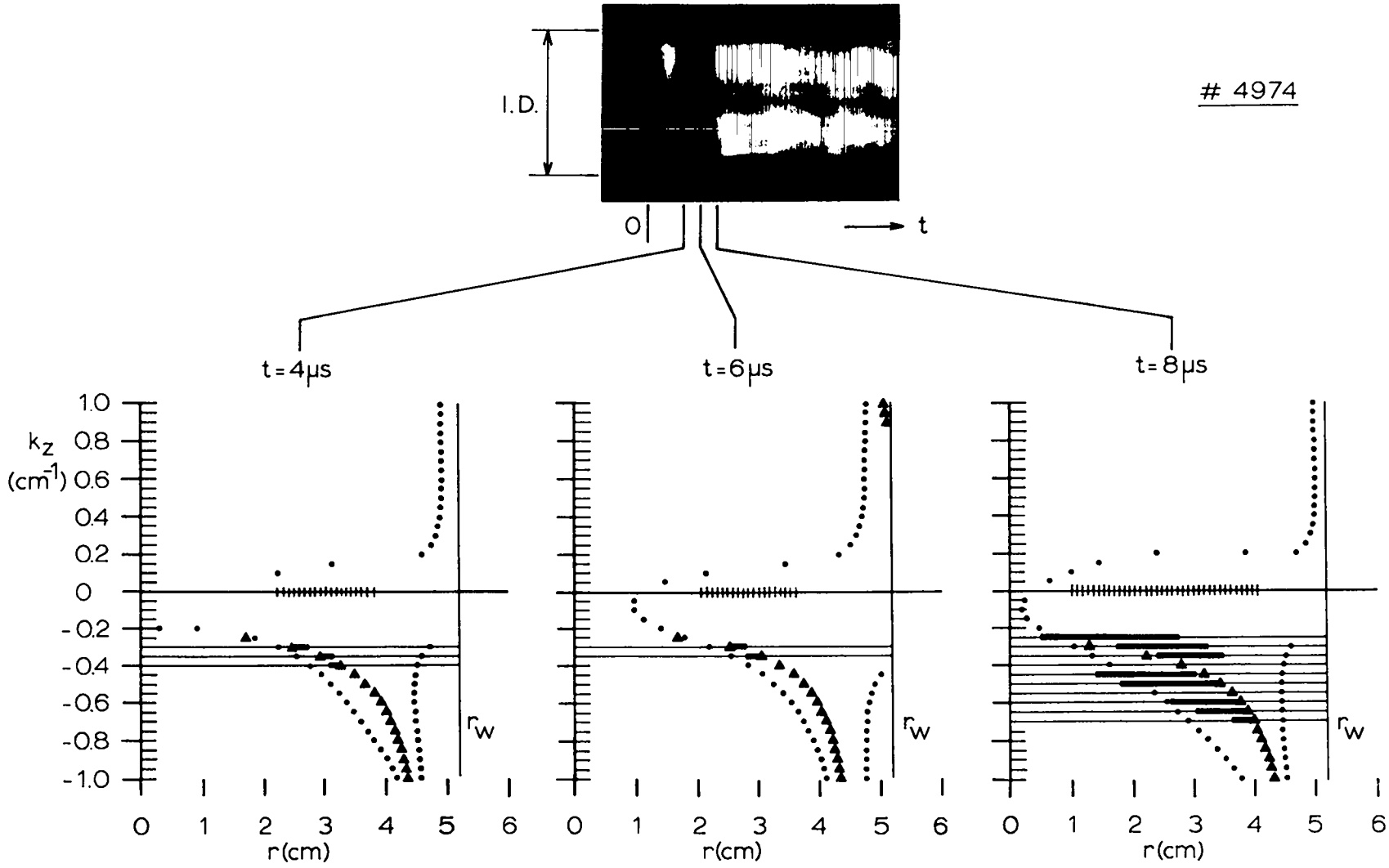

Fig. III-17.

Streak photograph and stability diagrams of a reversed B_z pinch at times t = 4, 6 and 8 μsec. I.D. is the wall diameter, and r_w = 5.2 cm is the wall radius.

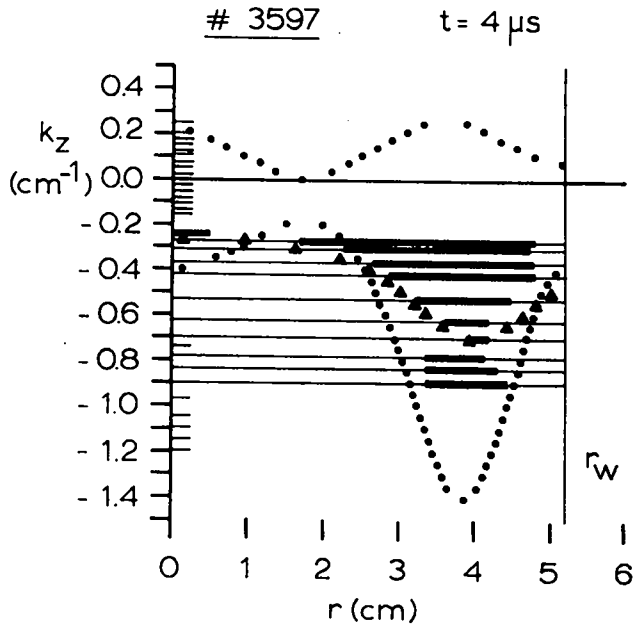

Fig. III-18.
Stability diagram of a nonreversed B_z pinch at time $t = 4$ μsec. Wall radius $r_w = 5.2$ cm.

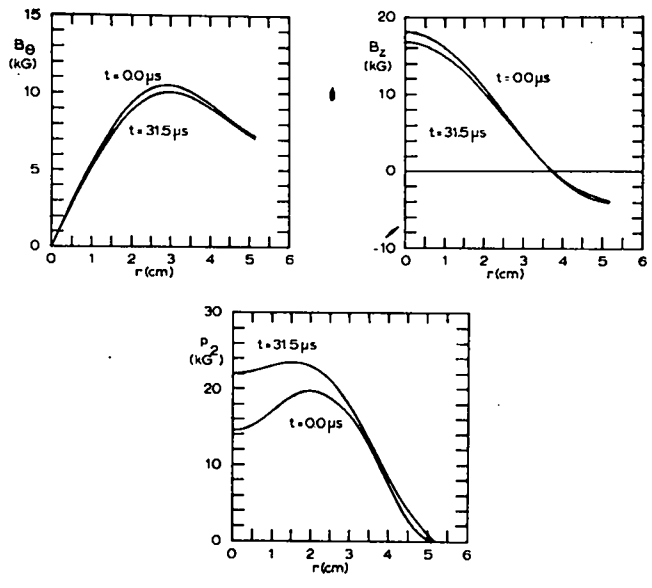

Fig. III-19.
Radial distributions of the magnetic fields B_θ and B_z and magnetic pressure p of an $m = 1$ stable theoretical configuration at times $t = 0$ and $t = 31.5$ μsec during classical diffusion. Wall radius $r_w = 5.2$ cm and electron temperature $T_e = 100$ eV.

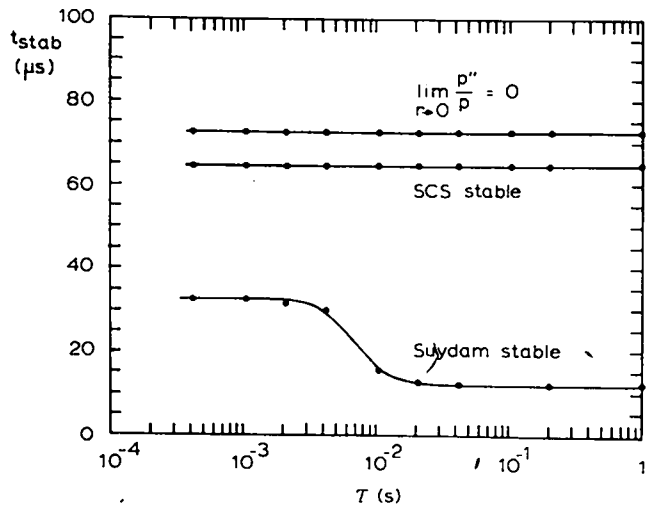

Fig. III-20.
Suydam stable time, time at which the method of completing squres (SCS) detects an instability, and time at which the second derivative of the magnetic pressure vanishes on axis, as functions of the e-folding time τ of the currents I_z and I_{Bz}, during classical diffusion of the theoretical configuration of Fig. III-19.

significantly. Figure III-21 shows the curvature on axis of the pressure profile as a function of time. The result is similar to Robinson's[8] and shows that the pressure profile can be expected to remain hollow for quite some time.

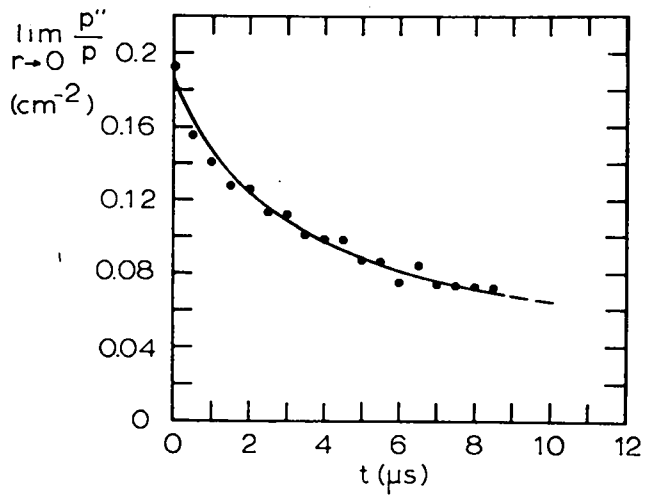

Fig. III-21.
Normalized second derivative of the magnetic pressure on axis $\lim_{r\to 0} p''/p$ as a function of time t, during diffusion of the theoretical configuration of Fig. III-19, using the full MHD code.

Looking back at the stability analysis of the measured reversed B_z profile, it appears that with a classical resistivity corresponding to an electron temperature of 100 eV, one should be able to extend the stable time well beyond 6 μsec. Whether the diffusion is faster than classical, the temperature lower than estimated, or the magnetic-field profiles only marginally stable to start with is to be investigated in the near future.

REFERENCES

1. B. R. Suydam, Los Alamos Scientific Laboratory, personal communication, 1972.
2. B. R. Suydam, "Stability of a Linear Pinch," Proc. Intern. Conf. Peaceful Uses At. Energy, 2nd, Geneva, 1958 (Columbia Univ. Press, New York, 1959), Vol. 31, pp. 157-159.
3. J. P. Freidberg, "Magnetohydrodynamic Stability of a Diffuse Screw Pinch," Phys. Fluids, 13, 1812-1818 (1970).
4. K. Hain and R. Luest, "Zur Stabilitaet zylindersymmetrischer Plasmakonfigurationen mit Volumenstroemen," Z. Naturforschg. 13A, 936-940 (1958).
5. D. C. Robinson, "High-β Diffuse Pinch Configurations," Plasma Phys. 13, 439-462 (1971).
6. T. E. Stringer, "Extension of Suydam's Condition for Plasma Stability to Include Finite Larmor Radius Effects," Princeton Plasma Physics Laboratory report MATT-289 (1964).
7. A. Haberstich, "Numerical Calculation of the Theta, Z, and Screw Pinches," Los Alamos Scientific Laboratory report LA-4782-MS (December 1971).
8. D. C. Robinson, J. E. Crow, C. W. Gowers, G. F. Nalesso, A. A. Newton, A. J. L. Verhage, and H. A. B. Bodin, "The High Beta Toroidal Experiment," Proc. 5th European Conf. on Controlled Fusion and Plasma Physics, Grenoble, 1972, Vol. 2, pp. 47-58.

D. CO_2 Holography (P. R. Forman, Stanley Humphries, Jr., and R. W. Peterson)

Excellent quality two-dimensional double-exposure holographic interferograms were obtained using a pulsed 10.6-μm CO_2 laser. The most successful recording medium has been thin bismuth films. Bismuth is deposited upon a glass substrate to a thickness of about 20 nm. When the film is subjected to the laser radiation there is local evaporation of the bismuth where the scene and reference beams constructively interfere. About 0.3 J/cm^2 is required to "expose" the film.

The development of a reproducible pulsed TEA laser with good mode characteristics was essential for the success of the experiments. A variation in geometry from the discharge system developed by Pearson and Lamberton[1] resulted in a laser that reliably produced a 1 ± 0.05-J pulse of 150-nsec duration predominantly in the TEM_{20} mode. The far field pattern was sufficiently uniform to expose the bismuth films properly.

The holographic interferometer schematic is shown in Fig. III-22. Either an exploding wire or a simple spark in air was used as the test object. The beam splitter is a germanium flat that is antireflection (AR) coated on one surface. The laser output is plane polarized so that in setting up the beam splitter with care, it is possible to get the two beams equal in intensity to within a few percent. AR-coated germanium lenses image the test object and the salt wedge onto the thermal detector. With double-exposure holograms the salt wedge is introduced into the reference arm on the second exposure to produce a uniform background fringe pattern.

Figure III-23 shows a reconstructed interferogram of a spark discharge in air. The dark protrusions are the shadows of the electrodes. The uniform fringe spacing produced by the salt wedge is seen near the base of the electrodes, and the severe distortion produced by the electrons in the air spark is seen near the main body of the electrodes. The clear region close to the points of the electrodes is caused by refraction due to a high-electron density gradient and does not represent lack of resolution of the film. Interferometry on a simple air spark

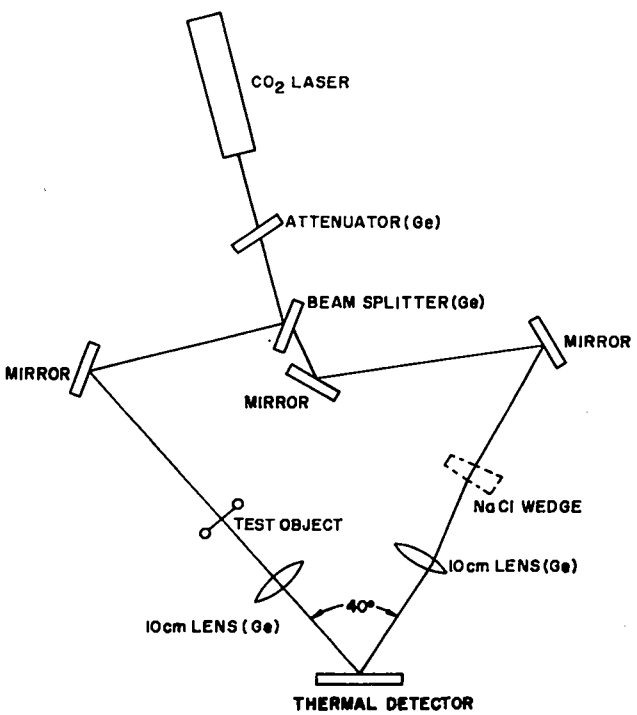

Fig. III-22.
Schematic diagram of CO_2 holographic interferometer.

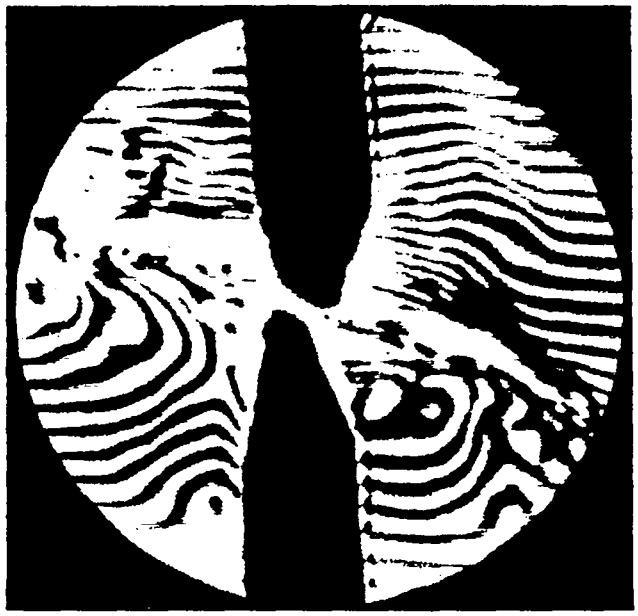

Fig. III-23.
Reconstructed holographic interferogram of an air spark discharge. The dark protrusions are the shadows of the electrodes.

demonstrates one of the advantages of CO_2 radiation over that of the ruby laser. Although 15 times more sensitive to electron densities, CO_2 radiation interferometry is 15 times less sensitive to perturbations in the density of neutrals, assuming that the neutral index of refraction has little dependence on λ. For measuring parameters of a plasma surrounded by neutrals, the CO_2 has a factor of 225 increase in S/N over ruby. In the hologram shown, even a complete removal of the background air would cause only a fraction of a fringe shift. This, coupled with the fact that the fringe shifts are toward shorter optical paths, shows that it is indeed electrons that are observed. Note that the quality of the fringe pattern produced is sufficiently good that fractional fringe measurements are practical.

The feasibility of good quality 10.6-μm holographic interferometry has been demonstrated. The exposure time of 0.1 μsec is very suitable for measurements of pinches. The type of laser preionization developed, irradiation through a screen electrode, is particularly good for extrapolation to much larger discharge volumes. This should allow the development of more powerful lasers capable of "exposing" large areas of bismuth film. A considerably more detailed article has been written on the above subject and has been accepted for publication in Applied Physics Letters.

Interferometry at 10.6 μm requires the use of special windows. Provisions for such windows are being made on the ZT-1 pinch. Because Scyllac operates at higher densities than ZT-1, it should be possible to sacrifice some sensitivity and use the bismuth film technique in conjunction with an HF laser ($\lambda \cong 2.8\ \mu$m) directly through the quartz discharge tube. Toward this end the laser is being modified in an attempt to investigate this possibility. This work is described in Sec. II.G.

REFERENCE

1. P. Pearson and H. Lamberton, IEEE J. Quantum Electron., Vol. QE-8, 145 (1972).

E. Transfer Capacitor Circuit (J. N. DiMarco)

This circuit (Fig. III-24a) offers the possibility of achieving rapid rates of current transfer into a load, requiring expensive fast capacitors for only part of the total energy storage. The transfer capacitor, C_t, is chosen to be much less than the primary energy storage capacitor C_o. If the circuit parameters are chosen correctly, characteristic oscillations of the two circuits are reduced or eliminated. This matching condition for the ideal circuit is $R^2 = L_s/C_t$.

The resistor R is a hindrance in that it removes some of the voltage from the load and dissipates most of the energy. The hybrid circuit shown in Fig. III-24b is

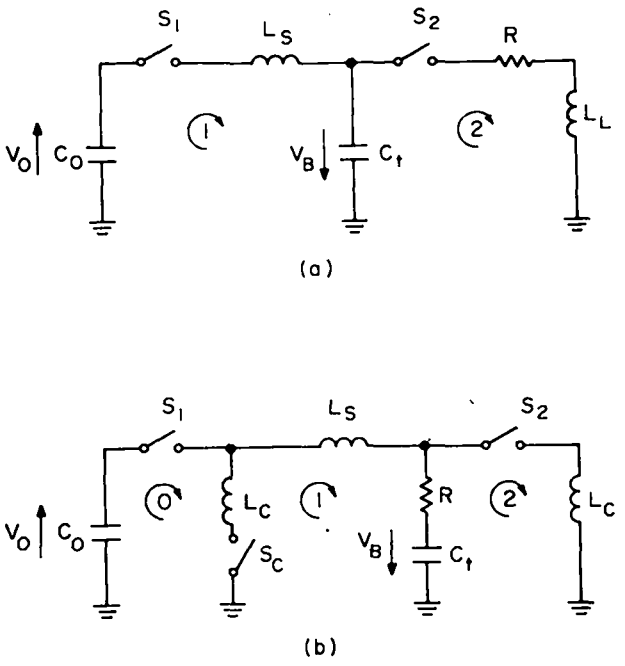

Fig. III-24.
(a) Schematic of the transfer capacitor circuit, and
(b) A modified circuit in which the resistance R does not dissipate energy after the current is transferred to loop 2.

suggested. Once transfer to loop 2 is complete, the resistor no longer dissipates energy. Switch S_c is now required to crowbar the current.

The results of a NET-2 circuit analysis for the hybrid circuit are shown in Fig. III-25. Its parameters are $V_o = 50$ kV, $V_B = -50$ kV, $C_o = 5.0\,\mu$F, $C_t = 0.5\,\mu$F, $L_s = 0.2\,\mu$H, $L_1 = 0.04\,\mu$H, and $R = 0.315\Omega$; S_2 closes at 0.5 μsec. The crowbar switch S_c was not activated. Initial transfer of current takes place at 1.2×10^{12} A/sec, as would be expected from the circuit parameters. The effect of placing the resistor in the transfer capacitor branch of the hybrid circuit is noted by the peaking of the current at 1.8 μsec. This peak could be reduced or increased by reducing or increasing the main bank capacitance C_o. Additional computation has shown that by suitably trimming the circuit parameters, a specified current can be obtained with the hybrid circuit.

The crowbar switch S_c need not be an extremely low-inductance switch as would be required if it were placed directly across the load inductor L_L.

This circuit offers the advantage of approximating an inductive energy storage system by back biasing C_t. The resistor R is removed from the load circuit so that it no longer is the main dissipative element, and, in addition, it helps to isolate the capacitor C_t from the load.

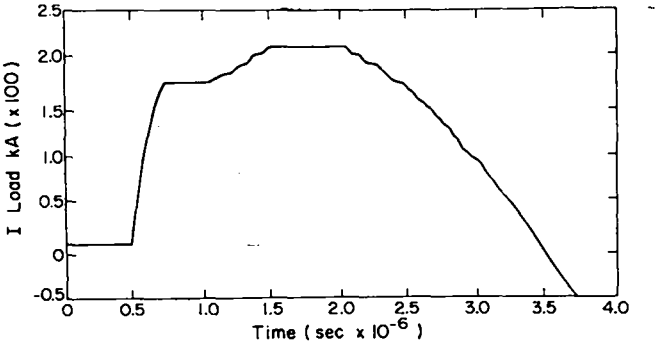

Fig. III-25.
Results of a circuit analysis for the modified circuit of Fig. III-24b. The initial rate of transfer of current is 1.2×10^{12} A/sec.

F. Detonator Crowbar Switch (L. Burkhardt, R. Dike, J. DiMarco, and R. Kewish)

The crowbar switch described in the last annual report (LA-4888-PR) has been modified to be placed in the four feedplates of ZT-1 with low inductance (Fig. III-26). The switch has been tested on the fast linear Z-pinch facility. Its performance approached the original design expectations, i.e., self-inductance ~3 nH and resistance $\lesssim 5\,\mu\Omega$. Closure time is $\sim 11.0 \pm 0.3\,\mu$sec, where t = 0 is defined as the start of current in the bridgewire of the detonator. In addition, an electric jitter is $\sim \pm 0.3\,\mu$sec.

High-voltage holdoff is important in the fuse-driven ZT-1 application. To test the voltage holdoff, a 42-kV square wave pulse of 20-μsec duration was applied, the length of which was clipped by crowbar closure. The average voltage breakdown time is $9.1 \pm 0.3\,\mu$sec. The high-current crowbarring time of $11 \pm 0.3\,\mu$sec is then only ~2 μsec longer than the 9.1 ± 0.3-μsec average time measured in the voltage holdoff test.

In these tests, the initial crowbar currents ranged from 180 to ~330 kA with L/R decay times of ~1.2 msec without burning. Four of these switches, one per quadrant, are installed in ZT-1.

G. An All-Metal Toroidal Discharge Tube (R. Dike and J. Phillips)

A toroidal discharge tube for ZT-1, using our aluminum washer design, is being fabricated. In this design the metal wall on which high electric fields, ~1 kV/cm, are to be applied is subdivided such that the voltage between adjacent conducting surfaces is less than the running voltage of an arc. Experiments have shown that this voltage is ~25 V. In our present design the discharge tube is fabricated from a stack of aluminum washers, 0.010 in. thick,

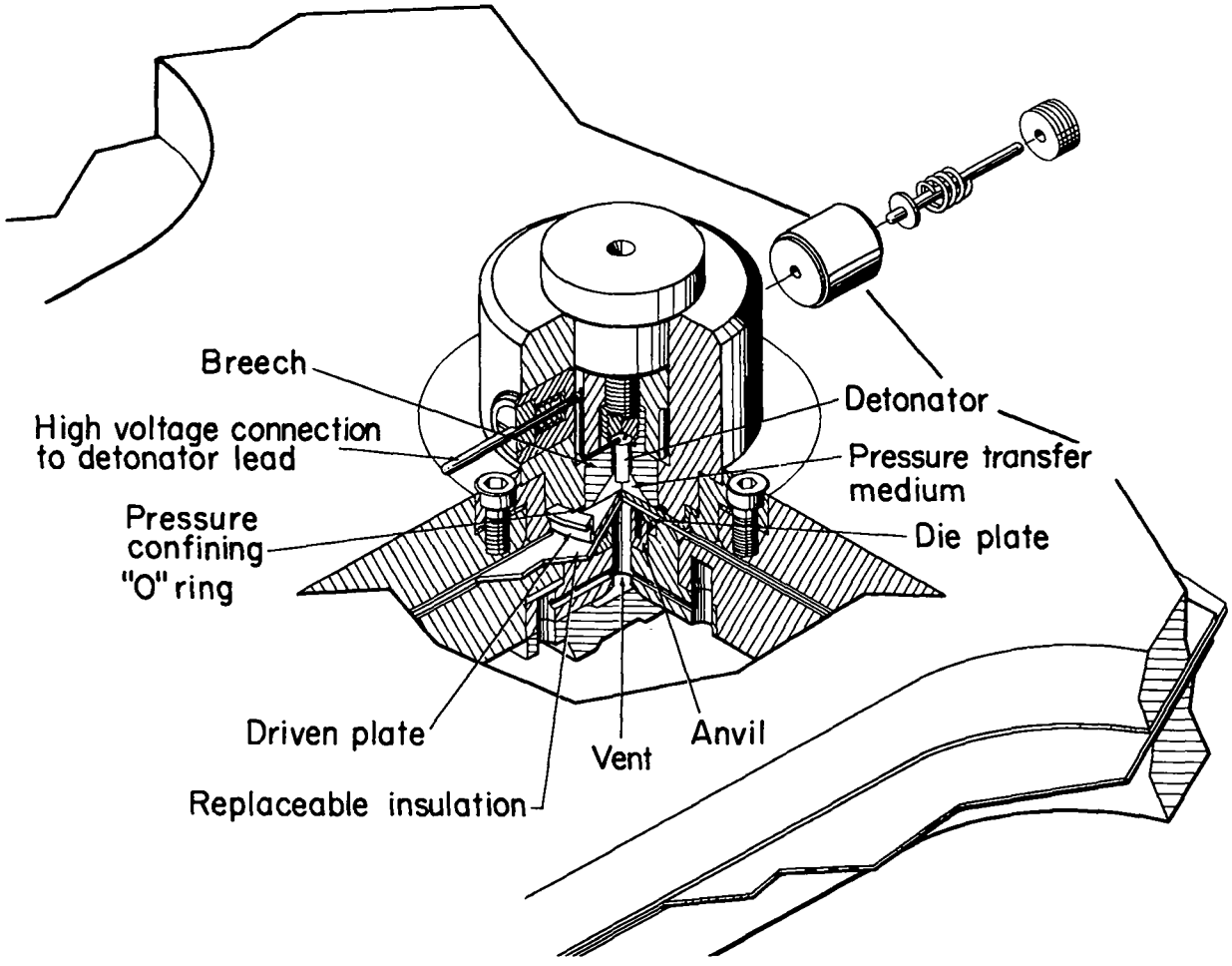

Fig. III-26.

Crowbar switch assembly is shown installed within the ZT-1 feed plate. When the detonator is fired the expanding gases of the explosion shears the replaceable insulation by deforming the driven plate into the die plate, thus making the desired electrical contact. Paraffin is used as the pressure-transfer material where it acts as a coupling medium between the pressure front and the deformation surface.

with adjacent surfaces anodized for insulation. Tests on a linear tube of similar construction showed that electric fields $\lesssim 1.2$ kV and discharge currents $\lesssim 0.45$ MA could be successfully applied.

A toroidal metal discharge tube (Fig. III-27) for ZT-1 is being fabricated. Each washer, ~0.010 in. thick, is tapered to match the major radius of the primary when packed in series. Also, each washer is subdivided 40 times in azimuth so that the voltage in this plane of 1 kV/turn can be applied. This latter subdivision allows β_z to be varied in the experiment as required for stability.

REFERENCE

1. Status Report of the LASL Controlled Thermonuclear Research Program for 12-Month Period Ending October 1970, LA-4585-MS, p. 39.

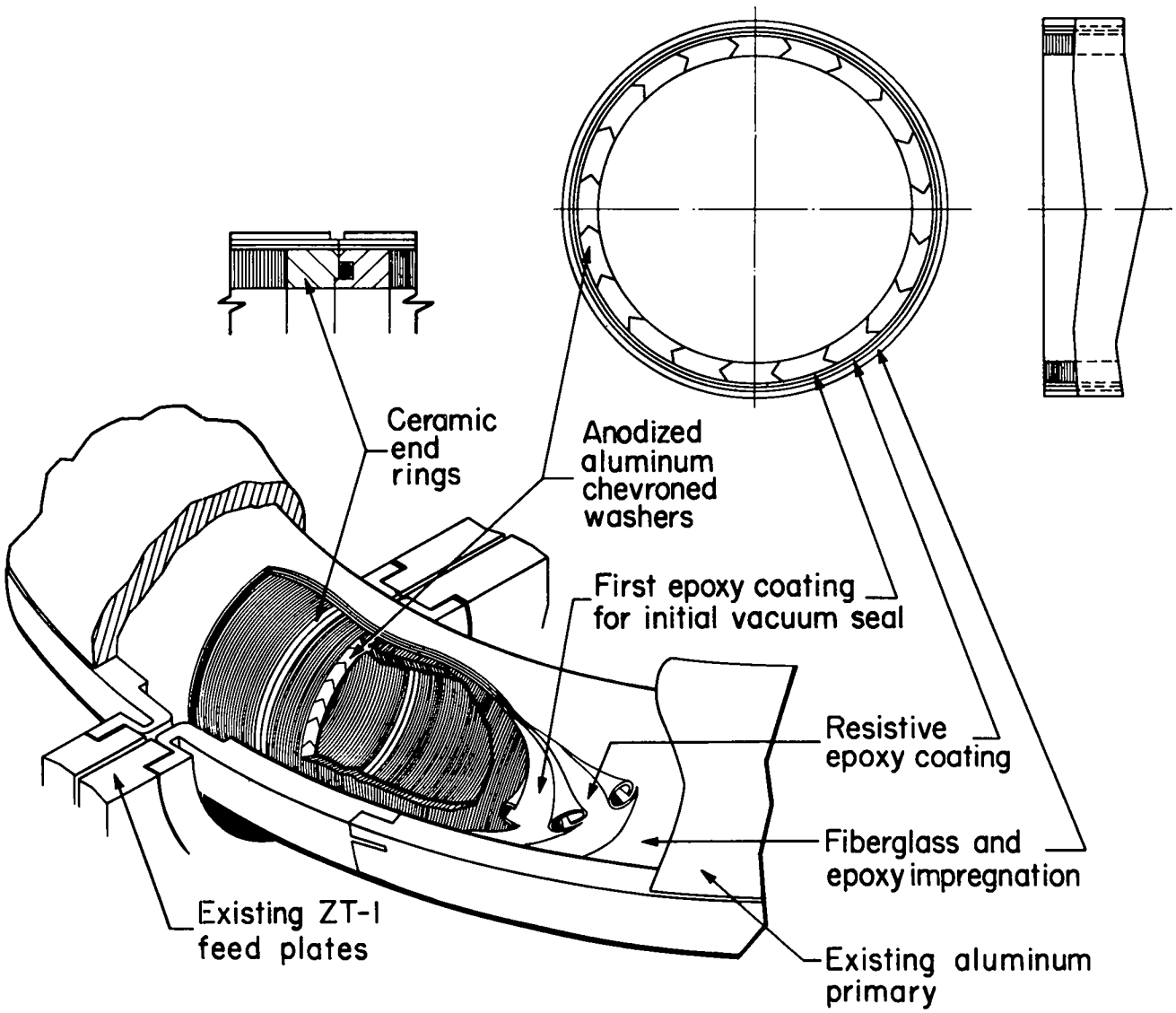

Fig. III-27.

The all-metal toroidal discharge tube installed within the ZT-1 primary. The aluminum chevroned washers are epoxy potted in 90° segments. Vacuum seals are at four places where thin ceramic spacers are used with O rings.

IV. EXPERIMENTAL PLASMA PHYSICS GROUP PROGRAM

A. Summary (H. Dreicer)

During the past year we continued to concentrate our experiments on the very fundamental processes that control the high-frequency electrical resistivity near the electron plasma frequency. This is the regime where theory predicts several interesting enhanced absorption effects. In particular, if the electric fields are intense enough (strong-field limit), the excitation and saturation of the high-frequency parametric instabilities make a large contribution to the resistivity of collisionless plasmas. It is of paramount importance from the standpoint of the controlled fusion problem that these strong-field effects be achievable with relatively modest powers.

Various laser research groups already expect these instabilities to play a dominant role in the heating of dense plasmas by laser light. It does not seem unreasonable to consider parametric heating as a possible auxiliary heating technique for Scyllac and Tokamak plasmas. In this connection, we wish to call attention to two related matters. (1) Parametric high-frequency instabilities must come into play when the dc ohmic heating currents in Tokamaks excite electron plasma waves to high levels. The saturation of these waves by their repeated decay to longer wavelengths and into ion waves can then be expected to have a strong influence on the dc electrical resistivity. (2) We suggested (LASL P-13 QPR, February 1971) the possibility of increasing the plasma dc electrical resistivity directly by subjecting a plasma simultaneously to a weak dc electric field and an ac electric field intense enough to excite strong ion density fluctuations by the parametric ac instabilities. We expect additional studies to clarify these matters.

In the past year we have seen significant advances in our understanding of the physics of high-frequency heating, extended the parametric instability threshold measurements to lower and higher densities, found a suprisingly large contribution to the weak-field resistivity from the excitation of Trivelpiece-Gould modes, and carried out detailed measurements on the effective collision rate and the velocity distribution function of the electrons heated anomalously above the threshold. The identification of anomalous absorption with the excitation of parametric instabilities, previously based upon threshold measurements, has now been placed on a firmer foundation by our spectral studies. The close correspondence between experiment and theory also suggests the future application of the high-frequency parametric instability process to fusion devices as a diagnostic technique.

B. Anomalous Absorption of Large Amplitude Electromagnetic Waves Near the Electron Plasma Frequency (J. H. Brownell, H. Dreicer, R. F. Ellis, and J. C. Ingraham)

Using the LASL alkali-plasma machine, we are studying collisional and collisionless absorption of intense 2-GHz microwave electromagnetic fields caused by a highly ionized plasma column. A small fraction of the microwave (pump) energy stored in a high-Q resonator that surrounds a short section of the plasma column (Fig. IV-1) is monitored and yields information about the field dissipation. Simultaneously, several retarding potential probes search for energetic electrons, and an RF probe and spectrum analyzer monitors the excitation of plasma oscillations. The electron density n is adjusted so that the microwave frequency ω is near the electron plasma frequency ω_p, and the possibility of coupling to collective plasma modes exists.

Our measurements show that the field dissipation and associated electron heating depends very much upon the magnitude of the pump (microwave) electric field E_0.

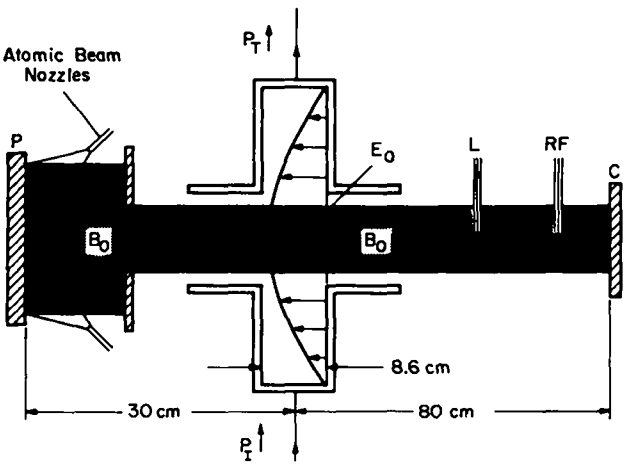

Fig. IV-1.
Experimental setup.

Generally, these phenomena can be discussed in a weak- and strong-field limit, depending upon the value of the ratio of the ac drift speed v_E to the electron thermal speed v_T, i.e.,

$$\frac{v_E}{v_T} = \frac{eE_o/(m\omega)}{(2kT_e/m)^{1/2}}$$

The lower limit of the strong-field regime is defined by the threshold electric field, E_{oc}, required for onset of anomalous absorption. The corresponding drift speed ratio is denoted by $(v_E/v_T)_c$.

In the weak-field limit, where $v_E/v_T \ll (v_E/v_T)_c$, our interest centers on the electrical resistivity measurement. Vlasov theory predicts that this resistivity will be the classical value produced by electron-ion encounters provided the ions are nearly uncorrelated in their positions. In the strong-field limit, where $v_E/v_T \geqslant (v_E/v_T)_c$, our studies have been devoted to the experimental and theoretical determination of the threshold for anomalous absorption as a function of n and E_o. Measurements of the absorption rate and the energy spectrum of the anomalously heated electrons at and above threshold have also been made.

We developed two different pulsed microwave methods, the AM and FM methods,[1] for measuring dissipation. Both methods determine the incremental change in the inverse Q of the resonator $\Delta(1/Q)$ when plasma is introduced, and both are carried out on a fast time scale to "freeze" the ambient plasma conditions as much as possible during the measurement. $\Delta(1/Q)$ is proportional to the microwave energy absorbed by the plasma. The pulse technique helps to avoid the errors that ambient low-frequency fluctuations introduce into the n and Q measurement. Moreover, it reduces the classical electron heating by the applied microwave field that otherwise could significantly alter the ambient electron temperature and thus complicate the interpretation of the data. By measuring $\Delta(1/Q)$ due to plasma absorption as a function of pulse length and electric field below the threshold for anomalous absorption, we find that the pulse technique is successful in avoiding classical heating provided the pulses are short enough and the electric fields are not too large. (The reader is reminded that $\Delta(1/Q)$ is proportional to $T_e^{-3/2}$ when classical heating occurs.)

1. Weak-Field Resistivity (H. Dreicer, R. F. Ellis, and J. C. Ingraham). The weak-field resistivity data observed at v_E/v_T=0.0035 and reported earlier[1,2] have been reanalyzed because of a more accurately determined hot plate temperature (T_o = 2250°K), and a more careful consideration of the low-density wings on the plasma-density profile. The result is shown in Fig. IV-2 as a function of the measured frequency shift Δf of the resonator. This quantity is proportional to plasma density. The solid and dashed theoretical lines indicate the range of uncertainty remaining in the theoretical value due to profile uncertainties. Asymptotic expressions given by Dawson and Oberman,[3] valid for $(\omega_p/\omega)^2 \ll 1$ and $(\omega_p/\omega)^2 \gg 1$, were used in the analysis. The agreement, shown in Fig. IV-2, between the Dawson-Oberman theory and our observations for the range $0 < (\omega_p/\omega)^2 \lesssim 1$ provides important evidence for the validity of our pulsed measurement technique and provides the first experimental evidence for the validity of the Dawson-Oberman resistivity calculation. No previous measurement of the weak-field ac resistivity appears in the literature.

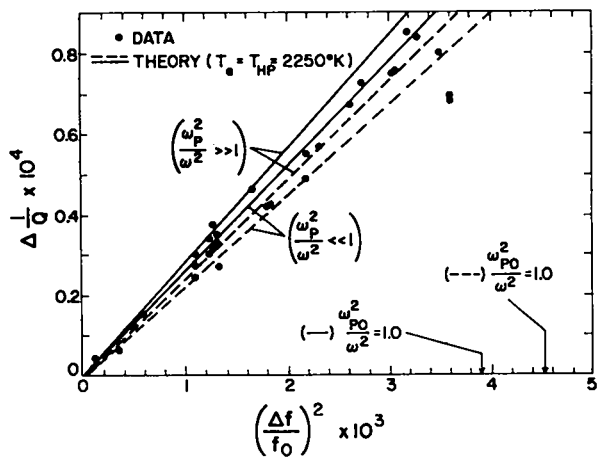

Fig. IV-2.
Microwave dissipation as a function of normalized density squared.

Further improvements in the analysis of this experiment require an improved theory for the relation between resonator frequency shift and electron density. A numerical computation of this relationship is being carried out in collaboration with John D. Thomas (Visiting Staff Member, New Mexico State University). When completed, the computation will apply to both arbitrary density profiles and resonators with plasma access holes, and will be free of the usual perturbation treatment requirement that $(\omega_p/\omega)^2 \ll 1$.

At higher plasma densities, i.e., $(\omega_p/\omega)^2 \geqslant 1$, our measurements (crosses and dashed line in Fig. IV-3) indicate a marked increase in the weak-field resistivity that is not predicted by the Dawson-Oberman theory. The onset of this large additional contribution coincides with the detection of high-frequency plasma oscillations in the plasma column outside of the resonator. We believe these waves are excited by linear coupling between plasma and

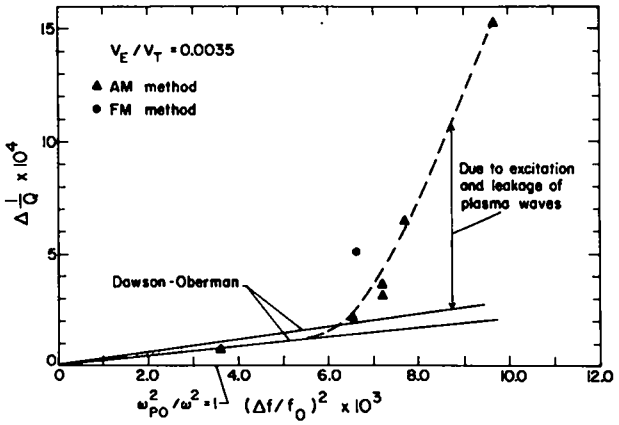

Fig. IV-3.
Microwave dissipation as a function of normalized density squared.

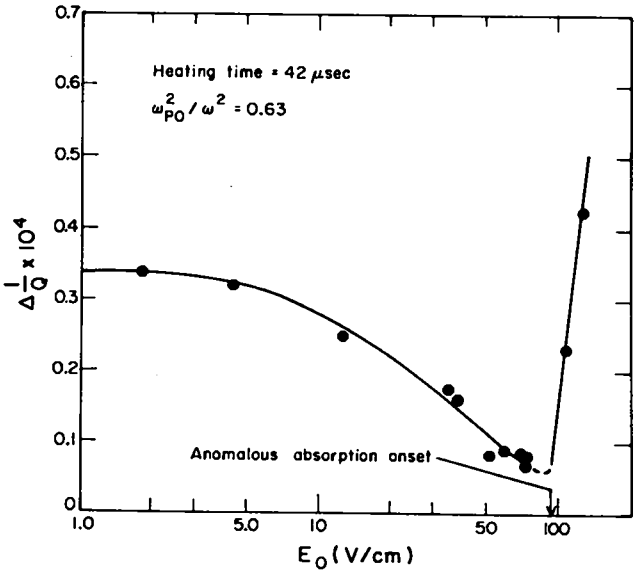

Fig. IV-4.
Microwave dissipation as a function of a pump electric field for a fixed heating pulse duration.

the microwave fields, and are a manifestation of Trivelpiece-Gould modes that can propagate throughout the plasma in the presence of a strong magnetic field. Our observations indicate that there is a threshold for the parametric decay of the microwave pump field into these Trivelpiece-Gould waves and ion acoustic waves. These data are presented below.

2. The Role of Heat Conduction (J. H. Brownell, H. Dreicer, R. F. Ellis, and J. C. Ingraham). Classical microwave pulse heating of plasma electrons is described by the source function

$$S(x,t) = \frac{\omega_p^2}{\omega^2 + \nu_{ei}^2} \nu_{ei} \epsilon_o E^2(x,t) \quad ,$$

which gives the power absorbed per unit volume at the time t and the position x (ν_{ei} is the electron-ion collision rate and ϵ_o is the permittivity of vacuum). The form of S is not well known when the electric field exceeds the threshold for anomalous absorption. Consequently, the standard approach is to retain the classical form for S with ν_{ei} replaced by an effective collision rate ν_{eff}, which characterizes the (generally unknown) strength of the anomalous absorption. (Some measured values of ν_{eff} are discussed in Sec. IV.B.5.) However, heating by the source S can alter the ambient plasma temperature and velocity distribution, and thus complicate the interpretation of resistivity measurements when the electric field becomes intense.

Figure IV-4 illustrates this effect for a heating pulse of 42-μsec duration, $(\omega_{po}/\omega)^2 = 0.63$, and a range of electric fields that includes the threshold. We find a marked decrease in $\Delta(1/Q)$ as the applied microwave field approaches the threshold value for anomalous absorption from below. Such a decrease corresponds to an increase in electron temperature. The pulse duration in this example exceeds the time required by a typical electron to collisionally diffuse from the resonator heat source to the axial boundaries of the plasma. We, therefore, expect the axial temperature distribution to closely approach the asymptotic steady-state distribution determined by a balance between the source S and the axial heat conduction. An encouraging, but preliminary, comparison between the electron temperature deduced from the $\Delta(1/Q)$ measurement shown in Fig. IV-4 and the theoretical electron temperature deduced from such a balance is shown in Fig. IV-5. More studies on this are under way.

3. Threshold Determinations (H. Dreicer, R. F. Ellis, and J. C. Ingraham). To avoid the complications that arise when the electric field alters the ambient plasma conditions, we use a microwave pulse length as short as several microseconds. Except for the largest field required (50 to 100 V/cm), this precaution is successful and $\Delta(1/Q)$ is found to be independent of E_o until threshold is reached. At the largest fields the question of classical heating is not yet resolved. The result of such threshold determinations is shown in Fig. IV-6 as a function of ω_{po}^2/ω^2. The theoretical thresholds that we computed, using the Marder-Freidberg infinite uniform plasma parametric instability code,[4] are shown for comparison (see

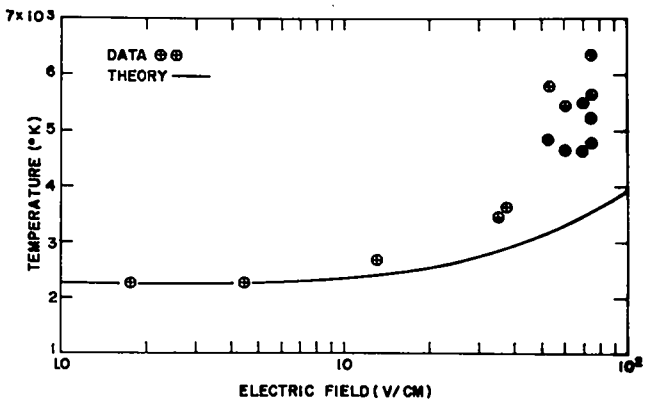

Fig. IV-5.
Electron temperature as a function of pump electric field.

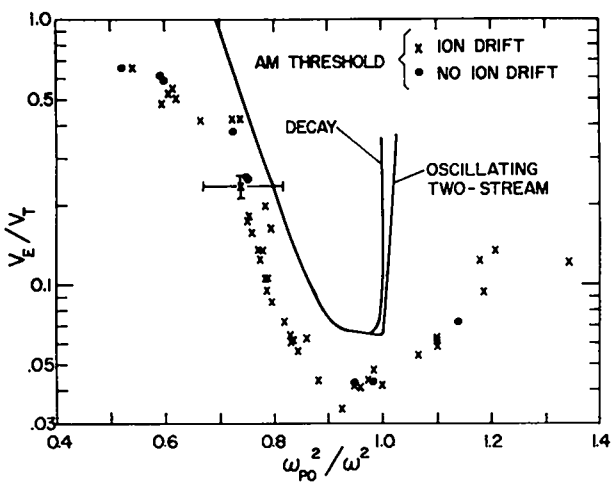

Fig. IV-6.
Threshold electric field as a function of ω_{po}^2/ω^2.

Sec. IV.B.6). We believe that the deviations at large ω_{po}^2/ω^2 are a density profile dependent effect in part related to the excitation of Trivelpiece-Gould waves.

The leveling off of the experimentally determined threshold at low $(\omega_{po}/\omega)^2$ is not understood. In the past, we suspected that this deviation might be due to classical electron heating because the electric fields at threshold are large. This contention is not verified by the computer results, which show that the threshold is insensitive to electron temperature at the low values of $(\omega_{po}/\omega)^2$. Other possibilities that remain to be examined are related to the fact that the sharp rise of the threshold for $(\omega_{po}/\omega)^2 \leqslant 0.9$ is predicted by theory to be due to Landau damping of the parametrically excited electron plasma wave. Thus, several other physical effects, for example electron trapping and distortion of the electron velocity distribution, which can sensitively affect the Landau damping, may account for the low-density deviation in the threshold.

The minimum in the threshold in the range $0.9 \leqslant (\omega_{po}/\omega)^2 \leqslant 1$ occurs because electron-ion encounters produce more wave damping than Landau damping does and are not sensitive to density changes in this small density range. The agreement between the theory and the threshold measurements, therefore, provides strong evidence that the value of the electron-ion collision rate we measured in the weak-field experiment and then assumed in the threshold theory (see Sec. IV.B.6) is correct. Moreover, it shows that Landau damping exists in the range $0.7 \leqslant (\omega_{po}/\omega)^2 \leqslant 0.9$. This Landau damping observation is in itself noteworthy because threshold theory predicts that the most unstable waves have $k\lambda_D \approx 0.1$. The plasma column radius and Debye length in our experiment are 1 cm and 2×10^{-3} cm, respectively. Therefore, we are observing Landau damping of waves for which $ka \approx 50$ (a = plasma radius). This seems to satisfy the infinite plasma conditions, to which Landau's theory applies, more closely than did previous experiments.

Another interesting feature observed in the past was the increase of the threshold field when the time during which the plasma was subjected to electric field became too short.* The data have been analyzed and are shown in Fig. IV-7. The vertical columns in Fig. IV-7 indicate the range in the threshold value of v_E/v_T produced by varying the microwave pulse length or excitation time. These times (in microseconds) are indicated near the tops and bottoms of the vertical columns. Where the tops remain unmarked, the pulse length was 0.7 μsec. The pulse length has considerable influence upon the threshold. The mechanism responsible for this effect has not been experimentally identified. At the larger fields, where $0.5 < v_E/v_T < 1.0$, classical heating may come into play. The role played by the small growth rate of parametric instabilities near threshold upon the determination of the threshold is not yet understood properly.

The data shown in Figs. IV-6 and IV-7 were obtained on a nearly trapezoidal radial density profile. Earlier data[2] observed on a bell-shaped profile differ somewhat from these measurements. The comparison is shown in Fig. IV-8 together with both profiles. A detailed understanding of these profile effects will require the development of a systematic technique for varying density profiles.

*We thank H. Hendel and T. K. Chu who suggested a pulse length effect on the grounds that the growth rate of the instability is small near threshold.

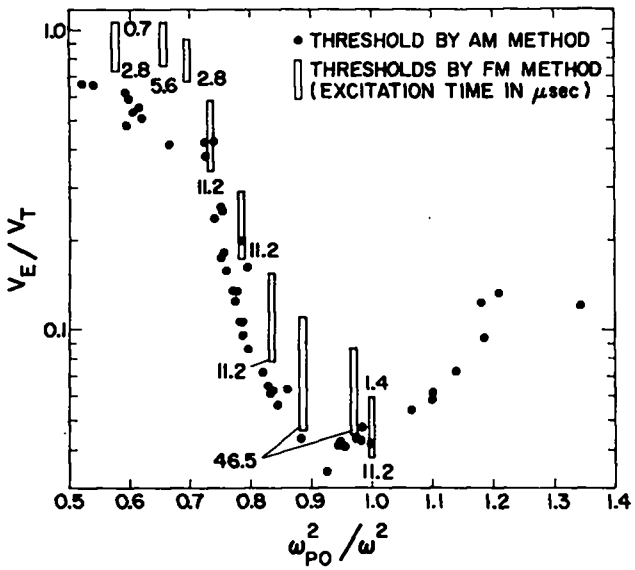

Fig. IV-7.
Threshold electric field as a function of ω_{po}^2/ω^2 for various excitation times.

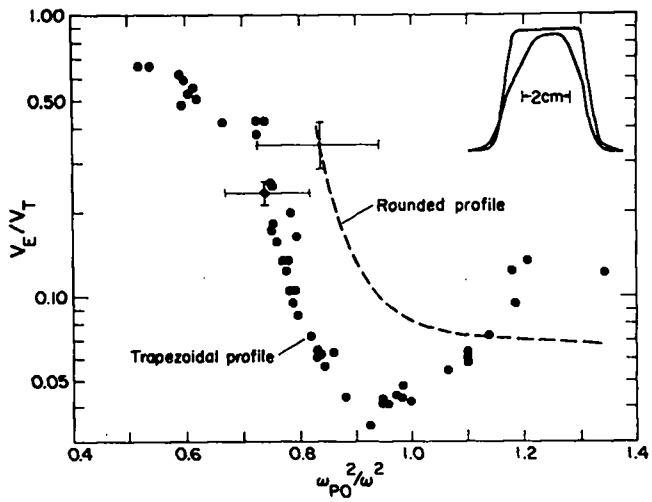

Fig. IV-8.
Threshold electric field as a function of ω_{po}^2/ω^2 for two different profiles.

The threshold data shown in Figs. IV-6, IV-7, and IV-8 are observed when the relative drift between the electrons and ions in the plasma is approximately equal to the ion thermal speed ($\sim 10^5$ cm/sec). No noticeable change in threshold was observed, as also indicated in Fig. IV-6, when this drift was reduced to zero.

4. Spectral Evidence for the Parametric Decay Instability (H. Dreicer, R. F. Ellis, and J. C. Ingraham). A miniature coaxial microwave probe (marked RF in Fig. IV-1) is located outside of the resonator and serves as a detector of plasma waves. Its output is monitored by a microwave spectrum analyzer whose local oscillator sweeps across the interesting spectral region at a low rate and displays the information obtained from many individual pulse excitations. An important observation made with this system concerns the dependence of the plasma wave intensity, as observed outside of the resonator, on the plasma density. No high-frequency plasma waves are detected for $(\omega_p/\omega)^2 \lesssim 1.2$. A sudden onset of wave oscillations occurs at $(\omega_p/\omega)^2 \approx 1.2$ and their intensity increases with increasing plasma density. These are probably Trivelpiece-Gould electrostatic waves.

The importance of this result is related to our other observation, documented in Fig. IV-6, that there is a relatively large range of densities below $(\omega_p/\omega)^2 \approx 1.2$ for which an anomalous absorption threshold exists and for which anomalously heated electrons are observed, although no plasma waves escape from the resonator. In this density range, plasma waves excited within the resonator are also absorbed. This is a distinct advantage from the standpoint of data interpretation because it allows us to relate microwave absorption and particle heating quantitatively without regard for energy deposited in plasma waves. However, there is also a disadvantage that becomes apparent when an attempt is made to directly identify the wave coupling mechanism responsible for anomalous absorption. To detect unstable plasma waves for $(\omega_p/\omega)^2 \lesssim 1.2$, the probe would have to be placed into the resonator where it might perturb the microwave fields, and this, so far, we have not done. However, we have obtained indirect evidence of plasma wave excitation from spectral analysis of the microwave signal transmitted by the resonator.

In the high-density range, the situation is different. Here we detect plasma waves outside of the resonator, but, as yet, have not calibrated the detector to account quantitatively for the absorbed energy. Below threshold, it is nevertheless quite clear that important contributions to the weak-field resistivity arise from the linear excitation and leakage of Trivelpiece-Gould modes from the resonator (see Sec. IV.B.2). During the past quarter, the behavior of these waves was studied in the strong-field regime as well. We find that the onset of anomalous absorption at threshold coincides with the appearance of one or more lower frequency sidebands adjacent to the microwave pump frequency. An example of observed spectra is shown in Fig. IV-9 for two values of E_o/E_{oc}. The main peak, observed both above and below threshold, is centered at $\sim$ 2.1 GHz. These results are preliminary in nature and will have to be studied further. At this stage, they suggest that the pump becomes parametrically unstable at $E_o = E_{oc}$ and decays into a Trivelpiece-Gould wave (the side band) and into a low-frequency ion wave whose frequency equals the difference between the pump and side band frequencies. It is also possible that the

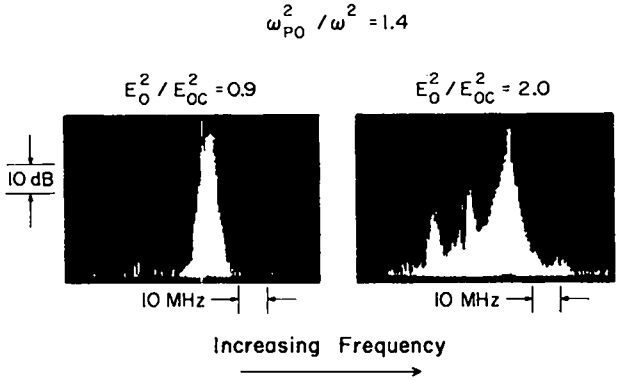

Fig. IV-9.
Spectral analysis of detected microwave signal above and below threshold.

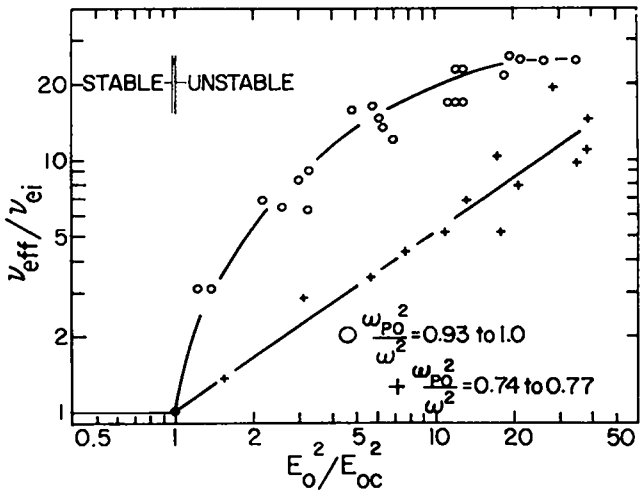

Fig. IV-10.
Normalized effective collision frequency as a function of the ratio of pump to threshold power.

linearly excited Trivelpiece-Gould wave itself acts like the pump wave for the parametric decay process. The appearance of the second lower side band may indicate a cascade process in which the first side band triggers a parametric decay instability.

A similar spectral distribution was observed in the spectral analysis of the microwave power transmitted through the resonator when $(\omega_{po}/\omega)^2 \leqslant 1$.

5. Strong-Field Resistivity and Anomalously Heated Electrons (H. Dreicer, R. F. Ellis, and J. C. Ingraham). Retarding potential probes have been used to monitor the time-of-flight, charge, and energy of various plasma particles after they have been subjected to the pump electric field in the resonator. Above threshold, we find a pulse of particles that persists as long as the microwave pulse persists and that consists of electrons that have been anomalously heated to as much as 40 to 80 times their ambient temperature. From their radial distribution and the measurement of $\Delta(1/Q)$, we can quantitatively deduce an effective collision rate ν_{eff} in the unstable strong-field regime provided wave leakage is absent. For reasons described in Sec. IV.B.4, this procedure is restricted to $(\omega_p/\omega)^2 < 1.2$. The ν_{eff} deduced, normalized to ν_{ei}, is shown in Fig. IV-10 as a function of the ratio of the square of the electric field in the resonator to the electric field at threshold. Note that the dependence of ν_{eff}/ν_{ei} on $(E_o/E_{oc})^2$ depends on whether the plasma density corresponds to the threshold minimum, $0.93 \leqslant (\omega_{po}/\omega)^2 \leqslant 1.0$, or to the steeply rising portion $0.74 \leqslant (\omega_p/\omega)^2 \leqslant 0.77$ (see Fig. IV-6). This strong dependence is mirrored in several other observations related to anomalous heating. For example, we find that the energy distribution F(E) of hot electrons develops a peak for large enough $(E_o/E_{oc})^2$ provided the plasma density corresponds to the threshold minimum. No such peaks are produced at the lower density, which corresponds to the steeply rising portion of the threshold curve. An example of F(E) distributions observed at $(\omega_p/\omega)^2 = 0.94$ is shown in Fig. IV-11 for three different electric fields above threshold. Another observation whose behavior is strongly dependent upon density is related to power balance. From the current of hot electrons collected by the cold end collector C (Fig. IV-1) as a function of retarding potential, we compute the total power, P_{HOT}, which appears in those hot electrons whose energy is greater than about 2 eV. When this quantity is compared to the total microwave power anomalously absorbed, P_{ANOM}, we come much closer to achieving power balance for the plasma densities corresponding to minimum threshold. This balance is illustrated in Fig. IV-12 as a function of $(E_o/E_{oc})^2$. Figure IV-13 illustrates a similar strong density dependence for ν_{eff}/ν_{ei} and the average hot electron energy U_{AVG} for a single value of $(E_o/E_{oc})^2$. The increase of U_{AVG} with increasing $(\omega_{po}/\omega)^2$ suggests that electron heating is at least partly due to trapping of electrons in the electrostatic potential of the unstable waves because their phase velocity increases as $(\omega_{po}/\omega)^2$ approaches unity. This conclusion is discussed in more detail in the following section (Sec. IV.B.6).

Analysis of our data shows that the density of hot electrons above 2 eV does not exceed 1% of the ambient density for the range of electric fields available in our work. However, we find that this density increases sharply with increasing (E_o/E_{oc}).

When near power balance is achieved (see Fig. IV-12), we conclude that, in the anomalous absorption process, a

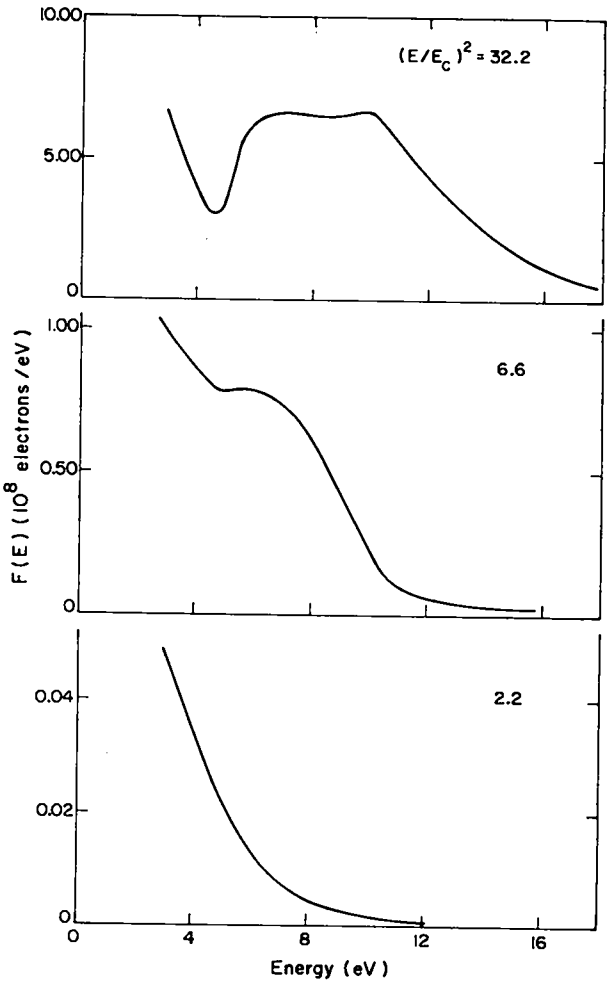

Fig. IV-11.
Hot electron energy distribution functions for three different powers.

small fraction of the electrons gain all of the energy transferred and are heated primarily in the direction of the applied electric field.

6. Computational Study of Parametric Instability Properties (J. C. Ingraham). We are using the computer code developed by Freidberg and Marder[4] to study those properties of the parametric decay and oscillating two-stream instabilities required for comparison with our experimental results. The code calculates the response of an infinite homogenous plasma to a uniform oscillatory electric field, $E_0 \cos \omega t$. Linearized electron and ion Vlasov equations, supplemented by particle-conserving collision terms, are the starting point for the self-consistent solution of the problem.

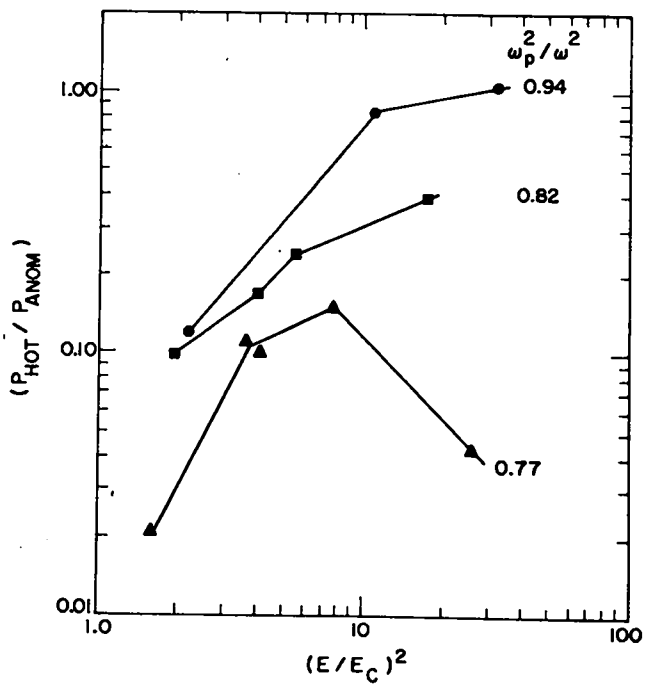

Fig. IV-12.
Ratio of hot electron power to microwave power absorbed as a function of pump power ratio.

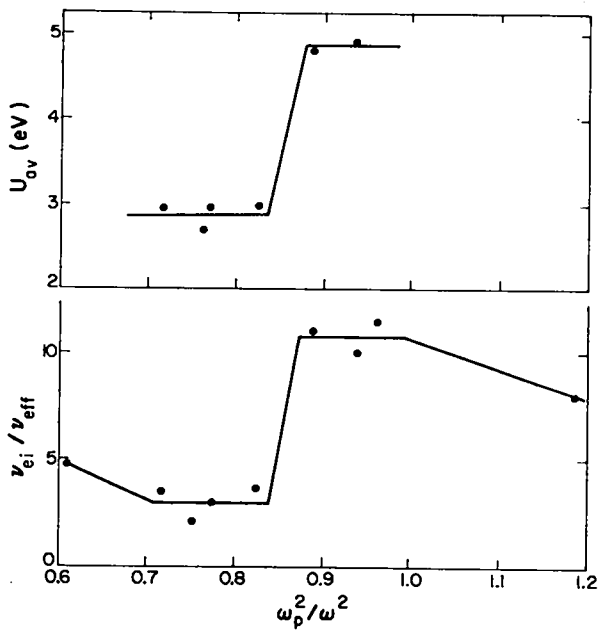

Fig. IV-13.
Average hot electron energy and normalized effective collision rate as a function of ω_p^2/ω^2.

A typical series of computations has produced the threshold curve that is compared with experimental data in Fig. IV-6. In these computations, we assumed the electron collision rate to be equal to the rate we measured in weak fields (Sec. IV.B.2). Ion collisional wave damping was ignored compared to Landau damping of ion waves. This is a good assumption because in our experiment $T_e \cong T_i$ (= 2250°K). The computer solutions show that for our experimental conditions the electric field thresholds for the parametric decay and oscillating two-stream instabilities are for all practical purposes equal in the range $0.7 < (\omega_{po}/\omega)^2 < 0.98$. For $(\omega_{po}/\omega)^2 < 0.7$, the parametric decay instability has the lower threshold, whereas for $(\omega_{po}/\omega)^2 > 1$, it cannot exist. In the overdense region only the oscillating two-stream instability is possible, although its threshold is very large.

As Fig. IV-6 shows, we observe the threshold electric field to be somewhat smaller than these computations predict. Better agreement is possible in the range $0.9 \leqslant (\omega_{po}/\omega)^2 \leqslant 1.0$ for an assumed temperature ratio T_e/T_i = 2, but this increase in electron temperature does not alter the theoretical threshold for $(\omega_{po}/\omega)^2 < 0.8$ where some discrepancy remains. Of course, nonlinear effects are not included in our computations, whereas the experimental determination of the threshold field may already involve such effects, as mentioned in Sec. IV.B.2.

The computations show that at threshold for a fixed density, there is a single wavelength λ that is marginally stable, whereas all the other wavelengths are still damped. The corresponding most unstable wave vector, normalized by the Debye length λ_D, is shown in Fig. IV-14 for each of the two instabilities as a function of $(\omega_p/\omega)^2$. Also shown in Fig. IV-14 is the kinetic energy of an electron whose speed equals the phase velocity of these most unstable waves. The marked increase of this kinetic energy as $(\omega_p/\omega)^2$ approaches unity is noteworthy because of the similar experimental observation made about the energy of hot electrons produced by the instability (Sec. IV.B.5). It seems reasonable, therefore, to suppose that some of the anomalously heated electrons obtain their energy as a result of being accelerated by the unstable plasma waves, possibly by trapping the electrons in the potential energy minima of the waves.

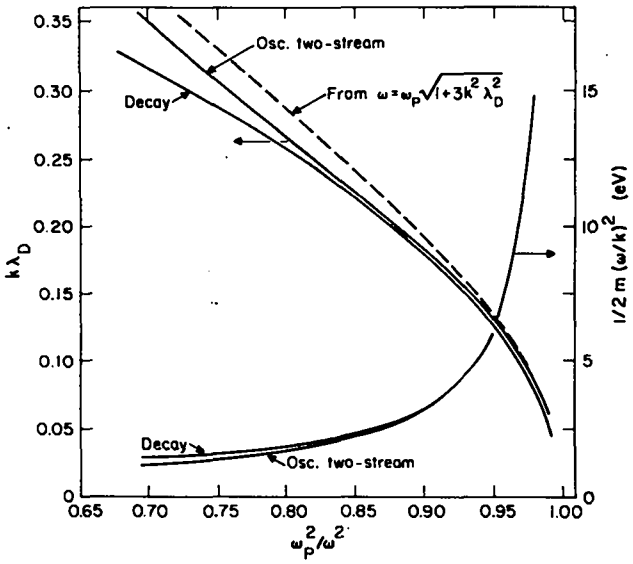

Fig. IV-14.
Normalized wave number for optimum growth and electron energy associated with the optimum phase velocity of the wave as a function of ω_p^2/ω^2.

REFERENCES

1. Status Report of the LASL Controlled Thermonuclear Research Program for a 12-Month Period Ending October 1971, Los Alamos Scientific Laboratory report LA-4888-PR (February 1972), p. 77.

2. H. Dreicer, D. B. Henderson, and J. C. Ingraham, Phys. Rev. Lett. 26, 1616 (1971).

3. J. M. Dawson and C. R. Oberman, Phys. Fluids 5, 517 (1962).

4. J. P. Freidberg and B. M. Marder, Phys. Rev. 4A, 1549 (1971).

V. IMPLOSION-HEATING EXPERIMENT

(J. E. Hammel, I. Henins, J. Marshall, and A. R. Sherwood)

A. Introduction and General Requirements

Preparations are being made for an experimental program aimed at the study of fast implosion heating in θ pinches. The program has two objectives, one scientific and one developmental. Scientifically, the purpose is to learn more about the physical processes involved in the initial implosion process. Developmentally, the object is to find ways of enhancing the amount of implosion heating. This requires the application of a higher initial electric field than has been θ-pinch practice in the past with faster risetimes to moderate magnetic fields of 10 to 20 kG. In principle, this would be followed by staging with slow energy sources to higher magnetic fields. The slow compression provides adiabatic heating beyond the temperature achieved in the initial implosion. By heating to higher initial temperature in the implosion phase, the amount of adiabatic compression required can be reduced and the plasma can occupy a larger fraction of the tube diameter so as to improve the effectiveness of wall stabilization.

The scientific aspect of implosion heating in θ pinches has been somewhat neglected in the past. This has been due to several causes. First, observations were difficult because of electrical transients accompanying the switching-on of the pinch current, second, the primary interest was in the containment of hot plasma 2 μsec and more later, and third, ordinary θ pinches are so small in diameter that there is only marginally sufficient time and space for the development of a well-defined implosion piston. Consideration of the possible development of θ pinches to the stage of feasibility demonstration has shown that it would be advantageous to achieve higher temperatures in the initial implosion. There are serious technical problems associated with the much higher electric fields that will be required, and it may be necessary to use some trick such as multiple pulses. Schemes for this are based on theoretical models having little experimental verification. Hopefully, this experiment will improve this situation.

Superficially the experiment resembles the collisionless shock experiments that have been carried out over the past few years at other laboratories (Garching, Jülich, Maryland, and NRL). Following their practice the discharge tube will be ~40 cm in diameter and 1 m long. The unusually large diameter for a θ pinch is intended to allow time and distance for study of the implosion process. This diameter has the inconvenient effect of requiring higher total voltage to be applied to attain the same electric field at the inside tube wall. In addition, a higher electric field is desired than has been used in θ pinches in the past. LASL θ pinches, which have generally used faster implosion than those elsewhere, have had electric fields of about 1 kV/cm with no plasma. Scylla IA has been operated as high as 1.2 kV/cm. The presence of plasma tends to reduce the initial electric field, which is zero inside the plasma if it is assumed to be a perfect conductor. The implosion-heating experiment is being designed to apply a field of 2 kV/cm to the inside of the tube with a perfectly conducting plasma containing 10^{15} deuterium ions per cm^3. Using a 40-cm-diam coil calls for 250 kV around the tube. The voltage is mainly the $\dot{I}L$ produced by the rapid change of inductance as the plasma implodes away from the wall of the discharge vessel. Initially, the rate of change of inductance, $\dot{L}$, is proportional to the radial velocity of the current sheath, and therefore is proportional to the driving magnetic field or the current in the coil. It is also inversely proportional to the square root of the plasma density, and therein lies the main difference between this experiment and the various collisionless shock experiments. The densities there have been of the order of 10^{11} to $10^{12}/cm^3$, whereas here it will be $10^{15}/cm^3$, so as to apply to LASL θ-pinch conditions. The higher density reduces the effective impedance of the plasma and thus requires a lower impedance current source than has been the practice in collisionless shock experiments. Using a 1-m-long coil, 40 cm in diameter, and a $10^{15}/cm^3$ fully ionized deuterium plasma, and assuming a bounce model, the plasma impedance at 800 kA is about 0.3 Ω. The bounce model assumes elastic reflection of ions from the imploding current sheath. If the ions are trapped in the imploding sheath by some inelastic process, so as to require a snowplow model, the impedance would be larger by $\sqrt{2}$.

The 1-m coil length has been arbitrarily chosen, as it was for the collisionless shock experiments, as a convenient length for construction and diagnostics. Neither it nor the coil and tube diameter of 40 cm is considered fixed. The 800-kA design current (10-kG magnetic field)

implies small magnetic forces, so that a relatively flimsy, easily changed coil structure is allowable. One meter is long enough so that no large fraction of the ions should escape from the ends during the implosion. The coil would have to be much longer for electron transport effects through the ends to be negligible during the implosion; this problem will have to be lived with. One meter is also convenient for diagnostic access through the ends.

The current pulse producing the implosion has been chosen to be as fast rising as possible, essentially flat topped, and lasting for about 500 nsec. The 500-nsec pulse length is chosen to allow time for the implosion to reach the axis. A somewhat longer time might be convenient for extended diagnostics on the compressed plasma, but longer times generally imply more energy and greater technical difficulty.

B. Preionization

Intimately connected with any experiment on implosion heating is the question of preionization. Here again the motivation is both scientific and technological. In the technological sense, a preionization system is useless unless it can be applied to long or perhaps toroidal θ pinches in the future. This eliminates the use of xenon-injected Z pinches beyond the ends of the coil for ultraviolet preionization, as at Garching. However, for scientific purposes, it is important to understand the effects of preionization, and to be able to control and measure the degree of preionization, whether or not the method can be used in a feasibility demonstration. No serious effort has gone into planning for the preionization of the experiment. Although the problems are quite important, we feel they must be deferred until a feasible high-voltage pulse generator can be developed and built. The initial preionization system will probably be a low-power Z pinch applied between electrodes beyond the coil ends.

C. The Search for a Pulse Generator System

Until June 1972, or for about eight months, several different conceivable high-voltage pulse-forming systems were evaluated and compared as to feasibility and performance for driving the implosion-heating experiment. The systems considered were, more or less chronologically, (1) Mylar-insulated stripline Blumlein generators immersed in water for voltage grading, (2) simple Mylar stripline systems, (3) combinations of Mylar striplines with capacitors, (4) coaxial transmission lines insulated by water, (5) capacitors, (6) lumped-constant transmission lines, and (7) lumped-constant abbreviated transmission line sections that use transfer capacitor effects from fast pulse charging. The last system was picked as being the least inconvenient to build, considering limitations of space, money, and in-house technical experience.

All systems were investigated by computation, with the plasma load simulated by assuming it to be a thin, perfectly conducting sheath, imploding at a velocity given by the bounce model, $2\rho v^2 = B^2/8\pi$. The calculations are outlined in more detail in Appendix V-A. The model used took no account of ions (near the outside of the tube) that would bounce more than once because of piston acceleration. This may be quite important in the structure of the real θ-pinch sheath, but should not affect the electrical characteristics violently. In general, we have neglected the possible effects of less-than-perfect preionization near the outside, a situation that is likely to arise in practice and that might have the effect of forming the sheath away from the wall. This would appear as an increase of initial inductance and would slow down the rise of the current.

1. Stripline Generators. The difficulty with all of the stripline generators boils down to the great bulk that the line must have. To generate the desired 0.5-μsec pulse length, the line has to be about 43 m long, and to reduce the impedance to a level commensurate with that of the plasma, the line has to be about 5 m wide. To fit into the available space the line must be folded both longitudinally and transversely. It appears to be dangerous to try to apply such high voltage to one feed slot in a θ-pinch coil ($\geqslant$ 250 kV with plasma, ~500 kV with no preionized gas filling). A reasonable arrangement appears to be four feed slots, each having one-quarter the insulation thickness required for one feed slot. Each line would have one-quarter the impedance of the single line, but the total souce impedance would be the same, with four lines in series. Thus, there would be four doubly-folded lines each immersed in a tank of water for voltage grading. Because of the large volume of Mylar insulation contained in each tank, and because there are a few tens of kilojoules stored in each, the damage resulting from a fault would probably be large. Keilhacker at Garching uses such a system, but because he operates at considerably higher impedance, having lower plasma density, he does not have to fold the line transversely.

There appears to be no great advantage in the Blumlein generator configuration. It provides voltage doubling, but at twice the impedance, because it amounts to two transmission lines in series at each feed point. If it is made of Mylar striplines it shares the problems of other stripline systems, aggravated by additional complexity.

2. **Water-Insulated Transmission Lines.** Following a suggestion of K. Prestwich at Sandia Corporation, the possibility of using water-insulated transmission lines was investigated. Water lines have the advantage of a slow wave velocity so they can be short enough to fit into the available space without folding. The difficulty is that, because of the low dielectric strength, a large spacing between conductors must be used, thereby raising the line impedance. The dielectric strength of water in the amounts required here is such that it appears barely possible to design for 50 kV/cm for 1-μsec exposure time. To achieve the desired low impedance for a two feed-point system it seemed necessary to use coaxial lines with a diameter considerably larger than the head room of the available space, or more reasonably, a number of smaller lines in parallel. When the water-line concept was finally abandoned each of two feed points was to be fed by nine lines in parallel, each line about 50 cm in diameter and separately switched with a spark gap where it connected to a coil-feed collector plate. Each line was to be ~8 m long, although there appeared to be some chance of adequate performance with shorter lines by exploiting the effects of fast charging. The main difficulties with water lines were: (1) inadequate dielectric strength resulting in an unacceptably high probability of a fault, (2) the probability of serious damage if a fault did occur, (3) the large bulk, and (4) the requirement for considerable development work outside the previous area of competence of the Laboratory.

3. **Fast Pulse Charging.** A useful result of the investigation of water-line systems was the idea of using fast pulse charging to augment the current delivered by a line. Pulse charging is necessary with water lines because of the relatively large conductivity of even the purest water (~5-MΩ cm with continuous deionization in stainless steel systems). A capacitor insulated by such water has an RC time constant of ~35 μsec. Fast pulse charging (~1 μsec) is a great advantage because the dielectric strength varies inversely as the cube root of the effective exposure time. Clearly, if a pulse-forming network is charged in 1 μsec and discharged in 0.5 μsec, the charging current is a respectable fraction of the discharge current and, if it can be added to the discharge current, can augment the load current in a useful way. The effect is similar to the operation of a peaking capacitor (transfer capacitor) system. Fast pulse charging can extend substantially the pulse length from a pulse-forming line or allow the use of a considerably shorter line.

4. **Lumped Constant Line.** F. L. Ribe and A. R. Sherwood visited and consulted with J. C. Martin and his staff of AWRE, Aldermaston. They provided considerable advice both on the design of water-line systems and the design of a lumped-constant line system using commercial capacitors. The lumped-constant line approach almost certainly could have led to a practical system. A number of line modules would have been connected in parallel to each of several coil feed points, each one switched by an individual spark gap, as would have been the case with water lines. The small lumped-constant line modules made it possible to develop the major parts of the system on a small scale, build a number of them, and connect them together to construct the machine. Each module was to contain twenty 100-kV plastic-case capacitors available from Maxwell, perhaps with modifications suggested by Martin. The capacitors, a narrow stripline forming the inductive elements of the transmission line module, and a spark gap were to be enclosed in a gas-tight box pressurized with SF_6 to provide protection against flashover. However, this system would have been quite expensive because of the large number (~400) of capacitors required.

5. **Final System.** The system finally selected for the main high-voltage pulse generator is a hybrid of a peaking capacitor system with a curtailed, lumped-constant delay line. It uses commercial capacitors of a type used in the Scyllac preionization system which are designed for 70-kV dc charge voltage and 120-kV pulse voltage. These are the conditions encountered in Scyllac service, where the capacitors are connected across the coil terminals and undergo surge voltages that almost double when the main bank is fired. We believe these capacitors can be obtained at any reasonable fraction of their standard 0.7-μF capacity with no degradation of voltage hold off and current-carrying capacity, and with no serious increase in inductance. Less capacitors are required here than for the lumped-constant line system discussed above because of the larger energy storage of each capacitor. However, to reduce the inductance sufficiently to achieve the desired risetime, the capacitors are reduced in capacity and several are used in parallel.

The system is conceived as using four coil feed points with a nominal 125 kV per feed point, totaling 500 kV. Each feed point would be energized by a two-element lumped-constant line as shown in Fig. V-1. This lumped-constant line is formed by two groups of the aforementioned Scyllac capacitors connected directly into a collector-plate transmission line system, with the two groups being separated by an extra inductive line section. The circuit uses fast charging from Marx generators through the inductance of the Marx generator and of the connecting cable system. This fast high-current charging is an essential part of the system. At the peak load current of 800 kA about 300 kA is contributed by the Marx

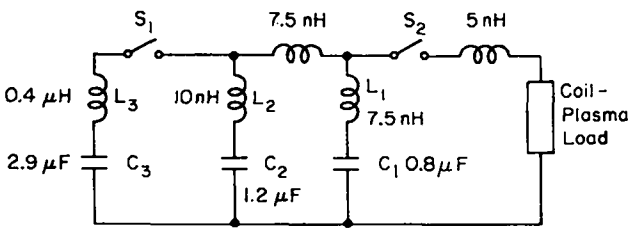

Fig. V-1.
The capacitor pulse-forming high-voltage generator. One such generator is required for each coil feed point.

charging current and 500 kA comes from the capacitors forming the lumped-constant line. The capacitors of the pulse-forming network can be reverse charged if the experimenter desires. Figure V-2 shows the calculated current as a function of time for the 30-kV reverse charging. With no reverse charging the load current begins to fall off somewhat sooner, thereby causing a current pulse with less of a flat top. The load switches are fired when the voltage on the pulse-forming network reaches 125 kV. This occurs shortly after peak charging current from the Marx supply and while the voltage is still rising rapidly. There is an element of danger here in that a delay of switching would result in overvolting the system. Protection against this will be provided by solid dielectric spark gaps arranged to dump the system if the voltage rises above 130 kV.

This system has been studied extensively using the NET-2 computer code available at LASL. This program performs nonlinear transient analysis of complicated networks and is capable of handling time-dependent nonlinear impedance elements. By coupling the equation for the plasma motion into the circuit analysis, we can include the effects of the varying inductance of the imploding plasma. The assistance of G. P. Boicourt (LASL Group P-16), who has been using NET-2 for analysis of Scyllac circuits, was invaluable in this work. A further discussion of these calculations is given in Appendix A.

Each of the four high-voltage pulse generators will be connected to the coil through two parallel-connected load switches. These low-inductance multichannel spark gaps will be rail gaps purchased from Physics International (P.I.). They are being developed from a rail-gap design used by P.I. to switch water-immersed, Mylar-insulated striplines. They have been used in the past under water, but are being modified by P.I. to operate in a LASL atmosphere (59 cm of mercury) of freon. Although the freon introduces mechanical design problems, it probably solves some problems in that the coil feed points can also be immersed in freon, thus alleviating insulation flashover problems there as well. A prototype rail gap will be tested for performance before a complete set is ordered.

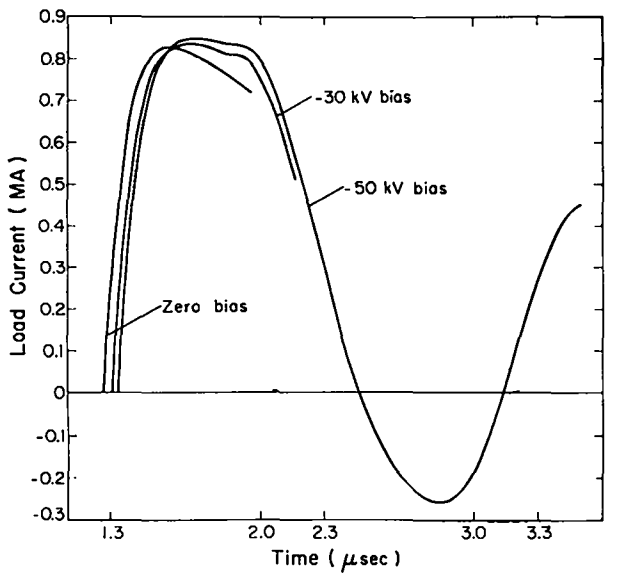

Fig. V-2.
The load current for the circuit of Fig. V-1. The bias voltage, if any, is applied to C_1 and C_2.

D. Diagnostics

Diagnostics, including probes, interferometry, etc., will be similar to those used on other plasma experiments. We will not enumerate them here; however, there are certain problems that are peculiar to this experiment because of its short time scale and high voltage. One problem that has already arisen is voltage measurement. A major part of the plasma diagnostics will probably be undertaken by workers from the established θ-pinch group in the Laboratory.

Because of good access through the ends it appears that, at least initially, no observational ports will be required through the sides of the discharge tube or the coil. This is fortunate because they might aggravate an already difficult situation with extra high-voltage insulation.

E. Chronology

Preliminary plans for the implosion-heating experiment were started in October 1971. These plans were originally purely conceptual and computational. The experimental space available, which previously had been used for the

quadrupole-injection experiment, was too small. We relocated the control functions next to the screen room in what had been a small ancillary laboratory and cut through a connecting door. This gave us a reasonably clear space of ~13 by 8 m with a clear height of 3.26 m. A new control system was designed, constructed, and installed.

The first high-voltage installation was a 200-kV, 90-kJ, ignitron-switched Marx generator. For economy reasons we used the standard 20-kV capacitors procured about 15 years ago for the Zeus bank. This was used to test out some design ideas for Marx generators and as a voltage source for high-voltage testing. It was apparent from the beginning that Marx charging would be used to drive the experiment no matter what system was decided on for the high-voltage pulse generator. A second Marx generator was designed using experience gained from the first design. It was brought into operation in November, tested, and found to be satisfactory as a standard module for pulse charging the final machine. The Marx generator is described in Appendix V-B.

The completion schedule has been delayed because of a lack of funds. The original completion date of the high-voltage system and initial operation of the experiment, perhaps with rudimentary preionization and diagnostics, was July 1, 1973. However, only about one-half of the estimated major procurement funds will be available in FY 1973. Therefore, it has been decided to build a half system initially, that is, feeding the coil at two instead of four points. No great inconvenience is caused by this necessity because capacitors and spark gaps can be split into orders to be delivered before and after the beginning of FY 1974. Initial operation will probably be undertaken with a 20-cm-diam tube instead of the ultimate 40-cm-diam tube. Initial operation and debugging of the high-voltage pulse systems can be undertaken with two instead of four systems, which will probably be an advantage. Ultimate full-scale operation of the experiment will probably be delayed, but not very seriously.

F. High-Voltage Technology

Along with the study of the main pulse-forming system discussed above, much work has been done to develop facilities, equipment, skills, standard practices, components, etc., which are necessary to enter the field of extra high-voltage technology. A few particular items that we have worked on are: field-distortion spark gaps for Marx generators, stabbed-polyethylene solid-dielectric switches arranged to break down at definite voltages, voltage gaskets to form high-voltage insulating junctions between insulators, investigating the electrical strength of the interface between water and various insulators, voltage dividers for measurement of high voltages with fast risetimes, high-voltage fast-rising trigger systems, and electrolytic resistors both as components of high-voltage systems and as diagnostic elements. Some of these items are discussed in more detail in Appendixes V-A through V-E. It has also been necessary to construct a reliable control system, including high-voltage power supplies for bank charging and a quiet screen-room system with appropriate oscilloscope facilities.

APPENDIX V-A

CALCULATIONS OF THE PERFORMANCES OF VARIOUS HIGH-VOLTAGE GENERATORS

I. Design Parameters and the Model for the Plasma

Considerable effort has been expended making calculations of the performance of several types of high-voltage generators for the implosion-heating experiment. Initially, these calculations were done with a desk calculator, but later the NET-2 code was used. The main problem is to solve the circuit equations for the generator, taking into account the changing of the generator's load due to the motion of the imploding plasma sheath. The sheath dynamics were always calculated using the bounce model, which assumes perfect elastic reflection of all ions from the impinging magnetic piston. We assumed the plasma to be perfectly ionized initially and to be distributed uniformly throughout the vacuum vessel within the volume enclosed by the θ-pinch coil. The initial plasma density was usually taken to be 10^{15} cm^{-3}. The coil was 1 m long and had a 0.20-m radius. The initial plasma radius was usually taken to be 0.18 m, so that 2 cm of radius was allowed for the interior coil insulation and the thickness

of the vacuum vessel. The implosion of the sheath was stopped suddenly and fixed in position when the sheath reached one-third of its initial radius because for the simplest model, the first ions from the other side of the plasma begin to collide with it at this position.

To produce ions having energies of about 2 keV, it is desired that the driving magnetic field have a strength of about 10 kG. This requires a coil current of 800 kA, one of our primary design goals. According to the bounce model, the ion transit time (from the imploding sheath radially through the axis and on to the sheath at the opposite side of the tube) is about 500 nsec for a 10-kG driving magnetic field and an initial density of 10^{15} cm^{-3}. The current should last at least 500 nsec in order to observe the effects of this second collision of the ions with the sheath. Plasma simulation studies of this problem, also based on the bounce model and conducted by members of LASL Group P-18, indicate that if the magnetic field rises in a time much slower than about one-fifth of the ion transit time a serious degradation of the ion energy achieved is to be expected. Thus it is desirable that the current rise in about 100 nsec or less.

II. Generators Based on Transmission Lines

The first calculations were for various Mylar-insulated stripline configurations. Initially, ideal transmission lines were assumed. Figure V-A-1 is typical of the results obtained. This figure shows the coil current, the sheath radius, and the voltage around the inside surface of the vacuum vessel plotted as a function of time for a generator that has a characteristic impedance of 0.4 Ω, charged to 500 kV, and switched at the load end (so that no voltage doubling occurs). In later calculations the skin effect due to the finite conductivity of the transmission line was taken into account. We used the Laplace transform technique as the analytical method, and included the effect of the changing inductance with current penetration as well as the usual change of resistance. For a copper stripline having a length of 100 m, the degradation of the current pulse due to the skin effect is noticeable; however, for copper striplines of 40-m length, the skin effect is quite small.

Calculations were also done for transmission lines using water as the dielectric. As with the Mylar striplines, the load current was calculated using the transmission-line equations with the skin effect included. The skin effect in the case of water lines was completely negligible. Figure V-A-2 shows the load current for an 8.4-m water line.

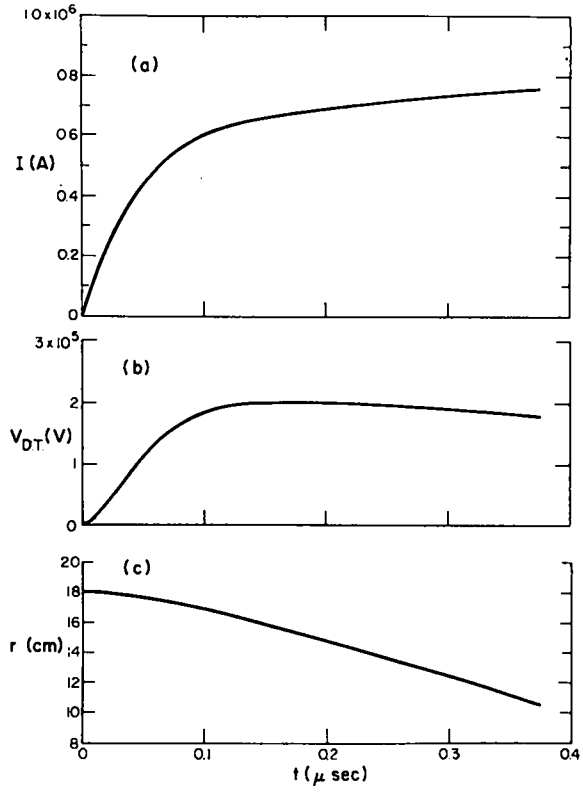

Fig. V-A-1.
The load current, the total voltage around the inside surface of the vacuum vessel, and the sheath radius for a 500-kV stripline generator having a characteristic impedance of 0.4 Ω.

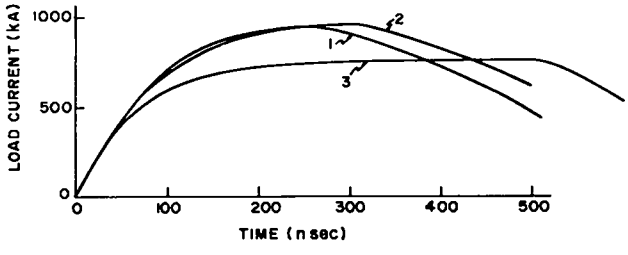

Fig. V-A-2.
Load current for a generator composed of a 125-kV water line at each of two feed points. Each water line has an impedance of 0.35 Ω.
Curve 1: length of each line - 4.2 m
Marx current per line - 320 kA
Curve 2: length of each line - 5.0 m
Marx current per line - 320 kA
Curve 3: length of each line - 8.4 m
Marx current per line - 0 kA

III. Use of Charging Current to Augment Load Current

In most high-voltage generators based on transmission lines it is advantageous to use pulse charging. Pulse charging is required for water lines because the dielectric strength of water is time dependent and because of the low shunt resistance. The usual technique is to close the switch between the high-voltage generator and its load when the pulse-charging current is near zero and the line is at maximum voltage. Our analysis has shown that for our application it is an advantage to switch at the time of maximum charging current so that the charging current supplements the discharge current of the transmission line. When applied to water lines this latter technique yields two advantages: (1) for the same voltage on the line, the peak load current is higher, and (2) for a given current pulse-length, the transmission line becomes shorter. The disadvantages are that the source of the pulse-charging current must have a reasonably low inductance (less than 0.5 μH for the Marx banks in our design), and the transmission line will be overvolted if the load switch is not closed at the proper time.

IV. Capacitor Pulse-Forming Network

The design finally chosen for the high-voltage generator resulted from the application of the fast pulse-charging technique described above to a lumped-constant transmission line. The circuit that evolved from these calculations is shown in Fig. V-A-1. This circuit represents the capacitor pulse-forming network that connects to each coil feed point, thus four high-voltage generators are required. In the search for this circuit, certain parameters were held fixed. These are: the 125 kV rating on the fast capacitors, a 30-nH series inductance per capacitor, the inductance of the load switch, and the fixed portion of the load inductance. All these inductances were chosen to be fairly low, but achievable in the proposed design. The other circuit parameters were varied until a suitable load current was obtained. These computations were done by G. Boicourt (LASL Group P-16) using NET-2. Figure V-A-2 shows the load current as a function of time for three possible initial bias voltages on the fast capacitors (C_1 and C_2). The load current rises to a value above the desired 800 kA in a time as short or shorter than that

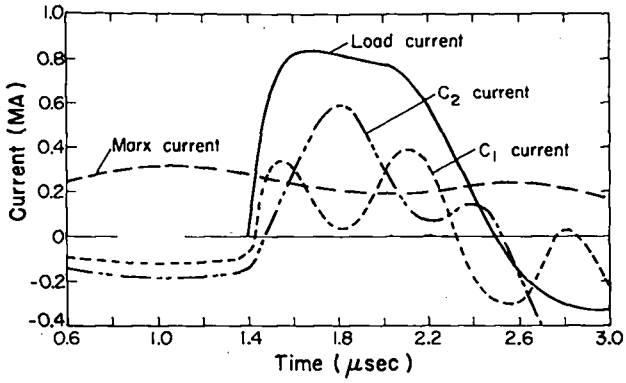

Fig. V-A-3.
Various currents for the circuit shown in Fig. V-1. Zero in time corresponds to the closing of switch S_1.

obtained from any of the proposed transmission-line high-voltage generators. There is some advantage to be gained by using an initial reverse bias voltage. Figure V-A-3 shows the load current, the pulse-charging current, and the currents in the branches containing C_1 and C_2 for the -30-kV-bias voltage. Zero in time in these figures refers to when switch S_1 is closed.

More detailed calculations for the circuit of Fig. V-1 are being made. These include (1) calculations of the average ion energy resulting from the sheath implosion, (2) extending the calculation of the sheath dynamics to longer times by taking into account the effect on the sheath of its collisions with accelerated ions, (3) the effect of possible piston formation away from the wall of the vacuum vessel because of poor preionization, (4) the effectiveness of various overvoltage protection switch designs, and (5) the voltages that would result for various types of misfire of the high-voltage generator. All of these calculations are being done with NET-2 and use the bounce model for the sheath. One preliminary result of these calculations is that the ion energy for the calculated current pulse shape is about 78% of what would be obtained from an ideal step pulse. Another is that if the sheath initially forms 1 or 2 cm away from the vacuum vessel, the ion energy is degraded by 73 or 69%, respectively.

APPENDIX V-B

MARX GENERATORS

From the numerical calculations for the high-voltage generator, presented in detail in Appendix V-A.I, it was determined that the total inductance of a Marx generator and its connections to the capacitor pulse-forming network should be 0.4 μH or less. A higher inductance than this value makes it difficult to achieve the necessary current from the Marx generator. To attain an inductance this low we plan to use two Marx banks in parallel to feed each of the capacitor pulse-forming networks. Thus, for the complete four coil-feed high-voltage generator, eight Marx banks are required. These banks are to be constructed from 20-kV, 14-μF Zeus capacitors and are designed to operate in air.

One such Marx bank has been constructed for temporary use as a high-voltage source for component testing. It consists of six 40-kV stages. Each stage consists of two capacitors in series housed in a steel box, with the capacitor cans connected electrically to the box. The boxes are stacked up (with insulation) and provide the mechanical structure of the bank. This arrangement allows easy replacement of the capacitors, yet requires only a minimum of floor area. The discharge current of this design follows the low-inductance path, largely on the surfaces of the boxes, and is shown in Fig. V-B-1. An electrical diagram of the bank is shown in Fig. V-B-2. The connection between a Marx bank and a capacitor pulse-forming network will be a sheaf of perhaps twenty RG/17-14 coaxial cables. The skinned-back portion of the cables will be brought down the side of the Marx bank so as to simulate a parallel-plate transmission line. The inductance of this cable connection scheme is anticipated to be about 50 nH.

Three stacks of electrolytic resistors are used in the charging circuit of this Marx bank. These resistors are all labled R_c in Fig. V-B-2. The center stack is for the purpose of holding all the midpoints of the capacitor pairs at the same potential during charging. Higher resistance electrolytic resistors, R_T, are used in the trigger circuit. The high capacitance of these resistors improves the coupling of the trigger pulse to the spark gap.

Figure V-B-3 shows the design of the field-distortion spark gaps used in this Marx bank. This gap uses a midplane ring trigger electrode with a sharp-edged hole in it.

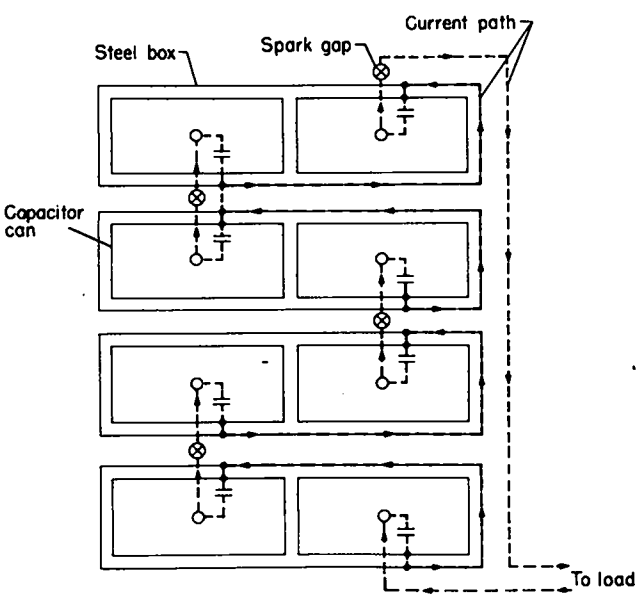

Fig. V-B-1.
The discharge current path for the prototype Marx bank.

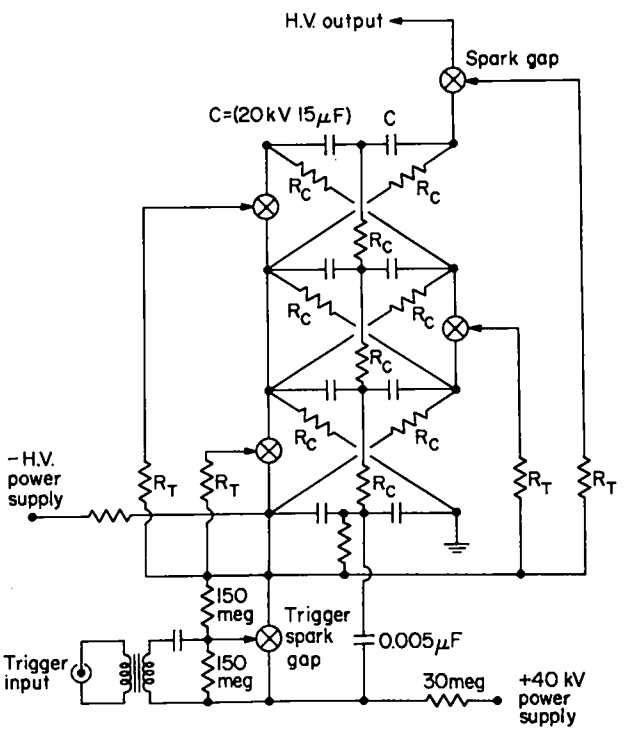

Fig. V-B-2.
The electrical circuit of the prototype Marx bank.

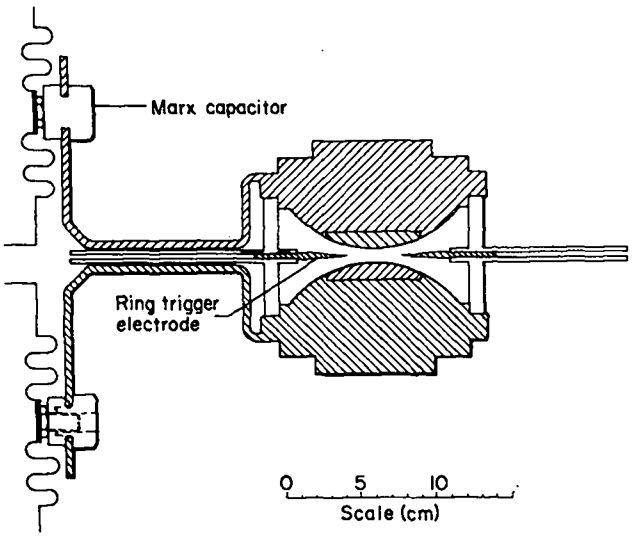

Fig. V-B-3.
The field-distortion spark gap used in the prototype Marx bank.

A 40-kV trigger pulse, provided by discharging a 0.01-μF capacitor into the trigger resistors through a small auxiliary spark gap, is applied simultaneously to all the trigger electrodes. The trigger electrodes are made of brass, and the main electrodes are modified standard Scyllac gap electrodes with tungsten alloy centers. The spark gap insulator is made in two halves; each half is a section of acrylic tubing glued to a 1/8-in.-thick acrylic sheet to form a "hat," as shown in Fig. V-B-3.

The Marx bank has been discharged into a short circuit load. Under this condition the maximum current was 300 kA. The first half-period of this ringing discharge current was 3.4 μsec. Using the 3.4-μsec figure, the inductance of this shorted six-stage Marx is calculated to be 956 nH. In the experiment itself, this Marx will only have five stages; thus this design seems to be about right for the requirement of 800 nH per Marx bank. Because no serious difficulties were encountered in this short-circuit load test, and because the experimental requirements are less stringent (e.g., lower voltage and lower current), we conclude that this design is probably adequate for our purposes.

In addition to the Marx bank, we have another that was constructed earlier and consists of ten 20-kV stages. This bank also uses the stacked electrolytic resistor arrangement in the charging circuit, but ignitrons are used instead of spark gaps. This Marx bank has performed reliably and is still in use for high-voltage testing; however, because of the long turn-on time for the ignitrons, this bank takes 10 μsec to erect and is therefore unsuitable for the fast pulse-charging of the capacitor pulse-forming network.

APPENDIX V-C

ELECTROLYTIC RESISTORS

Many problems in pulsed high-voltage systems are most conveniently solved by the use of electrolytic resistors. They are cheap, simple, and, with appropriate design, are capable of absorbing large pulsed energies. They can have very low inductance and are particularly convenient for high-voltage applications because of the uniform grading of potential, which they provide. This results in minimal problems with flashover along the outside of insulation tubes filled with electrolyte to make resistors. They suffer from a large temperature coefficient of resistivity, ($\approx -2\%/^\circ C$), which creates problems for precise electrical measurements. In addition, there are problems of corrosion, electrolytic gas generation, and variations of conductivity caused by electrolyte contamination. We have been using electrolytic capacitor-bank dump resistors for years. This is an ideal application because the exact value of the resistance does not matter.

A convenient resistor design uses electrolyte contained in a cylindrical insulating tube of acrylic plastic closed at each end by metal electrodes. Holes in the upper electrode allow communication with a reservoir to allow for thermal expansion and for the escape of electrolytically derived gas bubbles. We have normally used K_2SO_4 solution as the electrolyte with stainless steel electrodes. Resistivities as low as 10 Ωcm can be achieved with slightly more than one normal K_2SO_4 (~100 g/liter, approximately saturated solution). Los Alamos tap water has ~6000-Ωcm resistivity, whereas ordinary distilled water is about 10 times as resistive.

The charging resistors for the Marx generators are conveniently made by stacking electrolytic resistors on top of each other, with small holes in sheet-stainless steel electrodes between acrylic plastic cylinders, so that one reservoir at the top serves the whole stack. With dimensions appropriate to those of the Marx bank (10 cm diam, 20 cm long), resistances from 3 to 300 Ω per resistor section are conveniently obtained. These give RC decay times of ~10 μsec to 1 msec for the Marx voltage after erection.

High-resistance, relatively low-power resistors are made by stoppering the ends of lengths of Tygon tubing with electrodes. Resistors of this kind are used extensively in high-voltage Marx generators elsewhere.

APPENDIX V-D

HIGH-VOLTAGE GASKET TESTS

I. The Capacitor Header Insulation Problem

As mentioned in the main text, the capacitors of the pulse-forming networks will be connected directly into a collector-plate system. It is important that the connection have as low an inductance as practical (i.e., only a few nanohenries), and that the electrical insulation method works very reliably at 125 kV. Away from these capacitor connections the insulation between the collector plates will consist of multiple layers of sheet Mylar. The joint between this Mylar insulation and the insulation of the capacitor header might be accomplished by using an elastomer high-voltage gasket between the bottom Mylar layer and a molded plastic insulation, as shown in Fig. V-D-1. Although the insulation scheme shown in Fig. V-D-1 looks quite promising, it is still being tested and evaluated.

For the preliminary tests of this general insulation configuration, the insulator was not the complicated molded shape shown in the figure, but rather was a "hat" constructed by gluing together acrylic sheet and tubing sections. With a 3/4-in.-wide silicone-rubber high-voltage gasket, difficulties were encountered at 145 kV, namely tracking along the acrylic-oil interface and subsequent breakdown through the acrylic "hat." In this configuration the oil extended only to the top of the capacitor insulator.

In the design shown in Fig. V-D-1 the space between the capacitor insulator and the molded insulator will be completely filled with oil by the technique of vacuum impregnation. We hope that high-pressure injection molding will produce a better quality insulator than the glued acrylic one. In addition, plastics of higher dielectric strength, such as poly-4-methylpentene-1 (TPX), can be used if necessary. The aluminum cylinder, which connects

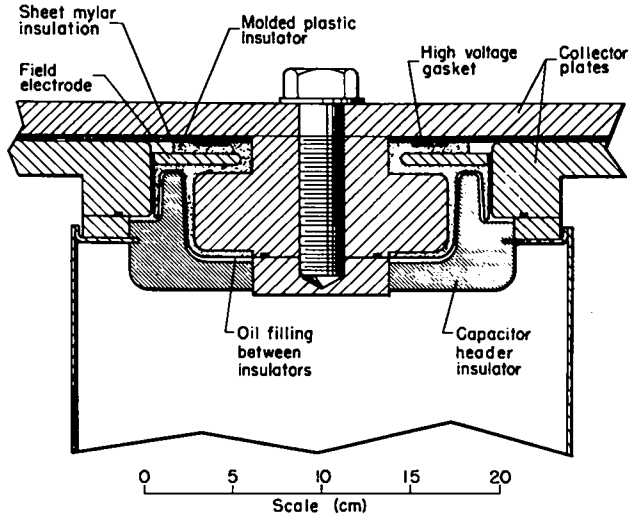

Fig. V-D-1.
The design for the connection of the fast capacitors into a parallel-plate transmission line.

the center electrode of the capacitor to the top collector plate, is made as large as practical to reduce the inductance, and the insulator must be molded onto this cylinder. The large bolt through the arrangement is primarily for making the necessary current joints. The other conductor molded into the insulator, called the field electrode, was found in our tests to be necessary to prevent breakdowns along the gasket surface at about 100 kV; it does this by making the electric field predominantly perpendicular to the flat gasket surface.

II. High-Voltage Gasket Tests

Independent tests of the breakdown strength of silicone-rubber high-voltage gaskets were conducted without the constraint of the geometry of the capacitor header. A diagram of the test apparatus is shown in Fig. V-D-2. In these tests and in the tests mentioned above, the multiple Mylar sheet insulation was simulated by four layers of 0.030-in.-thick polyethylene for convenience. A thin layer of Dow Corning No. 5 silicone grease was applied between each of the polyethylene sheets in the region of the gasket as well as on the gasket surfaces themselves. This was to help prevent voltage tracking between the sheets and along any scratches on the polyethylene surface next to the gasket. A pressure of ~400 psi was applied to the gasket. Under these conditions, breakdown strengths of about 180 and 150 kV were measured for 1-in.- and 1/2-in.-wide gaskets, respectively. Interestingly, the same breakdown strength was obtained by omitting the gasket entirely and just using the silicone grease on the polyethylene sheets. However, for an actual working high-voltage system, we doubt the reliability of this scheme and feel that the elastomer gasket should be used.

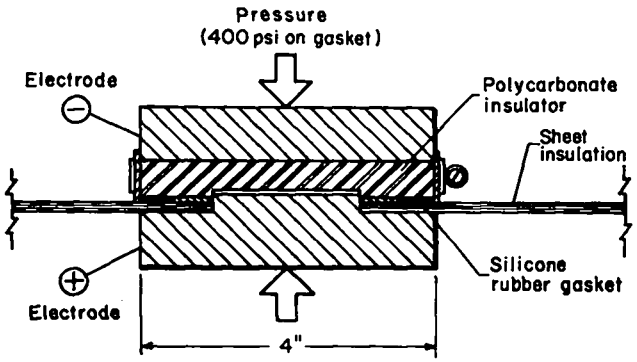

Fig. V-D-2.
The test apparatus for the high-voltage gasket tests.

It is planned that 8 to 10 layers of 0.010-in.-thick Mylar will form the insulation between the collector plates of the pulse-forming network. Using grease between that many layers is messy. Therefore, an investigation was made as to the possibility of gluing the Mylar sheets together in the regions of the interruptions in the Mylar caused by the capacitor connections. The gluing together of the Mylar was accomplished by means of a heat-meltable glue (DuPont No. 46950), which is a polyester similar to Mylar and is supposed to have a dielectric strength of 2700 V/mil. The glue is applied as a solution in an organic solvent (dioxane-toluene), but when the solvent evaporates a film of glue less than 0.001 in. thick remains. The Mylar sheets are then pressed together in a heated clamp (280°F) to make the joints. Mylar sheets glued in this manner have been tried in some of the high-voltage gasket tests mentioned above, and they have worked well. Failures were always due to some other component of the insulation system, e.g., an acrylic hat.

APPENDIX V-E

THE ELECTRICAL STRENGTH OF WATER-INSULATOR INTERFACES

Some experimental work was performed investigating the problem of electrical breakdown at the interface between a coaxial water line and a parallel plate-collector system. This work was done at a time when water-insulated transmission lines were under active consideration for the high-voltage generator. A mock-up was constructed with sheet insulation terminating coaxial cylindrical electrodes, with the central electrode electrically connected to a metal plate extending radially beyond the outer electrode on the other side of the insulation. Such an interface was found to be as electrically strong as the water itself provided the insulation was one thick sheet (3 mm of polyethylene, acrylic, polycarbonate, or PTFE), and there were absolutely no air bubbles present. Multiple sheets of Mylar filled with bubble-free water were marginally acceptable, although they would not have been practical in the end application. When separated by layers of silicone grease they were completely unsatisfactory, puncturing the Mylar-grease sandwich at low voltage on every shot. Ian Smith at P.I. explains this as being caused by the low dielectric strength of the grease. Equally stressed as the Mylar, a breakdown is initiated in a grease layer that, once started, propagates on into the Mylar.

VI. THEORETICAL PHYSICS PROGRAM

A. Summary (W. B. Riesenfeld)

During the past year the mathematical and computational plasma physics group has continued to fulfill its prime programmatic responsibility in providing analytical and numerical support to all experimental CTR programs at LASL, including the Scyllac, θ-pinch, profile-tailored toroidal Z-pinch, and magnetic implosion-heating projects. Special emphasis was placed on the study of plasma equilibrium and stability in complicated toroidal configurations, using MHD or Vlasov models as dictated by the physics of the situation. This study was general enough to include a preliminary assessment of the properties of pinches of noncircular cross sections, such as belt pinches and high-β Tokamak geometries, which may conceivably have a future in the pulsed, high-density approach to controlled fusion. An organizational change early in the reporting year split the theoretical support for the laser-related programs from that of the CTR program, with concomitant transfer of manpower and assignments. The staff of the CTR theory group was proportionally reduced. The present reports are confined to CTR-related work. Laser-related work is now presented in separate reports.

Considerable progress has been made in studying the mode structure and growth rates (or frequencies of stable modes) of general diffuse two-dimensional MHD equilibria. This work, which bears intimately on the choices available for a toroidal scientific feasibility configuration, has provided information both on gross displacement modes and modes localized in the radial dimension. It is a combined analytical and numerical approach based upon Fourier analysis of perturbation functions with subsequent numerical minimization of the potential energy operator. A second major effort on toroidal numerical codes has produced MHD-stable diffuse-profile toroidal Z-pinch equilibria for confined plasmas. These configurations are being checked for their analytic stability properties. The same technique has been applied to investigate configurations with noncircular cross sections. As a result, a promising line of research may be opening up to find systems that maximize the poloidal β without sacrificing other desirable features of the equilibrium.

This year we have also seen progress in the development of a Vlasov-fluid model for a high-β plasma column, which treats the ions as particles following Vlasov trajectories and the electrons as a charge-neutralizing MHD fluid. A new numerical formulation was devised with computational features of great practical convenience, and which is expected to yield exact evaluations of the exponential stability properties of the model. One of the aims of this technique is to augment an existing approximate analytical account of the stabilization of modes with $m \geq 2$ relative to MHD predictions. Equally interesting results are expected in connnection with localized modes.

Various other programs have called for the development of a number of smaller but nevertheless important computational tools. Thus a new two-dimensional Fokker-Planck code has been developed to provide a description of the electron runaway phenomenon for weak electric fields. Interest in this problem was reawakened by new data on the behavior of toroidal discharges, such as the radial current distribution and the presence of enhanced resistivity. Also, a new particle-in-cell fluid code was devised to provide accurate treatment of shocks, contact discontinuities, and rarefactions. This code, which boasts simplicity and excellent numerical stability, is being considered for application to a major design problem. As a third example, an axisymmetric particle-in-cell code was written to simulate the behavior of a linear θ pinch after the ionization and compression phase. This code is in use as a particle and energy bookkeeping tool for diagnosing the performance of the 5-m linear Scyllac θ pinch.

The theory group also supported the design of experimental devices by providing basic engineering computations. Thus design studies were performed for the magnetic mirror end sections of the 5-m linear Scyllac θ-pinch experiment. These studies determined the field distributions and inductances of mirror coils having various cross-sectional shapes and found optimum coil lengths for maximizing the magnetic field on axis of a mirror coil pulsed from a given energy supply. Practical mirror designs were obtained and fabricated. Calculations were also performed on tailoring the primary current at the feed slots of the ZT-1 toroidal Z-pinch device to maintain an axisymmetric equilibrium.

B. Summary of the Scyllac-Related Theory (J. P. Freidberg)

Scyllac theoretical research during the past year has led to some interesting new results. The newest, most

encouraging result is that the $\ell = 1$ dipole wall stabilization, upon which the future of Scyllac is strongly dependent, has been shown to exist for diffuse profiles as well as the sharp boundary profile. There was some concern that this might not be true, but a careful study verified the existence of wall stabilization.

A second encouraging result is that a numerical procedure has been developed for studying the stability of diffuse two-dimensional MHD equilibria. The procedure was applied to the problem of the bumpy pinch and appears to work quite well. With some very careful preparation it should be possible to investigate diffuse, finite distortion $\ell = 1$ systems in the future.

A neutral result was obtained in the study of finite distortion, finite β,$\ell = 2$ stellarators. We were motivated to look at this problem to (1) see if $\ell = 2$ was a viable alternative to $\ell = 1$, or an improvement over $\ell = 0$ as a sideband field, and (2) lay the groundwork for future $\ell = 1$ calculations where the plasma is allowed to have an elliptical distortion. The basic result of this calculation is that $\ell = 2$ is not advantageous compared to $\ell = 1$, and is neither more nor less attractive than $\ell = 0$ as a sideband field.

An interesting result developed from an investigation of scaling laws for "fatter" plasmas that are envisioned in future Scyllac experiments. To satisfy the requirements of (1) toroidal equilibrium, (2) m = 1 wall stabilization, and (3) $m \geqslant 2$ finite gyro radius stabilization, theory predicts a value for the major radius that is extremely sensitive to certain plasma parameters. There is no question that the theories from which these scaling laws have been derived have a limited reliability. However, it does point out some problems of great importance that should be studied very carefully, both theoretically and experimentally, in the near future.

1. $\ell = 2$ Scyllac Configuration. The stability of an infinitely long, high-β, $\ell = 2$ stellarator has been investigated using the ideal magnetohydrodynamic sharp boundary model. This problem was studied to determine whether the $\ell = 2$ configuration would have favorable stability properties in a parameter range of interest to the Scyllac[1,2] program.

There is preliminary evidence that such desirable stability properties should exist. To understand this we first briefly review some relevant Scyllac and low-β stellarator theory. The difference between each of these theories is associated with the relative size of three dimensionless parameters that appear and are used as expansion parameters. These are β = plasma pressure/magnetic pressure, ϵ = plasma radius times helical pitch number, and δ = helical plasma distortion/plasma radius. Current ideas on Scyllac can be traced back to the stability results of the "old" Scyllac expansion[3-5] in which it is assumed that $\beta \sim 1$ and $\delta \ll \epsilon < 1$. The corresponding dispersion relation for m = 1, k = 0 modes is given by

$$\frac{\omega^2}{v_a^2/a^2} = -\ell^2(\ell-1)\,\epsilon^2\delta^2\,\frac{\beta(2-\beta)}{2} \quad ,$$

where v_a is the Alfvén speed. From this result it follows that the system is m = 1 unstable for any ℓ except $\ell = 1$. On this basis the Scyllac experiment was designed as an $\ell = 1$ system. Recent calculations pertaining to Scyllac[6-8] have been concerned with calculating higher order $\ell = 1$ terms in the m = 1, k = 0 dispersion relation because the leading order term vanishes. In particular, the $\epsilon^4\delta^2$ correction has been found for the old Scyllac expansion. Further, a "new" Scyllac expansion has been devised where $\beta \sim 1$ and $\epsilon \ll \delta < 1$. The leading order term again vanishes for $\ell = 1$ and the $\epsilon^2\delta^4$ correction has been calculated. Thus, most of the effort on Scyllac has been concerned with $\ell = 1$ because all other ℓ values are m = 1 unstable. However, in a paper by Grad and Weitzner[4] a more optimistic result concerning higher ℓ numbers is pointed out. (This result is closely associated with the earlier critical β calculations of Johnson et al.)[9] Using low-β stellarator theory, which assumes $\beta \sim \delta^2 \ll \epsilon < 1$, they find an m = 1, k = 0 dispersion relation given by

$$\frac{\omega^2}{v_a^2/a^2} = -\ell^2(\ell-1)\,\epsilon^2\delta^2\,[\beta - 2(\ell-1)\delta^2] \quad .$$

Thus, for any $\beta \leqslant \beta_{crit} = 2(\ell-1)\delta^2$, the system is stable to this mode. Also, with sufficiently large helical fields (i.e., large δ), substantial critical β's ~ 0.5 could be obtained. Admittedly these values are somewhat artificial because the expansion is being used outside its range of validity. Nonetheless it is suggestive that such a scaling may persist even at finite β and finite δ. To answer this question correctly, we see, by examining the existing theories, that what is required is a calculation of $\ell = 2$ stability using the new Scyllac expansion and including the $\epsilon^2\delta^4$ correction. We have pursued this problem during the past year. By calculating the growth rates numerically we were able to do the above calculation for both β and δ arbitrary and $\epsilon \ll 1$, keeping only the leading order term in ϵ^2.

The results of this calculation follow. For m = 1, k =,0, a critical β is found as would be predicted from low-β stellarator theory. For finite β,δ the value of β_{crit} is somewhat lower than predicted by the low-β theory in the regime of experimental interest. In fact the highest value of β_{crit} for any strength $\ell = 2$ filed is about 0.17. This is somewhat discouraging from the Scyllac point of view because of the high-β requirements of implosion heating. However, the stability picture is much worse. The reason for this is that as in low-β stellarators, the worst

modes are not k = 0 modes, but interchange modes in which the perturbation remains in phase with the rotational transform of the magnetic field. We have shown that if the wavenumber k of the perturbation satisfies

$$\frac{k}{h} = (2p + m)\left(1 - \frac{\iota}{2\pi}\right) - m \quad |p| = 0,1,2,\ldots \quad ,$$

then the critical β is reduced to zero. Here h is the helical pitch number, m is the mode number, and $\iota/2\pi$ is the rotational transform. Thus, if one allows long but not infinite wavelength m = 1 modes, wavenumbers k exist that are unstable for all β. Clearly this configuration does not, as it stands, possess any of the favorable stability properties anticipated earlier.

At first glance these results might appear to contradict early low-β stellarator results that predict stability to all k modes. A more careful examination indicates that no such contradiction exists. The reason for this is associated with the fact that the early stellarator theory contains terms that are of very high order in the Scyllac expansions and are therefore not included. Of course many of the finite-β effects of the Scyllac expansion are not found in the stellarator expansion. The point is that these higher-order effects in stellarators can be stabilizing, thereby increasing the critical β away from zero. There are two such effects—one is shear and the other is possible favorable curvature arising because of the toroidal geometry. Each of these leads to a small critical β. These effects are important for stellarators that are intended to operate at very small β; however, they do not appear important for finite-β devices such as Scyllac.

2. Stability of Diffuse Two-Dimensional MHD Equilibria. We have gained much insight pertaining to gross plasma stability from the study of sharp boundary plasma models. As experiments become more sophisticated, we need diffuse profile theories to be able to make quantitative as well as qualitative comparisons.

In many experiments of current interest, the problem of including profiles is quite difficult, requiring the computation of stability of a diffuse two-dimensional, high-β magnetohydrodynamic equilibrium. Such experiments include Tokamak, Scyllac, finite-β stellarators, and toroidal screw pinches with circular and noncircular cross sections.

We have developed a numerical procedure for performing the stability calculation based on the variational form of magnetohydrodynamics. The object of the procedure is to minimize δW subject to the correct magnetohydrodynamic normalization and thus obtain the actual eigenvalues and eigenfunctions of the system. In the minimization we first Fourier transform the perturbation with respect to the ignorable coordinate of the equilibrium. The remaining part of the perturbation is expanded as a double series of complete admissible functions of the equilibrium coordinates. The minimization is then performed over the expansion coefficients.

The double expansion procedure has been tested on the problem of the bumpy θ pinch with arbitrary size bumpiness. Here, the procedure proved to be quite satisfactory, easy to code, gave good accuracy, and required relatively few functions for convergence.

The procedure details are outlined below for the bumpy pinch. If we assume slow z variation, then the energy principle for the bumpy pinch can be cast in the following form.

$$\omega^2 = \frac{\delta W(\xi,\xi)}{K(\xi,\xi)}$$

with

$$\delta W = \tfrac{1}{2}\int \left[(\underline{B}\cdot\nabla\xi)^2 + \left(\underline{B}\cdot\nabla\frac{\partial}{\partial r}r\xi\right)^2 + r\frac{\partial p^*}{\partial r}\left(\frac{\partial\xi}{\partial r}\right)^2\right]\underline{dr} \, ,$$

$$K = \tfrac{1}{2}\int \rho\left[\xi^2 + \left(\frac{\partial}{\partial r}r\xi\right)^2\right]\underline{dr} \quad ,$$

and

$$\frac{\partial p^*}{\partial r} = \underline{B}\cdot\nabla B_r \quad ,$$

where $\underline{B}$ is the equilibrium magnetic field and ξ is the radial component of plasma displacement.

The essence of the numerical minimization is that the function $\xi(r,z)$ is expanded in a truncated double Fourier series and ω^2 minimized over this class of functions. The actual minimization procedure is performed with respect to the coefficients of the double series. Because the true eigenfunctions can be represented by a Fourier series, this method can, in principle, achieve arbitrary accuracy by including more terms. In practice, physical insight can guide the choice of expansion functions, and therefore, few are needed for good convergence.

For the bumpy θ pinch, the eigenfunctions behave as r^{m-1} for small radius and are periodic in z. Also, we anticipate that the worst mode will probably have the form of a gross displacement. Thus, an appropriate m = 1 expansion is

$$\xi(r,z) = \sum_{\ell,n} C_{\ell n} J_o\left[\sigma_n \frac{r}{a(z)}\right] e^{i\ell hz} \quad .$$

By defining σ_n so that $J_o(\sigma_n b_o/a_o) = 0$, we ensure that $\xi(r,z)$ vanishes on the flux surface given by

$r/a(z) = b_o/a_o = \text{const}$. The $C_{\ell n}$'s are complex coefficients that are to be determined. Substituting, we obtain

$$\omega^2 = \min_{C_{ij}} \frac{\sum_{\ell npq} C_{\ell n} W_{\ell npq} C^*_{pq}}{\sum_{\ell npq} C_{\ell n} D_{\ell npq} C^*_{pq}} ,$$

where $W_{\ell npq}$ and $D_{\ell npq}$ are numerically computed matrix elements depending only on the equilibrium and the Fourier expansion functions. It can be shown that $D_{\ell npq}$ and $W_{\ell npq}$ are both real and satisfy $W_{\ell npq} = W_{pq\ell n}$ and $D_{\ell npq} = D_{pq\ell n}$.

A more convenient expression can be obtained by writing the $C_{\ell n}$ as a one-dimensional vector, $\underline{x}$, of length (L x N), the number of cosines times the number of Bessel functions retained. We then find

$$\omega^2 = \min \frac{\underline{x}^T W \underline{x}}{\underline{x}^T D \underline{x}}$$

with W and D being (L x N) x (L x N) symmetric matrices. Because D is positive definite, this equation can be put into standard form by defining

$$\underline{x} = D^{-1/2} \underline{y} ,$$

where $D^{-1/2}$ is also real and symmetric. This yields

$$\omega^2 = \min \frac{\underline{y}^T D^{-1/2} W D^{-1/2} \underline{y}}{\underline{y}^T \underline{y}} = \min \frac{\underline{y}^T S \underline{y}}{\|y\|^2} .$$

To find $D^{-1/2}$, we note that D can be expressed as $P^{-1}QP$ with Q an (L x N) x (L x N) diagonal matrix consisting of the eigenvalues of D; that is, $Q_{ij} = \lambda_i \delta_{ij}$ where $D\underline{z}_i = \lambda_i \underline{z}_i$. P can be constructed to satisfy $PP^T = I$. By choosing the $\underline{z}_i$ orthonormal, it follows that $P = [\underline{z}_1, \underline{z}_2, \ldots \underline{z}_{(L \times N)}]$. From P and Q we then compute $D^{-1/2} = P^T Q^{-1/2} P$. We see that to find $D^{-1/2}$ requires the evaluation of the eigenvalues and orthonormal eigenvectors of the symmetric matrix D, a simple numerical procedure. To complete the minimization all that is required is to find the eigenvalues ω_n^2 and eigenvectors $\underline{y}_n$ of the symmetric matrix $S = D^{-1/2} W D^{-1/2}$.

The growth rates and eigenfunctions for the m = 1, k = 0 mode of a bumpy θ pinch were computed for a large range of equilibrium parameters. The results were interpreted with respect to two basic aims.

First, as a test of the numerical procedure, the results were compared with existing small δ_o analytic theory in the appropriate limits. Here $\delta_o = \Delta B_z/B_z$ is a measure of the bumpiness. Our second aim was to examine the effects of arbitrary δ_o on the growth rates.

There are two calculations of direct interest in the existing analytic theory. The first is the sharp boundary calculation of Haas and Wesson.[10] They calculate an m = 1 growth rate given by

$$\frac{\gamma^2}{h^2 v_a^2 \delta_o^2} = \frac{\beta(3-2\beta)}{4(1-\beta)^2} \left[\frac{1-\beta(1+a^2/b^2)}{2-\beta(1-a^2/b^2)} \right] ,$$

where $v_a^2 = B_o^2/\mu_o \rho_o$ and a/b is the ratio of plasma to wall radii. If we conserve line density, then the sharp boundary a/b is related to our a_o/b_o by the relationship $a^2/b^2 = (a_o^2/b_o^2)/(1 + \sqrt{1-\beta})$. A more recent calculation by Weitzner[11] treats the stability of the bumpy pinch also in the small δ_o limit but for diffuse profiles. There a dispersion relation is obtained of the form

$$\frac{\gamma^2}{h^2 v_a^2 \delta_o^2} = F\left(\beta, \frac{a_o}{b_o}\right) ,$$

where the Alfvén speed is normalized to the center density and external B field. The profiles chosen by Weitzner were Gaussian. The function $F(\beta, a_o/b_o)$ was tabulated by Weitzner by numerically solving a couples set of ordinary differential equations.

To test our numerical procedure, we chose similar profiles, set $b_o/a_o = 2.5$, $\delta_o = 0.01$, and computed the growth rates as a function of β. For a value of δ_o this small, we would expect good quantitative as well as qualitative agreement with Weitzner's results. The value $b_o/a_o = 2.5$ represents a wall-to-center density ratio of about e^{-12}, indicating a substantial distance between plasma and wall. The comparison is illustrated in Fig. VI-1 where the solid curve represents the eigenvalue corresponding to our fastest growth rate and the dots represent the growth rates given in Weitzner's table. We see that our numerical procedure agrees with Weitzner's theory over the whole range of β in the appropriate small δ_o limit. Note that the sharp boundary growth rates in Fig. VI-1 are generally higher than for diffuse profiles except at very high β, where the wall effect dominates.

In both Weitzner's and our diffuse calculations, there is no wall stabilization for high β as in the sharp boundary model if the plasma extends to the wall, even with exponentially small density. This result is consistent with a small δ_o diffuse theory in which δW is minimized without regard to normalization. If one treats δ_o as a small parameter and substitutes a $\xi(r,z)$ of the form $\xi(r,z) = \xi_o(r) + \delta_o \xi_1(r) \cos hz$ into δW, then after a lengthy calculation it can be shown that a necessary and sufficient condition for m = 1 stability is

$$\tfrac{1}{2} \int_0^r \frac{r'dr'}{B^2} > \frac{r^2}{B^2}$$

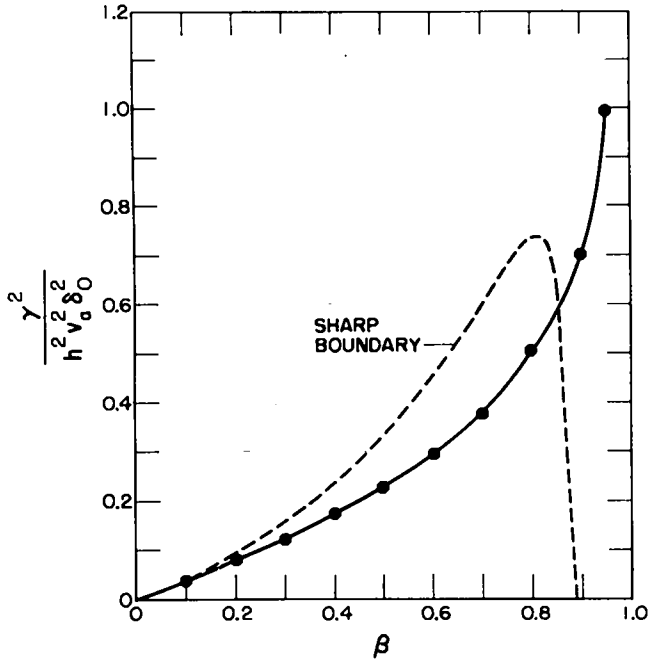

Fig. VI-1.
Haas-Wesson (dashed), Weitzner (dots), and our (solid) growth rates vs β curves for $b_o/a_o = 2.5$.

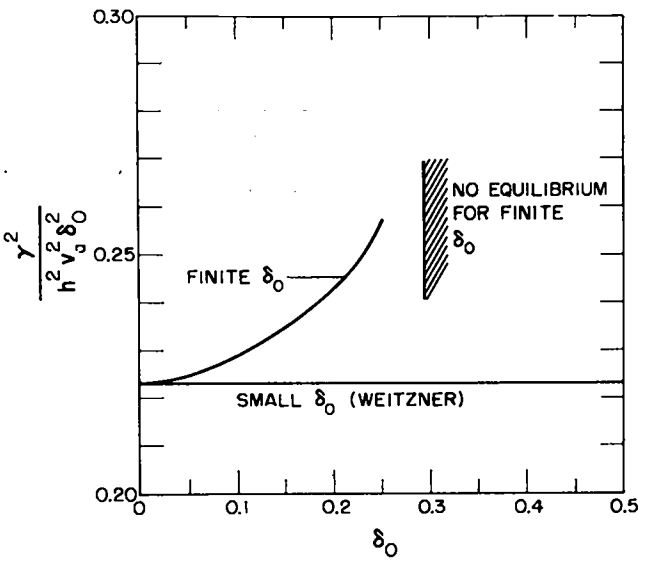

Fig. VI-2.
Growth rate vs δ_o compared with Weitzner's theory for $b_o/a_o = 2.5$ and $\beta = 0.5$.

for any r and where B(r) is the θ-pinch field. This inequality is always violated near r = 0 and hence the bumpy pinch is always m = 1 unstable. Haas and Wesson[10] also considered diffuse profiles and derived a necessary condition for stability by setting $\xi,1 = 0$. However, it is clear from the above that we can always choose a $\xi \neq 0$ that leads to instability.

The final result concerns the effect of finite δ_o. To investigate this question we computed growth rates vs δ_o for $\beta = 0.5$ and $b_o/a_o = 2.5$. In Fig. VI-2 these growth rates are compared with Weitzner's predictions. We see that for m = 1 modes in a bumpy pinch the normalized growth rate is fairly insensitive to δ_o, becoming only slightly larger as δ_o increases. This insensitivity of normalized growth rate on bump strength is desirable from the point of view of understanding and interpreting experimental data.

Summarizing, we have developed a numerical method for computing the growth rates and eigenfunctions for an arbitrary two-dimensional, diffuse, high-β, magnetohydrodynamic equilibrium. As a test of the procedure we treated the problem of the bumpy θ pinch with arbitrary size bumpiness. Our results agree with the existing diffuse theory of Weitzner in the limit of small bumpiness. As the bumpiness increased, we found that the normalized growth rates increased only slightly; that is, the normalized growth rate is insensitive to bump strength. Further, the sharp boundary wall stabilization effect is not found for diffuse profiles.

The numerical procedure is easy to code, requires only moderate storage, and runs quickly. In addition, by choosing appropriate expansion functions, there is considerable flexibility in applying boundary conditions.

Presently, the method appears to be applicable to a wide class of diffuse equilibria including the finite β, $\ell = 1$ Scyllac, finite-β stellarators, Tokamaks, and toroidal screw pinches.

3. Diffuse Wall Stabilization. An important problem in the Scyllac program is the understanding of wall stabilization. This, of course, is because the only known static effect for stabilizing the m = 1 mode in the $\ell = 1$ Scyllac configuration is wall stabilization arising from dipole currents flowing in the plasma.

At the beginning of our investigations, there was serious concern that perhaps the wall stabilization did not exist for diffuse profiles. This concern arose from a study of wall stabilization in sharp boundary and diffuse profiles in pure $\ell = 0$ systems. In this case there existed the well-known sharp boundary result of Haas and Wesson[10] that predicted that the m = 1 mode could be stabilized if

$$\beta > \frac{1}{1 + a^2/b^2} \quad .$$

Recent studies by Weitzner[11] and at LASL (Sec. VI.B.2)

showed that any diffuse profile must be unstable to an $m = 1$ mode.

To resolve this discrepancy we examined the eigenfunctions and spectral properties of a small bumpiness $\ell = 0$ configuration, using both the procedure discussed in Sec. VI.B.2 and a differential equation solver. Using the same techniques we investigated the wall stabilization effect in a slightly distorted pure $\ell = 1$ system. The results are as follows.

The basic source of the discrepancy in the $\ell = 0$ system has to do with the difference in the structure of the spectrum between sharp boundary and diffuse profiles. In the diffuse case, the unstable spectrum consists of an infinite but discrete set of modes whose eigenvalues form a point of accumulation at $\omega^2 = 0$. The most unstable mode has no nodes and is a true gross mode for sufficiently low β. The second worst mode has one node, the third worst mode, two nodes, etc., as would be found in a classical Sturm-Liouville problem. We emphasize that this structure pertains only for low β (i.e., less than required for wall stabilization), and that all but the worst gross mode are localized in the vacuum region. As the β is increased over the value where one would expect wall stabilization in the sharp boundary model, the diffuse spectrum changes dramatically. The gross mode with no nodes becomes stable, whereas the fastest growing mode now has one node and a comparable if not higher growth rate that the low-β gross mode. Further, the structure of this one-node mode shifts from being localized in the vacuum to extending over the full plasma, and is thus a potentially dangerous mode.

As one steepens the profile, all that remains intact is the gross no-node mode. The growth rates in both the low- and high-β region of the modes with higher nodal structure decrease as the profile steepens and eventually approach zero in the limit of the sharp boundary. It is this behavior of the spectrum that explains the apparent discrepancy between sharp and diffuse profiles in an $\ell = 0$ system; that is, those modes that are unstable for diffuse profiles above the critical β for wall stabilization have a growth rate that approaches zero as the profile steepens and thus are not seen in the limit of the sharp boundary.

A similar investigation was carried out for the diffuse $\ell = 1$ system. Here the spectral picture was considerably simpler and in fact confirmed predictions of earlier LASL work,[12] which was based on an energy principle argument. This earlier work showed that in the limit of small helicity and long pitch length any diffuse profile would be stable to the $m = 1$ mode if the weak condition

$$\frac{1}{B}\frac{dB}{dr} > 0$$

is satisfied. Here B is the θ-pinch field. A simple scaling argument also predicted that the stabilizing effect of the gross mode would scale as $(a/b)^4$ as was found in sharp boundary theory.

An examination of the $\ell = 1$ spectrum verified this behavior for the gross mode and uncovered many other, more highly structured modes. These modes were discrete and their eigenvalues were all stable forming a point of accumulation at $\omega^2 = 0$. The eigenvalues of these modes were very insensitive to wall radius in contrast to the no-node gross mode.

In summary, the wall stabilization effect for $\ell = 1$ systems seems to exist for the gross mode in diffuse as well as in sharp boundary profiles. We must still examine the structure of the spectrum, including higher order effects in helicity and pitch length, to determine what effect diffuseness has on the destabilizing terms.

4. Scaling Laws of Toroidal, Wall-Stabilized θ Pinches. The plans of the Scyllac program are directed toward the study of heating and stability of "fatter" plasmas than have been used in conventional θ pinches. As such, it is useful to investigate the scaling laws from existing theory and see their implication on future experiments, such as the scientific feasibility experiment. Before doing so we must emphasize that the existing theories have been derived from sharp boundary models, and thus at best the results will be semiquantitative. In addition, there is essentially no experimental verification (with the exception of the toroidal equilibrium constraint) that the various phenomena listed below are actually the relevant ones to consider. This is basically due to the enormous difficulty of doing such experiments. It is anticipated, however, that in future experiments some of these effects will actually be measured.

The basic question is as follows. Consider a feasibility experiment where we fix the temperature, $T_i \approx 5.4$ keV, the B field, $B \approx 50$ kG, plasma β, $\beta \approx 0.85$, and the ratio of plasma to wall radii (as big as possible for maximum wall stabilization), $a/b \approx 0.3$. Under these conditions we must determine what existing theory requires of the plasma radius a, the major radius R, the pitch number h of the helical $\ell =$ field, "δ_1," the $\ell = 1$ plasma distortion, and the $\ell = 0$ plasma distortion δ_o to satisfy the following three conditions:

(1) sufficient $\ell = 1$ and $\ell = 0$ fields for toroidal equilibrium,

(2) sufficient wall stabilization to stabilize the $m = 1$ mode, and

(3) sufficient finite gyro radius effects to stabilize $m \geq 2$ modes.

These three conditions can be expressed mathematically as follows.

Toroidal Equilibrium

$$\delta_o \delta_1 = \frac{g_1(\beta)}{h^2 aR} \quad .$$

m = 1 Stability

$$\delta_1^2 \left(\frac{a}{b}\right)^4 = g_2(\beta) h^2 a^2 \delta_1^2 + g_3(\beta) \delta_o^2 \quad .$$

m = 2 Stability

$$\left(\frac{r_L}{a}\right)^2 = g_4(\beta) h^2 a^2 \delta_1^2 \quad .$$

The functions, $g_i(\beta)$, as determined by sharp boundary theory, are given by

$$g_1(\beta) = \frac{2}{3-2\beta} \quad ,$$

$$g_2(\beta) = \frac{(4-3\beta)(2-\beta)}{8\beta(1-\beta)} \quad ,$$

$$g_3(\beta) = \frac{(3-2\beta)(1-\beta)}{\beta(2-\beta)} \quad ,$$

and

$$g_4(\beta) = \frac{8\beta^2(1-\beta)}{2-\beta} \quad .$$

For convenience we shall maintain the g_i notation to determine how sensitive the results are to particular coefficients.

We consider β, a/b, and the gyro radius r_L as fixed parameters and eliminate δ_o and h from these equations leaving a relationship between a, R, and δ_1. This relationship is given by

$$R^2 = g_3 g_1^2 g_4^2 \frac{a^8}{r_L^4} \frac{1}{a^2\left(\frac{a}{b}\right)^4 - \frac{g_2}{g_4}\left(\frac{r_L}{\delta_1}\right)^2} \quad .$$

If we examine R as a function of a for a given δ_1, we note that the above expression has a very narrow minimum at some critical value of a. If the value of a does not coincide with this minimum, large values of major radius R are required to satisfy the three given conditions. The value of a at this minimum is given by

$$a = \left(\frac{4}{3}\frac{g_2}{g_4}\right)^{1/2} \frac{r_L}{\delta_1}\left(\frac{b}{a}\right)^2 \quad .$$

Using this expression we find that the acceptable minimum value of major radius is

$$R = \frac{16}{9}\left(\frac{3 g_3 g_1^2 g_2^3}{g_4}\right)^{1/2} \frac{r_L}{\delta_1^3}\left(\frac{b}{a}\right)^8 \quad .$$

The corresponding values of h and δ_o are given by

$$ha = \left(\frac{3}{4g_2}\right)^{1/2}\left(\frac{a}{b}\right)^2$$

and

$$\delta_o/\delta_1 = \left(\frac{1}{4g_3}\right)^{1/2}\left(\frac{a}{b}\right)^2 \quad .$$

We note the strong eighth power dependence of R on b/a. It also varies as $1/\delta_1^3$ and $g_2^{3/2}$, which corresponds to the third power of the $\ell = 1$ growth rate coefficient. To minimize the dimensions of a feasibility experiment, it is desirable to make the $\ell = 1$ distortion δ_1 as large as possible.

The implications of these relations are noted in the following four examples. In each example we take $\beta = 0.85$, a/b = 0.3, and $r_L = 0.3$ cm (corresponding to deuterium at 5.4 keV and 50 kg).

Case 1. The choice of parameters for this case is based on experimental intuition that indicates that m = 2 stability and $\ell = 0$ stability are not actually important constraints because they are not observed experimentally. These are design parameters for a feasibility experiment as given in the staged θ-pinch proposal. Here we use a value of $\delta_1 = 1.5$.

Case 2. Corresponds to straightforward substitution in the formulas using the theoretical values of the g_1 and taking $\delta_1 = 1.4$.

Case 3. Same as Case 2 except an experimental value of $\ell = 1$ growth rate is used, which is a factor of 2 smaller than the theoretical one; that is, we replace g_2 by $g_2/2$.

Case 4. Same as Case 3 except we reduce the slightly uncomfortable value of δ_1 from 1.4 to 1.0.

The results are given in Table VI-1.

We note the sensitivity of the results, particularly between Cases 2 and 3. In fact, as the $\ell = 1$ growth rate changes by a factor of 2, a feasibility experiment goes from nearly impossible to embarrassingly simple.

TABLE VI-1

SUMMARY OF CASES

Case No.	a (cm)	R (m)	ha	δ_0/δ_1	δ_1
1	3	30	0.07	0.15	1.5
2	4	84	0.06	0.1	1.4
3	2	10	0.12	0.1	1.4
4	3	29	0.12	0.1	1.0

Because the stability terms for m = 1 or 2 have not been quantitatively verified experimentally yet, one should not take the actual numbers too seriously. However, the results are sufficiently sensitive that in the future very careful experimental studies will be necessary to determine just which terms are important and to experimentally measure the relevant coefficients.

REFERENCES

1. S. C. Burnett, W. R. Ellis, C. F. Hammer, C. R. Harder, H. W. Harris, F. C. Jahoda, W. E. Quinn, A. S. Rawcliffe, F. L. Ribe, G. A. Sawyer, R. E. Siemon, and K. S. Thomas, *Plasma Physics and Controlled Nuclear Fusion Research*, (IAEA, Vienna, 1971), Vol. III, p. 201.
2. W. R. Ellis, C. F. Hammer, F. C. Jahoda, W. E. Quinn, F. L. Ribe, and R. E. Siemon, *Proc. Second International Conference on Pulsed High-Beta Plasmas* (Garching West Germany, July 1972) paper A1.
3. A. A. Blank, H. Grad, and H. Weitzner, in *Plasma Physics and Controlled Nuclear Fusion Research* (International Atomic Energy Agency, Vienna, 1969) Vol. II, p. 607.
4. H. Grad and H. Weitzner, Phys. Fluids 12, 1725 (1969).
5. M. N. Rosenbluth, J. L. Johnson, J. M. Greene, and K. E. Weimer, Phys. Fluids 12, 726 (1969).
6. H. Weitzner, Phys. Fluids 14, 658 (1971).
7. J. P. Freidberg, Phys. Fluids 14, 2454 (1971).
8. H. Weitzner, *Plasma Physics and Controlled Fusion Research*, (IAEA, Vienna, 1971), Vol. III, p. 223.
9. J. M. Greene, J. L. Johnson, and K. E. Weimer, J. Nucl. Energy Pt. C8, 145 (1966).
10. F. A. Haas and J. A. Wesson, Phys. Fluids 10, 2245 (1967).
11. H. Weitzner, to be published in Phys. of Fluids.
12. J. P. Freidberg and B. M. Marder, Phys. Fluids 14, 174 (1971).

C. Summary of Toroidal Z-Pinch Work (W. B. Riesenfeld)

Properties of toroidal belt pinches have been investigated through numerical solution of the nonlinear toroidal MHD equilibrium equations. Profiles were obtained for a perfectly conducting and closed outer boundary with rectangular cross section, and for a mock-up of the Garching separatrix configuration that is experimentally produced with pitched windings. Two types of equilibria were found for a given boundary condition, and illustrative flux plots are provided for each type. The basis for a physical selection between these equilibria remains unclear, but the preferred equilibrium, possessing high-ellipticity cross sections, exhibits high β although still remaining on the safe side of the Kruskal-Shafranov limit.

A research note was written to put into perspective some of the basic advantages and disadvantages of various axisymmetric toroidal configurations. A uniform system of theoretical ordering of the relevant parameters in terms of the inverse aspect ratio was applied to low- and medium-β Tokamaks, high-β θ pinches, profiled Z pinches, and belt pinches. The discussion examines these equilibrium configurations in their stability properties with respect to magnetic well stabilization and wall stabilization.

D. Summary of Vlasov-Theory Work (W. B. Riesenfeld)

To compute instability growth rates of a wide range of high-β equilibria, including diffuse profiles, using the Vlasov-fluid model, a new and numerically advantageous formulation was developed based upon Hamilton's variational principle for collisionless Vlasov plasmas. The technique was tested on an azimuthally and axially symmetric sharp boundary equilibrium and was found to have excellent convergence properties.

A new numerical simulation approach to Vlasov plasmas has been worked out in which the particles are distributed continuously in coordinate space. This approach significantly decreases the computer storage requirements compared to that for discrete particle simulation. The technique is being tested on a one-dimensional electrostatic problem. In addition, several one-dimensional simulation algorithms were compared using a stable plasma as a test problem. The purpose was to investigate the utility of using higher order than piecewise linear representations of the scalar potential and the effects of electric field smoothing. Tests of two-dimensional numerical simulation algorithms for electrostatic oscillations were performed, using two-stream unstable test

problems, to check the utility of the nine-point scheme for the Laplacian operator and the effects of field smoothing.

Work has been performed in collaboration with LASL Group P-4 to establish empirical closure relations for the Vlasov moment equations, using data on the proton and electron velocity distributions obtained from the IMP-6 spacecraft. Simple statistical relations between the third moments (heat fluxes) and second moments (temperatures) were found. A report of these relations will soon be published. These results may lead to a useful truncated moment equation description of collisionless plasmas with fully developed turbulence that is applicable to CTR situations.

E. Toroidal Belt Pinch Equilibria (D. A. Baker and L. W. Mann)

We have investigated the properties of toroidal belt pinch equilibria in cooperation with the Garching belt pinch group. We have by numerical means obtained solutions to the full nonlinear toroidal equilibrium equation as derived from the static pressure balance and Maxwell equations.

Some sample results on calculations for two types of boundary conditions are presented. The two boundary conditions are (1) a perfectly conducting and closed outer boundary having a rectangular cross section and (2) a mockup of the Garching separatrix configuration that is produced experimentally with a pitched winding. All calculations reported here use the Garching boundary dimensions, i.e., a mean major radius of 22.5 cm and a rectangular cross section of 15 by 110 cm.

1. Closed Conducting Boundary. An interesting feature that became apparent early in our studies was the existence of two types of solutions for the same boundary conditions. We were able to find equilibria of two types by iterative means. The first type is typified by the poloidal flux plot of Fig. VI-3, which shows a short contracted pinch having a cross section of small ellipticity in spite of the elongated conducting boundary. The other type is typified by Fig. VI-4, which corresponds to a plasma having an elongated cross section. Our main interest is with the latter class of solutions that are expected to allow the determination of high-β plasma configurations that operate below the Kruskal-Shafranov limit. One possible concern about the existence of the short contracted solutions is that experimentally the plasma may tend to the low ellipticity equilibrium thus defeating the purpose of the elongated cross sections.

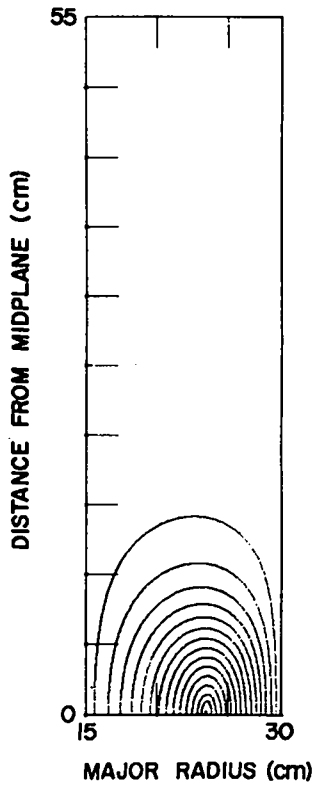

Fig. IV-3.
Plot of the poloidal flux surfaces on a cross section of a closed conducting boundary belt pinch. The configuration is symmetric about the midplane and only half the cross section is shown. Level contours for a contracted type of solution are given.

Figure VI-5 shows plasma pressure and the poloidal and toroidal field distributions along a radius (at the symmetry plane) for the elongated configuration of Fig. VI-4. Figure VI-6 shows the q value, $1/2\pi \oint B_T/RB_p d\ell$ (B_p and B_T are the poloidal and toroidal fields), as a function of the major radius of the innermost position of the associated flux surface. This particular choice of profiles shows that the q value passes through a minimum, but always exceeds unity so the Kruskal-Shafranov limit is not exceeded on any flux surface. The large depression of toroidal magnetic field demonstrates that indeed the equilibrium can have a high β and still remain below the Kruskal-Shafranov limit. There are many ways of defining β values. For our purposes here we define the toroidal β_T and poloidal beta β_p. $\beta_T = 1-(B_T/B_o)^2$ evaluated at the point of maximum depression of the toroidal field (B_o is the undepressed toroidal field), and β_p = maximum plasma pressure/maximum poloidal field pressure. For the equilibrium of Figs. VI-4 and VI-5, the beta values are

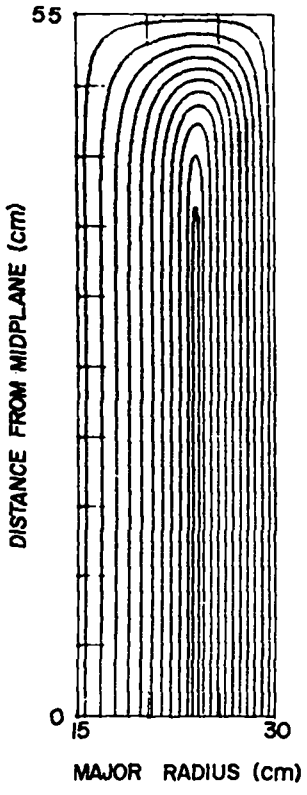

Fig. VI-4.
Poloidal flux plot for a closed boundary belt pinch equilibrium representing an elongated type of solution.

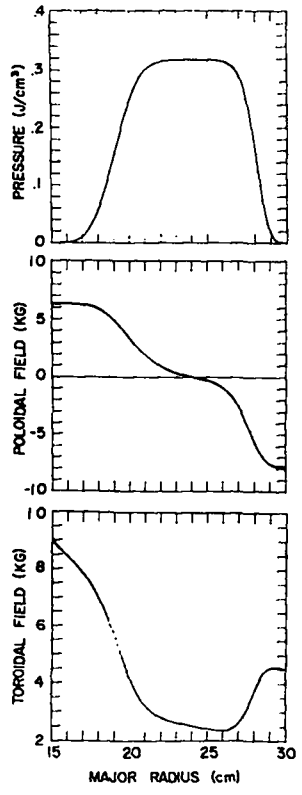

Fig. VI-5.
Pressure, poloidal, and toroidal magnetic field distributions along a major radius at the midplane for the closed boundary configuration.

$\beta_T = 0.8$ and $\beta_p = 1.4$. The total pressure and field values correspond to a total toroidal pinch current of one megampere.

2. Open Boundary Configuration. The configuration of the Garching experiment is attained using a pitched winding that produces both components of the magnetic field. The winding is designed to produce open and closed flux surfaces divided by a separatrix. Conditions are chosen to cancel the radial toroidal shift of the equilibrium position so that the plasma is located midway between the concentric cylindrical boundaries. In the actual device there is some flux passing through the latter boundaries but communications with the Garching group indicate that the major leakage is at the ends. For these calculations, the cylindrical walls were treated as perfectly conducting with all the flux leakage at the ends.

The corresponding set of plots given for the closed boundary case is shown for the open configuration in Figs. VI-7, VI-8, and VI-9. The separatrix location was adjusted to center the pressure profile. The β values and the total toroidal current are essentially the same as quoted for the closed geometry.

We conclude that in both the open and closed configurations, diffuse profile equilibria exist having q values on all flux surfaces greater than unity and β values on the order of unity. The full stability studies of these equilibria are presently in progress.

F. Perspective on Various Axisymmetric Toroidal Devices

(J. P. Freidberg, F. A. Haas,* and W. B. Riesenfeld)

This section puts into perspective some of the major advantages and disadvantages of various axisymmetric toroidal configurations. The classification of each

*F. A. Haas is currently on leave of absence from Culham Laboratory, United Kingdom Atomic Energy Authority, Abingdon, Berkshire, England.

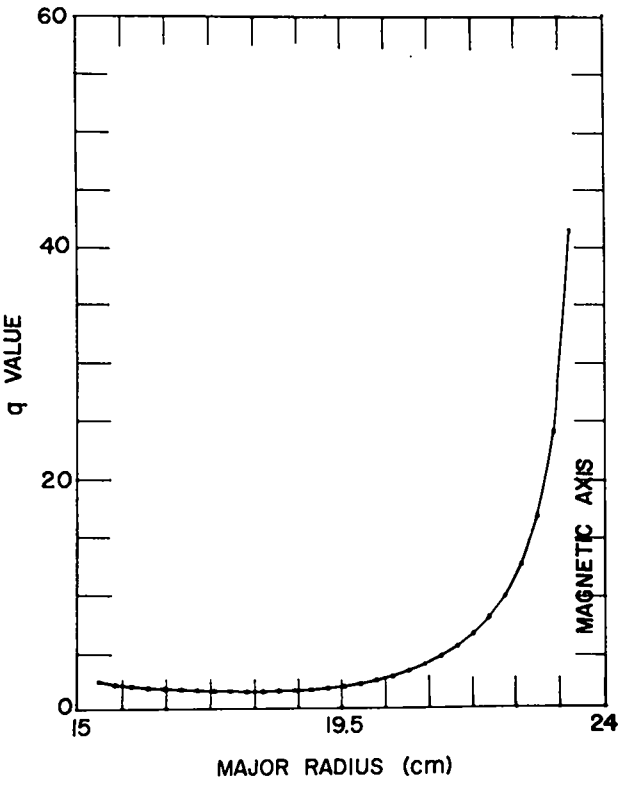

Fig. VI-6.
Distribution of q values vs the major radius for the closed configuration of Fig. VI-4.

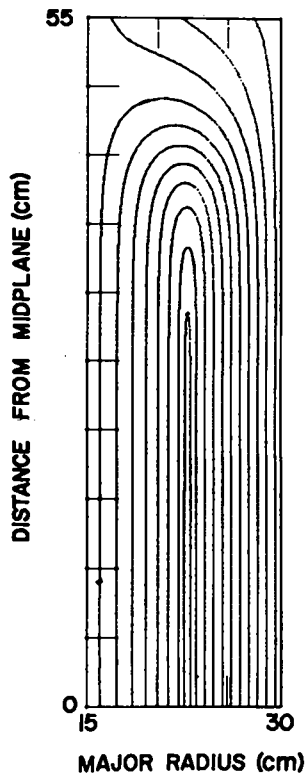

Fig. VI-7.
Poloidal flux plot for the open-end boundary condition for an elongated type of belt pinch solution.

configuration is based upon a theoretical ordering of the relevant parameters in terms of the inverse aspect ratio.

To be selective among the myriad of possibilities, the configurations discussed here were chosen on the basis of some approximate favorable stability properties as well as desirable equilibrium properties. We refer to gross kink modes as stability, and a given configuration will be said to have desirable stability properties if it possesses either well stabilization ($q > 1$), or wall stabilization, or both.

In several of the configurations, there is no existing justification for assuming that $q > 1$ is sufficient for stability. We use this criterion partly for convenience and partly from past experience and physical intuition.

A final point is that stability against localized modes is not yet known for all the configurations discussed here, and before any real precise comparison is made between the different configurations, this question must be answered. The following note provides a rough comparison of equilibria and kink stability in various toroidal configurations. The comparisons and a short descriptive paragraph of each configuration are given in Table VI-2.

We use the following notations in Table VI-2.

a	=	plasma toroidal minor radius
R	=	toroidal major radius
b	=	plasma height for elliptical cases
$\epsilon \equiv a/R$	=	inverse aspect ratio (we assume $\epsilon \ll 1$)
B_T	=	toroidal magnetic field in the plasma
$\hat{B}_T$	=	toroidal magnetic field in the vacuum
B_P	=	poloidal magnetic field on plasma surface
P	=	plasma pressure
β	=	toroidal $\beta \equiv 2P/\hat{B}_T^2$
β_P	=	poloidal $\beta \equiv 2P/\hat{B}_P^2$
q	=	safety factor $= (1/2\pi) \oint (\hat{B}_T/R\hat{B}_P)d\ell$.

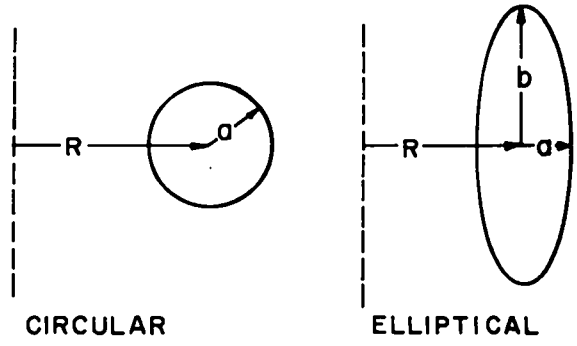

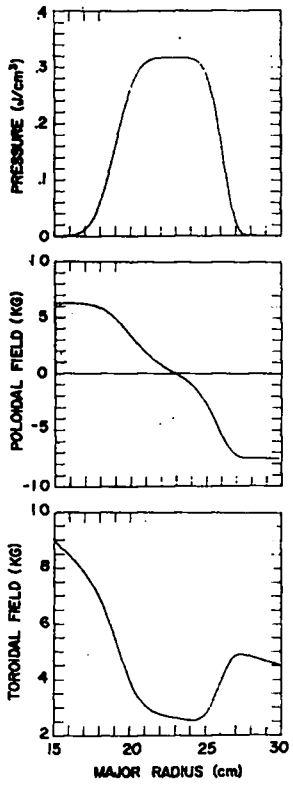

Fig. VI-8.
Pressure and field distributions for the open-end boundary of Fig. VI-5.

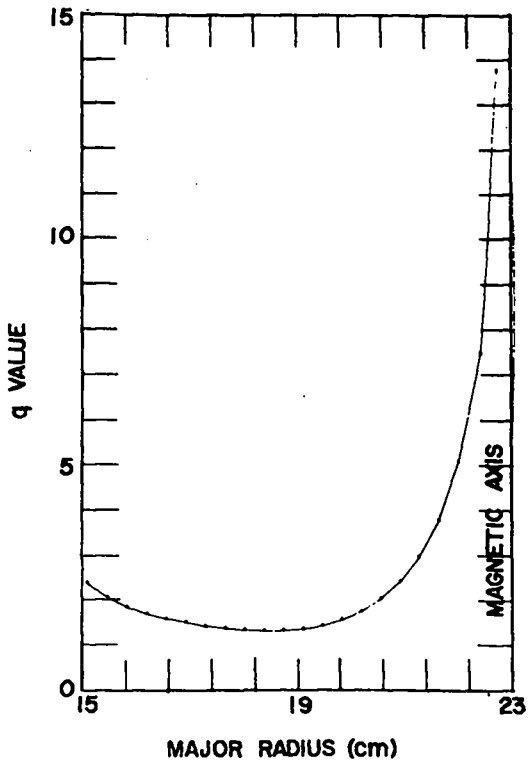

Fig. VI-9.
Plot of q values for the open-end geometry of Fig. VI-5.

1. Very Low-β Tokamak. This configuration has a very low $\beta \sim \epsilon^2$ and corresponds to the current operation of most Tokamaks. It is confined basically by poloidal pressure, and its stability properties are reasonably well investigated theoretically and experimentally. Its stability is quite favorable, being stable for most modes for any $\beta \sim \epsilon^2$ if $q > 1$.

2. Low-β Takamak. In this configuration, by confining the plasma only with the toroidal field, it is possible to have equilibria with β increased to $\beta \sim \epsilon$ over the very low-β Tokamak while maintaining a circular cross section and $q \sim 1$. Little is known about the gross stability of this configuration, although this problem is currently being studied at LASL.

3. High-β θ Pinch with Small Poloidal Field. If while maintaining a circular cross section, we try to increase the β even further, to $\beta \sim 1$, we find that we are forced to make $q \sim \epsilon^{1/2}$. This configuration is theoretically and experimentally unstable.

4. Garching Belt Pinch. By elongating the cross section of a Tokamak, it is possible to achieve $\beta \sim 1$ equilibria with a sufficiently large perimeter so that $q \sim 1$. In the Garching belt pinch the poloidal and toroidal fields are of the same order and hence both contribute to equilibrium confinement. Relatively little is known theoretically, and although the experimental results are not as complete as desired, they are encouraging from the stability point of view.

5. Short Belt. By using a smaller poloidal field, hence confining the plasma by toroidal forces, we can create a $\beta \sim 1$ equilibrium with $q \sim 1$, although requiring less ellipticity than in the Garching belt pinch. That is, the Garching belt pinch has $b/R \sim 1$, whereas the short belt has $b/R \sim \epsilon^{1/2}$. This configuration is currently being investigated theoretically at LASL.

6. Reversed-Field Z Pinch. All of the previous configurations aimed at achieving stability by having sufficiently high q. In the reversed-field z pinch, which is confined entirely by poloidal pressure at high $\beta \sim 1$, the safety factor is $q \sim \epsilon$ and thus not useful for stability.

TABLE VI-2

SUMMARY OF CONFIGURATIONS

Configuration	Cross Section	b/R	β	β_P	$\hat{B}_P$	B_T	$\hat{B}_T$	$\hat{B}_T - B_T$	Pressure Balance	q	Stability
Very Low-β Tokamak	Circular	ϵ	ϵ^2	1	ϵ	1	1	ϵ^2	Poloidal and Toroidal	1	Well
Low-β Tokamak	Circular	ϵ	ϵ	$\frac{1}{\epsilon}$	ϵ	1	1	ϵ	Toroidal	1	Well?
High-β θ Pinch With Small Poloidal Field	Circular	ϵ	1	$\frac{1}{\epsilon}$	$\epsilon^{1/2}$	1	1	1	Toroidal	$\epsilon^{1/2}$	Unstable
Garching Belt Pinch	Elliptic	1	1	1	1	1	1	1	Poloidal and Toroidal	1	Well?
Short Belt	Elliptic	$\epsilon^{1/2}$	1	$\frac{1}{\epsilon}$	$\epsilon^{1/2}$	1	1	1	Toroidal	1	Well?
Reverse-Field Z Pinch	Circular	ϵ	1	1	1	1	~ 0	-1	Poloidal	ϵ	Well

Complete MHD stability (to gross and local modes) can be found for some diffuse profiles in this configuration by wall stabilization and shear. This fact, wall stabilization and shear vs well stabilization, distinguishes the reversed-field Z pinch from all other configurations.

In addition to the ordering, a major experimental feature that distinguishes the configurations is the heating method. Thus a mainline heating approach that singles out the Tokamaks is anomalous ohmic heating followed by adiabatic compresssion. However, the LASL conception of a $\beta = 1$ belt pinch would prescribe magnetic implosion heating with subsequent slower compression. Our ideas of the reversed-field pinch similarly incorporate implosion heating as an essential element.This concept is not necessarily shared by other laboratories on other continents.

G. Stability of Diffuse Toroidal Z-Pinch Equilibria (D. A. Baker and L. W. Mann)

We have been successful in demonstrating the existence of diffuse toroidal Z-pinch equilibria that are MHD stable. Previous Z-pinch stability analyses have applied to cylindrical straight systems only.

The numerical approach offers a method for studying realistic diffuse profile toroidal equilibria that are free from restrictions on boundary shapes and aspects ratios.

1. Method Summary. We first determine a numerical solution to the static MHD equations*

$$\vec{j} \times \vec{B} = \vec{\nabla} p$$
$$\vec{\nabla} \times \vec{B} = \mu \vec{j}$$
$$\vec{\nabla} \cdot \vec{B} = 0$$

subject to boundary conditions for a perfect conductor. The solutions are obtained by iteration of the difference equation corresponding to the nonlinear differential equation governing the poloidal flux function ψ.

$$r \frac{d}{dr} \frac{1}{r} \frac{d\psi}{dr} + \frac{d^2\psi}{dZ^2} = F(r,\psi) \quad .$$

The source function F depends upon the choice of pressure and toroidal current distributions that are used.

*We use rationalized MKSD units with vacuum permeability denoted by μ.

Having the equilibrium solution, we test it for MHD stability by first expressing δW as a discrete quadratic form. For Z-pinch configurations having nearly circular cross sections, a truncated double Fourier expansion of the integrand of the δW integral in the toroidal and poloidal field directions (suggested by LASL's B. R. Suydam) has proven to be practical. This allows an analytic integration over two variables. The final integration is written using a finite-difference formula. This results in δW being represented by a large quadratic form. The stability test proceeds by diagonalizing the coefficient matrix for each toroidal mode number. The appearance of any negative coefficient in the diagonalized form corresponds to instability. If a particular equilibrium has a positive definite quadratic form, stability is demonstrated within the resolution of the calculation.

2. Application. We used this method to solve the problem of finding an MHD stable toroidal Z-pinch configuration that is directly applicable to the LASL ZT-1 experiment. We imposed the following requirements on the equilibrium: (1) hollow pressure profile, (2) vacuum-field region outside the pinch with a small amount of reversed toroidal field, and (3) aspect ratio and field configurations having general characteristics similar to ZT-1. The result of this study is the toroidal equilibrium having the profiles shown in Fig. VI-10. This equilibrium was tested for stability for toroidal wavelengths extending from 1 mm to the machine circumference (240 cm) with 17 coupled poloidal m modes and 24 integration intervals and found to be stable for this numerical resolution. In a numerical approach such as this one, a question always arises concerning the resolution to be used, i.e., the fineness of the equilibrium mesh, the number of modes included, and the size of the integration intervals. This is particularly important if extremely localized unstable modes exist. For these calculations, we used a resolution comparable to radius. More refined calculations extend beyond the applicability of the MHD model.

Our studies so far indicate that stable profiles may exist with poloidal β of 50% when the equilibrium currents extend all the way to the walls. We are currently investigating the β limitations imposed by stability when vacuum fields exist between the plasma and the wall as typified in Fig. VI-10. We also expect this method to be useful for studying high-β Tokamaks.

The work done to date demonstrates that a numerical approach is practical in achieving a closer correlation between experiment and MHD theory by allowing analyses of toroidal equilibria with realistic profiles.

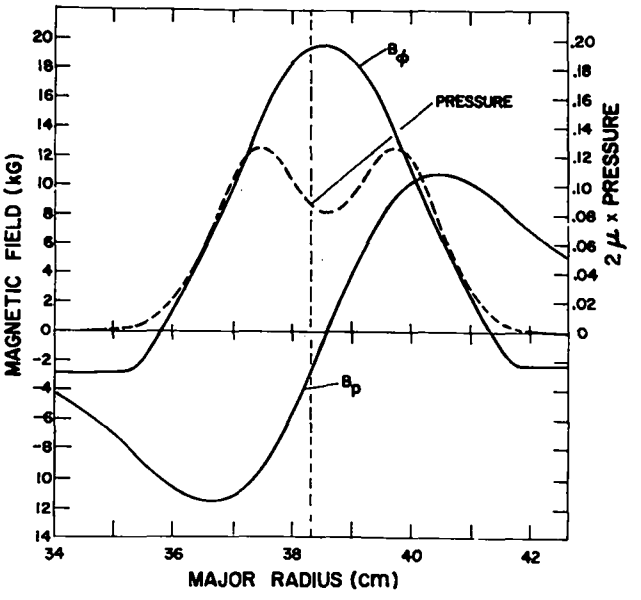

Fig. VI-10.
Distributions of plasma pressure, toroidal and poloidal magnetic fields ($B_\theta B_p$) along a major radius of a numerically determined MHD stable toroidal Z-pinch equilibrium.

H. Numerical Simulation with a Continuous Distribution of Initial Particle Positions (H. R. Lewis and I. J. Cherry)

A different approach to the numerical treatment of Vlasov plasmas was worked out wherein the particles are distributed continuously. This is an outgrowth of previous work.[1] A major objective is to significantly decrease the computer storage requirements compared to the storage necessary for simulation with discrete particles. Although only the relatively simple problem of electrostatic oscillations in one dimension has been considered, the approach can be extended to include more dimensions and magnetic forces.

In the one-dimensional electrostatic problem, we allow only a discrete set of initial velocities, but for each initial velocity the particles are distributed continuously with respect to their initial positions. (The restriction to a discrete set of initial velocities was made for convenience, and is probably not necessary.) For each initial velocity the time-dependent particle position is approximated as a time-dependent piecewise linear function of initial position. The values of position at the nodes of these piecewise linear functions are the dynamical variables.

Between each pair of adjacent nodes a continuum of particles is represented. This should lead to a significant reduction in the computer storage requirement by reducing the number of dynamical variables required. The equations of motion are determined from the variational principle.

The use of piecewise linear functions has two important consequences. First, when piecewise linear functions are used, we find that the electric field can be calculated in closed form in terms of simple functions. Second, definite integrals that occur in the equations of motion and that must be evaluated at each time step can also be calculated exactly in closed form in terms of simple functions. This overcomes a difficulty that was encountered in the previous attempt to treat a continuum of particles.[1] A possible disadvantage of this procedure is that the computational time may turn out to be excessive.

A computer code has now been written to implement this approach. The code will be used to investigate the merits of the approach.

REFERENCE

1. H. R. Lewis, chapter in *Methods in Computational Physics* (Academic Press, Inc., New York, 1970), Vol. 9, edited by B. Alder, S. Fernbach, and M. Rotenberg.

I. An Empirical Closure Relation for the Vlasov Moment Equations (H. R. Lewis and B. J. Feldman)

Satellite measurements of the interplanetary plasma have recently become sufficiently detailed to provide rather complete knowledge of the proton and electron velocity distributions. Recently, with LASL equipment aboard the IMP-6 spacecraft, the velocity distributions projected onto the ecliptic plane were measured repeatedly at 5-min intervals with a 90-sec sampling time. The zeroth through third moments of the proton velocity distributions measured over a three-month period have been computed. During that time we observed the plasma to be in various stages ranging from nearly isotropic to highly anisotropic and nonthermal. Analysis of the data indicates a simple statistical relationship between each of the third moments, $Q_{\parallel}$ and $Q_{\perp}$, and the two second moments, $T_{\parallel}$ and $T_{\perp}$. The range of observed values of $T_{\parallel}/T_{\perp}$ is divided into small subintervals. For each subinterval the mean values of $q_{\parallel} \equiv Q_{\parallel}/(1.5nkT\sqrt{2kT_{\parallel}/m})$ and $q_{\perp} \equiv Q_{\perp}/(1.5nkT\sqrt{2kT_{\parallel}/m})$ are computed, where $T = (T_{\parallel} + 2T_{\perp})/3$, n = proton number density, k = Boltzmann's constant, and m = proton mass. The statistical relations are that the mean values of $q_{\parallel}$ and $q_{\perp}$ are linearly related to $T_{\parallel}/T_{\perp}$, that is,

$$\langle q_{\parallel} \rangle = A + B\,(T_{\parallel}/T_{\perp})$$

and

$$\langle q_{\perp} \rangle = C + D\,(T_{\parallel}/T_{\perp}) \quad .$$

These relations are in effect empirically determined average closure relations for the Vlasov moment equations. A description of the satellite observations and a discussion of these relations will soon be published.[1]

The possibility that these results are evidence for a valid and useful truncated moment equation description of fully developed nonlinear collisionless plasmas that may be applicable to CTR devices is being pursued.

REFERENCE

1. W. C. Feldman, J. R. Asbridge, S. J. Bame, and H. R. Lewis, to be published in Phys. Rev. Letters.

J. Linear Stability Analysis of High-β Plasmas (J. P. Freidberg and H. R. Lewis)

The Vlasov-fluid model[1] was proposed as the starting point for a more realistic study of the stability of high-β plasmas than is possible in terms of the usual ideal MHD approximation. In the Vlasov-fluid model the ions are treated as collisionless, the electrons are treated as a massless fluid, charge neutrality is assumed, and the displacement current in Maxwell's equations is neglected. Also, the equilibrium ion distribution function is required to be a function only of the total energy. With these assumptions, the allowed equilibrium configurations of the magnetic field, the criterion for marginal stability, and an estimate of the m = 1 growth rate for the case of a θ pinch with a small azimuthal magnetic field are identical in the Vlasov-fluid model and ideal MHD. However, an estimate of the growth rate for m = 2 can be much smaller in the Vlasov-fluid model than in ideal MHD for a hot θ pinch with a small azimuthal magnetic field. These estimates of m = 1 and m = 2 growth rates within the framework of the Vlasov-fluid model are in semiquantitative agreement with experimental observations. This agreement encourages further application of the model to experimental situations.

To enable numerical computation of growth rates using the Vlasov-fluid model for a wide range of equilibria, including diffuse profiles, a new formulation[2,3] of the linearized Vlasov-fluid model was developed using ideas that were effective in a numerical treatment of

one-dimensional electrostatic oscillations, which were based on Hamilton's variational principle for collisionless plasmas.[4] The formulation is in terms of two functions, $s(\underline{r},\underline{v},t)$ and $\underline{\xi}(\underline{r},t)$. The function $s(\underline{r},\underline{v},t)$ is related to the perturbed ion distribution function and particle orbits, and $\underline{\xi}(\underline{r},t)$ is related to the perturbed vector potential and is analogous to the MHD plasma displacement function. The function $s(\underline{r},\underline{v},t)$ is expanded in a series of eigenfunctions of the unperturbed Liouville operator, and $\underline{\xi}(\underline{r},t)$ is expanded in a series of eigenfunctions of the incompressible ideal MHD operator. Use of the functions $s(\underline{r},\underline{v},t)$ and $\underline{\xi}(\underline{r},t)$ with these expansions has two important practical consequences. First, it is expected that a few MHD eigenfunctions are required for representing $\underline{\xi}(\underline{r},t)$ in order to determine the effect of finite ion gyro radius on the gross stability properties of the plasma. Second, the algebraic eigenvalue equation that determines the eigenfrequencies has a particularly advantageous form for computational purposes. The form is

$$\det\left[(L-\omega)-\omega\sum_{\ell=1}^{N}\left(i\omega a^{(\ell)}-b^{(\ell)}\right)c^{(\ell)\,\dagger}\right]=0\quad,$$

where L is a diagonal hermitian matrix, $a^{(\ell)}$, $b^{(\ell)}$, and $c^{(\ell)}$ are column vectors, ω is the eigenfrequency, and $\dagger$ denotes hermitian adjoint. The integer N is the number of MHD eigenfunctions used for $\underline{\xi}(\underline{r},t)$. The dimension of the matrix quantities equals the number of eigenfunctions of the Liouville operator used to represent $s(\underline{r},\underline{v},t)$. Because the number of Liouville eigenfunctions required can be quite large, the dimension can easily be too large to enable the determinant to be evaluated by usual techniques. However, this particular form of the determinant allows it to be evaluated in terms of an N x N determinant whose elements can be computed from inner products involving L, $a^{(\ell)}$, $b^{(\ell)}$, $c^{(\ell)}$, and ω. Because N is expected to be small, the determinant can be evaluated and the eigenfrequencies determined.

A computer code has been written that applies this formulation of the Vlasov-fluid model to equilibria that are axially and translationally symmetric, that is, to equilibria that depend only on the radial distance from an axis of symmetry. Computations have been carried out for an equilibrium with a sharp boundary profile. For this example we verified analytic estimates of growth rates given in Ref. 1, and observed that growth rates for unstable perturbations are insensitive to the number of MHD eigenfunctions used to represent $\underline{\xi}(\underline{r},t)$. That is, all values of N between 1 and 5 give nearly the same growth rate in each example that has been considered so far. This is an encouraging result. Also encouraging is the observation that growth rates are not very sensitive to the number of eigenfunctions of the Liouville operator used to represent $s(\underline{r},\underline{v},t)$. If these preliminary observations remain valid for diffuse profiles, then this method of stability analysis will be quite powerful.

We acknowledge the contributions made to the numerical and computational aspects of this work by P. N. Iwanchuk, B. L. Buzbee, and J. H. Hancock of LASL's C-Division, and G. H. Golub, C-Division consultant.

REFERENCES

1. J. P. Freidberg, Phys. Fluids 15, 1102 (1972).

2. H. R. Lewis and J. P. Freidberg, Bull. Am. Phys. Soc. 17, 846 (1972).

3. H. R. Lewis and J. P. Freidberg, paper 41 in Proceedings of the Fifth European Conference on Controlled Fusion and Plasma Physics (Grenoble, France, August 21-15, 1972).

4. H. R. Lewis, Phys. Fluids 15, 103 (1972).

K. Comparison of Numerical Simulation Algorithms

1. One-Dimensional Algorithms (H. R. Lewis, LASL, and S. J. Gitomer and D. I. Brown, University of Pennsylvania). We recently compared four plasma simulation algorithms in one dimension using a stable plasma as a test problem.[1] The objectives of the comparison were to investigate (a) the utility of using a higher-order representation of the scalar potential than piecewise linear, and (b) the effects of smoothing the electric field as opposed to calculating it from the gradient of the scalar potential at every point. No marked differences between the four algorithms were noted with the stable test problem, but it was nevertheless a possibility that significant differences might be manifest if an unstable plasma were used. The same algorithms have now been compared using a plasma that is two-stream unstable. Again, no marked differences between the algorithms were observed. However, as in the stable test problem, a strong dependence of the long-time behavior on initial conditions was noted with the unstable test problem for each algorithm. The differences in temporal behavior that result from differences between the algorithms could not be distinguished from differences in temporal behavior that result from differing random numbers used in generating the initial conditions for each algorithm.

2. Two-Dimensional Algorithms (H. R. Lewis, C. W. Nielson, and L. Rudsinski). Tests of some two-dimensional numerical simulation algorithms for electrostatic oscillations have been made using two-stream unstable test problems. The objectives were to investigate

(a) the utility of using the nine-point variational scheme for the Laplacian operator[2] as opposed to the usual five-point scheme, and (b) the effects of smoothing the electric field as opposed to calculating it from the gradient of the scalar potential at every point. The results were much the same as with the one-dimensional tests described above. No significant difference between the algorithms was observed. It was difficult to distinguish differences resulting from differences between the algorithms from the strong dependence of the temporal behavior on initial conditions that exist for each algorithm.

REFERENCES

1. H. R. Lewis, A. Sykes, and J. A. Wesson, J. Computational Physics 10 85 (1972).

2. H. R. Lewis, *Methods in Computational Physics*, Vol. 9, p. 307 (Academic Press, New York, 1970).

VII. SHERWOOD ENGINEERING

A. Scyllac Support

1. Toroidal Sector (W. H. Borkenhagen, C. F. Hammer, and K. W. Hanks). The first five racks of Scyllac were installed as a 120° sector of a 2.5-m-major-radius toroidal system. These racks were first fired into a 5-m-long coil sector on April 1, 1971. The final sector shot, No. 2117, was fired December 29, 1972. Approximately 65% of these shots were fired at 45 kV; the remainder were fired at 50 kV. During this period the sector operated with 525 capacitors and spark gaps and 3,150 load cables, which accounted for only one-half of the components available in the racks. This reduced energy allowed more time to study the plasma drift in the curved geometry.

The sector experiment was plagued with the usual start-up problems during the first 200 to 300 shots. There were numerous prefires until the cause was diagnosed as a loss of bias problem. This we corrected by connecting a ballast capacitor to the common bias circuit and by adding a 300-Ω resistor in series with the charge lead of each capacitor. The only other circuit modification was a cross-triggering scheme for the crowbar circuit so the system is crowbarred even if one-half of the crowbar trigger system malfunctions. The only significant component problem was the reliability of the crowbar trigger cables. These cables were seriously overstressed due to space limitations, but they did not prevent the system from operating satisfactorily for 50 to 100 shots with a minimum of maintenance.

The physics experiments involved various combinations of $\ell = 0$ and $\ell = 1$ fields being applied to the plasma column. The main field coil was redesigned and remachined for the majority of the experiments. The $\ell = 0$ fields were generated by making periodic grooves in the main field coil. Three different groove depths were tried; each groove was filled with a different Inconel insert called a stuffer. The stuffer generated a smooth field during the implosion phase of the discharge and became an inverse mirror as the flux leaked through the hollow, high-resistant insert. In one experiment the Inconel stuffers were replaced with polyethylene-coated shells to simulate a smooth coil surface.

After various experiments with helical $\ell = 1$ windings, the main field coil was redesigned and machined with a sinusoidal helical bore along the Z axis to produce a passive $\ell = 0$ and $\ell = 1$ field. The $\ell = 1$ windings were retained to vary the $\ell = 1$ field.

Finally, a new main coil was designed for passive $\ell = 0$ and $\ell = 1$ fields. Also incorporated into the design was a feedback stabilization coil system. The $\ell = 1$ helical bore of this coil was machined in 0.050-in. steps, thereby producing a relatively smooth field. This coil was used for the final experiments on the toroidal sector.

New load coils and transition sections have been designed for the 4-m-radius machine.

2. Linear Experiment (W. H. Borkenhagen, K. W. Hanks, and W. H. Harris). The linear experiment shown in Fig. VII-1 consists of five racks driving a 5-m-long plasma coil with an additional rack on each end to drive a mirror coil. The first plasma shot on this system was fired on March 13, 1972. All the linear racks use the full complement of components: 1,050 capacitors and spark gaps and 6,300 load cables in the plasma system, with another 420 capacitors and spark gaps and 2,520 load cables in the mirror racks. The five plasma racks have been fired on over 400 shots, whereas the mirror racks have been fired on about 50 shots. Approximately 95% of the shots have been fired at 45 kV.

The linear system was installed after the sector system was in operation, thus most of the system problems were corrected during installation. No new problems appeared in the energy system, but an insulation problem did occur in the mirror-coil collector plates. The mirror coils typically operate at ~180 kG thereby causing some flexing in the transition section between the coils and the collector plates. This flexing cuts through the insulation between the plates after ~10 shots, allowing a voltage puncture with a resulting mechanical shock that crushes the discharge tube. This problem could be solved by adding an elaborate "C" clamp, but the time schedule for this experiment does not permit for its design and fabrication. Therefore, after each 10 shots, the mirror coils and transition sections are disassembled and new insulation is installed. The linear experient was terminated by the end of February 1973.

3. Toroidal Conversion (H. W. Harris, C. F. Hammer, K. W. Hanks, W. H. Borkenhagen, and J. J. Banta, ENG-7). Scyllac was proposed in 1966 as a 15-m circumference, completely toroidal experiment, but was initially

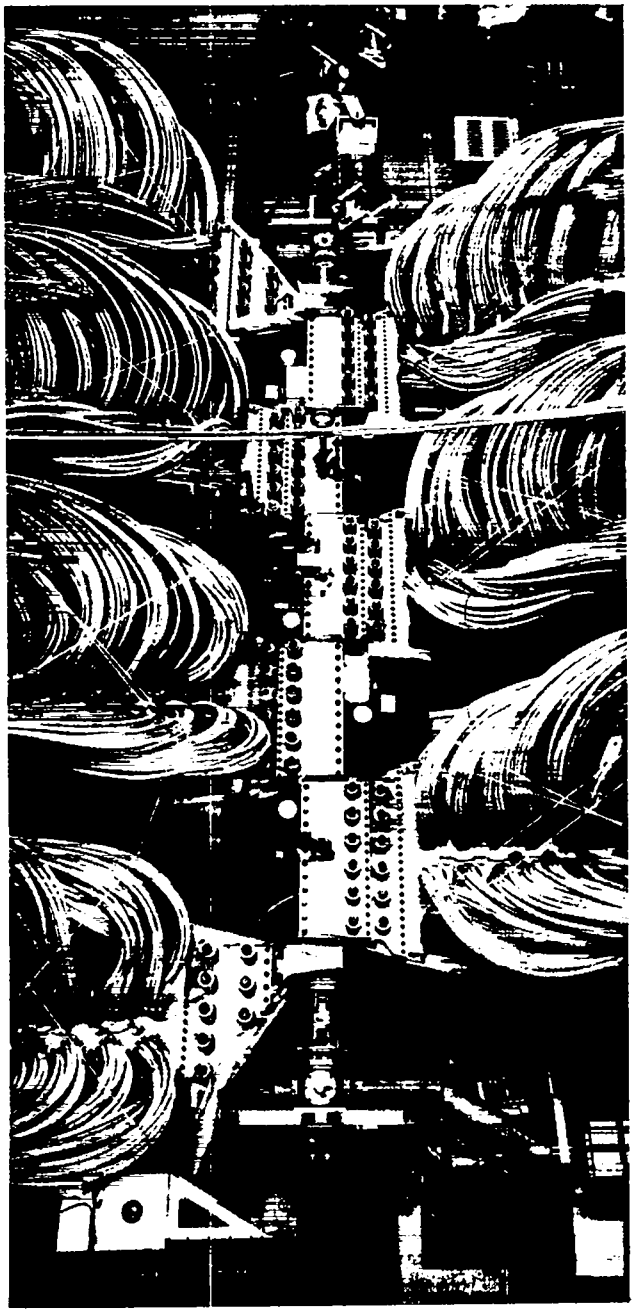

Fig. VII-1.
Linear Scyllac compression coil.

installed as a 120°, 5-m-long toroidal-sector experiment, and a 5-m-long linear experiment with mirrors on each end. Early plans called for the conversion to a full torus to begin in 1973; this is now being done.

When the physics data from the 5-m sector indicated that a larger torus would be desirable, a study was made to determine the maximum radius torus that could be installed in the Scyllac building using the existing energy system. This study showed that an 8-m-major-radius experiment that would produce a hot, dense plasma comparable to the Scyllac toroidal-sector plasma could be installed. Although this scheme was not formally proposed until mid-November, the plan was implemented on January 2, 1973. The new plan adds about $250,000 to the original $800,000 conversion cost, but the time schedule remains at one year.

The principal considerations in the conversion design study were to minimize the time and labor involved in moving the capacitor and machine racks, and to avoid the necessity of new hardware in the larger radius system. The original conversion scheme involved the disassembly of each rack and reassembling it at its new location. This expensive and time-consuming plan was abandoned after a careful study showed that an entire rack structure, consisting of a capacitor rack and an independent machine rack, could be moved as one assembly with the use of air pallets. Air pallets are round, flat devices that have been commercially developed to lift considerable loads on a cushion of escaping air around their periphery. After the machine and capacitor racks are firmly clamped together with large structural beams, 42 air pallets are installed under each rack. When a constant pressure of ~18 psi is applied to the air pallets, the entire 90-ton structure is lifted about ¼ in. and is moved to its new location by one or two men with "come-along" jacks. All five of the sector racks were moved without difficulty. This technique has saved an immense amount of electrician and rigger time in disconnecting, moving, and reconnecting a rack.

The collector plate system was a serious concern in the consideration of a larger radius system. Each existing collector plate is ~7 ft wide at the back with a taper at the front to match a 1-m-long coil. A design study showed that if the plate were installed with the wide section toward the coil, it could match the longer, ~1.66-m coil by adding a new transition section. The cost of the entire 15-rack modified collector plate system is about $75,000 vs over $200,000 for a new collector plate system. Fabrication of the modified system is under way.

The general conversion schedule is as follows. Relocation of the five racks in the toroidal sector began January 2, 1973, whereas the linear experiment operated for eight more weeks. The sector racks are being moved back 39 in., and their collector plates modified to accommodate the larger radius coil. The present blast wall was removed in March, and two of the linear racks were moved into their proper position adjacent to the five sector racks. A blast wall was installed in front of the seven racks. The original five-sector racks will be used for physics experiments with an 8-m-long coil from April until October. During this period the remaining eight racks will be arranged to complete the toroidal geometry, connected,

and checked out. In October the blast wall will be removed and the entire system integrated. Toroidal physics experiments will begin by January 1974.

4. Mirror Coil Development (A. G. Bailey, G. P. Boicourt, and K. W. Hanks). A typical θ pinch requires a maximum field strength of ~100 kG; therefore, it is common to make the one-turn field coils from a high-strength aluminum alloy. However, the mirror coils for the linear Scyllac experiment anticipated a maximum field requirement of 250 kG; thus a program was instituted to develop a high-strength coil for this application. The coil was evaluated on the Scyllac prototype system, which includes a 178-kJ, 60-kV capacitor bank with a scaled-down Scyllac collector plate.

Preliminary design considerations showed that the current density along the length of the coil would exceed 200 kA/cm of length. This dictated the general outline of the coil assembly, which had a wide termination ~14 in. at the collector plate and tapered to a narrow coil. This type of coil should have a welded joint at the midplane to increase the stiffness of the entire assembly and minimize the deflection of the tapered plates between the coil and the collector plate. In addition, the coil should have a low electrical resistance to maximize the current from the capacitor bank.

Calculations were made to determine the coil bore and length required to produce a 250-kG field with the Scyllac prototype energy system. The first calculation assumed a copper-lined coil and suggested a 2-in. bore, 5.75-in.-wide coil with generous end radii. The second calculation assumed an all-steel coil and suggested a 1.6-in. bore with all other dimensions being the same as the copper-lined coil.

Both designs were built and tested; the copper-lined model first, and two steel models later. The copper-lined coil was made by forming a 3/8-in. continuous copper sheet to the proper contour and placing it inside two steel clamshells that were bolted together at the midplane. This coil was tested to determine the accuracy of the design calculations and the mechanical characteristics of the design.

Although the calculations predicted a maximum field of 250 kG, the initial measured peak field was only 200 kG. Refinements of the calculations finally predicted a maximum field of 215 kG, and when the capacitor bank was well tuned and warmed-up, it produced a measured peak field of 215 kG.

The current risetime in the coils under test was ~2.5 μsec, which was a bit too fast for effective crowbarring at the peak field. The coil current was usually crowbarred about 75% after peak and then decayed with an L/R characteristic of 200 μsec. Because the peak field was applied for such a short time, the actual field of interest was the crowbarred field. This value will be used as the applied field in the following discussion.

The copper-lined steel coil was run for over 350 shots to determine its mechanical characteristics with the last 40 shots at 150 kG or above. The outer steel geometry was essentially unaffected from the test. The copper liner in the coil area showed little damage, but the copper feed plates from the collector plate termination to the coil were literally extruded out the sides. This was probably due to flexing of the steel coil at the midplane joint, which allowed the whole coil to scissor open and slap back together thus deforming the copper plates outward. This design was deemed unsuitable for the linear mirror coils.

The first prototype all-steel coil was made from Type 250 Maraging steel, which is a high-strength steel with relatively low resistance after heat treatment. This material has good welding characteristics and will not deform in heat treatment. This coil was machined with a flat butt joint at the midplane that was suitable for electron-beam welding. An x-ray inspection of the first electron-beam weld revealed considerable porosity. The coil had to be remachined and rewelded several times before a suitable joint was attained.

The coil assembly was then tested before heat treatment with an applied field of 141 kG and operated satisfactorily for over 50 shots. The coil was then modified with a larger radius on each end and heat-treated to improve its resistance. This version produced an applied field of 186 kG. This coil was run for 100 shots above 180 kG with no detectable yielding or other difficulties so it was decided to make the Scyllac linear experiment mirror coils from Maraging 250 steel.

The Maraging 250 steel was ordered but a very slow delivery time precluded its use for the first mirror experiments on the linear experiment. Instead, two coils were made from T-1 structural steel, which has lower strength, but was considered adequate for the initial lower mirror field experiments. Various samples of T-1 steel plates were electron-beam welded to develop the proper technique for this material. However, several problems were discovered when the machined coil sections were welded. The residual magnetism in the material and the nonsymmetrical geometry of the pieces caused the electron beam to drift away from the joint. These problems were partially corrected by degaussing the pieces and inserting a dummy shim to correct the geometry problem.

After considerable fabrication development, two T-1 steel mirror coils were installed on the linear system and operated with an applied field up to 180 kG. However, due to the flexing in the feed plates, the insulation punctured on both coils on the same shot. The resultant

blast and shock wave cracked the midplane welds on both mirror coils. The coils were then machined for a sandwich current joint at the midplane and were reinstalled. They are presently operating at a maximum field of 180 kg, although they must be disassembled for new insulation after each 10 shots as mentioned earlier.

Although there have been few failures with aluminum coils in normal θ-pinch experiments, no actual tests have been made at this Laboratory to determine the maximum field for aluminum coils. A 2014-T652 aluminum coil, 1.6-in. bore by 5.75-in.-wide with a 1.25-in.-end radii, was fabricated and tested to failure to provide some data for future designs. This coil assembly was fired for 100 shots with ~70% of them with an applied field of ~150 kG. The remaining shots were above this value with six shots, including the final one, at 212-kG applied field. On the last shot the coil failed at the welded midplane joint and at the joint to the collector plate. It was observed that the midplane failure was in the parent material rather than in the welded material.

This development program showed that the coil designs now used for our θ-pinch machines are limited by the coil geometry, including the feed plates, rather than by the pressure-vessel characteristics of the coil itself. This investigation also showed that aluminum coils with the usual unsupported feed-plate designs should not be used above ~125 kG.

B. Z-Pinch Support

High-Energy Fuse Development (R. S. Dike and R. A. Haarman). The ZT-1 toroidal Z pinch uses four identical fuses to interrupt the current flowing through a storage inductor from a capacitor bank. When this current is suddenly interrupted it generates a voltage spike that breaks down a spark gap and transfers the current into the primary of the toroidal Z pinch. Although the present fuse design operates satisfactorily in the ZT-1 experiment, a larger energy fuse or pair of smaller fuses will be required for the next larger version of this experiment. The following gives the characteristics of the present fuse and those required for the larger fuse.

	Present Fuse	Larger Fuse
Bank charge voltage	14 kV	20 kV
I_p through fuse	250 kA	1000 kA
Energy dissipated in fuse	12 kJ	40 to 60 kJ

An experimental test system was built to evaluate various fuse concepts. The energy system consists of an ignitron-switched, 20-kV, 60-kJ capacitor bank with an 85-nH inductor in series with the fuse. The phenolic fuse clamp assembly is adaptable to various fuse packages. The system is instrumented to accurately measure and record the fuse current and voltage waveforms.

The first objective was to duplicate the performance of the sand fuses being used on ZT-1. The second objective was to develop a larger fuse, or to develop a fuse design that would allow two more modest fuses to be mounted, one above the other, at the fuse termination on the ZT-1 experiment.

The sand fuse consists of a 0.002-in.-thick hairpin-shaped copper foil, 7 in. long with various widths of 1 to 2 in., depending on the energy involved. This geometry is inserted into an insulated container, which is then filled with a fine glass-bead material that is always referred to as sand. Over 100 sand fuses were fired.

The experimental system duplicated the performance of the fuses in ZT-1 that conduct 250 kA, generate 55 to 60 kV at current interruption, and dissipate 12 kJ. These tests also showed that this fuse package can dissipate 30 kJ, while conducting 350 kA, and generate an 80-kV voltage spike at current interruption. The biggest disadvantage of the sand fuse is the installation and removal problem in the ZT-1 machine. The sand often spills, or some of it is ejected when the fuse explodes. This problem has led to the investigation of other quenching materials and containment geometries.

The sand in the sand fuse serves two purposes—it absorbs the blast wave from the exploding foil, and it extinguishes the arc. A basic objective of the new fuse design was to separate these two functions. A fuse container was designed with two chambers, a shock absorber, and an arc-quenching chamber. The shock-absorbing chamber is a split right-circular cylinder, each half having a rubber-diaphragm wall with the volume behind it filled with lead shot. These two half cylinders are separated to allow various fuse-quenching packages to be installed between them. The shock-absorbing chamber works quite well up to energies of 15 kJ.

Various materials have been evaluated in the arc-quenching package. Figure VII-2 shows the results of several tests. The sand, glass bead, result is from the conventional sand-fuse design and is used as a reference. The best fuse package used fine fibrecloth to extinguish the arc and gave about 70% of the sand-fuse voltage. The other materials gave even less voltages. This program will continue with the study of more materials and different package designs including an enclosed sand-fuse package that can be mounted in an inverted position, a feature not possible with the present ZT-1 fuse package.

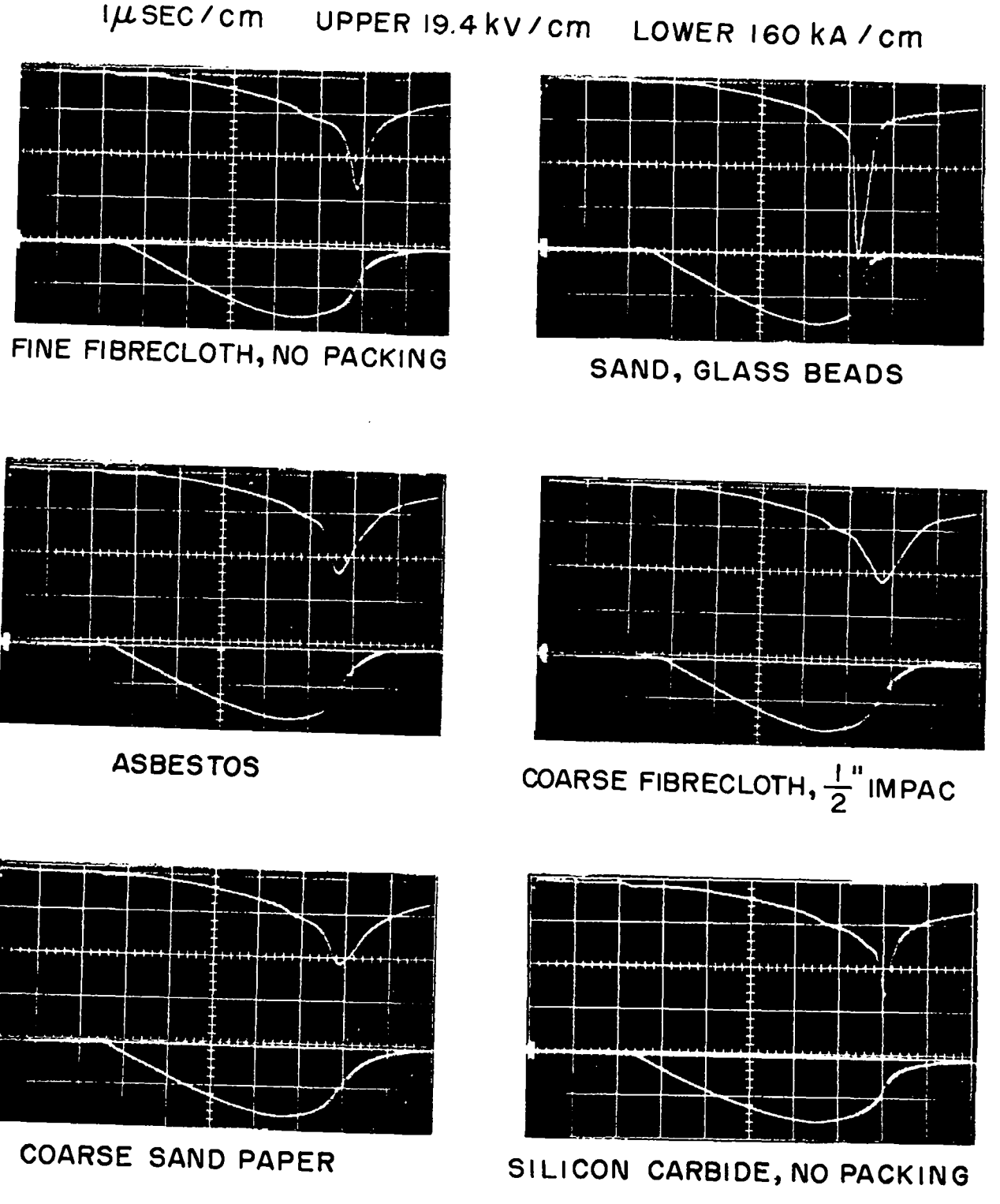

Fig. VII-2.
Voltage and current pulses for various quench materials.

C. Implosion-Heating Experiment (G. P. Boicourt, K. W. Hanks, and R. W. Kewish, Jr.)

The basic objective of the implosion-heating experiment is to heat a preionized plasma with a magnetic field that rises to 10 kG in ~100 nsec and remains at near that value for ~500 nsec. Several different concepts were investigated. These investigations included a mechanical design study and a circuit analysis of the system. The system selected for this experiment consists of four 125-kV, pulse-forming networks feeding a 40-cm-diam, 1-m-long, quarter-turn coil. Each network will be pulse charged with two 160-kV low-inductance Marx banks in parallel. The pulse-forming networks will use groups of 0.2-μF, 125-kV and 0.4-μF, and 125-kV low-inductance capacitors and will be switched with multichannel rail spark gaps. The circuit performance of the mechanical design has been extensively analyzed and appears satisfactory. Most of the hardware has been designed or specified and ordered. The final design of the transmission system only awaits the imminent solution to a voltage-creepage problem. A new 40-kV, field-distortion Marx gap was designed and is being evaluated for its voltage holdoff and triggering characteristics.

VIII. FUSION TECHNOLOGY

A. Introduction (F. L. Ribe)

During the past year there has been a considerable increase in fusion-technology activities. For the first time an integrated attempt is being made to formulate a Reference Theta-Pinch Reactor (RTPR), which includes studies on essentially all thermonuclear reactor system components. This work represents the beginning of a continued effort by LASL in collaboration with the Argonne National Laboratory (ANL). The initial results of the RTPR studies are reported in Ref. 1; reports incorporating modifications and improvements will be issued periodically.

B. Time History of the Thermonuclear Cycle (T. A. Oliphant)

The plot of the magnetic confining field vs time in Fig. VIII-1 gives a frame of reference for a discussion of the time history of the events that take place during a single pulse of the RTPR.

The initial sudden increase of B at point a follows the end of the piston-heating process that takes place on a relatively short time scale. The curve between a and b represents the time variation of the field as energy is transferred from the cryogenic storage to the confining field. The plateau between b anc c represents the constancy of the confining field during the main part of the burn. The curve between c and d represents the transfer of energy from the confining field back to cryogenic storage, thereby causing the thermonuclear reaction to be quenched. The magnetic field between d and e is held at a value that keeps the plasma away from the wall at all times during the removal of heat from the burnt plasma. The heat removal is accomplished by thermal conduction through a neutral gas layer that is introduced between the plasma and the wall at the time corresponding to point d in Fig. VIII-1. The cold fuel ash is then pumped out for recycling and replaced by fresh fuel.

C. Reversible Magnetic Energy Transfer and Storage (RETS) (K. I. Thomassen)

Reversible magnetic energy transfer and storage systems (RETS), appropriate to the compression, burn, and quenching phases of the reactor (points a through d in Fig. VIII-1), have been studied in detail by Thomassen.[2] Energy is transferred from a cryogenic magnetic energy source to the reactor compression coil by a torque-free system of coils. Because of the inertial nature of the transfer coils, the magnetic field rise in the compression coil takes on a roughly $\sin^2 \omega t$ form as shown in the curve from a to b of Fig. VIII-1. After the burn phase, the energy in the compression coil is returned to the cryogenic source. The wave form during this phase is shown in the curve from c to d of Fig. VIII-1. This latter energy will be reduced by dissipation in the reactor materials, but increased as a result of the work ΔW done on the field by the burning plasma. This energy transfer termed "direct conversion" is accomplished at essentially 100% efficiency.

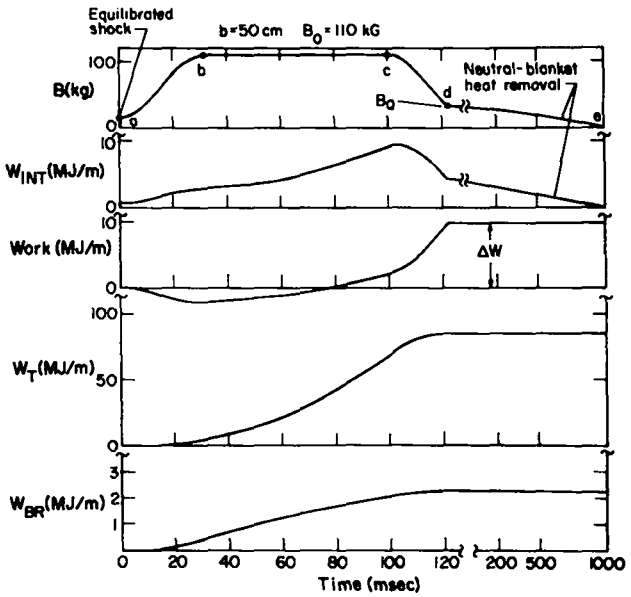

Fig. VIII-1.
Time history of a D-T plasma burn. The magnetic confining field B(kG), the time-accumulated values of the internal plasma energy W_{INT}(MJ/m), the work done by the plasma WORK(MJ/m), the total thermonuclear energy output W_T(MJ/m), and the bremsstrahlung energy W_{BR}(MJ/m) are plotted vs time (sec).

D. Staging

The technology involved in the initial implosion represented by the initial portion of the graphs in Fig. VIII-1

is discussed in Sec. V of this report. An interim experiment is being planned in which this type of technology will be used for the implosion phase of the heating, and the compression phase will be done using the Scylla-IV capacitor bank rather than the RETS system.

E. Numerical Studies of the D-T Plasma Burn

A basic thermonuclear burn code FP-29[3] (now called BURN-1) has been updated and modified to allow for a time-dependent magnetic confining field. The time-dependence feature is necessary because considerable burn takes place during the compression and quenching phases. The scope of the code encompasses the energy transferrence and burn plotted between points a and d in Fig. VIII-1. The initial conditions for input are the values of the basic parameters obtained at the end of the piston heating phase.[4]

The output of primary interest has been plotted in the remaining four curves in Fig. VIII-1. The quantities plotted are the internal energy in the plasma W_{INT}, the work done by the plasma WORK, the total thermonuclear energy carried by neutrons W_T, and the bremsstrahlung energy output W_{BR}. All of the energy quantities are given in megajoules per meter of length of the reactor and all are time-accumulated values.

F. Flushing and Refueling of a Pulsed Thermonuclear Reactor by Means of a Neutral Gas Layer

An attractive feature of a pulsed fusion reactor is the possibility of removing the alpha-particle "ash" resulting from the deuterium-tritium (D-T) fuel burnup and injecting new fuel by D-T gas flow between burning pulses. Thus, no diverter is required as in the case of a steady-state toroidal reactor. A layer of gas between the hot central plasma and the first wall can be used to cool, neutralize, and replace the partially burned D-T plasma. Sputtering problems are alleviated because heat transfer to the wall, which would otherwise occur by energetic ions, will now occur primarily by means of low-energy neutral atoms and to a lesser extent by ultraviolet and visible radiation. Cooling takes place between points d and e in Fig. VIII-1, and the removal of cold fuel ash takes place after point e.

The cooling process has been treated by the following simple mathematical model. It is assumed that at the initial time, i.e., immediately after quenching by magnetic expansion, the cooling layer is formed instantaneously by the introduction of a neutral gas of uniform density n_B and the temperature of the wall T_w. A quasisteady temperature profile quickly builds up by heat condution through the layer to the wall. Because the central plasma contains little or no magnetic field ($\beta \sim 1$), the thermal conduction in it is high enough to maintain an essentially uniform temperature. Therefore, the central plasma is represented in the model by a rigid, isothermal cylinder with a temperature T_a that decreases in time in accordance with the heat extraction. Although the central plasma radius R_a and the wall radius R_w are fixed, there will be internal motion as a result of pressure gradients arising from the changing temperature profile as heat flows through. The degree of ionization at various points will also change with changing densities and temperatures. We can assume that at each point in the layer the plasma and neutral gas are in temperature and ionization equilibrium. The plasma and neutral components are assumed to move together as a single fluid, although, as reported by Lehnert,[5] the pressure gradients of the separate components will tend to drive a relative motion. This effect is minimized in this system by a proper inclusion of the $\vec{v}\cdot\nabla\vec{v}$ terms in the momentum equations. Another assumption is that the D-T gas enters in the atomic rather than in the molecular state. This is not actually the case because the gas enters at the wall temperature of about 800°C. Although it is possible to consider the molecular dissociation in detail, it is not expected to make much difference because the dissociation energy is small compared to atomic ionization and excitation energies, and the change in thermal conductivities between atomic and molecular gases is insignificant compared to that between ionized and neutral gases.

Based on the above assumptions, we have obtained an analytic solution for the temperature profiles across the cooling layer for various times for a given initial cooling layer density n_B. The profiles for $n_B = 3 \times 10^{14}$ are plotted in Fig. VIII-2. The "breaking point" or "foot" of these profiles, which is a distinguishing feature, occurs at the transition from ions to neutral atoms and reflects the fact that atom thermal conduction is much greater than ion thermal conduction, and requires a much smaller temperature gradient.

Various values of n_B were selected, and, for each value, a number of profiles were calculated for different central plasma temperatures T_a. A corresponding value of the rate of heat flow $Q(T_a)$ was obtained for each profile. The time integral of the resulting function yielded T_a as a funtion of time t. This function was plotted in Fig. VIII-3 for a series of values of n_B. The intercepts of these curves with the t-axis gave a sequence of values of the "cooling time" τ or the time required to extract all the heat from the central plasma. These values were plotted against n_B in Fig. VIII-4 (solid curve) along with the fit (dashed curve) obtained by the expression

$$\tau = 0.0098\, n_B^{-1.56} \quad . \qquad (1)$$

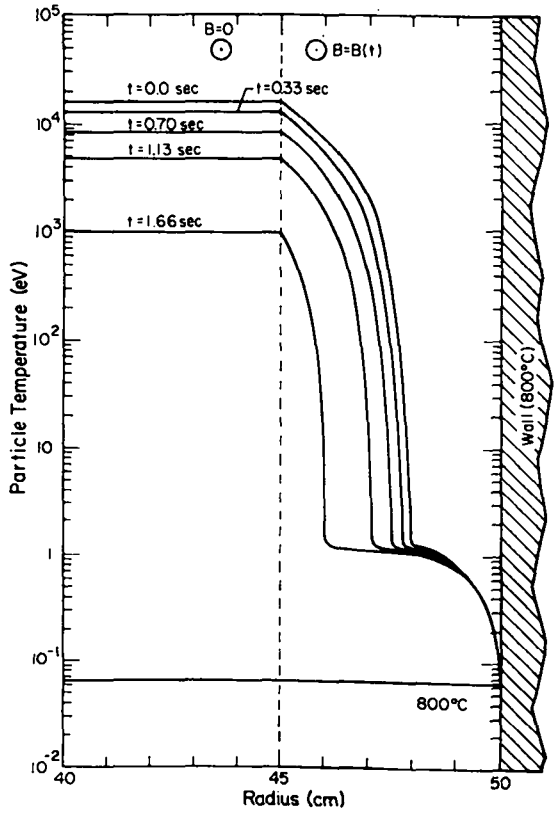

Fig. VIII-2.
Plasma temperature as a function of radius and time during the flushing cycle for an initial cooling layer density n_B of 3.0×10^{14} cm^{-3}.

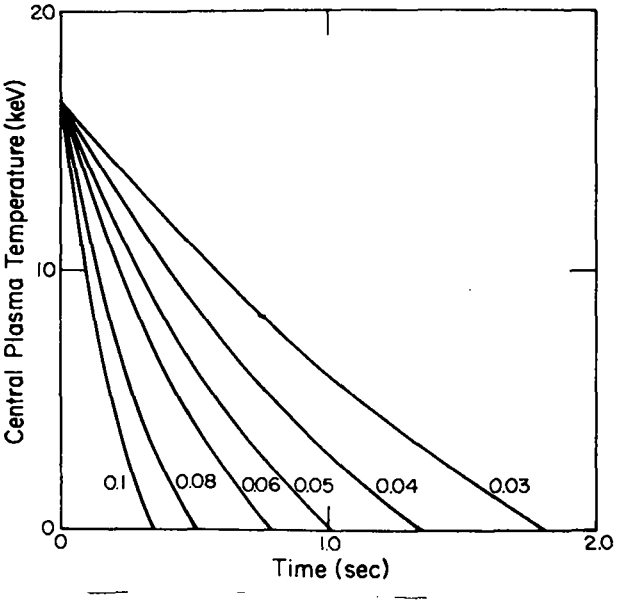

Fig. VIII-3
Central plasma temperature as a function of time during the flushing cycle for various initial cooling layer densities n_B scaled to 10^{16} cm^{-3}.

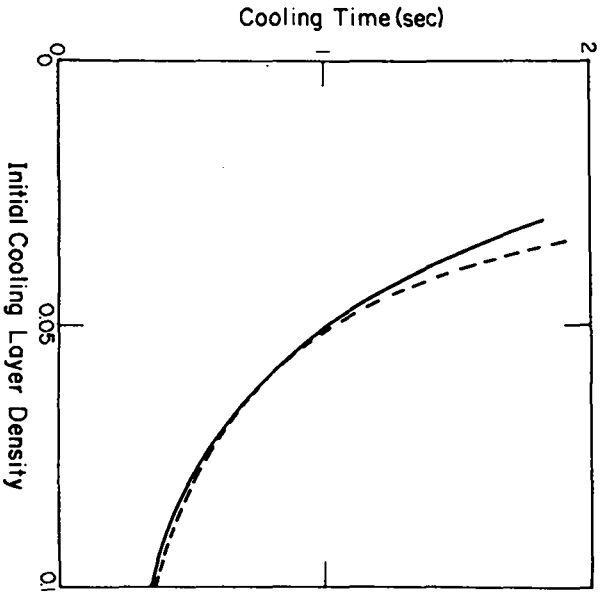

Fig. VIII-4.
Time required for complete cooling of central plasma as a function of the initial cooling layer density n_B scaled to 10^{16} cm^{-3} (solid curve), and the result obtained from the approximate formula (4.5) (dashed curve).

For different final burn conditions the constant in Eq. (1) changes, but the exponent stays very close to the same value. This result is very convenient for overall energy balance bookkeeping.

An important feature shown in Fig. VIII-3 is that the central plasma temperature drops approximately linearly with time. Therefore, to a good approximation, it is possible simply to use a constant value for heat flow through the first wall for wall-damage estimates. The physical reason for the almost constant heat flow rate is that the thermal conductivity in the maximum slope region in the curves shown in Fig. VIII-2 remains almost constant in time. This region mainly determines the rate of heat flow.

G. Federal Council on Science and Technology (FCST) Energy Study (S. C. Burnett, D. J. Dudziak, and F. L. Ribe)

During the first half of 1972, a major part of the LASL CTR program was concerned with the FCST study. After an initial meeting of the CTR Technology Committee in February, a review[6] of all major technological problems for a pulsed CTR was assembled. This review included 17 major technological areas defined at the February

meeting; input for many of these areas was received from LASL staff members with appropriate expertise. A draft of the review was used at a one-week working session at ORNL, where LASL presented a preliminary definition of technological problems to be overcome before entering the prototype reactor stage in approximately 1980.

At the ORNL working sessions, a special presentation was made on the neutronic aspects of the LASL conceptual design for a pulsed, high-β fusion reactor. This presentation was based principally on the neutronics calculations of George Bell. First wall integrity problems, hybrid fission-fusion systems, and radiation damage aspects of the LASL concept were discussed in detail. During the week at ORNL a special meeting on chemical aspects of CTR's was held to familiarize chemists and other CTR technologists with problems of chemical compatibility, tritium removal from lithium, corrosion, etc.

Dudziak assumed responsibility for chairing a Neutronics and Hybrid Systems Subcommittee. A report was prepared which included an eight-year national program for neutronic and photonic calculations, cross-section measurements and evaluations, integral experiments, and a proposed budget for FY 73 through FY 80. Chairmen of subcommittees on other technology areas made similar reports, which were then reviewed in preparation for the meeting at ANL. A tentative technological program was formulated, and a preliminary report was sent to the CTR Standing Committee. Also, the environmental and economic considerations for CTR's were discussed.

A final report for the FCST Energy Study was submitted in May 1972 by the CTR Technology Subcommittee. LASL's contributions to this report concentrated principally on defining the environmental and economic aspects of a fusion reactor penetration into the national energy grid. Specific systems studies were made to explore the perturbation of a reference energy system[7] for the year 2020, assuming introduction of commercial fusion reactors in the year 2000. To achieve the goal of a commercial reactor by the year 2000, reactor development programs for post-1980 were proposed and development costs estimated.

H. Neutronic Analysis (D. J. Dudziak)

1. Neutronic Analyses of the RTPR. A thorough neutronics analysis was performed for the current θ-pinch reactor reference design. A detailed model that consisted of 12 regions and 73 mixtures was devised. Difficulties experienced because of the size of the problem, which uses 100-group P_0 through P_3 cross sections with a table length of 60, were overcome by premixing cross sections for the discrete-ordinate transport code DTF-IV.[8] Initially, a one-dimensional DTF-IV calculation, which provided a detailed reference design calculation, was performed with premixed cross sections. In the future the cross sections will be collapsed to a more manageable group structure for parametric studies of the design. We have acquired a code that will perform flux-weighted regional (space-energy) collapsing by using DTF cross sections and output fluxes. Studies will be performed to determine a sufficiently accurate minimum group structure. Similar collapsing will need to be performed on 100-group kerma factors, radiation damage (displaced atom), and other response functions.

Neutronic analyses have provided complete information for breeding ratio, neutron balance, neutron and gamma heating, helium production, displaced atom (dpa), transmutation, and other reaction rates. Although optimization studies have not yet been started, two obvious variations of the RTPR design were analyzed in an attempt to improve breeding. The first variation, Mod 4, replaced 10% of the graphite region (see Fig. VIII-1) with natural lithium and improved the breeding ratio by 0.03. The second, Mod 5, replaced 10% of the copper compression coil with natural lithium, adding only 0.01 to the breeding ratio. In the original RTPR analysis (Mod 1), about 10% of the neutrons produced are absorbed parasitically by niobium structure in the graphite region. Another 10% are absorbed in the copper compression coil. Replacing 10% of the graphite with lithium is feasible and perhaps even desirable from an engineering design and heat-removal viewpoint; replacing 10% of the copper coil is much more difficult.

All transport calculations thus far have been performed with DTF-IV, using S_4-P_3 in cylindrical geometry. Previous studies on the CTR Benchmark showed S_4 to be adequate to predict integral quantities, such as breeding ratio, within 2%. The assumption of cylindrical geometry is an excellent approximation because of the very high aspect ratio ($\sim$40) of the θ-pinch reactor. Cross sections for the nine materials comprising the reactor blanket were 100-group, infinitely dilute, P_3 multigroup values processed from ENDF-III. Many studies have demonstrated the sufficiency of a P_3 truncation of scattering matrices.

Figure VIII-5 shows a section of the cylindrical model used for all calculations. Because the θ-pinch reactor concept is not sensitive to neutron transport through the outer shield, i.e., no superconducting-coil magnet surrounds the reactor, the model included only the "mop-up" blanket. This blanket provides a very minor contribution of 0.0027 to the total breeding ratio of 1.071,* thus

*Accounting for resonance self-shielding in niobium is estimated to raise the breeding ratio by about 5 to 1.12%.

it may well be replaced by shielding in further detailed optimization of the RTPR. In fact, even the beryllium provides a greater contribution to breeding, raising it by 0.005. Approximately 60% of the breeding occurs in the first lithium region (66 vol% Li, 25 vol% Be, 4 vol% Al_2O_3, 5 vol% Nb), with the remainder in the 95 at.% enriched ^{6}Li region (92 vol% Li, 4 vol% Al_2O_3, and 4 vol% Nb).

As with all CTR concepts, radiation damage to the first wall is of major concern. Accordingly, helium production and atom displacement rates were determined for the niobium structure, assuming a 3.5 MW/m^2 time-average wall loading. Values of 97 ppm He/yr and 59 dpa/yr were determined for the first wall. These compare with values of 94 ppm He/yr and 74 dpa/yr for a reference ORNL Tokamak reactor at the same wall loading. Displacement damage that was computed using recently available damage functions[9] is approximately half that for structural materials of a typical experimental fast breeder reactor. However, possible synergistic effects of displacement damage and much higher helium production in CTR's are still unknown.

Neutron heating in the copper of the compression coil (67 vol% Cu, 33 vol% Al_2O_3) is of potential importance because of heat removal requirements. Using multigroup kerma factors, the neutron energy deposition in copper was found to be representable as $0.1178 \exp-[0.1243\,(r-70)]$ W-cm^{-3}, for $70 \leqslant r \leqslant 110$. At an incident 14-MeV current on the first wall of 3.5 MW/m^2, total neutron heating in the copper coil is ~31 kW/m along the z-axis. This is considerably less than the gamma heating (see below). Neutron heating was determined with kerma factors from ORNL-TM-2564* (1970). However, no major changes in energy deposition are anticipated with the new values for kerma.

To compute gamma energy deposition throughout the RTPR, a series of simple utility codes was written for determining the gamma-ray source spatial-spectral distribution. One of these codes operates on the multigroup microscopic photon-production matrices with neutron flux vectors from the DTF-IV neutron-transport calculations, thus producing multigroup gamma-ray sources. The gamma-ray "microscopic" sources at each spatial mesh point are then normalized to the appropriate reactor power and material atom densities at that space point. Another utility code constructs multigroup photon-interaction cross-section sets for DTF-IV with gamma-ray kerma factors in the first position for activity prints. Kerma factors were taken from ORNL-TM-2564 for most materials in the RTPR, but aluminum, oxygen, and titanium had to be approximated by other elements of similar atomic number. Using 21 groups, gamma transport calculations were performed in the S_8-P_3 approximation by the DTF-IV code. Resulting gamma energy deposition is shown in Table VIII-1 for the cylindrical blanket regions of the RTPR, assuming a first wall loading of 3.5 MW/m^2 from 14.06-MeV neutrons. Also shown in Table VIII-1 are the peak energy deposition rates in each region, which generally occur at the inner surface of the region.

To help evaluate the reference insulator, alumina (Al_2O_3), transmutation, and gas generation rates were determined. Stable transmutation products were considered for all cases where production cross sections were available, and equilibrium concentrations were determined for the radioactive species ^{28}Al, ^{27}Mg, ^{24}Na, and ^{16}N. Table VIII-2 presents a summary of the transmutation product buildup in the shock-heating coil liner for a wall loading of 3.5 MW/m^2. Radioactive species had negligible concentrations (<3 ppm), and total tritium production was less than 1 ppm/yr. Burnout of aluminum and oxygen occur unequally, giving a net shift toward an oxygen excess in the alumina of 1430 ppm/yr.

In summary, the RTPR has an adequate breeding ratio, which has been conservatively calculated by ignoring resonance self-shielding in the structure. The "mop-up" blanket contributes little to the breeding and may be eliminated for more lithium within the inner blanket. Alternate design options desirable from a neutronics viewpoint are (1) using lithium coolant in the graphite region to reduce the capture by niobium of moderated neutrons (~10% of the neutrons from the D-T reactions are captured by niobium in this region); (2) replacing the

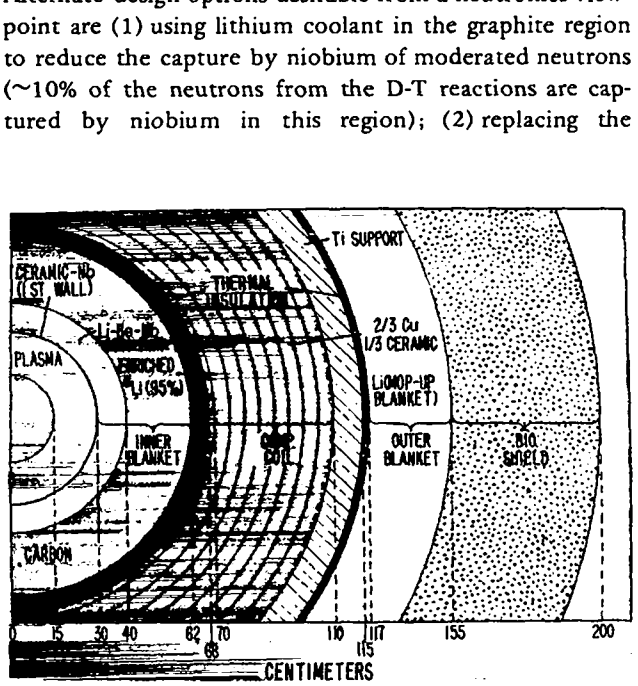

Fig. VIII-5.
Schematic cross section of blanket and shield of RTPR core.

*J. J. Ritts, M. Solomito, and D. Steiner, "Kerma Factors and Secondary Gamma-Ray Sources for Some Elements of Interest in Thermonuclear Blanket Assemblies,[10] Oak Ridge National Laboratory report, ORNL-TM-2564 (1970).

TABLE VIII-1

GAMMA HEATING IN THE RTPR (3.5 MW/m^2)

Region	Total Gamma Energy (kW/m)	Maximum Energy Deposition Rate (W/cm^3)
Electrical Insulation (Al_2O_3)	19.5	10.3
First Wall (Nb)	221.0	29.7
Li-Be	596.0	3.53
Graphite	1,170.0	3.34
Enriched Li	67.4	0.309
Thermal Insulation–both (Al_2O_3)	19.4	0.224
Compression Coil	811.0	1.71
Ti Support	5.06	0.0189
Mop-Up Blanket	1.78	0.000850

TABLE VIII-2

TRANSMUTATION PRODUCT BUILDUP IN ALUMINA SHOCK-HEATING COIL LINER

Element	Production (ppm/yr)[a] In Oxygen	In Aluminum	Total
H	631	4,906	5,537
He	3,760	1,419	5,179
C	3,760	—	3,760
N	187	—	187
Na	—	41	41
Mg	—	5,255	5,255
Si	—	84	84

[a]Reactions considered:

O – (n,α), (n,p), (n,d), (n,α), (n,n'p), and (n,n'α).

Al – (n,α), (n,p), (n,d), (n,t), (n,α), (n,n'p), and (n,n'α).

graphite with beryllia (BeO); and (3) introducing lithium in the copper compression coil to reduce the present loss of ~10% of the neutrons by capture in copper. Energy deposition in the copper is low enough to allow reasonable cooling-system parameters.

All information on neutron and gamma heating in the RTPR has been sent to ANL for system design studies of a θ-pinch reactor concept. Arrangements were made for a meeting with P. Persiani of ANL, who is determining both activation in the RTPR structure and some preliminary shielding estimates. Continual liaison is being maintained with cognizant ANL personnel on the θ-pinch reactor systems study.

A paper on the RTPR neutronics analyses[10] was presented at the Austin symposium on CTR technology. This paper reviews all tritium breeding, nuclear heating, and radiation damage calculations for the RTPR.

To expedite neutronic analyses of future variations on the RTPR design, efforts have started on a post processing code; i.e., a code that will automatically compute neutron and gamma-ray heating, helium production, displacement damage, transmutation, and other reaction rates from output fluxes of transport codes.

2. CTR Blanket Benchmark. A Neutronics Benchmark Committee was formed as a result of discussions at the June 1971 Working Sessions on Fusion Reactor Technology. A standard model of a Tokamak reactor was specified for neutronics calculations, and comparisons of calculations by various laboratories are being made by the Committee. The problem, a 10-region cylindrical array of Nb, ^{6}Li, ^{7}Li, and C, was calculated in S_4-P_3, S_8-P_3, and S_{12}-P_3. Differences of up to ~4% were noted between the three calculations in certain total reaction rates, e.g., NB(n,2n) and ^{7}Li(n,n'T). Results of these calculations were analyzed in detail and indicated total reaction rates agreed with results of calculations reported by other laboratories. However, no exact comparisons with other laboratories are possible yet because of different

TABLE VIII-3

COMPARISON OF SELECTED CTR BLANKET BENCHMARK CALCULATIONS

Case	Data File	Processor	Total Reaction Rates	
			Nb(n,2n)[a]	^{7}Li(n,n'T)
LASL S_8-P_3	All ENDF-III	ETOG-3	1.81(−1)	5.22(−1)
LASL S_4-P_3	All ENDF-III	ETOG-3	1.85(−1)	5.07(−1)
ORNL S_4-P_3	Li - ORNL translation of AWRE data Nb,C - ENDF-II	SUPERTOG	7.36(−2)	4.86(−1)

[a]The Nb(n,2n) cross section was increased by a factor of ~2.5 between the ENDF-II and the ENDF-III evaluation.

TABLE VIII-4

TOTAL REACTION RATES

Reaction	S_4	S_8	S_{12}	$\left(\frac{S_4}{S_{12}}-1\right)\times 100$	$\left(\frac{S_8}{S_{12}}-1\right)\times 100$
Niobium (n,2n)	1.85(−)	1.81(−1)	1.79(−1)	3.35	1.11
Total (n,2n)	2.41(−1)	2.39(−1)	2.37(−1)	1.69	0.84
^{6}Li(n,α)T	8.88(−1)	8.91(−1)	8.92(−1)	−0.45	−0.11
^{7}Li(n,n'α)T	5.07(−1)	5.22(−1)	5.29(−1)	−4.16	−1.32
Total T	1.40	1.41	1.42	−1.41	−0.70
Niobium parasitic absorption	2.80(−1)	2.81(−1)	2.80(−1)	0.0	0.36
Total parasitic absorption	3.02(−1)	3.03(−1)	3.02(−1)	0.0	0.33

cross-section data file sources used. We used the standard GAM-II energy group structure and a thermal group. All cross sections were processed using ENDF-III data and the ETOG-3 multigroup averaging code. Edits by space point and zone were provided for the following reactions in each constituent material: (1) n,2n, (2) tritium production, and (3) parasitic absorption.

Table VIII-3 presents a comparison of the S_4-P_3 and S_8-P_3 results, as well as an ORNL S_4-P_3 first-round calculation with the same multigroup structure as ours, but using different cross-section data and processing codes. LASL's S_4 and S_8 calculations of ^{7}Li(n,n'T) reaction rates are within the range of values, 3.98 (−1) to 5.62 (−1), reported by other laboratories using S_4-P_3 discrete-ordinates calculations. However, the S_8 calculation was more consistent with the Monte Carlo range of values, namely, 5.00 (−1) to 6.70 (−1). Some of the differences between S_4 and Monte Carlo calculations may be due partly to using an S_4 quadrature with P_3 cross sections. The results of all our calculations have been sent to the Neutronics Benchmark Committee for intercomparison with a second round of results from other laboratories. In addition to the calculations requested by the Committee, we have made a study of the convergence of integral quantities with order of quadrature. As an example, Table VIII-4 shows the variation of several selected reaction rates, integrated over all regions, with order of quadrature; all calculations used P_3 expansions of scattering matrices, i.e., multitable-multigroup. Using S_{12} as a basis for comparison, convergence within 1% is achieved with S_8, but only within 4% with S_4. This agrees with similar studies for fission reactor and weapons shielding

problems, where rules of thumb normally prescribe S_8-P_3 calculations for accurate results. Table VIII-4 shows much better agreement than that found for individual regions because of compensating errors in the sum over regions and small fractional contributions of some regions. A difference of up to 43% between S_4 and S_{12} was found in particular regions for the important $^7Li(n,n'\alpha)T$ reaction. Even greater differences occur for Nb(n,2n) reaction rates in some regions. Some of the discrepancies between S_4 and Monte Carlo calculations, as noted by the Benchmark Committee in previous comparisons, could be due to the inadequacy of low-order quadratures, i.e., S_4.

Analysis of the banchmark model may be pursued using a multigroup Monte Carlo code, which is a modification of the LASL code QANDY. The code is being modified to accept cross sections in the general DTF format. Source and edit routines are also being written, and the code input is being modified for convenience reasons. Discrepancies between multigroup Monte Carlo and S_n calculations have already been resolved by groups at ORNL and the Institut für Reaktorentwicklung in Jülich, Germany, both of which used identical cross section sets. Thus, our Monte Carlo calculations are expected to be in essential agreement with S_{12} results, and the benchmark will hopefully serve as a reference calculation for debugging the Monte Carlo code.

Comparison of our second-round results with other contributions from various laboratories revealed differences that were attributed by Steiner of ORNL to multigroup cross-section differences. Further investigation revealed that the laboratories using the ETOG-3 processing code produced multigroup absorption cross sections that were considerably higher in the upper resolved resonance region than those produced by the SUPERTOG code. Initial evaluations indicate that the ETOG-3 values are too high as compared to other data, such as infinitely dilute resonance integrals; thus, the benchmark calculations may be repeated in the future using an agreed upon standard set of multigroup cross sections. Minor differences were also noted in within-group scattering cross sections of high-energy groups, but the effect on breeding ratio is negligible. However, present indications are that proper treatment of the resonance absorption in the multigroup cross section processor ETOG-3 may add about 4% to the computed breeding ratio of the benchmark. The same may be true of the RTPR breeding ratio because the same cross sections were used for both neutronic analyses.

Results of our CTR Benchmark analysis[11] were presented at the ANS 1972 International Meeting. Summary information concerning the results of the analysis was transmitted to the Seminar on Nuclear Data and Neutronics of CTR Blankets.

3. CTR Radiation Damage Facility at LAMPF. We met with W. N. McElroy of Hanford last June to define dosimetry needs at the LAMPF beam-stop irradiation facility. McElroy used our predicted neutron fluxes for a copper beam-stop facility[12] to compute the expected response of several threshold detectors and the relative helium production rates in the LAMPF and EBR-II fast reactor spectra. The conclusions resulting from this meeting are (1) we will require a foil dosimetry program similar to that used in fission reactor irradiations, (2) new threshold detectors will need to be devised for the high-energy tail ($\gtrsim$15 MeV) at LAMPF, (3) detailed three-dimensional flux maps of the LAMPF irradiation cavity should be computed and checked experimentally before irradiation experiments begin, and (4) a method for perturbing flux maps to account for the effect of the irradiation furnace and sample and spectral unfolding capabilities should be developed. These points were reiterated at a later LAMPF Radiation Damage User's Group meeting, and a request for new calculations was made. Of particular interest to the group was the spectral hardening effect of placing beryllium in the proton beam. We felt this to be of primary importance for experiments simulating CTR neutron environments.

As a result of these discussions, a calculational program was initiated in cooperation with LASL Group CMB-13. Initially, one-dimensional DTF calculations were performed using the neutron source from NMTC (intranuclear cascade code) calculations. These will hopefully be followed by multigroup Monte Carlo three-dimensional calculations. The objective of the one-dimensional calculations was to analyze feasible beam-stop materials and radii for optimization of the total flux and the fraction of the flux greater than 10 MeV. Neutron source spectra for 400- and 750-MeV incident protons were obtained from published ORNL calculations. These calculations provide both the angular dependent intranuclear cascade and the isotropic evaporation source. High-energy intranuclear cascade neutrons are emitted predominantly in the forward direction, thus the flux calculations were done for various angular intervals.

Initial studies were performed for a beryllium beam stop to obtain approximate spectra for presentation at the July meeting on CTR radiation damage at AEC headquarters. Neutron source data for a limited number of materials were available from the ORNL calculations, thus sources in beryllium at 400 MeV were approximated by those for carbon. Table VIII-5 gives a summary of the calculations for beryllium, graphite, and aluminum–three potential beam-stop materials that are feasible within current engineering technology. The spectral indices in Table VIII-5 are of particular interest in CTR applications where helium production is a major damage mechanism.

TABLE VIII-5

PARAMETRIC STUDY OF LOW-Z BEAM STOPS

Material	Neutron Source Proton Energy, Target (MeV)	Radius (cm)	Angular[a] Interval	Percent of Total Neutron Flux[b] ≥10 MeV	10-50 MeV	10-25 MeV	He ppm/dpa[c]
Be	400, Carbon	7.5	0°-30°	12.4	3.1(25)	2.3(19)	1.3
Be	400, Carbon	7.5	30°-60°	8.6	3.5(41)	2.6(30)	1.0
Be	400, Carbon	7.5	60°-90°	4.8	3.5(73)	2.8(58)	0.7
Be	400, Carbon	7.5	90°-180°	2.9	2.8(97)	2.6(90)	0.5
Be	400, Carbon	10.0	0°-30°	9.1	2.2(24)	1.6(18)	1.2
Be	400, Carbon	10.0	30°-60°	5.5	2.1(38)	1.6(29)	0.9
Be	400, Carbon	10.0	90°-180°	1.6	1.5(94)	1.4(88)	0.4
Be	750, Oxygen	7.5	18.20°-25.85°	6.7	4.0(60)	3.6(54)	0.9
Be	750, Oxygen	7.5	85.27°-95.73°	4.4	3.9(89)	3.8(86)	0.6
Be	750, Oxygen	7.5	113.58°-126.90°	3.9	3.9(100)	3.8(97)	0.6
C	400, Carbon	7.5	0°-30°	15.6	4.1(26)	3.2(21)	1.4
C	400, Carbon	7.5	30°-60°	12.1	5.1(42)	4.0(33)	1.0
C	400, Carbon	7.5	60°-90°	8.3	6.2(75)	4.9(59)	0.9
C	400, Carbon	7.5	90°-180°	5.2	5.0(96)	4.7(90)	0.6
C	750, Oxygen	7.5	18.20°-25.85°	10.4	6.5(62)	5.9(57)	1.0
C	750, Oxygen	7.5	85.27°-95.73°	8.1	7.1(88)	6.9(85)	0.8
C	750, Oxygen	7.5	113.58°-126.90°	7.4	7.1(96)	6.9(93)	0.8
Al	750, Aluminum	7.5	18.20°-25.85°	9.0	5.4(60)	4.9(54)	0.9
Al	750, Aluminum	7.5	85.27°-95.73°	5.9	5.7(97)	5.5(91)	0.7
Al	750, Aluminum	7.5	113.58°-126.90°	5.9	5.7(97)	5.6(93)	0.7

[a]Laboratory system.

[b]Numbers in parentheses are percentages of fraction above 10 MeV.

[c]Ratios given are for a niobium sample ~5 cm out from the surface of the beam stop, as in a radiation damage furnace. Values for a θ-pinch CTR are 1.6 and below; value for EBR-II core center is 0.02.

The results of these calculations were presented to the User's Group so that they could decide on recommendations to present to the LAMPF management for future beam stop designs. Determination of neutron flux intensities must await two- or three-dimensional transport calculations because of the axial and angular dependence of the source. Spectra for a copper target have also been determined by one-dimensional calculations. The spectrum at 126 to 180° agrees with that previously determined from three-dimensional Monte Carlo calculations. A discussion of the one-dimensional survey calculations[13] was presented at the International CTR Technology Conference. Also, the results of the neutron flux spectrum calculations have been provided to G. L. Kulcinski of the University of Wisconsin, who is comparing neutron irradiation facilities. A figure of merit that he uses is the ratio of helium production by (n,xα) reactions to atomic displacements. Compared to fission reactors, the LAMPF beam-stop irradiation facility is expected to more closely approximate a CTR in this figure of merit.

Dosimetry requirements for the LAMPF beam-stop neutron irradiation facility were formulated at two

meetings of the Dosimetry Committee of the LAMPF Radiation Damage Users Group. A cooperative program has been initiated for dosimetry at the LAMPF beam-stop radiation damage facility. J. Horak of the University of New Mexico and C. Serpan of the Naval Research Laboratory will participate in dosimetry planning, multiple foil activation experiments, and spectral unfolding calculations. They are also planning materials science experiments at the facility.

A code to calculate recoil atom spectra and displacement damage response functions is being activated in support of the CTR radiation damage program. The code RICE was converted from IBM 360 to CDC-6600 FORTRAN. Damage functions for several structural and electrical conductor materials will be needed for the LASL θ-pinch CTR neutronic analysis. Meanwhile, multigroup damage functions for niobium, molybdenum, and vanadium were acquired from the University of Wisconsin.

4. Miscellaneous. A summary of our work on higher Legendre moments of photon-production matrices,[14] and their effect on coupled neutron-photon transport calculations, was presented at the Fourth International Conference on Reactor Shielding. Also, an invited seminar-workshop[15] on LAPHANO, the P_0 photon-production matrix code, was presented to the NEA Code Center at Ispra, Italy.

An appointment was accepted to the U.S. Nuclear Data Committee's Subcommittee for CTR Nuclear Data Needs. A review of CTR neutron cross-section requirements and priority judgements were presented at the first meeting held in January 1973.

Contributions were made to a study committee for an intense 14-MeV neutron source. These consisted of helping define needs for irradiation facilities in the fields of radiation damage and integral neutronics experiments, along with the constraints the experiments place on the accelerator target area.

Planning has begun for a special session of the American Nuclear Society Shielding and Dosimetry Division on the subject of CTR blanket transport calculations.

I. The LASL/CTR Nuclear Data Library (D. W. Muir, R. J. LaBauve, L. Stewart, and N. L. Whittemore)

Multigroup P_0 through P_3 cross sections for neutron transport (using ETOG-3[16]), photon production (using LAPHANO[17]), and photon transport (using GAMLEGX[18]) were prepared for D, ^{6}Li, ^{7}Li, Be, ^{12}C, ^{16}O, Al, Ti, Cu, and Nb. These 100 neutron group by 21 gamma-ray group cross sections have sufficient detail for accurate calculations and form the basis for the construction of the group-collapsed, transport-corrected cross sections that are required for extensive CTR parameter studies.

Multigroup cross sections for the important (n,2n), tritium production, and parasitic neutron absorption reactions have been determined for all 10 materials in the LASL/CTR library. In addition, multigroup cross sections for chemical-helium and chemical-hydrogen production and all major transmutation rates in the insulating materials Al_2O_3 and BeO have been determined. ETOG-3 was modified for this purpose. Neutron and gamma-ray energy-deposition cross sections have been obtained.[19] The neutron-energy deposited code MACK[20] has been obtained and is being evaluated for future applications.

Further development work has been done on the program BINAR. BINAR has been used to merge the cross sections described above onto a single-binary (unformatted) tape, presently containing 340,000 individual data entries. These cross sections can be accessed by preprocessors (if group collapsing or transport correction is needed), or directly by neutron-transport codes.

J. Integral Data Testing with the Wyman Experiment (D. W. Muir)

Several fusion reactor technology groups have proposed integral experiments on large assemblies neutronically similar to fusion reactor tritium-breeding blankets. A tritium-production experiment[21,22] performed in 1954 at LASL can be used as an additional test of tritium-breeding calculations. We have developed benchmark specifications and have performed a neutronic analysis for this experiment.

In this experiment, a 14-MeV neutron source was surrounded by a sphere of ^{n}LiD 30 cm in radius. Samples of metallic ^{7}Li and ^{n}Li (natural lithium) were placed in the sphere, and after irradiation were analyzed for tritium content by counting the tritium β decays. If the number of 14-MeV neutrons released at the source is Q, the number of tritons in the sample at position R is T, and the number of ^{6}Li and ^{7}Li atoms in the sample is L, we can define the tritium-production density, f(R), as follows:

$$f(R) = 10^{25} \times \frac{4\pi R^2 T}{L Q} \quad (\text{cm}^2 \text{ tritons/atom}) \quad . \qquad (2)$$

To distinguish between the two sets of samples, we shall use $f_n(R)$ and $f_7(R)$ for the natural and enriched samples, respectively.

In the transport calculations, the neutron interaction and tritium-production cross sections were taken from the

TABLE VIII-6

CONVERGENCE PATTERNS

DTF Parameters[a]				Percent Differences from Reference					
				R = 7.5 cm		R = 17.5 cm		R = 27.5 cm	
R_s(cm)	S_n	P_m	i	δf_7	δf_n	δf_7	δf_n	δf_7	δf_n
0	4	3	30	+5.2	+6.7	−2.2	+3.5	−5.5	+2.1
2.0	16	3	30	−0.5	+0.7	−1.9	+0.2	−1.8	−0.1
1.0	16	3	30	+1.0	+1.8	−1.5	+0.6	−2.4	0.0
0.5	16	3	30	+1.0	+1.7	−1.5	+0.6	−2.3	0.0
0.5	16	3	60	+0.2	+0.3	−0.2	+0.1	−0.4	0.0
0.5	16	3	120	Reference Calculation					
0.5	16	2	120	+0.8	+0.8	−2.4	−0.8	−0.6	−0.4
0.5	16	1	120	−5.9	−5.6	+4.7	+0.3	+13.1	+4.0

[a]These parameters are defined in the text.

LASL/CTR multigroup library. The neutron data for this library is taken from the national nuclear data file ENDF/B (Version III) for all materials except deuterium. The deuterium cross sections are based on a recent LASL evaluation[23] that has been translated into ENDF/B format. We feel that the angle-energy distributions for secondary (n,2n) neutrons from deuterium are more realistic in the LASL evaluation than in ENDF/B (Version III).

The transport code used in these calculations is the one-dimensional S_n code DTF-IV.[24] In particular, we have used the DTF-IV version that, together with the LASL/CTR library, currently is being used at LASL for design studies on conceptual θ-pinch fusion reactors.[25] To use DTF-IV, we have formulated a one-dimensional benchmark model that neglects the holes in the sphere that accommodated the accelerator structure. Also, the neutron source is assumed to be isotropic and uniformly distributed throughout a central sphere of radius R_s.

To study the sensitivity of the calculated results to the mode of calculation, we have varied the order of angular quadrature S_n, the degree of the Legendre expansion of the scattering matrices P_n, and the number of radial subdivisions i. Also studied was the effect of varying the source radius R_s. The results of this study, given in Table VIII-6, indicate essential convergence at S_{16}, P_3, and i = 120, which we call the "reference" calculation.

The experiment results are compared with the reference calculation in Table VIII-7. The overall agreement is within the estimated 10% accuracy of the absolute normalization of the experimental data. We are confident

TABLE VIII-7

TRITIUM PRODUCTION DENSITY

Radius	$f_7(R)$[a]			$f_n(R)$		
(cm)	Exp.	Calc.	Diff.	Exp.	Calc.	Diff.
7.5	$\binom{3.17}{2.96}$	3.57	+16%	4.27	5.26	+23%
9.6	—	3.42	—	4.71	5.95	+26%
10.0	2.87	3.38	+18%	—	6.06	—
12.5	$\binom{2.98}{2.69}$	3.13	+10%	—	6.71	—
15.0	—	2.86	—	6.30	7.14	+13%
17.5	$\binom{2.68}{2.24}$	2.57	+ 4%	—	7.28	—

that the multigrouped cross sections for D, ^{6}Li, and ^{7}Li in the LASL/CTR library are basically sound. However, the discrepancy between the shapes of the experimental and calculated distributions is too large to be attributed solely to experimental error.

From an examination of the neutron-energy spectra at various radii, we conclude that the discrepancy in the shapes of the $f_7(R)$ distributions could be explained if the ENDF/B ^{7}Li(n,n'α)T cross section was about 35% too high at 14 MeV and about 12% too low at lower energies. However, errors of this magnitude in the ^{7}Li cross section are unlikely. For example, Crocker, Blow, and Watson[26]

estimate that the uncertainty in this cross section is only about 15% at 14 MeV and about 25% at 8 MeV. Although the entire discrepancy probably cannot be explained in this way, note that even a 15% reduction of the 14-MeV cross section would improve the agreement significantly. The disagreement between the $f_n(R)$ experimental and calculated distributions at large R is probably related to the treatment of transport processes rather than the $^6Li(n,\alpha)T$ cross section, which produces most of the tritium in this region.

K. Radiation Damage to Metals in θ-Pinch Reactors (W. V. Green, and R. A. Yeske)

The vacuum wall and surrounding structure of future θ-pinch power reactors will be exposed to intense neutron irradiation at temperatures from 500 to 1000°C. This irradiation will displace atoms at a rate of about 60 dpa/yr, produce about 100 ppm of helium/yr and transmute niobium to other elements at a rate slightly less than 1 at.%/yr at the RTPR wall loading. Cyclic mechanical stresses and heat loads will be imposed on the structure. Swelling by void growth and helium bubble growth, and loss of high-temperature ductility are expected. These will limit the life of structural components. The objective of this work is to determine these limits and to improve them if this is possible and necessary.

1. The Methods and Progress.

a. Theory. Two manuscripts on the interaction of cyclic stresses on high-temperature radiation damage were submitted for publication. These present an analysis of the effect of dislocation vibration on the efficiency of a dislocation line as a sink for point defects. (Cyclic stresses will cause dislocations to move in cyclic motion.) It is concluded that a dislocation will act as a better sink whenever the amplitude of vibration λ is larger than the characteristic diffusion distance $d = (D/4\nu)^{1/2}$, where ν is the frequency of vibration and D is the diffusion coefficient of the point defect. Because D is so large for interstitial atoms, it is not expected that this effect ever is important for interstitial atoms. The effect can be important for lattice vacancies and can counteract the effect of the stress field of a dislocation that makes a dislocation line a more efficient sink for interstitial atoms than for vacancies. The present theories of void growth in irradiated metals depend on the assumption that dislocation lines are better sinks for interstitials than for vacancies. If these theories are correct, one can expect that void growth can be prevented by vibrating dislocations over a large enough amplitude at a high enough frequency. A θ-pinch reactor will generate cyclic mechanical stresses and therefore make dislocations vibrate. High-temperature swelling and the associated embrittlement might then be less than that for steady-state CTR reactors. This implies another advantage for pulsed operation. Experimental verification of this is a major goal of the experimental program.

b. LAMPF. Steady progress has been made toward the development of LAMPF as a neutron source for high-temperature neutron irradiation of samples under cyclic mechanical stresses. The initial facility design is complete. Twelve stringers, each able to mount three sample furnaces, could be used all at the same time with independent stress and temperature control. The furnace design uses a three-zone resistance heater to provide a gradient-free hot zone. Double walls of the furnaces will allow the use of the tritium trick (Sec. K.1.d). With it, the helium production rate-to-displacement rate ratio can be ranged over wide limits through variations of the tritium partial pressure. This ratio is considered to be an important variable in high-temperature radiation damage swelling and embrittlement. Mechanical force will be developed by pressure gradients in a double bellows pneumatic system and will be transmitted to the sample under test through a short load train. When necessary, strain, produced either by mechanical deformation or by swelling, can be determined by either of two methods. The first method is free of radiation effects because it involves only gas pressure measurements. In it, a tapered needle constricts the flow of gas flowing through an orifice. The needle constricts the gas flow more as the sample deforms or swells. This method has been used extensively for many years in high-temperature irradiation experiments in Canada. The second method of measuring strain and/or swelling will utilize newly developed radiation-resistant linear-variable differential transformers as transducers.

The time table for LAMPF neutron irradiations is as follows. The proton beam will achieve 1/10 full beam current in January 1974. Practical irradiation times (4 days to 2 weeks) will be achieved at that beam current for high-temperature swelling experiments in molybdenum. The furnace irradiations will begin as soon as the proton beam is scheduled for steady operation at 1/10 full beam for several days.

A radiation damage working group was formed for LAMPF. Two meetings have been held at LASL with W. V. Green serving as Chairman. A talk was presented at the Annual LAMPF Users meeting describing LAMPF as a radiation damage facility.

c. Fatigue Studies. The response of the likely structural metals, molybdenum, niobium, and vanadium, to cyclic stresses at temperature must be established. This is

necessary to establish a base line for comparing the results that will be obtained in later testing as described in Sec. K.1.b and to establish strength limits under cyclic stressing at elevated temperatures. Three mechanical testers will be used for this base-line work. Bench-top fatigue testing with the "LAMPF furnaces" will provide the necessary experience needed to optimize their operation. An MTS programmed mechanical tester, equipped with a furnace that can heat samples under test to temperatures as high as 1100°C, will be used. Comparison of results between the MTS tester and the LAMPF testers will serve to calibrate the latter. The third tester is the high-temperature testing machine used in earlier CMB-13 work on high-temperature creep of refractory metals. It will not be as convenient for high-cyclic fatigue testing as the LAMPF or MTS testers, but will nonetheless be useful in calibration work.

d. Tritium Trick. Helium generation rates in the first wall of a CTR reactor will be large, about 100 ppm/yr in niobium. Many suspect that this will cause helium bubble formation with associated swelling and embrittlement. This would be similar to damage through void formation but different in origin. Relevant helium production rates are not possible at present by (n,α) reactions because sources are not intense enough. Beta decay to ^{3}He of tritium gas dissolved in massive samples is known as the tritium trick. With it, relevant ^{3}He production rates are easily achieved. D. T. Eash of LASL Group CMB-13 has designed and built a double-walled furnace for safe handling of tritium gas. The outer chamber traps, detects, and recovers any tritium that escapes the inner chamber. A power supply with all the necessary components to safely handle, control, and store tritium is being assembled in Group E-5.

e. Electron Microscopy. L. S. Levinson has established proficiency at thinning niobium and molybdenum for electron transmission microscopy. Helium bubble formation, void formation, and fatigue damage will be studied by this method.

f. Dosimetry. The purpose of essentially all radiation damage experiments is to predict the response of materials to radiation damage in power reactors. Radiation damage experiments at LAMPF will require neutron spectrum flux and fluence measurements. As indicated earlier, our first goal will be to determine how cyclic stressing influences high-temperature swelling and embrittlement. The most direct evaluation will be achieved by irradiating two side-by-side samples within one furnace. One sample will undergo cyclic stressing, the second will not. The differences between the two samples after irradiation will indicate whether the hoped for and predicted dislocation vibration effect is real. In this way, flux level variations and spectrum variations will not influence our results greatly. In spite of this direct comparison technique, some flux level and spectrum measurements will be necessary for correlation. LAMPF will be a spallation-evaporation neutron source, with neutron energies ranging to high values. Foil-activation flux-unfolding spectrum determinations may or may not be appropriate. A committee was formed to evaluate dosimetry at LAMPF. This committee proposes to calibrate the foil-activation method with neutron time-of-flight measurements. The gradients within the neutron-irradiation damage cavity of LAMPF can be mapped, and subsequent irradiations monitored. The time-of-flight measurements could be done by January 1974 at the earliest. The suggested method requires a chopped beam at LAMPF, which will not be available until then. The calibration work will apply to both LAMPF and BLIP, but will not impose a large cost of effort or money on the participants.

g. Spectrum Tailoring. Max Sherman, CMB-13 summer graduate student, and D. Dudziak computed the neutron-energy spectrum after transport of the proton induced source spectrum out of a LAMPF beam stop. Various beam-stop materials were considered in an attempt to tailor the spectrum of LAMPF to that of a CTR reactor. The most favorable combination appears to be a thin graphite facing on a copper beam stop. Seven percent of the neutrons will have energies between 10 and 25 MeV, and the fraction about 50 MeV will be negligible. The first wall of a CTR reactor will have one-fourth of its neutrons near 14 MeV and none above.

b. Committees. Contributions were made to three subcommittees (Radiation Effects, Cyclic Pressure and Thermal Stress, and Structural Materials) of the CTR Technology Committee (FCST Energy Study) in the capacity of member of these subcommittees.

An informal committee has served under R. Emigh of LASL. Its purpose is to consider the possibility of building an intense 14-MeV neutron source.

A Study Committee for LASL Use of LAMPF was formed to provide a channel of communication between the LASL Director's Office, the LASL Users, and the MP-Division organization, to make recommendations on the use of LAMPF, and to evaluate levels of effort, proposals, and new uses of LAMPF. Serving on this has helped pave the way toward CTR motivated radiation damage studies with LAMPF.

L. Electrical Insulator Studies (F. Clinard and J. Bunch)

During 1972 work on electrical insulators was directed toward: (1) a general understanding of the problem areas, (2) theoretical analyses of some of these areas, (3) determination of experimental approaches and results needed, and (4) initiation of several experimental programs.

In this section the major problem areas are summarized and commented upon from the standpoint of present knowledge. Emphasis is on the insulating inner liner of the first wall, where the most severe conditions will be encountered. Experiments currently under way are described.

1. High-Temperature Problem Areas. The operating temperature of the first wall insulator in the RTPR is ~800°C, with excursions of perhaps several hundred degrees accompanying each pulse. Most of the heat results from the plasma heat dump, i.e., the transfer by conduction of the heat content of the spent plasma through the first wall to the lithium coolant (Sec. VIII-F). There is a smaller contribution from the absorption of bremsstrahlung and gamma rays during the burn.

a. Electrical Problems. Electrical resistivity and (usually) dielectric strength of insulators are lower at 800°C than at room temperature, whether charge transport is by electronic or ionic motion. (The insulating properties are needed only at the start of each burn, not during the subsequent temperature excursion.) Reactor design considerations require that resistivity should be at least 10^6 Ω-cm and dielectric strength about 200 kV/cm. The better insulators can meet the resistivity requirement, but their DC dielectric strength is only about 100 kV/cm at 800°C. Fortunately, the voltage in the pulsed reactor is applied across the first wall insulator for only ~1 μsec, and dielectric strength for many materials is considerably higher (by about a factor of two) under such conditions.

b. Structural Problems. The thermal pulses to which the insulator will be subjected may cause cracking or spalling. Such tendencies can be minimized by using a material with high-dielectric strength (to allow a thin layer) and high-thermal conductivity. The thermal conductivity at 800°C should be ~0.1 W/cm°C or higher, a value attained by some ceramics but no glasses.

Another structural problem may arise if the neutral fuel gas in contact with the wall during the plasma heat damp is sufficiently hot to be dissociated into atomic rather than molecular species. Then chemical sputtering (an erosion process) may occur. The resistance of an insulator to such sputtering is a function of its thermodynamic stability and surface reaction rates, and is difficult to predict quantitatively. The seriousness of this potential problem cannot be determined until the fuel gas temperature at the wall is known.

2. Neutron Bombardment Problems. The first wall insulator will be subjected to a fluence of ~3×10^{22} n/cm^2 in one year, of which 20% have energies of 14 MeV. The damage dose is pulsed, with neutrons striking the wall in 0.1-sec bursts about every 10 sec. This irradiation will create atomic displacements, ionization electrons, and transmutation products.

a. Electrical Effects. Electrical resistivity and dielectric strength may decrease because of the generation of point defects (which can serve as electron and hole traps, or enhance ionic conductivity) and free electrons (which can populate the traps and may contribute to electronic charge transport). The electrical behavior of irradiated insulators is not understood, thus it is difficult to estimate the extent of this problem. Because voltage is applied almost 10 sec after irradiation, i.e., just at the start of the next pulse, much of the damage may have been thermally annealed by the time the insulating properties are needed. Insulators that anneal rapidly could prove relatively insensitive to pulsed reactor-type radiation damage insofar as electrical properties are concerned. (The point defects will not all disappear, many will agglomerate into larger defect clusters that can still affect structural properties.)

Transmutation product buildup will be significant because of the high dose of high-energy neutrons. For example, calculations show that Al_2O_3, after a one-year exposure to first wall conditions, will contain ~0.5% each of magnesium, carbon, hydrogen, and helium. The role of such impurties in electrical properties depends on whether they remain in solution or precipitate. If in solution, they may behave similarly to displacement-generated point defects. If precipitated, they could cause localized field effects and premature dielectric breakdown. It may be possible to use gettering or precipitating agents to control the effects of transmutation products.

b. Structural Effects. Neutron bombardment will create vacancies and interstitials that can, as isolated point defects, result in volume changes. These changes are usually small and may anneal out at the operating temperatures expected. More serious will be pore formation, caused by the agglomeration of vacancies into voids (often assisted by insoluble gas atoms, in which case the pores become bubbles). Swelling of several percent may occur by this mechanism and could result in destruction of an insulator bonded to the metal first wall. It has been found recently that crystalline materials can be stabilized against swelling by the introduction of small precipitates.

These can either pin bubbles while still small and relatively harmless or induce recombination of vacancies and interstitials and thus prevent any pore formation. This technique holds great promise in controlling swelling in insulators.

Metallic transmutation products, whether in solution or as precipitates, can result in volume changes. The extent to which this will be a problem will depend on the insulator in question and its transmutation products.

Another problem may be neutron sputtering. This phenomenon, although not as serious as charged particle sputtering (the latter to be avoided in the pulsed reactor by controlled relaxation of the magnetic field), must still be considered. The critical parameter is the number of atoms sputtered by an incident neutron, known as the sputtering yield. Our calculations, although crude, suggest that the sputtering yield will be between 10^{-5} and 10^{-7}. A value of 10^{-5} would result in an erosion rate of $\sim 10^{-5}$ cm/yr, which is acceptable. The rather sparse experimental data seem to point to a sputtering yield of $\sim 10^{-3}$. Even this, however, would result in a tolerable erosion rate (10^{-3} cm/yr). Thus it appears that neutron sputtering will not be a serious problem from the standpoint of the insulator. However, plasma contamination could be a problem if the sputtering yield is as high as 10^{-3}.

Another structural problem may be a decrease in thermal conductivity resulting from radiation damage. Heat transport in opaque insulators is almost entirely by lattice conduction, and the lattice damage caused by irradiation of crystalline materials disrupts this conduction. For example, it is known that Al_2O_3 suffers a loss in thermal conductivity by about a factor of 2 when exposed to fission reactor irradiation at 750°C.

The higher temperatures expected for the first wall insulator may help by accelerating the annealing of the damage. It is also possible that transparent insulators could be used, thus increasing the effective thermal conductivity by adding a radiation-conduction component. However, radiation-induced coloration and translucency would have to be suppressed.

3. Bremsstrahlung and Gamma-Ray Bombardment. The first wall insulator will be subjected to intense bremsstrahlung (of which, however, a large portion will pass through the insulator and deposit in the metal backing), and gamma rays from the activation of other blanket materials. Such photon irradiation will produce photoelectrons and could, in some materials, result in copious atomic displacements.

a. Electrical Effects. The effect of photon bombardment on insulators is highly variable; some dielectrics (mainly alkali halides) have been shown to suffer severe displacement damage from ionizing radiation, but the mechanism thought to be responsible (the Pooley-Hirsch effect) is not operative in most materials. Usually, lattice damage from photons can result only from the rather inefficient process of high-energy photoelectron impacts with ions. Thus, photon-induced displacements could only be caused by high-energy gamma rays. This contribution is calculated to be small compared to neutron-induced displacements. However, the photoelectrons created will be much more plentiful than the ionization electrons generated by neutron bombardment, and may contribute strongly to electronic charge transport.

b. Structural Effects. Most insulating materials will be only slightly damaged structurally by photon bombardment. Thermal stresses will result from bremsstrahlung and gamma-ray absorption, but the contribution from the plasma heat dump is expected to be much larger. However, the details of neutron damage can be influenced by the charge state of the defects, which is affected by photon irradiation.

4. Experiments Under Way.

a. Correlation of 14-MeV Neutron and Ion Irradiation Damage Effects. A major problem in radiation damage studies for the pulsed fusion reactor is selection of a suitable irradiation facility. Until high-intensity 14-MeV neutron sources are developed, it will be necessary to simulate the expected damage either by ion irradiation or by bombardment with neutrons of different energy spectra or intensities from that expected in the fusion reactor. The simplest simulation experiments are those involving ion irradiation, if the characteristic short penetration ranges can be tolerated. In fact, only ion irradiation can simulate the high instantaneous damage rates anticipated in the pulsed reactor.

To interpret ion irradiation studies properly, their correlation with 14-MeV neutron damage effects should be established experimentally. One physical property of insulators that can be used for correlation studies is optical absorption. This property offers a unique opportunity for study because it is sensitive to the very low fluences of 14-MeV neutrons currently available.

Evaluation of optical absorption will yield information as to the behavior of isolated point defects, and is therefore a measure of the effect of radiation damage on electrical properties. Vacancies and interstitials created by irradiation can be populated with electrons or holes by exposure to ionizing x rays. In this state they act as color centers, preferentially absorbing light of certain wavelengths; thus the color centers serve as a label for the defects present. The mobility of the defects can be determined by step-annealing the samples until the defects disappear.

An experiment has beeen initiated to exploit this phenomenology by irradiation of single-crystal Al_2O_3 (sapphire) samples at the Lawrence Livermore Laboratory's 14-MeV neututron source. A one-week exposure, giving a fluence of $\sim 10^{17} n/cm^2$, will be carried out at room temperature. The samples will then be returned to LASL, where light absorption will be evaluated by use of a spectrophotometer.

The results should be of considerable intrinsic interest because 14-MeV neutron-damage effects will have been measured directly. Of equal importance, however, is the opportunity that this presents for correlation with ion-irradiation effects. Accordingly, the results will be compared with those from a similar experiment conducted using ion bombardment at the LASL Van de Graaff facility. This comparison will indicate the relationship between damage effects from 14-MeV neutrons and ions, and will allow optimization of ion-simulation studies by proper choice of bombarding particles and energies.

b. Electrical Resistivity During and After Irradiation at High Temperatures. It is important to determine the magnitude of anomalies in electrical properties induced by irradiation and the kinetics of their recovery after irradiation. Such effects are difficult to calculate from first principles because of their complexity, thus it is not now definitely known whether radiation effects on electrical properties will be a significant problem in the pulsed reactor. Therefore, an experiment has been initiated to allow monitoring of electrical resistivity of thin insulating samples while simultaneously subjecting them to heating and ion bombardment at the LASL Van de Graaff accelerator. It may also be possible to measure dielectric breakdown in this apparatus, depending on sample and electrode characteristics.

Ion bombardment will create atomic displacements and ionization electrons, and can therefore simulate approximately the radiation environment at the first wall. For example, a 5-MeV proton flux of $\sim 2 \times 10^{14}$ ions/cm^2 sec is calculated to generate defects in Al_2O_3 at the rate of ~100 displacements/atom (DPA)/yr. For a sample 5×10^{-2} mm thick (with thin metallized electrodes front and rear) The damage distribution should be fairly uniform, with the proton energy having been degraded to 3.7 MeV at the rear surface and the damage rate rasied to ~130 DPA/yr.

It is known that ion irradiation often only roughly simulates neutron damage because of the different defect distributions that result. An effort will be made to optimize the simulations by proper selection of the type and energy of bombarding ions. The results of the 14-MeV neutron simulation study described earlier will be of great value in this optimization.

An apparatus is being constructed for this experiment. Of special importance is its ability to measure decay of anomalies in electrical properties after irradiation ceases. Previous studies of anomalous conductivity have for the most part focused on effects during irradiation. Electrical measurements made on insulators under these conditions are known to be subject to considerable experimental error, and great care will be required to interpret the results properly. Fortunately, the need for comparative rather than absolute values will alleviate some of these problems.

First studies will evaluate a variety of both single-crystal and polycrystalline Al_2O_3 samples. The goal will be to determine the contribution of impurities, normal and glassy grain boundaries, and isolated and clustered dislocations to anomalous conductivity. Structural degradation will also be evaluated in these samples after irradiation.

c. Dielectric Strength of Insulators under Pulsed-Voltage Conditions at High Temperatures. It is important that the first wall insulator have as high a dielectric strength as possible so that a thin layer can be used and heat transfer difficulties thus alleviated. The pulsed nature of the applied voltage at the first wall (lasting only $\sim 10^{-6}$ sec) may result in breakdown strengths significantly larger than those normally observed.

Dielectric strength is a complex property and results from different physical processes depending on sample temperature and duration of application of the applied field. At low temperatures dielectric strength is high, and breakdown appears to be an intrinsic property of the material. At high temperatures with dc or slowly increasing fields, breakdown strength is usually lower. Under these conditions breakdown apparently occurs as a result of Joule heating in a time-dependent way. If, therefore, the time of voltage application at high temperature is short enough, it would be predicted that the high-temperature breakdown mechanism would not have time to operate, and that failure might then occur at the higher-voltage characteristic of intrinsic (low-temerpature) breakdown. This prediction agrees qualitatively with published experimental data for NaCl and several glasses, for which dielectric strengths at appropriate temperatures are roughly doubled for pulsed fields (10^{-3} sec or less duration) as compared to the values measured with dc fields.

An apparatus is presently being built to evaluate dielectric strengths of insulators under pulsed-voltage conditons at high temperatures. The purpose of the experiment is not just to measure pulsed breakdown in various insulators, but also to study the material parameters that allow maximum dielectric strength under these conditions. These parameters can then be optimized to obtain the

maximum pulsed-voltage dielectric strength for a given material. First studies will be on various forms of Al_2O_3, single and polycrystal, of differing chemical and structural perfection.

REFERENCES

1. S. C. Burnett, W. R. Ellis, T. A. Oliphant, and F. L. Ribe, Los Alamos Scientific Laboratory report LA-5121-MS (1973).

2. K. I. Thomassen, Los Alamos Scientific Laboratory report LA-5087-MS. Paper presented at the Texas Symposium of the Technology of Controlled Thermonuclear Fusion Experiments and the Engineering Aspects of Fusion, University of Texas, Austin, November 20-22, 1972.

3. T. A. Oliphant, Proceedings of the BNES Conference on Nuclear Fusion Reactors, UKAEA Culham Laboratory, September 17-19, 1969, p. 309.

4. J. P. Freidberg, R. L. Morse, and F. L. Ribe, paper presented at the Texas Symposium of the Technology of Controlled Thermonuclear Fusion Experiments and the Engineering Aspects of Fusion, University of Texas, Austin, November 20-22, 1972.

5. B. Lehnert, Nuclear Fusion 8, 173 (1968).

6. Donald J. Dudziak, "Summary of Technological Problems for a Full-Scale Pulsed Fusion Reactor System," paper presented at meeting of Technical Committee of the CTR Task Force of FCS Energy Study.

7. Reference Energy Systems and Resource Data for Use in the Assessment of Energy Technologies, AET-8, Associated Universities, Inc., Upton, N.Y. (April 1972).

8. K. D. Lathrop, "DTE-IV, A FORTRAN-IV Program for Solving the Multigroup Transport Equation with Anisotropic Scattering," Los Alamos Scientific Laboratory report LA-3373 (1965).

9. G. L. Kulcinski, University of Wisconsin, personal communication, July 1972.

10. Donald J. Dudziak, "Discrete-Ordinates Neutronic Analysis of a Reference Theta-Pinch Reactor (RTPR)," paper presented at Texas Symp. Tech. of Controlled Therm. Fusion Expt. and the Eng. Aspects of Fusion Reactors, November 1972. Proceedings to be published.

11. Donald J. Dudziak, "Neutronic Analysis of a CTR Blanket Benchmark by Discrete Ordinates," Trans. Am. Nucl. Soc., Vol. 15 (2), 630 (1972).

12. Donald J. Dudziak et al., "A Meson Factory as a Neutron Irradiation Facility," Trans. Am. Nucl. Soc., Vol. 15 (1), 240 (1972).

13. Donald J. Dudziak and Max A. Sherman, "Neutron Flux Spectra at LAMPF for CTR Radiation Damage Studies," paper presented at Texas Symp. Tech. of Controlled Therm. Fusion Expt. and the Eng. Aspects of Fusion Reactors, November 1972. Proceedings to be published.

14. Donald J. Dudziak and Gerald E. Bosler, "Anisotropy of Photon Emission in Transport Calculations," paper presented at Fourth Int. Conf. on Reactor Shielding, Paris (1972). Proceedings to be published.

15. Donald J. Dudziak, "Use of LAPHANO for Gamma-Ray Shielding Studies," paper presented at Seminar-Workshop on Shielding Programs, Ispra, Italy, October 1972. Proceedings to be published.

16. D. E. Kusner and S. Kellman, "ETOG-1, A FORTRAN Program to Process Data from the ENDF/B File to the MUFT, GAM, and ANISN Formats," Westinghouse Nuclear Energy Systems report WCAP-3845-1 (ENDF-114) (December 1969).

17. D. J. Dudziak, R. E. Seamon, and D. V. Susco, "LAPHANO: A P_0 Multigroup Photon-Production Matrix and Source Code for ENDF," Los Alamos Scientific Laboratory report LA-4740-MS (ENDF-156) (January 1972).

18. K. D. Lathrop, "GAMLEG - A FORTRAN Code to Produce Multigroup Cross Sections for Photon Transport Calculations," Los Alamos Scientific Laboratory report LA-3267 (April 1965).

19. J. J. Ritts, M. Solomito, and D. Steiner, "Kerma Factors and Secondary Gamma-Ray Sources for Some Elements of Interest in Thermonuclear Blanket Assemblies, Oak Ridge National Laboratory report ORNL-TM-2564 (1970).

20. M. A. Abdou, C. W. Maynard, and R. Q. Wright, "MACK, A Computer Program to Calculate Neutron-Induced Energy Release Parameters (KERMA) and Multigroup Neutron Reaction Cross Sections from Nuclear Data in ENDF Format," Oak Ridge National Laboratory report ORNL-TM-3994 (to be published).

21. D. W. Muir and M. E. Wyman, "A Tritium-Production Measurement with Application to Fusion Reactor Blanket Design," Trans. Am. Nucl. Soc., 15: 631 (1972).

22. M. E. Wyman, "An Integral Experiment to Measure the Tritium Production from Li by 14-MeV Nuetrons in a Lithium Deuteride Sphere," Los Alamos Scientific Laboratory report LA-2234 (Rev) (November 1972).

23. A. Horsley and L. Stewart, "Evaluated Neutron Cross Sections for Deuterium," Los Alamos Scientific Laboratory report LA-3271 (1968).

24. K. D. Lathrop, "DTF-IV, A Fortran Program for Solving the Multigroup Transport Equation with Anisotropic Scattering," Los Alamos Scientific Laboratory report LA-3373 (1965).

25. Donald J. Dudziak, "Discrete-Ordinates Neutronic Analysis of a Reference Theta-Pinch Reactor (RTPR)," to be published in the Proceedings of the Texas Symposium on the Technology of Controlled Thermonuclear Fusion Experiments and the Engineering Aspects of Fusion Reactors, November 20-22, 1972, Austin, Texas.

26. V. S. Crocker, S. Blow, and C. J. H. Watson, "Nuclear Cross-Section Requirements for Fusion Reactors," in *Nuclear Data for Reactors*, Conference Proceedings, Helsinki, Finland, June 19, 1970, pp. 67-91, International Atomic Energy, Vienna, 1970.

IX. MAGNETIC ENERGY TRANSFER AND STORAGE

(H. L. Laquer, J. D. G. Lindsay, E. M. Little, G. A. Miranda, J. D. Rogers, and D. M. Weldon)

The objective of the superconducting magnetic energy storage and transfer project is to provide an alternative to capacitor banks in the 200-MJ range. The proposed method of operation will use energy transfer from a superconducting storage inductor into a transformer-coupled plasma-compression coil. Energy transfer is made by triggering a superconducting "switch" from the superconducting ($R = 0$) into the normal ($R = R_N$) state.

The study of small 10- to 30-kJ energy storage systems reported in the previous annual report has continued with the goal of determining those methods of construction that allow the quenching currents for a system to reach the short sample critical currents of the superconducting material used.

The circuit shown in Fig. IX-1 has been used in these studies, where R_p is a resistive load, R_N is the normal state switch resistance, and the two capacitors open the switch by driving a current through it larger than the critical current. Typical model coils used to date store energies of up to 20 kJ at 1000-A currents, are 20 cm long with an i.d. of 14 cm, and contain 450 to 1000 turns. Voltages of over 2 keV have been developed across the load resistance. Some experiments were also performed with a transformer-coupled inductive load coil, producing peak load currents of 60 kA.

Conductors selected for the initial work consisted of braided, insulated, 8-mil (0.02 cm)-diam, twisted, multifilament, Nb-Ti wires with copper to superconductor ratios between 1 and 5. The inherent springiness of braided materials makes the coils very compressible so that the Lorentz force can cause wire motion that in turn produces local heating, hence degradation of the superconductor, i.e., a coil normality well below short sample critical current. Bonding or potting reduces this degradation but at the expense of much reduced heat-transfer rates to the helium bath. Another means of achieving a less compressible structure is to have a circular braid of superconducting wires braided over a tightly compressed core of fiberglass cord. Such a coil does attain short sample critical current, at least in the 14- by 20-cm size. Finally, solid mixed-matrix superconductors (Fig. II-2), where each Nb-Ti filament is surrounded by a copper shell and is in turn distributed throughout a cupro-nickel matrix, offer the rigidity needed to reduce motion sensitivity and usually perform up to their short-sample characteristics.

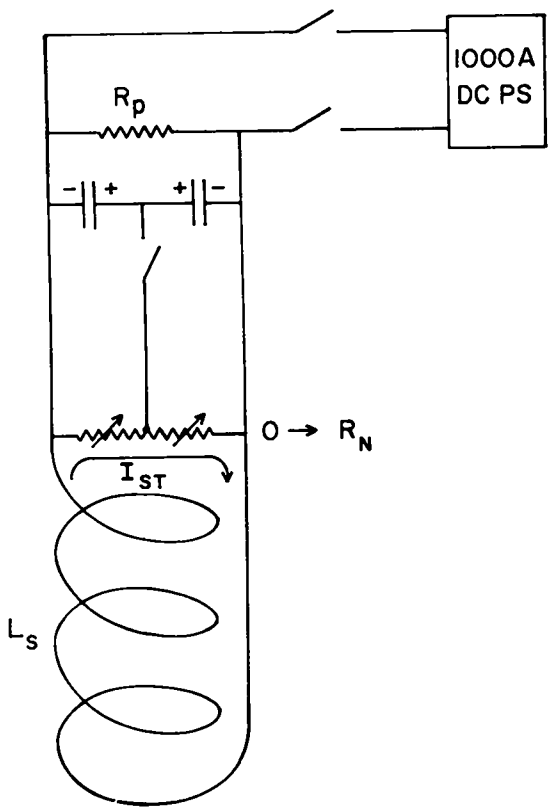

Fig. IX-1.
Energy transfer circuit triggered by discharging capacitors through a superconducting switch.

The actual performance of a superconducting switch depends critically on its geometry, inductance, and the circuit into which it is incorporated. If the switch is being opened by exceeding its quenching current, switch inductance should be minimized to reduce the impedance. The low-inductance Ayrton-Perry configuration of counter-wound helices has proven most successful to date. Work reported last year showed that the fastest switching speed

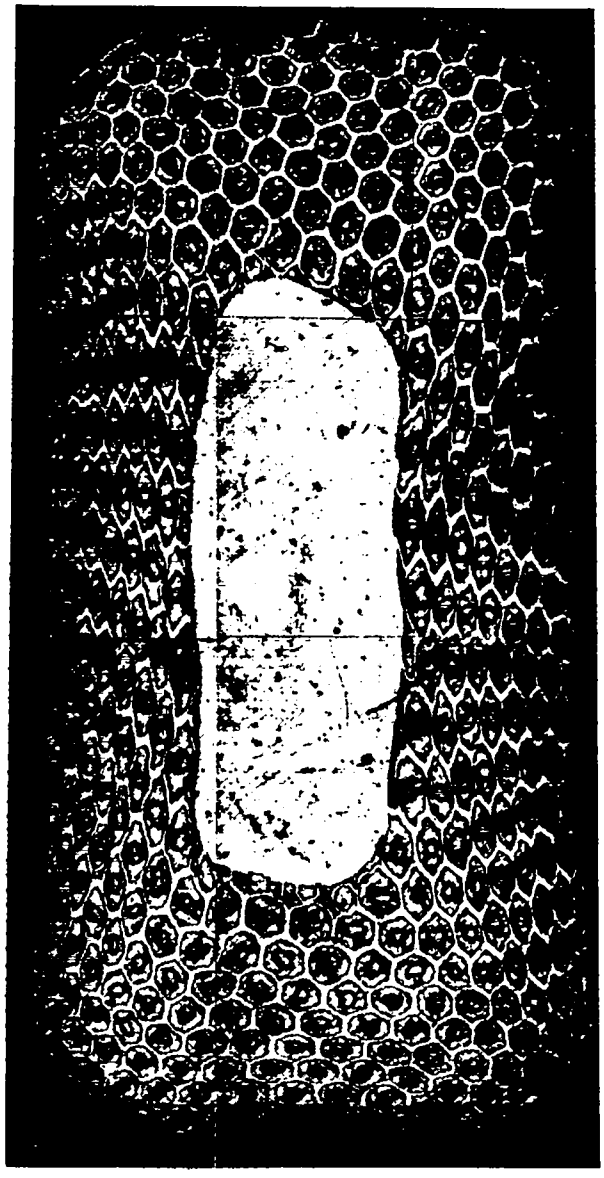

Fig. IX-2.
Photomicrograph of a mixed-matrix superconductor.

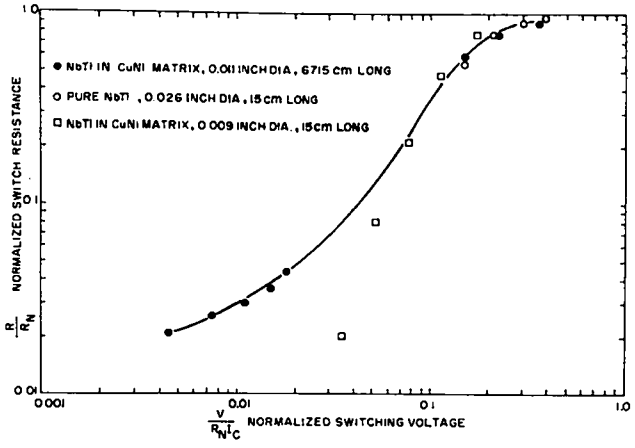

Fig. IX-3.
Variation of switch resistance with voltage in current density switching.

of superconducting wire depended on the wire diameter and that typically for a 0.2-mm-diam wire, switching speeds of 200 nsec could be obtained. However, if the switching process does not deposit sufficient energy to raise both the switch and all closely coupled material above the superconductor's critical temperature, states can arise in which the resistance is much less than the fully normal resistance and is either stationary or increasing very slowly. For current density switching, Fig. IX-3 exemplifies the partial switching for several wires of various lengths and types that have been used in superconducting switches. The normalized switch resistance R_s at 10 to 1000 μsec divided by the fully normal resistance R_N is a function of the normalized applied voltage V_s (furnished by a capacitor, transformer, or battery) divided by $I_c R_N$ (where I_c is the critical current in the switch). This empirical relation does not specify the length of time V_s needs to be applied, but suggests that 30% of the normalized voltage is needed to obtain 90% of the fully normal resistance as quickly as permitted by circuit inductances. Once R_N is attained, a current I needs to be maintained only for a time t so that the energy $I^2 R_N t$ delivered to the switch is sufficient to provide the above-mentioned change in temperature. Typically this can be less than 0.1% of the energy stored in the storage coil.

A 300-kJ energy storage and transfer system has been designed and is scheduled for operation later in the year. This system, shown in Fig. IX-4, will consist of a two-dewar assembly, one containing the energy storage coil (a 60-cm-i.d. epoxy-fiberglass laminated dewar) and the other containing the switch (a 43-cm-i.d. stainless steel dewar). The coil and switch are to be connected with superconducting lines run through vacuum-jacketed, superinsulated transition pieces between the dewars. The energy will be transferred into an inductive load at room temperature. The presently planned design of the 300-kJ storage coil calls for edge winding of a 0.5 by 1.0 cm mixed-matrix superconductor in a single layer. Current in the storage coil conductor will be 10,000 A and the peak magnetic field will be 20 kG. When the system is discharged, peak currents in the secondary circuit will range from 300 to 700 kA depending on the inductance of the load coil attached to the secondary.

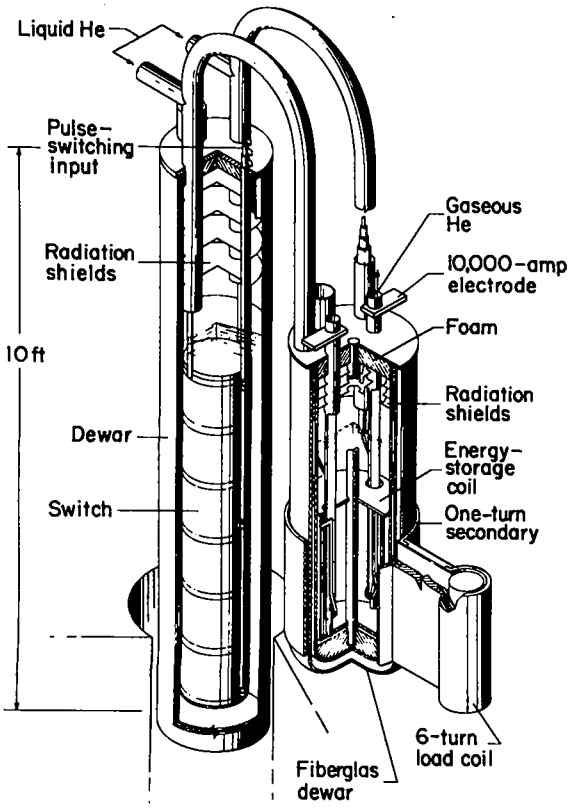

Fig. IX-4.
The 300-kJ energy storage experiment.

Because the industry is at present unable to test 5000- to 10,000-A superconducting materials, and because we must be able to verify the manufacturer's claims, a high-current, critical-current apparatus has been designed and is now being assembled. With this apparatus, it will be possible to make critical-current measurements on samples 10 to 25 cm long, carrying currents up to 12,000 A in magnetic fields up to 55 kG.

PAPERS PUBLISHED OR PRESENTED

D. W. Forslund J. Fu (EG&G) R. L. Morse C. W. Nielson	Electron Cyclotron Drift Instability and Turbulence	Phys. Fluids 15, No. 7 (1972)
J. P. Freidberg R. W. Mitchell R. L. Morse L. I. Rudsinski	Resonant Absorption of Laser Light by Plasma Targets	LA-4852-MS Phys. Rev. Lett. 25, No. 13 (1972)
R. L. Morse C. W. Nielson	Occurrence of High Energy Electrons and Surface Expansion in Radiantly Heated Target Plasmas	LA-4986-MS
H. R. Lewis	Variational Algorithms for Numerical Simulation of Collisionless Plasma with Point Particles Including Electromagnetic Interactions	J. Comput. Phys. 10, No. 3 (1972)
J. P. Freidberg	Vlasov-Fluid Model for Studying Gross Stability for High-Beta Plasmas	Phys. Fluids 15, No. 6 (1972)
K. S. Thomas C. R. Harder W. E. Quinn R. E. Siemon	Helical Field Experiments on a Three-Meter Theta Pinch	Phys. Fluids 15, 1658 (1972)
F. C. Jahoda R. E. Siemon	Holographic Interferometry Cookbook	LA-5058-MS
K. I. Thomassen	Reversible Magnetic Energy Transfer and Storage Systems	LA-5087-MS
S. C. Burnett W. R. Ellis T. A. Oliphant, Jr. F. L. Ribe	A Reference Theta Pinch Reactor (RTPR)	LA-5121-MS
J. L. Tuck	L'Energie De Fusion	La Recherche V. 3, No. 27 (1972)

Fusion Vacuum-Wall Meeting, Washington, D.C., January 27-28, 1972

W. V. Green F. L. Ribe	First-Wall Materials Problem in a Pulsed Fusion Reactor

American Physical Socity Meeting, San Francisco, California, January 31-February 3, 1972

J. C. Ingraham	Anomalous Absorption of Electromagnetic Waves Near the Electron Plasma Frequency of Laboratory Plasma
J. L. Tuck	Energy and the Future of Nuclear Fusion

Ames Research Center, Moffett Field, California, February 16, 1972

J. A. Phillips	The Stabilized Z-Pinch Program at Los Alamos

Lawrence Livermore Laboratory, California, February 17, 1972

J. A. Phillips	The Stabilized Z-Pinch Program at Los Alamos

Courant Institute, New York, New York, March 3, 1972

J. P. Freidberg	Stability of a Finite Beta $\ell = 2$ Stellarator

Texas Tech, Lubbock, Texas, March 6, 1972

J. L. Tuck	Energy and Controlled Fusion

University of Texas, Austin, March 8, 1972

J. L. Tuck	Conjectures on the Nature of Ball Lightning

Annual Institute on Petroleum Exploration and Economics, Southern Methodist University, Dallas, Texas, March 15, 1972

J. L. Tuck	Current Energy Situation

Meeting on Anomalous Absorption of Intense Radiation, University of Colorado, Boulder, March 21-22, 1972

H. Dreicer J. C. Ingraham	Anomalous Microwave Absorption Near the Plasma Frequency
J. C. Ingraham H. Dreicer	Interpretation of Anomalous Microwave Absorption Measurements
J. P. Freidberg B. M. Marder	High Frequency Electrostatic Plasma Instabilities with Collisions
R. L. Morse C. W. Nielson L. E. Rudsinski	Absorption of Very Intense Laser Radiation in Overdense Targets
J. M. Kindel D. W. Forslund E. L. Lindman	Parametric Instabilities of Finite Amplitude Whistlers

Sherwood Theory Meeting, Los Alamos, New Mexico, March 23-24, 1972

J. M. Kindel F. W. Perkins	Fast Wave Heating of Tokamak Plasmas
J. M. Kindel H. Okuda	Parametric Instabilities at Low Frequencies Above the Lower Field

J. P. Freidberg H. R. Lewis	Application of the Vlasov-Fluid Model to the Screw Pinch
J. P. Freidberg B. M. Marder	MHD Stability of Diffuse Two-Dimensional Equilibria
J. P. Freidberg	Stability of a Finite Beta, L Equals Two Stellarator
D. W. Forslund J. M. Kindel E. L. Lindman	Parametric Instabilities of Whistlers

Thirteenth Annual NW Regional Science Fair, Albuquerque, New Mexico, March 25, 1972

J. L. Tuck	Guessing the Future from the Past

Columbia University, New York, New York, April 3, 1972

H. Dreicer	Anomalous Microwave Absorption Near the Plasma Frequency

Symposium on Plasma Waves, Instabilities, and Interactions, Nord-Torpa, Norway, April 5-12, 1972

H. Dreicer	Parametric Plasma Decay Instabilities

Technical Committee of the Federal Council on Science and Technology, Argonne National Laboratory, Argonne, Illinois, April 10-12, 1972

S. C. Burnett W. R. Ellis T. A. Oliphant F. L. Ribe	Parameter Study of a Pulsed High-Beta Fusion Reactor
S. C. Burnett	Information for the Environment and Economics Subcommittee of the CTR Technology Committee of the FCST Energy Study Group
S. C. Burnett W. R. Ellis F. L. Ribe	Energy Balance, Circulating Power, and Plant Efficiency for a Pulsed Theta-Pinch Reactor

National Science Foundation, Washington, D.C., April 13, 1972

J. L. Tuck	Conjectures on the Nature of Ball Lightning

Rutger's Physics Department, New Brunswick, New Jersey, April 19, 1972

J. L. Tuck	Conjectures on the Nature of Ball Lightning

Fifty-Third AGU Annual Meeting, Washington, D.C., April 17-21, 1972

D. W. Forslund E. L. Lindman	The Microstructure of the Earth's Bow Shock

J. M. Kindel E. L. Lindman D. W. Forslund	Parametric Instability of Large Amplitude Whistlers

Plasma Physics Seminar, University of Pennsylvania, Pittsburgh, April 21, 1972

J. A. Phillips	Stabilized Z-Pinch Program at Los Alamos

1972 Applied Superconductivity Conference, Annapolis, Maryland, May 1-3, 1972

H. L. Laquer J.D.G. Lindsay E. M. Little D. M. Weldon	Supersonducting Magnetic Energy Storage and Transfer

Technology Committee of CTR Task Force Federal Council on Science and Technology, Washington, D.C., May 24-25, 1972

S. C. Burnett	The Ultimate Potential of Fusion Reactors
F. L. Ribe A. F. Fraas (ORNL) F. Tenney (PPPL)	Post-1960 Reactor Test Program

American Physical Society Meeting, Albuquerque, New Mexico, June 5-7, 1972

A. Haberstich	Numerical Solution of a Non-Linear Diffusion Problem
J. N. DiMarco L. C. Burkhardt H. J. Karr P. R. Forman J. A. Phillips	Preionization and Its Effects on Pinch Formation in ZT-IA
P. R. Forman L. C. Burkhardt J. N. DiMarco H. J. Karr J. A. Phillips	Plasma Pressure Profiles of ZT-IA
W. R. Ellis F. C. Jahoda R. E. Siemon	Measurements of Plasma Parameters in the Scyllac Five Meter Toroidal Sector
W. E. Quinn C. F. Hammer G. A. Sawyer	Plasma Experiments on $\ell = 1,0$ Helical Equilibria in the Scyllac Five-Meter, Theta-Pinch Toroidal Sector
R. F. Gribble S. C. Burnett C. R. Harder	Feedback Stabilization on a Theta-Pinch Plasma Column
K. S. Thomas H. W. Harris F. C. Jahoda G. A. Sawyer	Plasma Experiments in the Scyllac Five-Meter, Linear Theta-Pinch

NRL Conference on Sub-LF Downlink Satellite Communications, Washington, D.C., June 6-9, 1972

D. W. Forslund J. M. Kindel E. L. Lindman	Non-Linear Evolution of Whistler Decay Instabilities
D. W. Forslund J. M. Kindel E. L. Lindman	Parametric Instabilities of VLF Waves

18th Annual ANS Meeting, Las Vegas, Nevada, June 18-22, 1972

T. A. Oliphant F. L. Ribe	Gas-Dynamic Fuel Cycling in a Pulsed Fusion Reactor
S. C. Burnett W. R. Ellis F. L. Ribe	Parameter Study of a Pulsed High-Beta Fusion Reactor

Gordon Research Conference, Tilton Academy, New Hampshire, June 19-23, 1972

J. C. Ingraham	Classical Heating Effects in Anomalous AC Restivity Measurements
D. W. Forslund	Theory of the Microstructure of the Earth's Bow Shock

CTR Standing Committee Meeting, Los Alamos, New Mexico, June 21-22, 1972

F. L. Ribe J. Marshall	Projected LASL Experiments to Study Shock Heating, Wall Stabilization, Theta-Pinch Staging and Plasma Sheath Scaling
F. L. Ribe	Theta-Pinch Research–Future Plans

Second Topical Conference on Pulsed High-Beta Plasmas, Garching bei Munchen, West Germany, July 3-6, 1972

L. C. Burkhardt J. N. DiMarco P. R. Forman A. Haberstich H. J. Karr J. A. Phillips	Recent Results from the Shock-Heated Toroidal Z-Pinch Experiment ZT-1
W. R. Ellis C. F. Hammer F. C. Jahoda W. E. Quinn F. L. Ribe R. E. Siemon	Plasma Experiments on $\ell = 1,0$ Helical Equilibria in the Scyllac 5-Meter Theta-Pinch Toroidal Sector
S. C. Burnett W. R. Ellis F. L. Ribe T. A. Oliphant, Jr.	Pulsed High-β Fusion Reactor Based on the Theta Pinch
R. F. Gribble S. C. Burnett C. R. Harder	Feedback Stabilization of an $\ell = 1$ Theta-Pinch Plasma Column

K. S. Thomas H. W. Harris F. C. Jahoda G. A. Sawyer R. E. Siemon	Plasma Experiments in the Scyllac 5-Meter, Linear Theta Pinch
D. A. Baker L. W. Mann	MHD Stability Studies of Numerically Obtained Toroidal Equilibria
J. P. Freidberg B. M. Marder	MHD Stability of Diffuse Two-Dimensional Equilibria
J. P. Freidberg H. R. Lewis	A Vlasov-Fluid Model for Studying Gross Stability of High-Beta Plasmas
J. P. Freidberg	Stability of a Finite Beta, L Equals Two Stellarator
R. L. Morse J. P. Freidberg	Two-Stage Heating of Theta-Pinches
W. P. Gula R. L. Morse	Modeling of Long Straight Theta-Pinches
R. L. Morse	Absorption of Laser Light by Solid Targets

Massachusetts Institute of Technology, Cambridge, Massachusetts, August 18, 1972

J. C. Ingraham	Anomalous Microwave Absorption Near the Plasma Frequency

Fifth European Conference on Controlled Fusion and Plasma Physics, Grenoble, France, August 21-25, 1972

H. Dreicer R. F. Ellis J. C. Ingraham	Anomalous Microwave Absorption Near the Plasma Frequency
L. C. Burkhardt J. N. DiMarco P. R. Forman A. Haberstich H. J. Karr J. A. Phillips	Results from the Toroidal Z-Pinch Experiment ZT-1
S. C. Burnett W. R. Ellis R. F. Gribble C. F. Hammer C. R. Harder H. W. Harris F. C. Jahoda W. E. Quinn F. L. Ribe G. A. Sawyer R. E. Siemon K. S. Thomas	Survey of SCYLLAC Experiments
H. R. Lewis J. P. Freidberg	Application of the Vlasov-Fluid Model to High-Beta Stability

LLL, Livermore, California, September 8, 1972

E. L. Kemp	Contemporary Capacitive Energy Storage Systems

Seventh Intersociety Energy Conversion Engineering Conference, San Diego, California, September 25-29, 1972

S. C. Burnett W. R. Ellis T. Oliphant, Jr. F. L. Ribe	Design Study of a Pulsed High-Beta Fusion Reactor

Arizona State University, Tempe, October 12, 1972

J. L. Tuck	Energy for the Future with Special Reference to Fission and Fusion

Tbilissi School on Plasma Physics, Tbilissi, USSR October 2-11, 1972

H. R. Lewis	Theory of Waves in High-Beta Plasmas

Seventh Symposium on Fusion Technology, Grenoble, France, October 24-27, 1972

C. F. Hammer H. W. Harris W. E. Quinn G. A. Sawyer K. S. Thomas E. L. Kemp	Scyllac, Eighteen Months Later

ANS-AIF Meeting, Washington, D.C., November 12-16, 1972

F. L. Ribe	Fusion Reactor Systems

American Physical Society, Division of Plasma Physics Meeting, Monterey, California, November 13-16, 1972

L. C. Burkhardt J. N. DiMarco P. R. Forman A. Haberstich H. J. Karr J. A. Phillips	Experimental Results from the ZT-1 Toroidal Pinch
P. R. Forman S. Humphries, Jr. R. W. Peterson	Holographic Interferometry at 10.6 μm
A. Haberstich	MHD Stability of the ZT-1 Toroidal Z-Pinch
S. Humphries, Jr.	Multiple-Pass Laser Heating of a Magnetically Confined Plasma
P. R. Forman S. Humphries, Jr. R. W. Peterson	Holographic Interferometry at 10.6 μm
D. B. Thomson A. G. Bailey R. Engleman, Jr.	VUV Emission from a Neon-Seeded θ Pinch
H. R. Lewis	Application of the Vlasov-Fluid Model to High-Beta Stability

J. M. Kindel D. W. Forslund E. L. Lindman	Role of Stimulated Backscatter Instabilities in Laser Plasma Irradiation
D. W. Forslund J. M. Kindel E. L. Lindman	Parametric Instability of Oblique Collision-Free Shock Waves
J. P. Freidberg B. M. Marder H. Weitzner (NYU)	Magnetohydrodynamic Stability Properties of the $\ell = 0$ Bumpy Pinch
S. J. Gitomer D. W. Forslund	Temporal Cyclotron Damping - Theory and Simulation
E. L. Lindman D. W. Forslund J. M. Kindel	Nonlinear Evolution of Electromagnetic Parametric Instabilities
D. A. Baker L. W. Mann	MHD Stability of Diffuse Toroidal Equilibria
J. Nachamkin R. L. Morse C. W. Nielson	A Model for Calculating the Motion of Hot-Electron-Driven Material
C. W. Nielson R. L. Morse	Collisional Transport of Energetic Electrons in a Radiantly Heated Medium
B. M. Marder J. P. Freidberg H. Weitzner (NYU)	Magnetohydrodynamic Stability Properties of a Helically Symmetric $\ell = 1$ Pinch
R. L. Morse C. W. Nielson	Occurrence of High Energy Electrons and Surface Expansion in Radiantly Heated Target Plasmas
S. C. Burnett W. R. Ellis T. A. Oliphant, Jr. F. L. Ribe	A Reference Fusion Reactor Based on the Theta Pinch
K. S. Thomas H. W. Harris F. C. Jahoda G. A. Sawyer R. E. Siemon	Plasma Experiments on the Scyllac 5-Meter Linear θ Pinch
S. C. Burnett R. F. Gribble C. R. Harder K. J. Kutac	Feedback Stabilization Experiments on the Scylla IV-3 Plasma Column
W. R. Ellis F. C. Jahoda R. E. Siemon	Measured Plasma Parameters in the Scyllac Toroidal Sector
W. E. Quinn W. R. Ellis C. F. Hammer F. L. Ribe	Plasma Experiments in the Scyllac 5-Meter Toroidal-Sector Theta Pinch
R. F. Ellis J. C. Ingraham H. Dreicer	Anomalous Microwave Absorption Near the Plasma Frequency: Effective Collisionless Frequency and Electron Heating
J. C. Ingraham H. Dreicer R. F. Ellis	Threshold for Onset of Anomalous Microwave Absorption Near the Plasma Frequency
H. Dreicer R. F. Ellis J. C. Ingraham	Weak Field Electrical Resistivity Observations Near the Electron Plasma Frequency

Texas Symposium on the Technology of Controlled Thermonuclear Fusion Experiments and the Engineering Aspects of Fusion Reactors, Austin, November 20-22, 1972

H. L. Laquer J. D. G. Lindsay E. M. Little J. D. Rogers D. M. Weldon	Design Options and Trade Offs in Superconducting Magnetic Energy Storage with Irreversible Switching
K. I. Thomassen (MIT)	Magnetic Energy Transfer and Storage Systems
R. F. Gribble	The SCYLLAC MHD Feedback System
E. L. Kemp	Fusion Engineering at the Los Alamos Scientific Laboratory
F. L. Ribe	Staged Theta Pinches with Implosion Heating
S. C. Burnett W. R. Ellis F. L. Ribe	Parameter Study of a Pulsed High-Beta Fusion Reactor

AGU Fall Annual Meeting, San Francisco, California, December 4-7, 1972

J. R. Asbridge S. J. Bame W. C. Feldman H. R. Lewis, Jr.	An Empirical Closure Relation for the Vlasov Moment Equations

IEEE 1972 Nuclear Science Symposium, Miami Beach, Florida, December 5-7, 1972

E. L. Kemp	Contemporary Capacitive Energy Storage Systems